Allosteric Modulation of Cys-loop Receptors

by

David Daniel Mowrey

B.S. Biochemistry Molecular Biology, Wittenberg University, 2008

Submitted to the Graduate Faculty of University of Pittsburgh School of Medicine
in partial fulfillment of the requirements for the degree of

Doctor of Philosophy

University of Pittsburgh

2014

UNIVERSITY OF PITTSBURGH

SCHOOL OF MEDICINE

This dissertation was presented

by

David Daniel Mowrey

It was defended on

January 30th 2014

and approved by

Dr. Pei Tang, Professor, Anesthesiology

Dr. Ivet Bahar, Professor, Computational and Systems Biology

Dr. Daniel M Zuckerman, Associate Professor, Computational and Systems Biology

Dr. Maria Kurnikova, Associate Professor, Chemistry, Carnegie Mellon University

Dissertation Advisor: Dr. Pei Tang, Anesthesiology

ALLOSTERIC MODULATION OF CYS-LOOP RECEPTORS

David Daniel Mowrey, PhD

University of Pittsburgh

The Cys-loop receptor superfamily includes the $GABA_A$, $GABA_C$, glycine, and serotonin receptors as well as the nicotinic acetylcholine receptors (nAChRs). Cys-loop receptors are important drug targets for Parkinson's disease, Alzheimer's disease, and nicotine addiction. They are also targets of general anesthetics. Understanding the mechanisms of allosteric modulation for Cys-loop receptors has implications for the design of novel therapeutics for the treatment of pain, inflammation, and neurological disease. I employed a combination of computational and experimental approaches to understand allosteric modulation of these receptors. Four major contributions resulted from my graduate research:

1) NMR structures of the transmembrane (TM) domains of the α7 and α4β2 nAChRs as well as the α1 glycine receptor were resolved to provide a scaffold for rationalizing drug-binding sites and drug action. While all structures revealed the typical four-helix bundle, differences were observed which could affect drug binding and allosteric modulation.

2) Computational and experimental results showed that the general volatile anesthetic halothane bound to both α7 and α4β2 nAChRs, despite different sensitivities of these receptors to halothane. NMR data also revealed that volatile anesthetics halothane and isoflurane bound to the EC end of the β2 TM domain, but only at the IC end of the α7 TM domain.

3) We not only revealed the drug binding sites but also determined that the binding site at the EC end of the TM domain is functionally relevant.

4) Several factors critical to allosteric modulation in Cys-loop receptors were identified. Applying the perturbation-based Markovian transmission model to GLIC, we identified signaling pathways of agonist-induced channel gating. Using NMR, we identified a link between protein dynamics changes and allosteric modulation. Molecular dynamics simulations suggested that asymmetric binding of the anesthetic propofol to GLIC facilitated the transition from an open- to a closed-channel structure. The study provides evidence that ligand-induced asymmetry facilitates conformational transitions.

ACKNOWLEDGEMENTS

I extend my sincerest thanks to my advisor Prof. Pei Tang for all of her support, guidance, and assistance that she has provided throughout my graduate studies. Additionally, I thank Prof. Yan Xu for his guidance and advice on various research projects. It has been a great honor to work in their labs.

I am grateful for all the members of the Tang and Xu labs for their help and support. In particular, I thank Dr. Vasyl Bondarenko and Dr. Tanxing Cui for their help with NMR data collection, processing, and analyses. I thank Dr. Tommy Tillman, Dr. Qiang “Charles” Chen and Mr. Edom Seyoum for their assistance with protein preparation, X-ray crystallography data, and electrophysiology measurements. I thank the former lab members Dr. Mary Cheng, Dr. Dan Willenbring, and Dr. Liu Lu for their help with MD simulations and data analyses. I thank Ms. Sandra C. Hirsch for her editorial assistance.

I thank all the members of my Thesis committee Prof. Ivet Bahar, Prof. Daniel Zuckerman, and Prof. Maria Kurnikova for serving on the committee and providing valuable feedback for this thesis.

I thank all of the collaborators for their contributions to the projects that lead to this thesis, namely Prof. Jie Wu, Prof. Jie Liang, Prof. Peijun Zhang, and Prof. Xinghua Lu. I also thank Prof. Chakra Chennubhotla for stimulating discussions concerning Markov propagation, and Dr. Hsiao-Mei Lu and Ms. Gamze Gursoy for help with the PMT Model. I thank Prof. Rieko Ishima for helpful instructions concerning NMR theory.

I thank the CPCB program for providing me with this great opportunity to pursue my graduate studies. Additionally I thank Ms. Kelly Gentille and Ms. Sandra Yates for all of their help with administrative details.

Finally, I express my great appreciation for my friends and family for all of their love and support. Especially, I thank my parents for their unconditional love, support, and guidance over the years.

TABLE OF CONTENTS

LIST OF TABLES

LIST OF FIGURES

LIST OF ABBREVIATIONS

5HT	5-hydroxytryptamine
ACSF	artificial cerebrospinal fluid
ANM	anisotropic network model
CBFS	8-(chloromercuri)-2-dibenzofuransulfonic acid
CD	circular dichroism
cryo-EM	cryo-electron microscopy
CSI	chemical shift index
DMSO	Dimethyl sulfoxide
DSS	2,2-dimethyl-2-silapentane-5-sulfonate
DTT	dithiotreitol
EC	extracellular
ECD	extracellular domain
ELIC	*Erwinia chrysanthemi* ligand-gated ion channel
EM	electron microscopy
$GABA_A$	γ-aminobutyric acid type A
$GABA_C$	γ-aminobutyric acid type C
GLIC	*Gloeobacter violaceus* ligand-gated ion channel
GluCl	glutamate-gated chloride channel
GlyR	glycine receptor
GlyR	glycine receptor
GNM	Gaussian network model
hGlyR-α1	human glycine receptor α1 subunit
HSQC	heteronuclear single quantum coherence
IC	intracellular
ICD	intracellular domain
LDAO	lauryl dimethylamine oxide
LPPG	lyso-1-palmitoylphosphotidylglycerol
LUV	large unilamellar vesicles
MAS	magic angle spinning
MD	molecular dynamics
MIT	magnetization inversion transfer
MLA	methyllycaconitine
MTSL	(1-oxy-2,2,5,5-tetramethyl-D-pyrroline-3-methyl)-methanethiosulfonate
nAChR	nicotinic acetylcholine receptor
NMA	normal mode analyses
NMR	nuclear magnetic resonance
NOE	nuclear overhauser effect
NOESY	nuclear overhauser effect spectroscopy
PC	phosphatidylcholine
PCA	principle component analysis
PCR	polymerase chain reaction

PDB	protein data bank
PG	phosphatidylglycerol
pLGIC	pentameric ligand-gated ion channel
PMT	perturbation-based Markovian transmission
PRE	paramagnetic relaxation enhancement
RDC	residual dipolar coupling
RMSD	root mean square deviation
RMSF	root mean square fluctuation
SCAM	substituted cysteine accessibility method
SEC	size exclusion chromatography
SEC-MALS	size exclusion chromatography–multi-angle light scattering
STD	saturation transfer difference
TEV	tobacco etch virus
TFA	trifluoroacetic acid
TFE	2,2,2-trifluoroethanol
[^{125}I]TID	3-trifluoromethyl-3-(*m*-[^{125}I]iodophenyl) diazirine
TM	transmembrane
TMD	transmembrane domain
TOCSY	total correlation spectroscopy
TROSY	transverse relaxation optimized spectroscopy
VDB	ventral diagonal band
VDW	van der Waals
VTA	ventral tegmental area

PREFACE

Much of this dissertation has been published. The list of publications is included below.

Mowrey D, Haddadian EJ, Liu LT, Willenbring D, Xu Y, Tang P. (2010). Unresponsive correlated motion in α7 nAChR to halothane binding explains its functional insensitivity to volatile anesthetics. *J Phys Chem B.* 114: 7649 – 7655.

Mowrey DD, Cui T, Jia Y, Makhov AM, Zhang P, Tang P, Xu Y. (2013). Open-Channel Structures of the Human Glycine Receptor α1 Full-Length Transmembrane Domain. *Structure.* 21(10): 1-8.

Mowrey DD, Liu Q, Bondarenko V, Chen Q, Seyoum E, Xu Y, Wu J, Tang P. (2013) Insights into Distinct Modulation of α7 and α7β2 nAChRs by the Volatile Anesthetic Isoflurane. *J. Biol Chem* 288(50): 35793-35800.

Mowrey D, Chen Q, Liang Y, Liang J, Xu Y, Tang P. (2013) Signal transduction pathways in the pentameric ligand-gated ion channels. *PLoS ONE* 8(5): e64326.

Mowrey D, Cheng MH, Liu LT, Willenbring D, Wymore T, Xu Y, Tang P. (2013). Asymmetric ligand binding facilitates conformational transitions in pentameric ligand-gated ion channels. *J Am Chem Soc.* 35(6): 2172-2180.

Bondarenko V, **Mowrey D***, Liu LT, Xu Y, Tang P. (2013). NMR resolved multiple anesthetic binding sites in the TM domains of the α4β2 nAChR. *Biochim Biophys Acta*. 1828(9): 398-404. *co-first author

Bondarenko V, **Mowrey D**, Tillman T, Cui T, Liu LT, Xu Y, Tang P. (2012). NMR structures of the transmembrane domains of the α4β2 nAChR. *Biochim Biophys Acta*. 1818(5):1261-1268

Bondarenko V, **Mowrey DD**, Tillman TS, Seyoum E, Xu Y, Tang P. (2014) NMR structures of the human α7 nAChR transmembrane domain and associated anesthetic binding sites. *Biochim Biophys Acta*. (Accepted)

Pan J, Chen Q, Willenbring D, **Mowrey D**, Kong XP, Cohen A, Divito CB, Xu Y, Tang P. (2012). Structure of the Pentameric Ligand-Gated Ion Channel GLIC Bound With Anesthetic Ketamine. *Structure.* 20(9): 1463-1469.

Two additional publications that have not been included in this thesis:

Willenbring D, Liu LT, **Mowrey D**, Xu Y, Tang P. (2011) Isoflurane alters the structure and dynamics of GLIC. *Biophys J*. 101(8):1905 -1912.

Cui T, **Mowrey D**, Bondarenko V, Tillman T, Ma D, Landrum E, Perez-Aguilar JM, He J, Wang W, Saven JG, Eckenhoff RG, Tang P, Xu Y. (2011) NMR structure and dynamics of a designed water-soluble transmembrane domain of nicotinic acetylcholine receptor. Biochim Biophys Acta. 1818(3): 617-626.

CHAPTER 1

INTRODUCTION

1.1. BACKGROUND

Cys-loop receptors mediate the fast synaptic transmission in the central and peripheral nervous systems. They are pentameric ligand-gated ion channels (pLGICs) formed from five identical or homologous subunits arranged symmetrically or pseudo-symmetrically around a central channel axis. Each subunit contains an extracellular domain (ECD), a transmembrane domain (TMD) comprised of four transmembrane (TM) helices (TM1 to TM4), and a large flexible intracellular domain (ICD) connecting TM3 and TM4 [1]. In the typical physiological response, neurotransmitters bind to the orthosteric sites located in the ECD and trigger the opening of the channel gate located in TM2 to allow the flow of ions (Figure 1.1.1). However, channel activity can also be modulated by a variety of ligands, including general anesthetics, binding to other allosteric sites on these receptors. The diverse responses to allosteric modulation of channel activities contribute to the pharmacological diversity of the Cys-loop receptor superfamily.

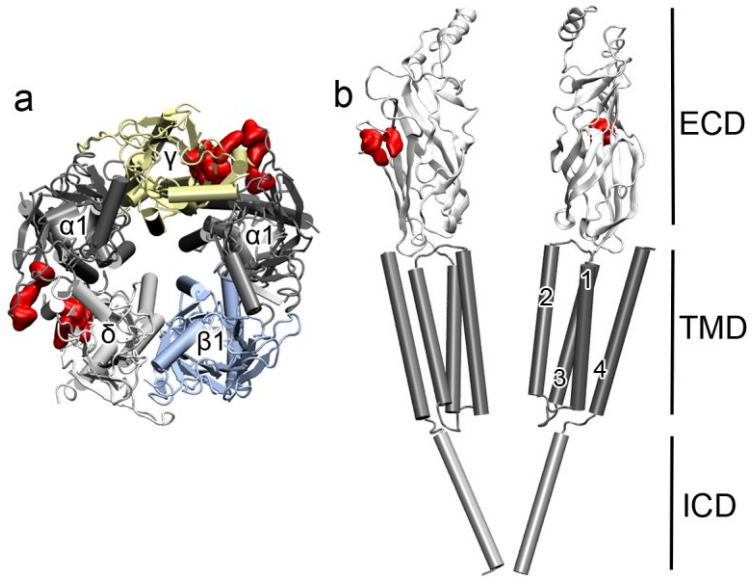

Figure 1.1.1. Structural topology of the Cys-loop receptor. (**a**) Top view of the Cys-loop receptor showing the quaternary arrangement of the five subunits around the central channel axis and side. (**b**) Side view of the Cys-loop receptor highlighting the extracellular (EC), transmembrane (TM) and intracellular (IC) domains. The four TM helices are labeled 1 through 4 corresponding to TM1 through TM4, respectively. The 4 Å resolution structure of the muscle-type nAChR (PDB ID: 2BG9) was used as the structural template [1]. The orthosteric binding sites are highlighted in red.

The Cys-loop receptor superfamily includes the γ-aminobutyric acid type A and type C ($GABA_A$ and $GABA_C$), glycine, serotonin ($5HT_3$) and the nicotinic acetylcholine (nACh) receptors. The GABA and glycine receptors are anionic or inhibitory channels that are selective for chloride and are potentiated by general anesthetics at clinically relevant concentrations. In contrast, nicotinic acetylcholine receptors (nAChRs) are cation selective or excitatory channels and are generally inhibited by anesthetics [2]. The diverse responses of Cys-loop receptors to allosteric modulators, particularly anesthetics, provide an intriguing base for research into the mechanisms of allosteric modulation. Diverse allosteric responses to anesthetics can even be found among the neuronal nAChRs, a

subset of the Cys-loop receptor superfamily. The neuronal nAChRs are comprised of α (α2–α10) and β (β2–β4) subunits. Among these subunit subtypes, the α7 subunit can exist as a functional homopentamer [3], while other subunits require combinations of α and β subunits to form functional pentamers [4], as is the case for the α4β2 nAChR. The α7 and α4β2 nAChRs exhibit highly distinct sensitivities to volatile anesthetics. Despite ~60% sequence homology, the α4β2 nAChR is hypersensitive to volatile anesthetics at clinically relevant concentrations, while the α7 nAChR is insensitive to volatile anesthetics at clinically relevant concentrations [5,6]. Differences in anesthetic modulation for such homologous subunits provide the platform to probe what makes one subunit more susceptible to allosteric modulation by anesthetics than the other. Functional α7β2 pentamers have been identified which offer the opportunity to compare effects of anesthetics between homopentameric α7 nAChRs and heteropentameric α7β2 nAChRs [7].

The functional diversity of receptor responses to allosteric modulation provides a great opportunity and challenge to determine the molecular mechanisms of allosteric modulation. Due to the complexity of these receptors, combined with intrinsic difficulties of working with membrane proteins, the molecular mechanisms of allosteric modulation of Cys-loop receptors have not been well understood. While the goal of fully understanding these mechanisms is too large to be covered in this thesis, the research presented here has made substantial contributions towards this goal. My thesis work provides insights into the action of allosteric modulators acting on Cys-loop receptors. To this end, I have employed a combination of computational and experimental approaches to determine the specific anesthetic binding sites within nAChRs, which binding sites are

functionally relevant, and the mechanism by which ligand binding affects the functional response.

1.2. MOTIVATION

Cys-loop receptors are important pharmacological targets for therapeutic drugs. In particular, the α7 and α4β2 nAChRs are found in high abundance in the brain [8,9]. Their roles in the central nervous system make them likely candidates for therapeutics targeting neurological diseases, including Parkinson's disease [10], Alzheimer's disease [11], and nicotine addiction [12,13]. The α7 nAChR is also a target for therapeutics involved with angiogenesis and inflammation [14,15]. Cys-loop receptors are also targets of general anesthetics. The nAChRs have been implicated in anesthetic action associated with memory [16], nociception [17], and the autonomic response [18]. The $GABA_A$ receptor has been implicated in sedation, amnesia, and muscle relaxation, while the glycine receptor has been implicated in immobility [19-21]. Understanding the mechanisms of allosteric modulation for Cys-loop receptors therefore has implications for the design of novel therapeutics for the treatment of pain, inflammation, and neurological disease.

1.3. GOALS AND ACCOMPLISHMENTS

1.3.1. Open Questions

While previous studies have determined the location of the neurotransmitter-binding site within Cys-loop receptors [22-25], the sites of anesthetic interaction within Cys-loop

receptors remain unclear. This is primarily due to the small size and low affinity of anesthetics, which makes specific protein-anesthetic interactions difficult to identify. The small size and low affinity of anesthetics also makes them more likely to bind to many non-specific locations. In order to determine how ligand binding affects channel function, one must determine the ligand binding sites and which binding sites are functionally relevant. Moreover, even though a functionally relevant site of ligand binding has been identified, as in the case of neurotransmitter binding, it is still challenging to determine the precise mechanism of allosteric action. In this thesis, my work has sought to provide insights into the action of allosteric modulators acting on Cys-loop receptors. To this end, I have employed and combination of computational and experimental approaches to address the following three questions:

1) What are the specific binding locations of general anesthetics within the structures of nAChRs?
2) Which binding sites are responsible for the functional response?
3) How does ligand binding at functionally relevant sites elicit the functional response?

1.3.2. Summary of Achievements

Four major contributions resulted from this thesis work: 1) resolved solution NMR structures for the α1 glycine receptor TMD, as well as the α4β2 and α7 nAChR TM domains that provide scaffolds for determining ligand-binding sites; 2) determined the sites of anesthetic binding within the α4, β2, and α7 nAChR subunits; 3) identified which site is most likely functionally relevant; and 4) finally, identified factors critical to the

allosteric modulation in Cys-loop receptors. Each of these contributions is summarized below and covered in detail in the subsequent chapters.

Structures of Cys-loop Receptor TM Domains (Chapter 2)

The Cys-loop receptor structure was first determined for the muscle-type nAChR found in *Torpedo marmorata* by cryo-electron microscopy (cryo-EM) at 4 Å resolution [1]. More recently, high-resolution crystal structures have been obtained from homologous receptors found in the bacteria *Erwinia chrysanthemi* (ELIC) [26] and *Gloeobacter violaceus* (GLIC) [27,28] as well as the glutamate-gated chloride channel (GluCl) found in *Caenorhabditis elegans* [29] determined at 3.3 Å, 2.9 Å, and 3.3 Å, respectively. While the EC domain has been well-characterized by crystal structures of acetylcholine binding proteins (AChBPs) [24,30,31], the ECD of the mouse α1 subunit [32], and the α7/AChBP chimera [33], structures for the TMD have remained sparse, primarily due to difficulties inherent in working with membrane proteins. Crystal structures of full-length receptors solved from bacterial homologues and the glutamate chloride receptor, as well as the low-resolution cryo-EM structure of the muscle type nAChR from *Torpedo marmorata,* have provided valuable information into the structure of the TM domains for Cys-loop receptors.

In the past, full-length structures for mammalian Cys-loop receptor TM domains were unavailable, despite their importance as drug targets [34,35]. In this section of the thesis the NMR determined structures for full-length TM domains of the human α7, α4, and β2 nAChRs in lauryldimethylamine-oxide (LDAO) [36,37] as well as the human glycine receptor α1 subunit in lyso-1-palmitoylphosphotidylglycerol (LPPG) [38] are discussed. While all structures revealed the typical four-helix bundle, subtle differences in cavity sizes and helical tilting have been observed among the solved structures, which could affect drug

binding and allosteric modulation of the channel [37,39,40]. This finding underscores the importance of full structure determination even when structures for homologous proteins exist. Furthermore, the NMR structure of human α1 glycine receptor revealed a novel kink in the TM3 helix, which is likely involved in the function of the glycine and $GABA_A$ receptors [38]. Structure determination of the full-length TM domains for human Cys-loop receptors are therefore an important contribution for the purpose of designing specific allosteric modulators.

Anesthetic Binding Sites (Chapter 3)

To determine sites of anesthetic interaction within Cys-loop receptors we employed both computational and experimental methods. Early work on the muscle-type nAChR using photo-affinity labeling suggested multiple binding sites for the volatile anesthetic halothane in the ECD and at the EC/TM interface [41]. Molecular docking and molecular dynamics (MD) simulation on the α4β2 nAChR performed previously in the lab demonstrated halothane-binding sites in the ECD and at the EC/TM interface similar to the previous study [42,43]. In subsequent work on the α7 nAChR, similar results were observed with the addition of a novel site observed at the intracellular (IC) end of the TMD [44]. The site at the EC/TM interface was later confirmed by solution NMR for the β2 nAChR for the volatile anesthetics halothane and isoflurane and the intravenous anesthetic ketamine [39,40], showing an intra-subunit site located at the extracellular (EC) end of the TMD. While not observed in the previous photo-affinity labeling experiments on the muscle-type nAChR, the computationally predicted site observed at the IC end of the TMD for the α7 nAChR was observed using NMR for the anesthetics halothane, isoflurane, and ketamine in the α7 nAChR [37,39,40].

Functionally Relevant Anesthetic Binding (Chapter 4)

Ligand binding does not necessitate a resultant functional effect. Therefore, it is necessary to ascertain which binding sites are necessary to produce the functional effect. MD simulations of the α7 nAChR compared to simulations of the α4β2 nAChR suggested that the β2 subunit was responsible for the difference in anesthetic sensitivity between α7 and α4β2 [44]. From this result, we predicted that the α7β2 nAChR would be sensitive to volatile anesthetics. In a subsequent study we experimentally confirmed our computational prediction. NMR data revealed that isoflurane bound to the EC end of the β2 TMD, but not the α7 TMD. Mutations to cavity lining residues in TM2 confirmed the result. Furthermore, significant dynamics changes were observed for the pore-lining residues, only in the β2 TMD, suggesting that only the drug binding that can affect the channel dynamics will produce a functional effect [40].

Our work has also covered potential sites of action for the intravenous anesthetic ketamine on the α7 nAChR. In contrast to volatile anesthetics, ketamine is a more effective inhibitor of the α7 nAChR than the α4β2 nAChR [45,46]. NMR studies on the α7 TMD demonstrated that the site of ketamine binding was similar to that of isoflurane or halothane binding in the α7 TMD. However, only ketamine binding affected the channel gate residue (L9'). While functional measurements confirmed that the α7 TMD could be inhibited by ketamine, we cannot rule out the possibility of ketamine inhibition via a site in the ECD, as suggested by our work with GLIC [47]. The crystal structure of the GLIC-ketamine complex showed ketamine binding to a site in the ECD of GLIC just below the C-loop. Functional investigation using site-directed cysteine mutagenesis confirmed the functional relevance of the site to GLIC inhibition. In this work it was suggested that

ketamine binding was facilitated by charged residues surrounding the observed ketamine binding site, a feature shared with α7, but not α4β2 [47].

Mechanisms of Allosteric Modulation (Chapter 5)

Perhaps the most challenging question to address is the molecular mechanism by which allosteric ligand binding to the receptor affects the conductance of ions through the channel pore. While this work does not fully provide the answer to this question, the work contributes toward achieving this goal. The contributions are three-fold. We computationally identified likely molecular pathways involved in agonist-induced channel gating. Using NMR, we identified protein dynamics changes linked to allosteric modulation of the channel. Finally, our results from molecular dynamics suggested that asymmetry of ligand binding may be important for conformational transitions in proteins.

Molecular pathways of agonist binding were determined by applying the perturbation-based Markovian transmission (PMT) model to the Cys-loop receptor homologue GLIC. The PMT model is a course-grained model developed by Lu and Liang [48] that builds on prior work by Chennubhotla and Bahar treating allosteric propagation as a Markov process [49]. The PMT model was used in conjunction with Yen's algorithm [50] to determine the most likely paths of allosteric transmission through the receptor. Among the top ten paths from nine different perturbations we achieved a consensus of two primary paths between the ECD and the channel gate residue. The first was an intra-subunit pathway consistent with the conformational wave theory for channel gating [51,52]. The second path, however, was a novel inter-subunit pathway between TM domains of adjacent subunits [53].

Previous studies have demonstrated that mutations affecting anesthetic modulation often concurrently affect the intrinsic gating dynamics of the channel [54-56], suggesting that the propensity of the channel to allosteric modulations is intrinsically related to the channel gating dynamics. Our structural studies on the hGlyR-α1 TMD revealed a dynamic segment between the EC ends of TM2 and TM3, which could be related to functional effects of observed for both agonist binding and the binding of other allosteric modulators [38]. The study suggested that allosteric modulation of the receptor was related to the dynamics of this site. This notion was supported by other studies demonstrating the importance of dynamics at the EC end of TM2 to channel gating [57,58]. Our NMR studies on the neuronal nAChRs also underscored the importance of dynamics to channel gating. Only the anesthetic binding that could significantly change the channel dynamics could be correlated to functional consequences. Particularly, it was observed that isoflurane binding at the EC end of the TMD could substantially reduce dynamics for nearby residues in TM2 [40].

Finally, our work has suggested that the symmetry of ligand binding may also play an important role in ligand-induced conformational transitions. Previous functional experiments have shown that ligand binding to only three of five symmetric agonist binding sites in homomeric Cys-loop receptors produces the maximum current response [59-61]. Our MD simulations suggest that asymmetric binding of the anesthetic propofol to GLIC can facilitate the transition from an open-channel structure to a closed-channel structure [62]. In the study, systems with propofol asymmetrically bound to one, two, or three sites could produce a greater conformational heterogeneity of TM2 tilting angles associated with more rapid channel dehydration as compared to symmetric systems with

zero or five propofol molecules bound. The results indicate that ligand-induced asymmetry may be necessary to facilitate conformational transitions from one channel state to another, and therefore play an important role in the molecular mechanisms of allosteric modulation.

CHAPTER 2

STRUCTURES OF CYS-LOOP RECEPTOR TRANSMEMBRANE DOMAINS

2.1. NMR STRUCTURES OF NEURONAL NACHRS

This section has been published in *Biochim Biophys Acta* **1818** (5): 1261-1268 and *Biochim Biophys Acta* (in press, 2014).

2.1.1. Background and Significance

The α7 and α4β2 nAChRs are two of the most abundant nAChR subtypes in the brain [3,8]. Both nAChRs have been recognized for the important roles they play in learning, memory, and cognition [16,63,64]. Consequently, they are likely candidates for therapeutics targeting a variety of neurological diseases, including Parkinson's disease [10], Alzheimer's disease [11,65], schizophrenia [65], and nicotine addiction [12,13]. The α7 nAChR is also a target for therapeutic modulation of angiogenesis and inflammation [14,15]. Despite the importance of the α7 and α4β2 nAChRs as targets for therapeutic modulation, experimental structural characterization of these receptors has remained sparse [66-68].

Structural characterization of the TM domains for individual Cys-loop receptors is necessary to identify drug-binding sites, design novel therapeutics, and discover the molecular mechanisms of drug action [69,70]. The TMD contains the channel gate and therefore is the critical region for controlling the flow of ions across the membrane [71].

Positive and negative allosteric modulators acting on the nAChR TM domains have been implicated as useful therapeutics for neurological diseases [72-74]. The TMD also provides binding sites for both intravenous and inhalational general anesthetics. The intravenous anesthetic etomidate binds to the TMD of the *Torpedo* nAChR [75]. The inhalational anesthetic halothane has shown evidence of binding to nAChR TM domains both experimentally in the *Torpedo* nAChR [41] and computationally in the α4β2 and α7 nAChRs [42-44]. High-resolution structural information of nAChR TM domains is important both for characterizing mechanisms of action for existing drugs and for indentifying plausible binding sites for new drugs.

In this section, we present the NMR structures for the TM domains of the α7, α4, and β2 nAChR subunits using LDAO micelles as a membrane mimetic. In LDAO micelles, both α4β2 and α7 nAChR TM domains spontaneously form pentameric assemblies. Reconstituting the α4β2 nAChR into lipid vesicles, we demonstrated that the α4β2 assemblies retained their functional capability to transporting Na^+ ions. Further functional assays performed by injecting the α7 nAChR TM domain into *Xenopus laevis* oocytes revealed that the α7 nAChR not only could conduct ions but also could be modulated by ivermectin and ketamine. Together the functional assays suggest that the α7 and α4β2 TM domains retain their pharmacologically relevant features. High-resolution structures of the individual α7, α4, and β2 TM domains, as well as the assembled pentameric structural model for the α4β2 nAChR TM domain, provide valuable templates for rationalizing mechanisms of channel function and drug action.

2.1.2. Methods

Sample Preparations

Proteins were expressed in *Escherichia coli* Rosetta 2(DE3) pLysS (Novagen) at 15 °C for ~3 days using the Marley protocol [76]. The ECD at the N-terminus was replaced with a TEV protease recognition site and a histidine tag. A short synthetic linker 'GGGEG' replaced the ICD for the α7 TMD. For α4 and β2 TM domains the synthetic linker 'GGGGG' replaced the ICD. Each α7, α4, or β2 TM domain contains 137 residues with an approximate molecular weight of 15 kDa. Glutamate mutations at the N- and C-termini, designed to lower the pI, were necessary to secure protein stability for NMR measurements. Mutation of three hydrophobic residues to serine within the TM2-TM3 linker of α7, α4, or β2 was also instrumental to prevent protein destabilization. Direct exposure of hydrophobic residues to the aqueous phase in the absence of the ECD resulted in protein aggregation and precipitation in a short time period. Amino acid sequences showing mutations of the α7, α4, and β2 TM domains are shown in Figure 2.1.1. The expressed proteins were purified by Ni-NTA (GE Healthcare) chromatography before and after overnight cleavage of the his-tagged region at 4 ºC. The purification buffer contained 50 mM Tris, 150 mM NaCl, and 0.5% LDAO, and proteins were eluted with imidazole. Each NMR sample had 0.25-0.3 mM protein, 1-2% (40-80 mM) LDAO, 5 mM phosphate acetate pH 4.7, 10 mM NaCl, and 20 mM 2-mercaptoethanol to prevent disulfide bond formation. 5% D_2O was added to the NMR samples for deuterium lock in NMR measurements. The α4 and β2 nAChRs natively form α4β2 heteropentamers. Therefore in the case of the α4 and β2 nAChR TM domains, we prepared four types of

samples: (1) pure α4; (2) pure β2; (3) α4:β2=2:3; and (4) α4:β2=3:2. The α7 nAChR natively forms homopentamers so only pure α7 NMR samples were prepared.

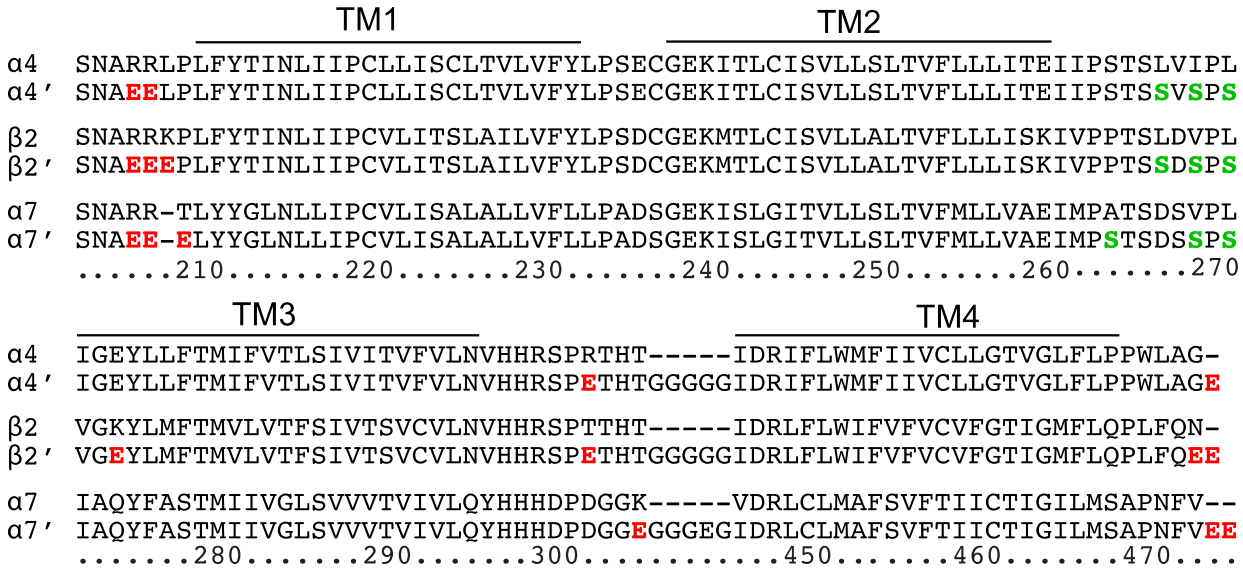

Figure 2.1.1. Sequence comparison for α4, β2, and α7 nAChRs and their respective NMR constructs, α4', β2', and α7'. Mutation of a few residues gave much more stable NMR samples. Glutamate mutations (highlighted in red), primarily at the N- and C-termini, lowered the isoelectric point and prevented protein precipitation at pH 4.7. Three serine mutations (highlighted in green) were introduced to the TM2-TM3 linker to increase sample stability in the absence of the ECD. The sequence numbering corresponds to that of the α7 nAChR.

NMR spectroscopy

NMR spectra were acquired at 45 ºC on Bruker Avance 600, 700, 800, and 900 MHz spectrometers equipped with a triple-resonance inverse-detection cryoprobe, TCI (Bruker Instruments, Billerica, MA). Spectral windows of 11 or 13 ppm (1024 data points) in the ^{1}H dimension and 22 or 24 ppm (128 data points) in ^{15}N dimension with a relaxation delay of 1 s (or 1.5 s at 900 MHz) were used for collecting ^{1}H-^{15}N TROSY-HSQC spectra. ^{1}H-^{13}C HSQC spectra were acquired as 1024 points in the ^{1}H dimension and 256 increments

in the ^{13}C dimension with spectral windows of 11 ppm (^{1}H) and 64 ppm (^{13}C). For α7 chemical shift assignment, a suite of NMR experiments were performed: HNCA (1024×28×72) and HN(CO)CA (1024×28×54), both with spectral windows of ^{1}H-12 ppm, ^{15}N-20.5 ppm, ^{13}C-19 ppm; HNCO (1024×32×40) with spectral widths of ^{1}H-11 ppm, ^{15}N-22 ppm, and ^{13}C-10 ppm; ^{15}N-edited NOESY (1024×36×104) with spectral windows of ^{1}H-11 ppm and ^{15}N-22 ppm, and a mixing time of 120 ms. For α4 and β2 chemical shift assignment, the NMR experiments performed included: HNCA and HN(CO)CA (1024 × 36 × 80) with a spectral window of 18 ppm in the ^{13}C dimension, HNCO (1024 × 36 × 40) with a ^{13}C spectral width of 10 ppm, ^{15}N-edited NOESY (1024 × 36 × 160) with a mixing time of 120 ms at 900 MHz and 150 ms at 700 MHz, and ^{13}C-edited NOESY (1024 × 36 × 192) with a mixing time of 150 ms. In addition, CBCA(CO)NH (1024 × 32 × 80) with a ^{13}C spectral window of 60 ppm was acquired. In order to evaluate the temperature dependence of individual residue chemical shifts, α4 and β2 ^{1}H-^{15}N TROSY-HSQC spectra were collected at 40, 43, 45, and 48 ºC. α7 ^{1}H-^{15}N TROSY-HSQC spectra were collected at 35, 40, and 45 °C The residues with temperature coefficients < 4.5 ppb/K were considered to have hydrogen binding [77]. The observed ^{1}H chemical shifts were referenced to the DSS resonance at 0 ppm and the ^{15}N and ^{13}C chemical shifts were indirectly referenced [78].

Size exclusion chromatography–multi-angle light scattering analysis

The molar masses of the protein-detergent complexes were determined using size exclusion chromatography (Superdex 200 10/300, GE Healthcare) coupled with multi-angle light scattering (HELEOS, Wyatt Technology), UV (Agilent 1100 Series; Agilent

Technology), and differential refractive index (Optilab rEX; Wyatt Technology) detection. The measurements were performed on the samples that had been used for NMR in 10 mM sodium acetate pH 4.6, 100 mM NaCl, 0.05% LDAO at a flow rate of 0.5 mL/min at room temperature. HELEOS calibration constants were determined in the same buffer using chicken egg lysozyme (Affymetrix) as the standard. Light scattering data was analyzed and the molar mass of the protein-detergent complex was determined using ASTRA software (Wyatt Technology) [79]. The conjugate analysis module of ASTRA was used to differentiate contributions of the protein and detergent to the molecular weight of each complex. The specific refractive index (dn/dc) values of 0.185 and 0.148 were used for the protein and LDAO detergent, respectively [80]. The UV extinction coefficients of α7, α4 and β2 were calculated from their sequences. A measured UV extinction coefficient of 0.06 for a 1% solution at 280 nm was used for LDAO.

Functional measurements for α7 in Xenopus laevis oocytes

The purified α7 TMD in LDAO detergent was reconstituted into asolectin vesicles by adsorption of detergent using Bio-Beads SM-2 non-polar polystyrene adsorbent (Biorad) in the presence of a 100:1 molar ratio of asolectin to protein following the manufacturer's instructions. The prepared vesicles (50 nl) containing 100 ng of α7 TM domain were injected into *Xenopus laevis* oocytes (stages 5–6). Oocytes were maintained in modified Barth's solution containing 88 mM NaCl, 1 mM KCl, 2.4 mM $NaHCO_3$, 15 mM HEPES, 0.3 mM $Ca(NO_3)_2$, 0.41 mM $CaCl_2$, 0.82 mM $MgSO_4$, 10 μg/mL sodium penicillin, 10 μg/mL streptomycin sulphate, and 100 μg/mL gentamycin sulphate, pH 6.7 at 18 °C. After 1-3 days, channel function was measured by two-electrode voltage clamp experiments [81].

Oocytes in a 20-µl oocyte recording chamber (Automate Scientific) were clamped at -60 mV with an OC-725C Amplifier (Warner Instruments) and currents were elicited using ivermectin as an agonist. The recording solutions contained 130 mM NaCl, 0.1 mM $CaCl_2$, 10 mM HEPES, pH 7.0 with the indicated concentrations of ivermectin and ketamine. Data were collected and processed using Clampex 10 software (Molecular Devices).

The Na^+ flux assay for functional measurements of α4β2

The Na^+ flux assay, as measured by the reduction of Sodium Green™ dye (Invitrogen, Carlsbad, CA) fluorescence due to Na^+ leaving the vesicles through open channels, is an effective way to macroscopically assess activity of the α4β2 TM channels. We prepared 25 mM vesicles with ~500 µM α4β2. The vesicles contained egg phosphatidylcholine (PC)/phosphatidylglycerol (PG) in a 3:1 molar ratio and lipid biotinyl-cap-PE (1 mol %). Lipids dissolved in chloroform were mixed with α4β2 and dried to a thin film by nitrogen gas. Residual organic solvent was removed by vacuum overnight. The lipid-protein mixture was hydrated overnight at 42°C with a buffer solution containing 20 mM Tris, 100 mM NaCl, and 3 µM Sodium Green™ at pH 7.5. The vesicles were obtained by multiple subsequent cycles of freeze/thaw and sonication. Sodium Green™ dye outside the vesicles was removed by extensive dialysis.

The Na^+ flux assay was performed using an Olympus IX81 microscope (Olympus America, Center Valley, PA), equipped with a Sutter Lambda xenon exciter light source, various excitation and emission filters, and an ORCA-ER digital camera. For each measurement, vesicles containing α4β2 were added onto the streptavidin coated glass slide. The image acquisition started before vesicles were washed with a buffer solution

(50mM $CaCl_2$ 20mM Tris at pH 7.5) to dilute the extra-vesicle Na^+ concentration. The resulting Na^+ concentration gradient drove Na^+ out of the vesicles when channels were formed. Consequently the fluorescence intensity resulting from Sodium Green™ trapped inside vesicles was reduced. Decay of the Sodium Green™ fluorescence intensity within each cluster of vesicles was recorded using the program In-vivo and analyzed by MetaMorph (Molecular Devices, Sunnyvale, CA).

Data processing, analysis and structure calculations

NMR data were processed using NMRPipe 4.1 and NMRDraw 1.8 [82], and analyzed using Sparky 3.10 [83]. ^1H, ^{15}N, and ^{13}C chemical shift assignments for the α7, α4, and β2 nAChR TM domains were performed manually using the acquired NMR spectra. Initial NOE cross-peak assignment was carried out manually and then more cross-peaks were assigned using CYANA 2.1 [84]. For α7, α4, and β2 subunits, a total of 100 monomer structures were calculated using CYANA 3.0 based on NOE and hydrogen-bonding restraints, as well as Talos dihedral angle restraints derived from the chemical shifts [85]. Restraints for α4, β2, and α7 are shown in Table 2.1.1, Table 2.1.2, and Table 2.1.3, respectively. Of these 100 structures, the 25 with the lowest target function underwent further refinement using Cyana 3.0. A final bundle of 20 structures with the lowest target function was analyzed using VMD [86] and Molmol [87].

The α4 and β2 structures with the smallest root mean square deviations (RMSD) from their respective average structures were used for building pentameric models. The MATLAB® programming environment was used to input structure coordinates, perform coordinate transformations, and save a pentamer model in PDB format. Individual

structures of α4 and β2 were first oriented such that each helical axis of TM2 was parallel to the *Z*-axis. The helical axis of TM2 was determined using only the backbone atoms of residues from 245 to 266 for α4 or 239 to 260 for β2. The structures were then duplicated to form $(\alpha4)_2(\beta2)_3$ and $(\alpha4)_3(\beta2)_2$ pentamers, where the center of the backbone atoms for each of the five TM2 helices was located on the vertices of a five-fold symmetric pentagon. Orientations of the α4 and β2 subunits were adjusted to satisfy the NMR chemical shift perturbation data, in which interacting residues between α4 and β2 were indicated. The pore lining residues (T248, S252, and V259) for the α4 subunit were also set to be consistent with experimental results from the substituted cysteine accessibility method [88]. We constructed two pentameric models of α4β2 with 2:3 and 3:2 ratios for α4 to β2. It is plausible that α4β2 in our sample preparation was in both stoichiometries [89,90]. The pentameric structural models were subjected to 2000 steps of steepest descent minimization in NAMD 2.6 [91] with a 100 kcal/mol restraint on backbone atoms. The pore radius profiles were obtained using the HOLE program [92] with a step size of 0.2 Å along the pore axis.

2.1.3. Structures of the α4 and β2 nAChR TM Domains

Structures of the TM domains for subunits α4 and β2 (Figure 2.1.2) were determined based on constraints generated from NMR experiments. (Figure 2.1.3, Table 2.1.1, and Table 2.1.2). The backbone RMSD of the helical regions among the 20 lowest energy structures for α4 or β2 is less than 1 Å. Because of their high sequence homology (~88%), the α4 and β2 TM domains share considerable structure similarity (Figure 2.1.2c), and the backbone RMSD of their helical regions is ~1.5 Å.

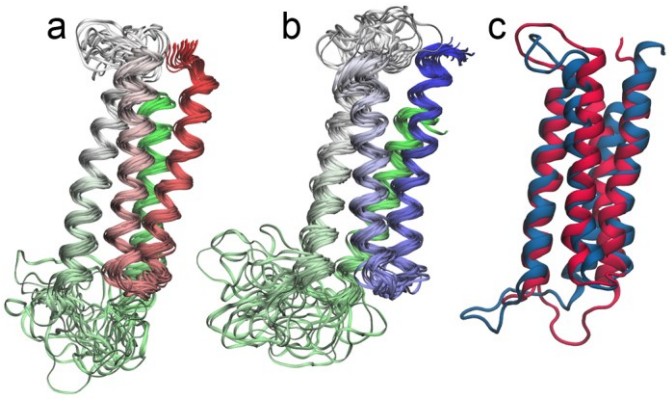

Figure 2.1.2. NMR structures of the α4 and β2 nAChR TM domains. Bundles of the 20 lowest-energy NMR structures for (**a**) α4 and (**b**) β2 nAChR TM domains**.** The color scheme varies from red in (a) or blue in (b) for TM1 to green for TM4. (**c**) Overlay of the representative structures of α4 (red) with β2 (blue).

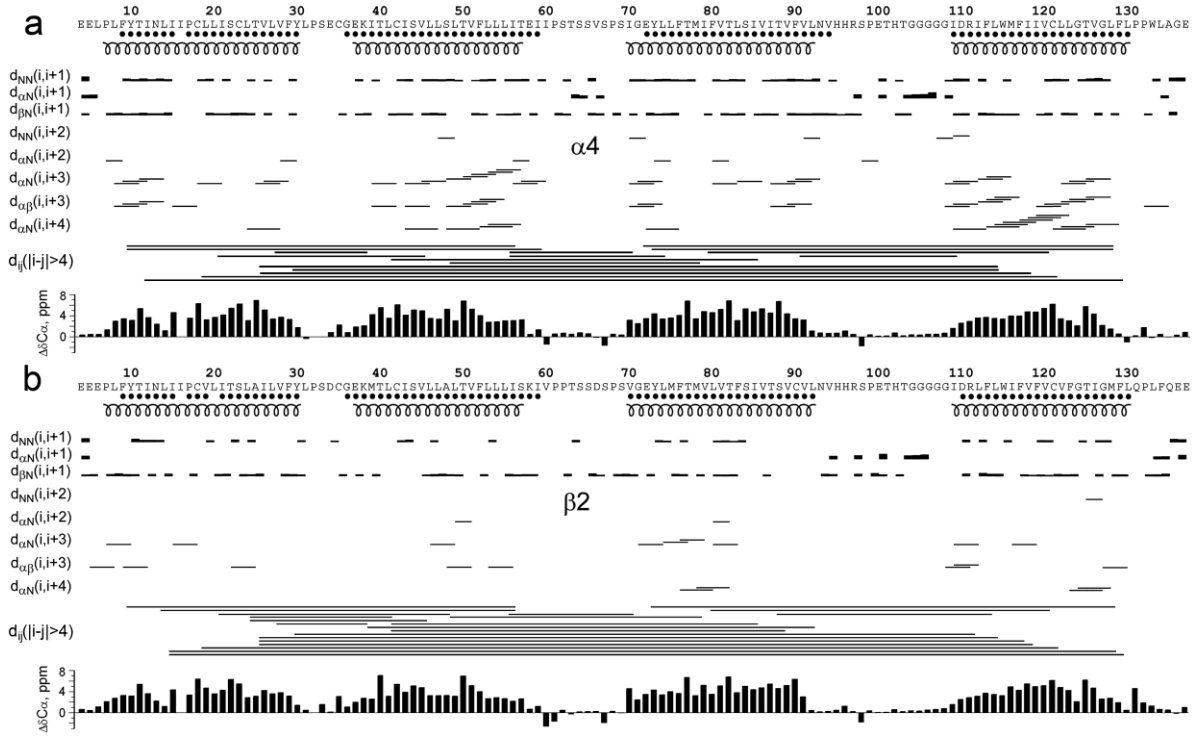

Figure 2.1.3. Summary of NMR restraints for structural calculations of the (a) α4 and (b) β2 TM domains. Structural restraints include hydrogen binding, NOE connectivity, and Cα chemical shift index. Residues with amide proton temperature coefficients < 4.5 ppb/K were considered to be involved in hydrogen bonding and are marked with (●). Sequential, midrange, and long-range NOE connectivities are linked by lines with widths proportional to the observed NOE intensities. The helical regions of the calculated protein structure are indicated below the sequence.

Table 2.1.1. Statistics for the 20 calculated structures of the human α4 nAChR TMD.

NMR structure	***Statistics***
Number of distance restraints	1070
Intraresidue ($\|i - j\| = 0$)	362
Short range ($\|i - j\| = 1$)	421
Medium range ($1 < \|i - j\| \leq 4$)	259
Long-range, inter-helical ($\|i - j\| \geq 5$)	28
Number of dihedral angle restraints	180
(Residues 8-16, 18-30, 35, 37-59, 70-92, 109-129)	
Number of hydrogen bond restraints	148x2
(Residues 9-30, 36-59, 72-94, 109-130)	
Number of upper limit restraints violations > 0.5 Å	0
Number of dihedral angle restraints violations > 5°	0
Backbone RMSD (Residues 9-30, 36-59, 72-94, 109-130)	0.87 ± 0.16 Å
Heavy atom RMSD (Residues 9-30, 36-59, 72-94, 109-130)	1.15 ± 0.18 Å
Ramachandran plot	
Residues in most favored regions	87.6 %
Residues in additionally allowed regions	9.7 %
Residues in generously allowed regions	2.2 %
Residues in disallowed regions	0.5 %

Table 2.1.2. Statistics for the 20 calculated structures of the human β2 nAChR TMD.

NMR structure	***Statistics***
Number of distance restraints	766
Intraresidue ($\|i - j\| = 0$)	328
Short range ($\|i - j\| = 1$)	289
Medium range ($1 < \|i - j\| \leq 4$)	114
Long-range, inter-helical ($\|i - j\| \geq 5$)	35
Number of dihedral angle restraints	184
(Residues 8-16, 18-30, 35, 37-58, 70-92, 109-131, 133)	
Number of hydrogen bond restraints	146x2
(Residues 9-31, 36-59, 70-92, 110-130)	
Number of upper limit restraints violations > 0.5 Å	0
Number of dihedral angle restraints violations > 5°	0
Backbone RMSD (Residues 7-30, 36-58, 70-92, 109-130)	0.95 ± 0.28 Å
Heavy atom RMSD (Residues 7-30, 36-58, 70-92, 109-130)	1.36 ± 0.26 Å
Ramachandran plot	
Residues in most favored regions	87.9 %
Residues in additionally allowed regions	10.2 %
Residues in generously allowed regions	1.7 %
Residues in disallowed regions	0.2 %

We compared the α4 and β2 NMR structures with the structures of GLIC, GluCl, and the α1 and β1 *Torpedo* nAChR. The helical length of the pore-lining TM2 in α4 and β2 resembles that in the GLIC and GluCl structures [27-29], but is shorter than that in the *Torpedo* nAChR structural model [1]. The c-terminus of the TM2 helix in α4, β2, GLIC and GluCl ends a few residues before the conserved proline in the TM2-TM3 linker. The same helical termination at the c-terminus of TM2 was also found previously in different membrane mimetic environments [66,93]. However, in the *Torpedo* nAChR structural mode, the TM2 helix ends three residues after this conserved proline. Another interesting observation is on the TM3-TM4 linkers of these proteins. Only two or six residues link TM3 and TM4 in GLIC or GluCl, respectively. On the other hand, the TM3-TM4 linker in the *Torpedo* or the α4β2 nAChR is large often containing over a hundred residues. To make the protein size manageable for NMR, we removed the majority of the TM3-TM4 linker in α4 and β2, keeping only 18 residues (13 original loop residues plus an additional 5 consecutive glycine residues). The drastic variations in the number of the TM3-TM4 linker residues among these proteins do not profoundly alter the four helical bundle motifs of the TM domains. The structural resilience to modification of the intracellular region is in accord with observations that the $GABA_A$ and $5HT_3$ receptors were functional after the deletion of their IC domains [94].

2.1.4. Structure of the α7 nAChR TM domain

A bundle of the 20 lowest target function structures of the α7 TMD (PDB ID: 2MAW), as shown in Figure 2.1.4a, were determined based on short-, medium-, and long-range NOEs, dihedral angle constraints, and hydrogen bonding constraints (Figure 2.1.5). The

average pair-wise RMSDs in the helical regions are 1.24 ± 0.32 Å for the backbone and 1.64 ± 0.30 Å for all heavy atoms. Detailed statistics of structural calculations are provided in Table 2.1.3.

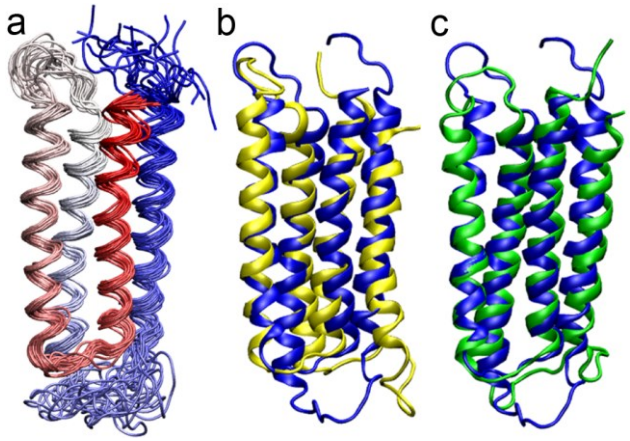

Figure 2.1.4. NMR structures of the α7 nAChR TMD. (**a**) A bundle of the 20 lowest-energy structures of the α7 TMD (PDB ID: 2MAW). The structures are colored from red for TM1 to blue for TM4. The backbone atom RMSD for the helical regions is 1.24 ± 0.32 Å. (**b**) Overlay of representative structures of α7 (blue) and α4 (yellow; PDB ID: 2LLY). The backbone atom RMSD for the helical regions between α7 and α4 is 2.9 Å. (**c**) Overlay of representative structures of α7 (blue) and β2 (green; PDB ID: 2LM2). The backbone atom RMSD for the helical regions between α7 and β2 is 2.1 Å.

The tertiary structure of the α7 TMD resembles those determined previously for the α4β2 (PDB IDs: 2LLY; 2LM2) nAChR [36] and other homologous pLGICs [26-29]. However, small structural differences can be observed among the nAChR TM domains. The angles between TM2 and TM4 helices are 3.9 ± 0.5° in α7, but 8.8 ± 0.9° and 10.5 ± 1.1° in α4 and β2, respectively. The angles between TM1 and TM3 helices are 3.8 ± 0.7° in α7, but 5.3 ± 0.6° and 5.7 ± 0.7° in α4 and β2, respectively. Structural alignment of α7 onto α4 or β2 (Figure 2.1.4b and c) shows that the α7 structure is more compact at the EC end of the TMD, where α7 has an intra-subunit cavity with a volume of 122 ± 10 $Å^3$. In contrast,

α4 and β2 have larger cavities in the same region with volumes of 232 ± 6 Å^3 and 179 ± 12 Å^3, respectively. The structural differences at the IC end of the TMD seem to be reversed. The intra-subunit cavities at the IC end of the TM domains have volumes of 209 ± 8 Å^3, 139 ± 11 Å^3, and 131 ± 10 Å^3 for α7, α4, and β2, respectively.

Table 2.1.3. Statistics for the 20 calculated structures of the human α7 nAChR TMD.

NMR structure	***Statistics***
Number of distance restraints	614
Intraresidue ($\|i - j\| = 0$)	239
Short range ($\|i - j\| = 1$)	223
Medium range ($1 < \|i - j\| \leq 4$)	109
Long-range, inter-helical ($\|i - j\| \geq 5$)	43
Number of dihedral angle restraints	196
(Residues 4-15, 17-29, 34, 36-58, 69-93, 107-130)	
Number of hydrogen bond restraints	152×2
(Residues 4-8,10-22, 24-25, 35-41, 43-47, 49-54, 69-89, 107-119, 121-125)	
Number of upper limit restraints violations > 0.5 Å	0
Number of dihedral angle restraints violations > 5°	0
Backbone RMSD (Residues 5-29, 36-58, 69-93, 107-130)	1.24 ± 0.32 Å
Heavy atom RMSD (Residues 5-29, 36-58, 69-93, 107-130)	1.64 ± 0.30 Å
Ramachandran plot	
Residues in most favored regions	86.2 %
Residues in additionally allowed regions	13.6 %
Residues in generously allowed regions	0.1 %
Residues in disallowed regions	0.1 %

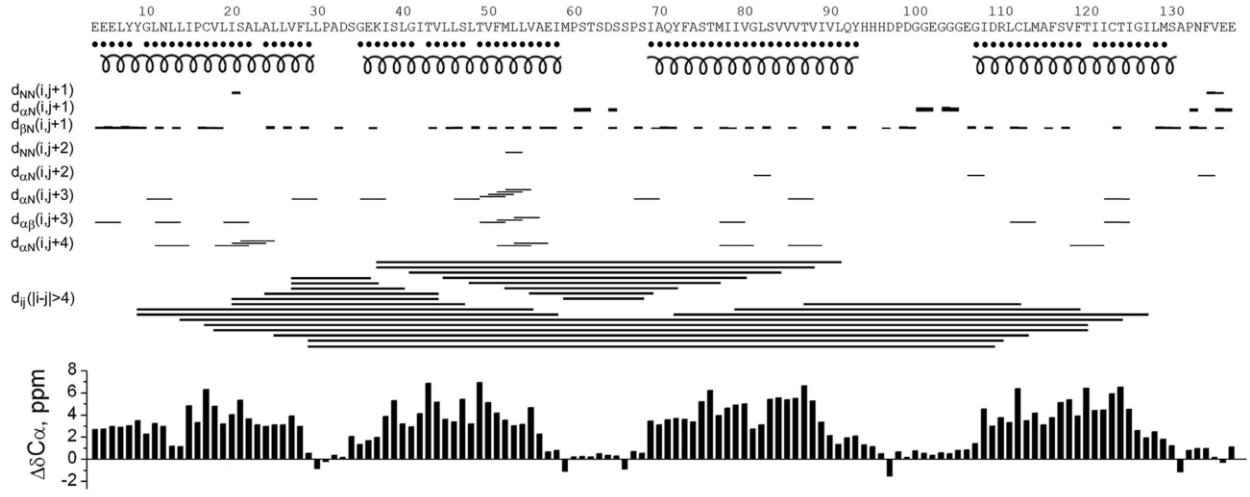

Figure 2.1.5. Summary of NMR restraints for structural calculations of the α7 nAChR TMD. Structural restraints include hydrogen binding, NOE connectivity, and Cα chemical shift index. Residues with

temperature coefficients for amide proton chemical shifts smaller than 4.5 ppb/K were considered to be involved in hydrogen bonding and are marked with (●) below the protein sequence. Sequential, midrange, and long-range NOE connectivities are demonstrated by lines. The Cα chemical shift index is shown below the long-range NOE connectivities. The helical regions of the calculated α7 structure are indicated below the sequence. To convert the residue numbering used in the NMR study to the numbering for the full-length α7 nAChR, add 202 for residues labeled 1 to 102 and add 337 for residues labeled 103 to 137.

2.1.5. Pentameric Structure Model of the α4β2 TMD

To determine whether the TM domains of α4 and β2 interact with each other and their oligomerization state in LDAO micelles, we performed NMR and SEC-MALS measurements on mixtures of α4 and β2.

For better resolution, only one subunit type in the α4β2 mixture was ^{15}N - or ^{13}C-labeled for each NMR spectrum. In other words, only one set of residues in the mixture, either from α4 or β2, was observed in the NMR spectrum. If α4 and β2 did not interact with each other, the NMR spectrum of the mixture would be the same as the spectrum of α4 or β2 alone. On the other hand, differences between the NMR spectra of a single subunit type and the α4β2 mixture are indicative of interactions between two different subunits. As shown in the spectral overlay of α4 and the α4β2 mixture in Figure 2.1.6a, several residues of the α4 subunit were perturbed by the addition of the unlabeled β2. Similarly, β2 was perturbed in the NMR spectra when it was mixed with the unlabeled α4. Fully annotated spectra for α4 in the presence of β2 or β2 in the presence of α4 are provided in the online supporting material of the published manuscript [36]. These NMR data suggested that the α4 and β2 TM domains interacted with each other and formed oligomers in LDAO micelles. The oligomeric state of the α4 and β2 TM domains in the

NMR samples was determined using size exclusion chromatography coupled with SEC-MALS. As shown in Figure 2.1.6b, the average molar mass of the α4β2 oligomers across the elution peak is 74.6 kDa, which is virtually the same as the expected molar mass of 75 kDa for a pentamer of the α4 and β2 TM domains. These results suggest that the TMD alone is sufficient for pentameric assemblies to spontaneously form in a membrane mimetic environment.

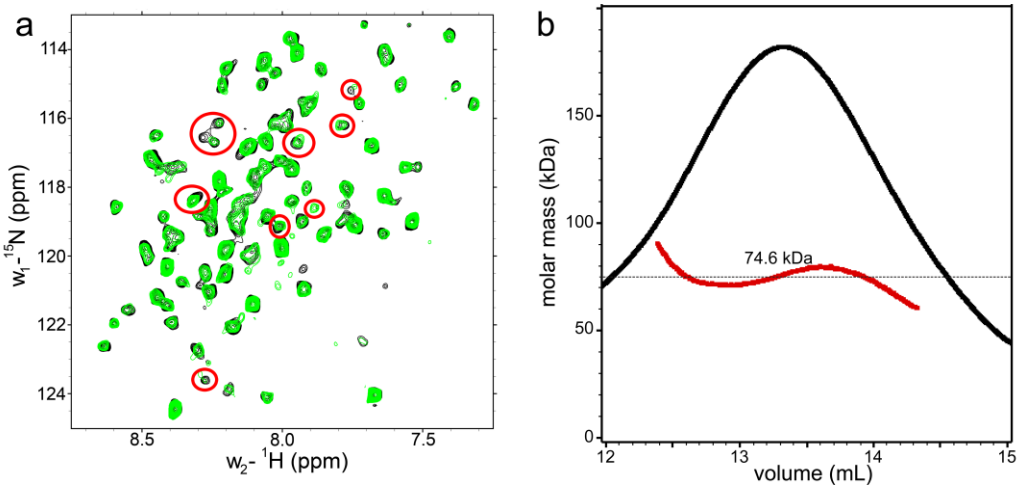

Figure 2.1.6. NMR and SEC-MALS data supporting pentameric assembly of the α4β2 nAChR TMD in LDAO. (**a**) Overlay of ^{1}H-^{15}N TROSY-HSQC spectra of α4 in the absence (black) and presence (green) of β2. Peaks circled in red showed changes in α4 chemical shift after the addition of β2, signifying interactions between α4 and β2. A limited number of residues experiencing changes in chemical shift suggested that the presence of β2 did not significantly alter the α4 structure. (**b**) SEC-MALS analysis indicated the formation of the α4β2 pentameric assembly. The molar mass (red) of the α4β2 assembly in the nAChR α4β2-detergent complex was obtained using conjugate analysis and is shown across the elution peak (black) from size exclusion chromatography. The average molar mass of the α4β2 assembly is 74.6 kDa. The dotted line indicates the expected molar mass of 75 kDa.

Changes in the α4 and β2 NMR spectra due to a perturbation from their interacting partners are relatively small and limited to only a few residues (Figure 2.1.6a). This is

understandable for at least two reasons. First, the pure or mixed subunits are in the same oligomeric state. Second, the α4 and β2 TM domains contain a high percentage of identical residues. Because of these reasons, when the adjacent subunit was changed from the same type to a different type in the pentameric assemblies, the structure of the α4 or β2 subunit did not change considerably. Thus, we built the α4β2 pentameric models using the NMR subunit structures (Figure 2.1.2). The NMR chemical shift perturbation data were used to guide spatial arrangement of interacting residues between α4 and β2 for building the model. For example, α4-L239 in the TM1 helix and β2-L294 in the TM3 helix were both affected by the presence of the complementary subunit in the chemical shift perturbation experiments. They are likely close to each other in space. Similar inter-subunit pairs were identified at different locations along the membrane normal (Figure 2.1.7). They were used for assembling pentameric models.

The α4β2 nAChR was originally found to exist in the $(\alpha4)_2(\beta2)_3$ stoichiometry [95,96], but later was also found to form $(\alpha4)_3(\beta2)_2$ [89,90]. Thus, we constructed models for both stoichiometries (Figure 2.1.8). The pore lining residues, T2', S6', L9', V13', L17', and α4-E20' or β2-K20', agree with those determined previously using the substituted cysteine accessibility method (SCAM) [88,97]. The pore radius profiles in Figure 2.1.9 show funnel shaped channels for $(\alpha4)_2(\beta2)_3$ and $(\alpha4)_3(\beta2)_2$, opening widely at the extracellular end and narrowing gradually toward the intracellular end. The funnel shaped pore profile with a widely opened extracellular end was also observed in the GLIC and GluCl structures [27-29]. The $(\alpha4)_2(\beta2)_3$ model is in an apparently open-channel conformation and its minimal pore radius at T2' (2.9 Å) is greater than that in GLIC (~2.5 Å). Although pore profiles resulting from backbones are nearly the same for both models, the pore radius at L9' is

smaller in the $(\alpha4)_3(\beta2)_2$ model. The sidechain of α4-L9' protruded into the pore lumen slightly more than the sidechain of β2-L9'.

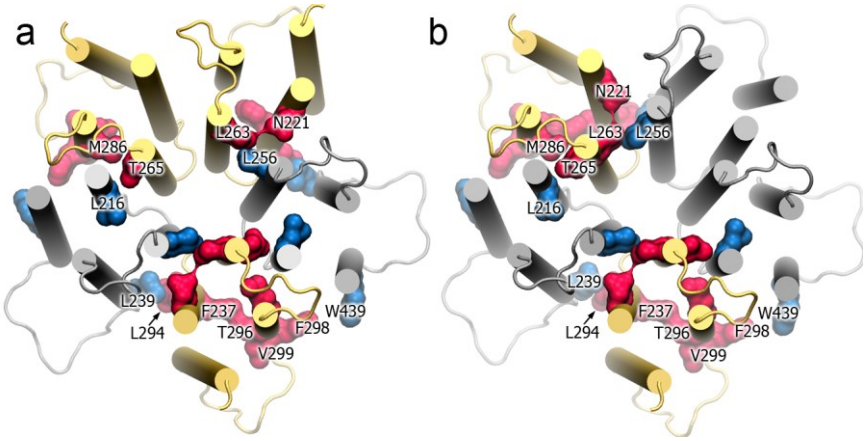

Figure 2.1.7. Top views of interacting residues between α4 (red) and β2 (blue) highlighted in (a) $(\alpha4)_3(\beta2)_2$ and (b) $(\alpha4)_2(\beta2)_3$ pentamer models. Interacting residues were identified by NMR chemical shift perturbation experiments. β2-L256 contacts α4-L263 closely. It is also adjacent to α4-N221. At another interface of the β2 and α4 subunits, β2-L216 contacts α4-T265 and α4-M286. β2-L294 and β2-W439 interact directly with α4-L239 and α4-F298, respectively. These interactions extended the perturbation effect to α4-F237, α4-T296 and α4-V299 and caused changes in chemical shifts of these residues.

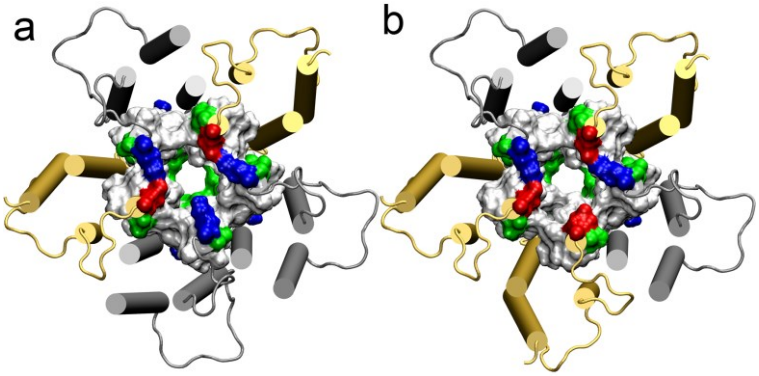

Figure 2.1.8. Top views of the α4β2 pentamer models: (a) $(\alpha4)_2(\beta2)_3$ and (b) $(\alpha4)_3(\beta2)_2$. Cartoon presentations for α4 and β2 subunits are colored orange and gray, respectively. Residues of TM2 are shown in surface representation and colored according to residue types, acidic in red, basic in blue, polar in green, and non-polar in white.

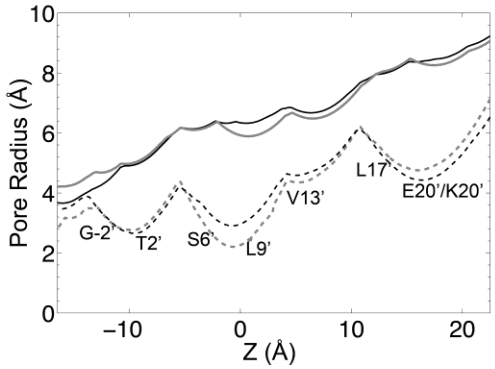

Figure 2.1.9. Pore-radius profiles for the $(\alpha4)_2(\beta2)_3$ (black) and $(\alpha4)_3(\beta2)_2$ (gray) models. The dashed and solid lines represent profiles determined by the backbone atoms or including the side chains, respectively. Positions of the pore lining residues are highlighted. Pore profiles were generated using the HOLE program [92].

The α4β2 nAChR structural models allow us to visualize findings observed in previous experiments. Changing the stoichiometry of α4 and β2 altered Ca^{2+} permeability in α4β2 nAChR. Increasing the proportion of negative charges in $(\alpha4)_3(\beta2)_2$ was found to be associated with increasing permeability to Ca^{2+} [98]. Indeed, as shown in Figure 2.1.8, positively charged β2-K20' and negatively charged α4-E20' are located at the extracellular pore entrance. A larger proportion of α4-E20' in $(\alpha4)_3(\beta2)_2$ provides a benefit by attracting Ca^{2+} to the pore entrance. Electrostatic interaction between β2-K20' and α4-E20' may also help to stabilize pentameric assemblies [99]. Results from previous photoaffinity labeling experiments on the α4β2 nAChR are well represented in, and explained by, our structural models. 3-trifluoromethyl-3-(*m*-[^{125}I]iodophenyl) diazirine ([^{125}I]TID), a hydrophobic probe [100], was photolabeled onto the α4β2 nAChR for mapping the protein/lipid interface [101]. We highlighted the residues labeled by [^{125}I]TID in our α4β2 models (Figure 2.1.10), including homologous residues α4-C582 and β2-C445 in TM4, α4-C226 and α4-C231 in TM1, and β2-C220 that is homologous to α4-C226 [101]. Our

structures show exposure of α4-C582 and β2-C445 in TM4 and α4-C231 in TM1 to lipids. More interestingly, our structures show that α4-C582 and β2-C445 of TM4 face towards α4-C226 and β2-C220 of TM1, respectively. They form a [^{125}I]TID binding pocket along with surrounding lipids. Although α4-C226 and β2-C220 are less exposed to lipids, their labeling by [^{125}I]TID could be facilitated by α4-C582 and β2-C445 in the same pockets. However, if the *Torpedo* nAChR model [1] is used for explaining the photolabeling data, α4-C582 and β2-C445 seem to have no association with α4-C226 and β2-C220, respectively (Figure 2.1.10).

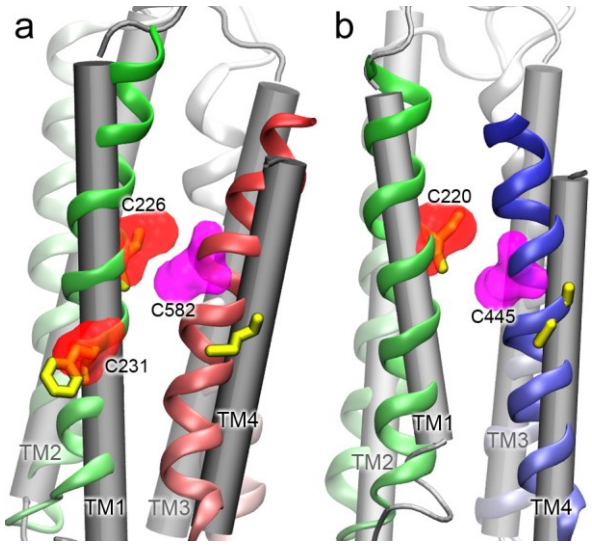

Figure 2.1.10. The NMR structures of the TM domains of (a) α4 and (b) β2 nAChRs showing residues photolabeled by [^{125}I]TID [101]. α4 and β2 are shown in ribbon and colored from green (TM1) to red (TM4) in (a), and from green (TM1) to blue (TM4) in (b). Residues photolabeled by [^{125}I]TID in α4 (C226, C231, and C582) and β2 (C220 and C445) are shown in a surface presentation. For comparison, the α1 (gray) and β1 (silver) subunits of the *Torpedo* nAChR structure were aligned with α4 and β2, respectively, and shown in cartoon presentation. Residues homologous to the [^{125}I]TID labeled residues are shown in yellow sticks. The NMR structures and the *Torpedo* nAChR structure show different positions of α4-C582 and β2-C445. In our NMR structures, α4-C582 and β2-C445 oriented towards α4-C226 and β2-C220, respectively, suggesting the likelihood of a [^{125}I]TID binding pocket involving α4-C226 and α4-C582 or β2-C220 and β2-C445. The *Torpedo* nAChR model, however, suggested no association between α4-C226 and α4-C582 or β2-C220 and β2-C445 for [^{125}I]TID binding.

2.1.6. Functional Measurements of the α4β2 Assembly

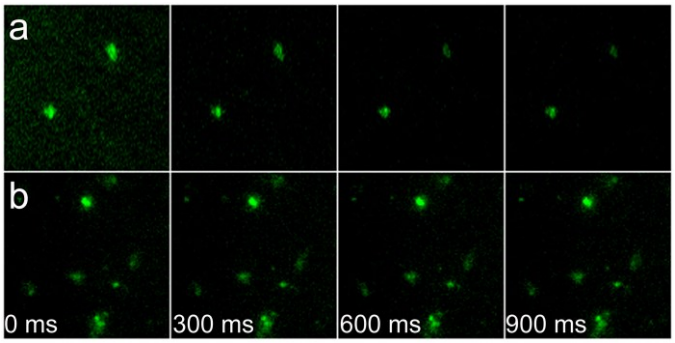

Figure 2.1.11. Fluorescence images of the Na^+ flux assay on vesicles in the (a) presence and (b) absence of the α4β2 nAChR TMD. Membrane-impermeable Sodium Green™ fluorescent dyes were enclosed inside the vesicles to probe intra-vesicle Na+ concentrations. The fluorescence intensity of the vesicles with α4β2 channels in (a) decreased significantly within a short period of time after washing away extra-vesicle sodium, indicating Na^+ efflux through the channels. However, fluorescence intensity of the control vesicles without α4β2 in (b) remained nearly constant before and after washing away extra-vesicle Na^+ during the same time period.

NMR chemical shift perturbation experiments in combination with the SEC-MALS analysis provided evidence for the formation of the α4β2 pentameric assembly. To assess whether the α4β2 TM domains formed ion-conducting channels, we performed a Na^+ flux assay. Significant reduction of Sodium Green™ dye fluorescence was observed in vesicles immediately after dilution of the extra-vesicle salt concentration only if the vesicles contained the α4β2 assembly (Figure 2.1.11a). During the same measurement time, however, fluorescence remained almost the same in vesicles lacking α4β2 (Figure 2.1.11b), confirming that the observed fluorescence reduction in Figure 2.1.11 was not due to fluorescence bleaching. Efflux of Na^+ from the vesicles containing α4β2 indicates that the α4β2 TM domains are capable of transporting Na^+ across a membrane. The data

in Figure 2.1.11 suggest that the open conformation of the α4β2 assembly is thermodynamically accessible at room temperature, though it cannot determine how rapidly the closed and open conformations spontaneously exchange.

2.1.7. Functional Measurements of the α7 nAChR TM domains

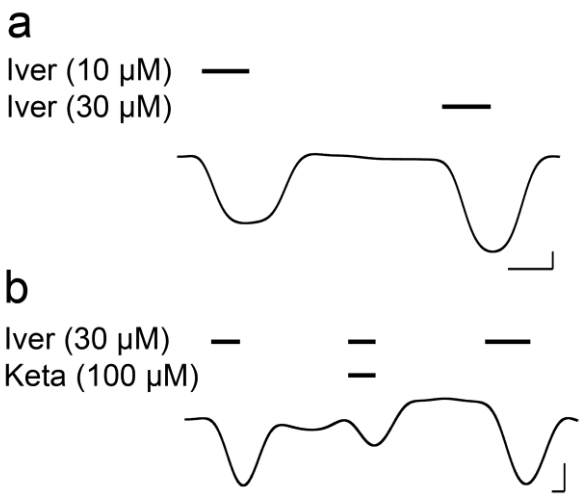

Figure 2.1.12. Representative traces of *Xenopus laevis* oocytes injected with vesicles containing the purified α7 nAChR TMD. (**a**) Current response at 10 and 30 μM ivermectin. (**b**) Inhibition of ivermectin (30 μM)-elicited current by 100-μM ketamine. Bars over the trace indicate length of application of the indicated compounds. Scale bars indicate 0.5 min and 0.1 μA.

The α7 TMD spontaneously formed ion-conducting channels when injected into *Xenopus laevis* oocytes as reconstituted asolectin vesicles (Figure 2.1.12). Although the α7 TMD does not possess the orthosteric agonist-binding site of native human α7 nAChRs, the channel current could be elicited by ivermectin, a known positive allosteric modulator acting through the TMD [102,103]. Ketamine inhibited ivermectin-induced current (Figure 2.1.12b), consistent with the effect of ketamine on native human α7 nAChR [45,46,104]. No ivermectin-elicited current was observed in control oocytes injected with the

asolectin vesicles not containing the α7 TMD. These data demonstrate that the α7 TMD retains pharmacological responses observed for the full-length α7 nAChR.

2.1.8. Conclusions

In this section we discussed the NMR derived structures of the α7, α4, and β2 nAChR TM domains in LDAO micelles. These structures are valuable for understanding the biological and pharmacological properties of both α7 and α4β2 nAChRs, particularly for characterizing binding sites and mechanisms of action for new and existing drugs. SEC-MALS and the Na^+ flux assay demonstrated that the α4β2 TM domains spontaneously form pentamers permeable to Na^+. We also found that the α7 nAChR TMD injected into *Xenopus laevis* oocytes retained pharmacological properties of the native α7 nAChR TMD, namely potentiation by ivermectin and inhibition by ketamine. Our data suggests that the presented NMR structures are biologically relevant and offer valuable frameworks for rationalizing drug binding and modulation for the α7 and α4β2 nAChRs.

2.2. NMR STRUCTURE OF THE GLYCINE RECEPTOR TM DOMAIN

This section has been published as a full article in *Structure* **21** (10): 1-8.

2.2.1. Background and Significance

The glycine receptor is an anion-selective channel and a major inhibitory receptor in the human adult spinal cord and brain stem. Anionic Cys-loop receptors include both the glycine and $GABA_A$ receptors. The $GABA_A$ receptor has been implicated in sedation,

amnesia, and muscle relaxation, while the glycine receptor has been implicated in immobility [19-21]. Prior to the publication of the structure discussed here, no structure was available for a mammalian anionic Cys-loop receptor TMD. The NMR structures of the human glycine receptor α1 subunit (hGlyR-α1) TMD offer a valuable complement to existing crystal structures of Cys-loop receptors [1,29,81] and their homologues [27,28]. The structures reveal features previously unobserved in crystal structures or the NMR structures of cationic Cys-loop receptors [36], which may be functionally distinct to anionic Cys-loop receptors.

The functional state of a crystal structure is often inferred from electrophysiology measurements under comparable conditions. However, crystallization conditions may bias the crystal structures into conformations that contradict electrophysiology results. The crystal structure of the mutation-stabilized open-channel ELIC is nearly identical to that of the closed ELIC [105]. Propofol inhibits GLIC current, but the crystal structure of the GLIC-propofol complex shows the same open channel conformation as that observed in GLIC [106]. Such complications highlight the limitation of crystal structures in revealing functional states of Cys-loop receptors and the need for complementary structural approaches.

In this section we present the NMR structures for the full-length hGlyR-α1 TMD determined in LPPG. Electron microscopy (EM) and functional measurements show that the TMD forms pentameric and spontaneously Cl^--conducting channels. The NMR data revealed structural and dynamic features of the hGlyR-α1 TMD that may be shared by other anion-selective Cys-loop receptors. The functional relevance of the TMD structures was validated by a recent study [107] showing that the hGlyR-α1 TMD in a chimera with the

GLIC ECD functions as an anion-selective channel and mirrors the pharmacological profile of the native hGlyR-α1.

2.2.2. Methods

Protein expression and sample preparation

The protein was expressed using the Novagen pET-31b(+) system (Novagen, Milwaukee, WI) in *E. coli* BL21(DE3)pLysS competent cells (Novagen). M9 minimum medium was used for protein expression with $(^{15}NH_4)_2SO_4$ and [U-^{13}C] glucose as the sole source of nitrogen and carbon for ^{15}N-labeling and ^{15}N ,^{13}C-double labeling. To assist in chemical shift assignment, specific ^{15}N labeling of alanine, phenylalanine, leucine, isoleucine, and valine were performed using a previously reported method [108]. The fusion protein was purified on staggered His-Bind chromatography columns (Novagen). Cleavage of the hGlyR-α1 TMD from the fusion protein was achieved using the standard protocol [109]. Final purification for the hGlyR-α1 TMD was carried out using reverse-phase HPLC with a C4 column (Vydac, Hesperia, CA). NMR samples were prepared as described previously [110,111]. Aliquots of the hGlyR-α1 TMD (4 mM) dissolved in trifluoroethanol (TFE) were titrated into a 200 mM solution of LPPG micelles (10 mM sodium phosphate buffer, pH 5.8) to a protein-to-LPPG ratio of ~1:200. Distilled H_2O was added to reach the water-to-TFE ratio of 16:1 by volume. The sample was vigorously mixed, rapidly frozen in liquid N_2, and lyophilized overnight at –80°C to remove all solvents, particularly TFE. The lyophilized sample was rehydrated in deionized H_2O with 5% D_2O for NMR field lock. NMR samples for structure determination typically had a protein concentration of ~500 μM with a protein-to-LPPG ratio of ~1:200 (pH 5.8).

For site-directed paramagnetic spin labeling, the wild-type hGlyR-α1 TMD (with one cysteine, C290) and two single-cysteine mutants (C290S/S296C and C290S/S308C) were prepared as described in the literature with minor modifications [112]. Cysteine was reduced using DTT at a 10-fold molar excess for 30 minutes at room temperature. Excess DTT was removed by dialysis overnight in 10 mM sodium phosphate buffer at pH 5.8. MTSL was added from a concentrated stock in acetonitrile to a MTSL-to-protein molar ratio of 5:1 and incubated overnight at room temperature before removing the free MTSL by dialysis in a 10 mM sodium phosphate buffer.

For functional measurements, large unilamellar vesicles (LUV) were prepared using the same method reported previously [113]. Briefly, PC and PG in a 3:1 molar ratio were dissolved and mixed in chloroform. The mixture was divided equally into three portions for use in: control samples without the protein, samples with the protein, and samples with the same amount of protein and picrotoxin (Tocris Bioscience, Ellisville, MO). The mixtures were dried into thin films under a stream of N_2 gas and left under vacuum overnight to completely remove the organic solvents. The dried films were rehydrated with one volume of 5 mM Tris-HCl buffer at pH 7.2 (buffer A) and four volumes of 0.5 M KCl in buffer A. After vigorous vortexing and brief sonication, the samples were subjected to two cycles of freeze and thaw alternating between –80°C and room temperature, respectively. Immediately before the magnetization-inversion transfer (MIT) experiments, the vesicles were expanded by adding buffer A to reach a final total lipid concentration of 25 mM, a KCl concentration of 200 mM, a protein concentration of 26 μM and a picrotoxin concentration of 1 mM.

For EM measurements, serial dilutions, using a buffer containing 10 mM HEPES and 50 mM KNO_3, were made from a stock solution in the same buffer with a protein concentration of 54 μM and a protein-to-LPPG ratio of 1:50. Five μl of diluted samples were deposited onto a glow-discharged carbon foil grid, blotted with filter paper, and stained with 2% uranyl acetate.

NMR spectroscopy

For backbone chemical shift assignment, the following spectra were collected: HNCO (1024x40x64) with ^{13}C spectral width of 12ppm, HNCA and HN(CO)CA (1024x40x80) with ^{13}C spectral widths of 32 ppm, and HNCACB and CBCA(CO)NH (1024x40x80) with ^{13}C spectral widths of 75ppm. HCCH-TOCSY was collected for side chain assignment. To obtain the distance restraints, ^{15}N- and ^{13}C-edited NOESY (1024x60x248) were acquired with spectral windows of 27 ppm and 80 ppm for the ^{15}N and ^{13}C dimensions, respectively. Mixing times were 150 ms for both ^{15}N- and ^{13}C-edited 3D NOESY. Unless otherwise specified, spectral windows for ^{1}H and ^{15}N dimensions were 12 ppm and 26 ppm, respectively. ^{15}N-edited 3D NOESY spectra were acquired for the samples with selectively ^{15}N-labeled Ala, Phe, Leu, Ile, or Val. Longitudinal (R_1) and transverse (R_2) ^{15}N relaxation rate constants and ^{15}N-{^{1}H} heteronuclear NOE were measured at 40°C on a Bruker Avance 700 MHz spectrometer. R_1 was determined using 9 delay values: 10, 100, 200, 400, 600, 800, 1000, 1500 and 2800 ms. The R_2 experiment also used 9 delay values: 16, 32, 64, 96, 128, 160, 240, 320 and 480 ms. For the steady-state ^{15}N-{^{1}H} NOE measurement, a train of 120 high-power pulses separated by 5 ms for the duration of 3 s was used for proton saturation and data was collected with and without proton saturation

in an interleaved fashion. Temperature effects on chemical shift were measured using a series of ^{1}H-^{15}N HSQC experiments collected at 35, 40, 45, and 50°C on a Bruker 900 MHz spectrometer. DSS was used as an internal reference for ^{1}H chemical shift, with ^{15}N and ^{13}C chemical shifts indirectly referenced [78]. Topspin and NMRPipe [82] were used to process NMR data. Sparky was used for resonance assignment [83].

The MIT experiments [113,114] were performed at 30°C using a 4 mm MAS probe on a Bruker Avance 600 MHz spectrometer. In the absence of the chloride shift reagent, only one peak was observed and manually set to 0 ppm. In the presence of ~20 mM $Co(gly)_3^-$, the extra-vesicle resonance ($^{35}Cl_{out}$) was separated from the intra-vesicle resonance ($^{35}Cl_{in}$) by ~25 ppm. A pair of hard 90° pulses, separated by the reciprocal of twice the chemical shift difference, was used to selectively invert the $^{35}Cl_{out}$ resonance while returning the $^{35}Cl_{in}$ magnetization back to the Z direction. The inversion-recovery time, *t*, varied from 10 μs to 0.5 ms, followed by a third 90° read pulse. Typically, 14 inversion-recovery times were used in each MIT experiment. The recycle delay was set to at least 10 times the T_1 value of the ^{35}Cl signals. The Mnova NMR program (Mestrelab Research, Escondido, CA) was used to measure the MIT peak intensities by spectral deconvolution. Influx and efflux rates were calculated using a two-site exchange mode. Details are described below.

NMR spectroscopy for measuring Cl− flux across the hGlyR-α1 TM channels

A two-site exchange model was used to derive the unidirectional flux rate constants from the MIT experiments. With the approximation that the longitudinal relaxation time, T_1, is similar for the intra- and extra-vesicle magnetizations, it has been shown [113] that the time

dependence of the uninverted magnetization, *I*, and inverted magnetization, *S*, on the inversion recovery time are given by:

$$I = I_0\left[1-\frac{2k_e}{k_i+k_e}e^{-(t/T_1)}(1-e^{-(k_i+k_e)t})\right] \quad (2.1)$$

$$S = S_0\left[1-\frac{2}{k_i+k_e}e^{-(t/T_1)}(k_e+k_ie^{-(k_i+k_e)t})\right] \quad (2.2)$$

where I_0 and S_0 are the spectral intensities of a fully relaxed spectrum, and k_i and k_e are influx and efflux rate constant. The thermal equilibrium condition is satisfied by $k_iS_0 = k_eI_0$. T_1 was measured using the conventional inversion-recovery method. The k_i and k_e values can be determined by non-linear least square fitting of the MIT data using Equation (2.1) and Equation (2.2).

Structure calculations

The upper and lower bound distance restraints were derived from NOESY and PRE data. Backbone dihedral angles were predicted from chemical shift values using the semi-empirical method implemented in TALOS [85]. Hydrogen bonding restraints were generated for those residues whose H-D exchange was in the slow category (absolute temperature slope < 4.5 ppb/K) [77] and in addition whose CSI and NOE restraints indicated a helical secondary structure. Restraints used in structure calculations are summarized in Table 2.2.1. The 76 backbone dihedral angle restraints were derived from the available chemical shift data of Cα, Cβ, C, N, H, and Hα. The long-range distance restraints for accurate tertiary structure determination were derived from PRE experiments [112], in addition to the unambiguous inter-domain NOESY cross peaks. We made three separate spin labeling positions along the length of the TM3 domain at C290, S296C, and S308C.

A simultaneous C290S mutation was made in the latter two cases, so that only one spin labeling position is present in each mutant. Distance restraints from PRE were generated using the established method [112].

Electron microscopy

The uranyl acetate stained samples were examined at 200 kV with a TF20 electron microscope (FEI, Hillsboro, OR). Images were recorded on a 4Kx4K Gatan CCD camera (Gatan, Inc., Warrendale, PA) at a nominal magnification of 50,000x and underfocus values ranging from 1.5 to 3.0 μm. The CCD images were processed using EMAN image analysis software [115]. Specifically, the particles were boxed manually with 72 x 72 pixels (2.14 Å/pixel), normalized, and then combined into one raw image stack file. A total of 526 individual particle images were initially chosen. These raw images were band pass-filtered and iteratively aligned to each other. About 210 good particle images were selected. The aligned raw projection images were classified and averaged within each class [115].

2.2.3. The hGlyR-α1 TMD Forms Spontaneously Open Cl^- Channels

A protein encompassing the entire sequence (Figure 2.2.1) of the hGlyR-α1 TMD was expressed and reconstituted in LPPG lipid micelles for structure determination using EM and high-resolution NMR. Unlike the GlyR ECD that assembles randomly into dimers and higher-order oligomers [116], the full-length hGlyR-α1 TMD spontaneously assembles into pentameric structures in LPPG lipid micelles. The negatively stained EM images (Figure 2.2.2) show face-on projections of pentamers. A small population of tetramers is also

discernible, in accordance with the tetrameric sub-conductance state measureable in the authentic GlyR from mouse spinal cord neurons [117]. Circular averaging of all face-on pentamer images yielded a ring diameter of ~45 Å for the peak intensities (Figure 2.2.3).

Figure 2.2.1. Sequence alignment of the hGlyR-α1 TMD and homologous proteins. The sequence of the construct under study (hGlyR-α1 TM) aligned with the TM domains of the native human GlyR-α1 subunit (GlyR-α1), the glutamate chloride channel from *C. elegans* (GluCl), four representative members in the Cys-loop receptor superfamily ($GABA_A$ α1 subunit, nAChR α1 and α4 subunits, and $5HT_3$ α subunit), and two bacterial homologues (ELIC and GLIC). An artificial loop between TM3 and TM4 and a 6-His tag at the C-terminal are shaded in light purple. Solid lines below six sequences mark the experimentally determined TM helices. Residues believed to be part of the ion selectivity filter are highlighted in red rectangle boxes. Sequence alignment was performed using Clustal X version 2.0 [118].

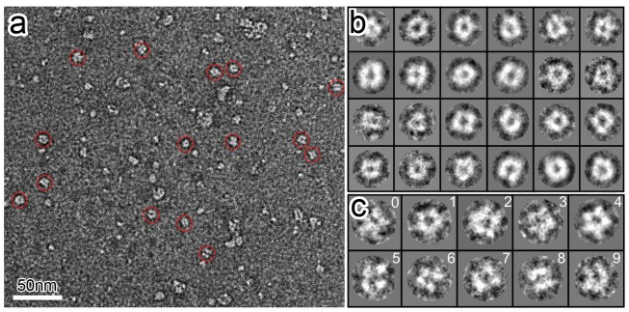

Figure 2.2.2. Electron microscopy analyses of the hGlyR-α1 TMD oligomeric complexes. (**a**) A raw electron micrograph of negatively stained hGlyR-α1 TMD oligomers in LPPG (scale bar, 50 nm). Representative particles are indicated with red circles. (**b**) Selected 2D class averages of hGlyR-α1 TMD oligomers from 210 particle images. Class averages show doughnut-shaped particles with a central channel and several oligomeric states, including pentamer and tetramer. (**c**) Representative raw particle images corresponding to the pentameric (0-3) and tetrameric (5-7) configurations. An average of the raw particles from panel 0-3 is shown in panel 4. Panel 8 and 9 show side views of the particles.

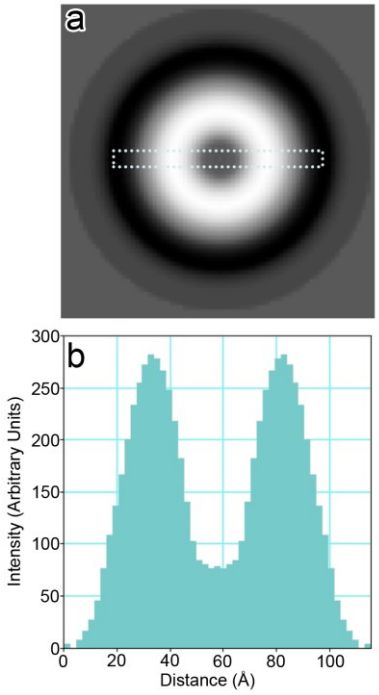

Figure 2.2.3. Radial intensity profiling of circular averaged pentameric particles in negatively stained EM images. (**a**) Radial averaging of pentameric particles. (**b**) Density line profile of the box region in (A). Peak to peak distance is ~45 Å.

We also reconstituted the same expressed protein into LUVs made of L-α PC and PG lipids. Function of the hGlyR-α1 channel for Cl^- transport was measured by NMR MIT experiments [113,114] using $Co(Gly)_3^-$ as a Cl^- shift reagent [119] to separate intra- and extra-vesicle ^{35}Cl resonances. We found that the channels are not only spontaneously open in the absence of the agonist-binding ECD, but also Cl^- permeable (Figure 2.2.4a). At a nominal channel density of ~20-2000 per vesicle, the unidirectional Cl^- efflux and influx rates [113] are 1350 ± 460 and 560 ± 290 s^{-1}, respectively. Moreover, the Cl^- transport across the TM channels can be completely blocked in the presence of 1 mM picrotoxin (Figure 2.2.4b), indicating that the quaternary association of the TMD is preserved to form a functional channel with a pore geometry resembling that of the authentic open channel.

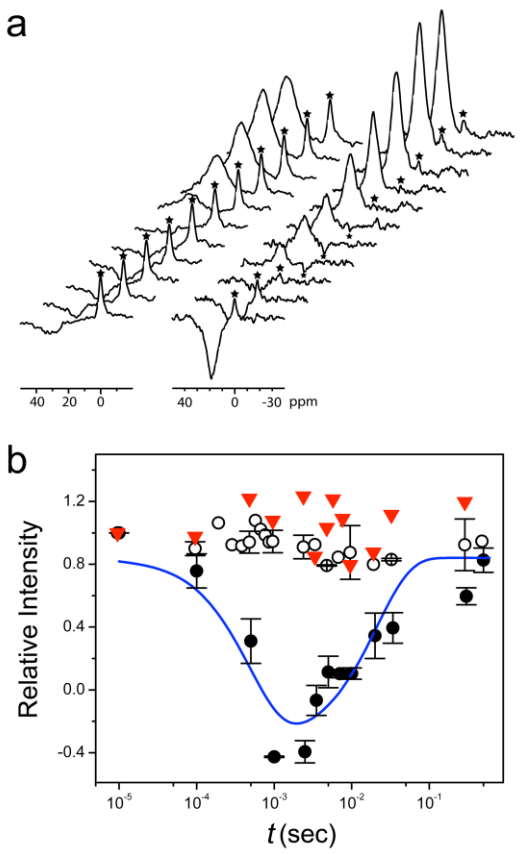

Figure 2.2.4. Channel functional measurements. (a) Stack plots of ^{35}Cl NMR spectra in Cl^- flux measurements across LUVs by NMR MIT experiments. Left: control vesicles without the protein; Right: vesicles having the hGlyR-α1 TMD channels. The Cl^- shift reagent $Co(Gly)_3^-$ separates extra-vesicle Cl^- signal from the intra-vesicle signal (marked by the asterisk *). The intensity of the intra-vesicle signal (*) changes as a function of the inversion-recovery time (t) due to the exchange of intra- and extra-vesicle Cl^-. (**b**) The rates of Cl^- influx (k_i) and efflux (k_e) are determined by fitting the intensity changes as a function of t with a two-site exchange model (solid line). ○, LUV without protein; ●, LUV with protein; ▼, LUV with the same amount of protein and with 1 mM picrotoxin. Error bars show the standard error of the mean.

2.2.4. NMR structure of the hGlyR-α1 TMD

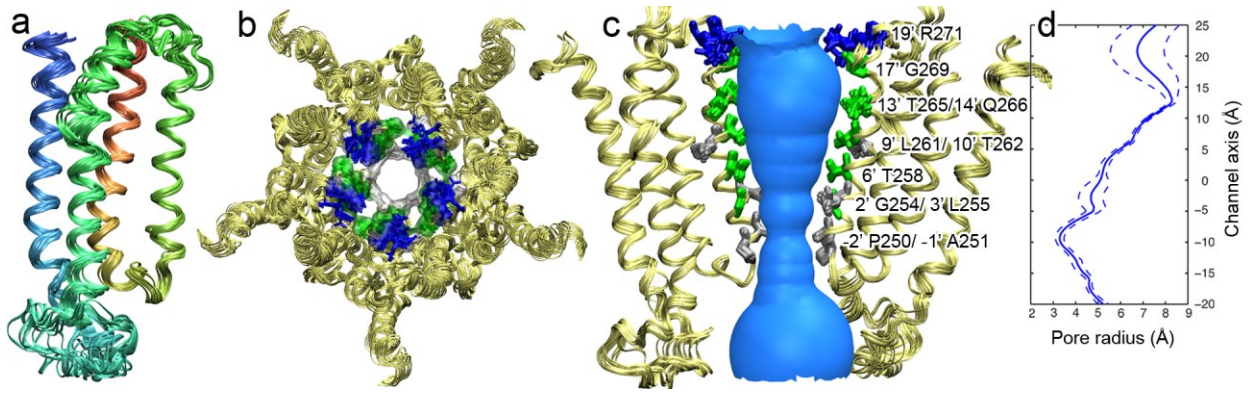

Figure 2.2.5. NMR structures of the hGlyR-α1 TMD. (a) The bundle of 15 lowest target function monomer structures of the hGlyR-α1 TMD (PDB ID: 2M6B). The TM1, TM2, TM3, and TM4 helices are indicated in red, light green, green, and blue, respectively. (**b**) Top view of the bundle of 15 lowest target function pentameric structures of the hGlyR-α1 TMD (PDB ID: 2M6I). Pore lining residues are highlighted based on residue type: green–polar, gray–nonpolar, and blue–basic. (**c**) Side view of the bundle of 15 lowest target function pentameric structures of the hGlyR-α1 TMD. For clarity, only two subunits are shown. Pore lining residues are labeled and colored based on their residue type. (**d**) The pore profile calculated using the HOLE program [92].

A bundle of 15 monomer structures of the hGlyR-α1 TMD with the lowest target function from the CYANA calculation (Figure 2.2.5) exhibits a typical four-helix-bundle fold, which has been observed in the TMD structures of the α4β2 nAChR [36] and other known structures of pLGICs [26,27,47,120]. The tertiary (Figure 2.2.5a) and quaternary (Figure 2.2.5b) packing of the TM helices were determined from the long-range intra-subunit and inter-helical NOE connectivity (Figure 2.2.6), PRE restraints [112], and diameter restraints derived from the EM images. The orientation of the TM2 helix relative to the membrane normal was determined using the residual dipole coupling (RDC) data from the TM2-TM3 helical segments in low-q bicelles as reported previously [121]. See 5.3.6.Appendix A for

details on structure calculation methods. The NMR structure statistics for the bundles of 15 monomers (PDB ID: 2M6B) and 15 pentamers (PDB ID: 2M6I) are summarized in Table 2.2.1. The pair-wise RMSD among the 15 lowest target-function pentamer structures are 0.50 Å and 0.91 Å for the backbone and all heavy atoms, respectively, in the four membrane-spanning helices.

Several structural features of the hGlyR-α1 TMD are worth noting. First, the pore-lining TM2 has a stable α-helix involving residues from P250 (–2') to S267 (15'). Residues from 16' to 18' show an unwound helix exhibiting a slightly larger helical pitch (Figure 2.2.5a). The residues after 18' in TM2 are non-helical. In contrast, structures of several pLGICs, including the α4β2 nAChR determined by NMR [36], show a longer TM2 α-helix that typically contains 23 residues (–2' to 20').

Second, unlike a straight helix observed in other pLGICs, the TM3 helix of hGlyR-α1 has a kink at A288 (Figure 2.2.5a). The kink changes the helix axis direction by ~33°. It is also notable that the fourth residue upstream from the kink is a conserved aspartate (D284). Aspartate is known to frequently locate at the i-4 position of TM helical bends [122].

Third, while most of the pore-lining residues in the hGlyR-α1 TMD structure (Figure 2.2.5c) agree well with homologous residues in the previously published pLGIC structures, one distinction is that the well-conserved L261 (9') in our open-channel structures does not directly face the lumen of the pore, but T262 (10') does.

Table 2.2.1. Statistics for the 15 calculated structures of the hGlyR-α1 TMD in LPPG micelles.

NMR Distance & Dihedral Restraints	Monomer	Pentamer
Distance restraints		
Total NOE	1014	1014 x 5
Intra-residue	321	321 x 5
Inter-residue	693	693 x 5
Sequential (|i-j| = 1)	348	348 x 5
Medium-range (|i-j| ≤ 4)	324	324 x 5
Long-range (|i-j| > 4)	21	21 x 5
Hydrogen bonds	106	106 x 5
Total dihedral angle restraints	152	154 x 5
Phi	76	77 x 5
Psi	76	77 x 5
PRE restraints	219	226 x 5
Upper	107	114 x 5
Lower	112	112 x 5
Inter-subunit distance restraints from EM and RDC[a]		
Total constraints		600
Upper		300
Lower		300
Structure Statistics		
Violations (mean and s.d.)		
Upper distance restraints (Å)	0.0075 ± 0.0008	0.0157 ± 0.0010
Lower distance restraints (Å)	0.0016 ± 0.0010	0.0102 ± 0.0012
Dihedral angle restraints (º)	0.130 ± 0.010	0.338 ± 0.028
Max. dihedral angle violation (º)	1.29	3.32
Max. distance restraint violation (Å)	0.24	0.63
Average pairwise RMSD[b] (Å)		
Heavy	1.04 ± 0.11[c]	0.91 ± 0.14[c]
	2.27 ± 0.25[d]	1.50 ± 0.36[d]
Backbone	0.67 ± 0.13[c]	0.50 ± 0.17[c]
	1.66 ± 0.18[d]	0.95 ± 0.30[d]
Ramachandran Plot		
Residues in most favored regions	88.6%	86.3%
Residues in allowed regions	11.3%	13.0%
Residues in disallowed regions	0.1%	0.7%
PDB ID	2M6B	2M6I

[a] RDC values used to generate pentamer restraints were obtained from the previous study [121].
[b] The rmsd to the average coordinates was calculated from 15 structures.
[c] Calculated over the helical TM regions (residues 220-241, 250-270, 289-305, 398-421)
[d] Calculated over residues 215-425

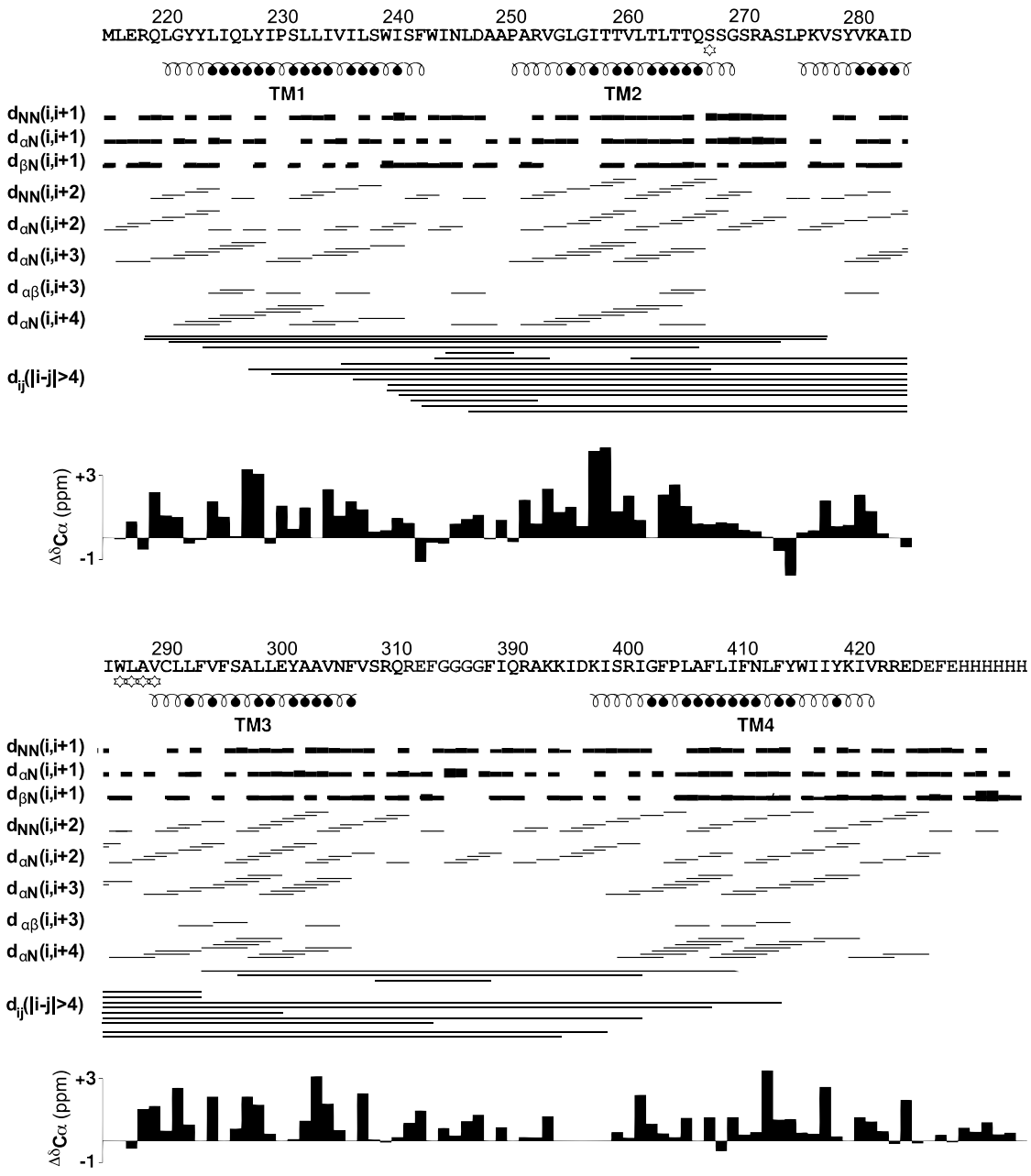

Figure 2.2.6. NOE connectivity and Cα chemical shift index for the hGlyR-α1 TMD in LPPG micelles. The line thickness of the NOE connectivity is proportional to the cross-peak intensities. The helical regions observed in the NMR structure (black coils) are shown underneath the sequence. The filled circles below the sequence mark the residues where backbone hydrogen-bond restraints were imposed on the basis of the temperature dependence of the exchangeable amide protons. The two ends of a segment from TM2 to TM3 that is highly dynamic are marked with stars below the sequence.

Finally, the open channel pore of hGlyR-α1 has a cone shape with the smallest diameter of 6.2 Å at a hydrophobic girdle defined by P250 (–2') and A251 (–1') side chains situated at the cytoplasmic side of the membrane (Figure 2.2.5d). The positively charged R252(0') side chains are tangential to the circumference of the pore. The constriction size of the hGlyR-α1 open pore is close to the estimated 6.2 Å for glycine and $GABA_A$ receptors based on the studies of ion permeability [123].

2.2.5. Dynamics of the hGlyR-α1 TMD

The dynamic characteristics of the TM2 and TM3 helices near the TM2-3 loop are observed not only in the bundle of structures (Figure 2.2.5a), but also directly in the high resolution NMR spectra, where two sets of NMR peaks are identifiable for several residues near the TM2 C-terminus, including S268(16'), G269(17'), and S270(18') (Figure 2.2.7a). The data suggest that at least two conformations coexist in this region and they undergo slow exchange on the μs timescale used for NMR data acquisition. It should be noted that a similar minor conformation was also observed in an extended TM2 segment of GlyR [124] and in the TM2-TM3 construct in lipid bicelles [121]. The NMR structures determined in the present study are associated with the major peaks. The structure in the minor conformation could not be determined because of insufficient NOESY connectivity.

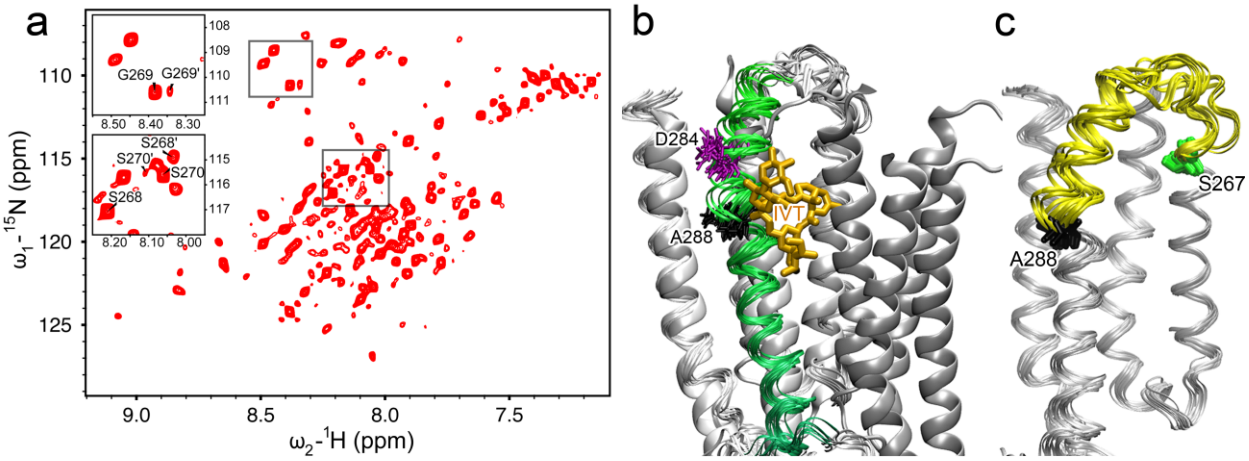

Figure 2.2.7. Conformational dynamics around the TM2-TM3 linker. (**a**) A representative ^{1}H-^{15}N HSQC spectrum of the hGlyR-α1 TMD in LPPG micelles at 40°C. Several residues at the C-terminus of TM2 show two sets of peaks, as exemplified in the insert for S268(16'), G269(17'), and S270(18'), indicating that two conformations coexist in this region and undergo slow conformational exchange. (**b**) The 15 lowest target function structures of the hGlyR-α1 TMD (ribbons) are aligned with the crystal structure of GluCl (cartoon, PDB ID: 3RHW). TM3 of the hGlyR-α1 TMD is highlighted in green. Ivermectin (orange sticks) observed in GluCl partially overlaps with the kink at A288 (black sticks) in the NMR structures of the hGlyR-α1 TMD. The residue D284 (purple sticks), located 4 residues upstream of A288, may be responsible for the kink [122]. (**c**) The segment showing high dynamics is highlighted in yellow between S267 (green) and A288 (black) in the bundle of 15 lowest target function NMR structures.

2.2.6. Structural Comparison of the hGlyR- α1 TMD with Other Cys-loop Receptors

The NMR-resolved structures of the hGlyR-α1 TMD show a general topological agreement with the pLGIC structures determined previously, but several notable differences may be functionally important. One distinct difference is the relatively short TM2 helix, which is about a half helical turn shorter than TM2 helices of ELIC [26,120], GLIC [27,28,47] and GluCl [29], but about two helical turns (7 residues) shorter than TM2 helices

shown in the cryo-EM structure of nAChR [1]. One may wonder if a shorter TM2 helix is due to different methodologies, NMR vs. X-ray. Our previously published NMR structures of the α4β2 nAChR TMD [36] negate this possibility. Both α4 and β2 show a TM2 helical length similar to that observed in ELIC, GLIC, and GluCl. The discrepancy in the TM2 helical length between hGlyR-α1 and other pLGICs occurs at the C-terminal end of TM2, where the helix ends at the 18' residue (with slight unwinding after 15') in hGlyR-α1, but at 20' in other pLGICs. Furthermore, the TM2 residues S268(16'), G269(17'), and S270(18') of hGlyR-α1 undergo slow exchange between two distinct conformations that have not been observed in the α4β2 nAChR using the same NMR method. These results demonstrate the unique structural flexibility at the EC end of the pore in hGlyR-α1. Compared to other pLGICs, glycine receptors are uniquely rich with serine residues (15', 16' 18') near the TM2 C-terminus (Figure 2.2.1). It is known that the OH group of serine can weaken the helical backbone hydrogen bonds by constraining the carbonyl oxygen through the O···H-O interaction [125]. The presence of a cluster of serines near the TM2 C-terminus may have contributed to the structural flexibility in the region.

2.2.7. Functional Importance of Observed Structural Dynamics

It is also notable in the bundle of NMR structures (Figure 2.2.5) that R271(19') shows conformational variation with a smaller population in a more extended helix and a larger population in an unwound conformation. Consequently, instead of facing the pore, R19' in some structures is mostly tangent to the pore, where R271(19') experiences a more hydrophobic environment. Indeed, such conformational flexibility was noted previously by tethering a rhodamine fluorophore to R271C [126], in which the experiment showed a

population shift of the fluorescence probe at 19' to a more hydrophobic environment upon channel opening, suggesting that conformational flexibility at the EC end of the pore is related to channel function. Ester substitution is expected to weaken the backbone hydrogen bonds and increase the flexibility of the pore-lining TM2 helix. Single-point amide-to-ester mutations at 13', 16', or 19' of nAChR increased the receptor's sensitivity to agonist more than tenfold [57]. A more recent study using electron paramagnetic resonance spectroscopy also observed greater conformational changes at the EC end of TM2 upon agonist binding [58].

The high flexibility of the TM2 C-terminus of hGlyR-α1 is likely coupled with the structural flexibility near the N-terminal helix of TM3. A helical kink (I285-A288) divides the TM3 domain into two α-helical segments: one from V277 to D284 and the other from V289 to V307 (Figure 2.2.5a and Figure 2.2.6). Three points about the kink are worth noting. First, statistically speaking, D284 is likely responsible for the kink formation. Analysis of nonredundant polypeptide chains revealed kinks in 64% of TM helices and aspartate showed notably high frequency at the i-4 position of the TM helical kink [122], though it remains unclear why aspartate promotes the helical disruption. Second, D284 is conserved in both glycine and $GABA_A$ receptors. It likely plays a similar structural and functional role in all anion-conducting Cys-loop receptors. Mutation of this conserved aspartate in the α1 $GABA_A$ receptor significantly reduced receptor activity [127]. Third, while the TM3 helices in the crystal structure of the GluCl and ivermectin complex show no kink [29], the kink may exist in the absence of ivermectin. When we aligned the TM structures of GluCl and hGlyR-α1, it became clear that ivermectin partially overlapped with the kink observed in the NMR structure (Figure 2.2.7b), suggesting that ivermectin binding may

have stabilized a straight helical conformation and that without ivermectin the flexibility would make it much more challenging to obtain high quality GluCl crystals for X-ray structure determination.

S267 and A288 mark the two ends of a dynamic region of the channel in our hGlyR-α1 TMD structures (Figure 2.2.7c). Intriguingly, mutations S267Y and A288W in the hGlyR-α1 TMD were found to substantially reduce general anesthetic and alcohol potentiation of GlyR responses [55]. Mutations at S267 showed that ethanol modulation was correlated with the volume but not the polarity or hydropathicity of the substituting side chains, suggesting that S267 itself is not directly involved in alcohol binding [128]. These functional consequences may result from the reduced conformational flexibility in the region due to bulky substitution at the S267 position. In fact, our previous NMR study demonstrated that the S267Y mutation increased the α-helix length at the TM2 C-terminus [111]. Mutation of A288 to an amino acid with a different size can also alter conformational flexibility in the region with functional consequences. Indeed, A288F and A288G have opposite functional impacts, with the former reducing and the latter increasing glycine-induced channel activation [54]. It is unlikely that glycine binding is affected by the mutations because the orthosteric agonist-binding site in the ECD is remote from A288. The changes in conformational flexibility due to mutations alter the channel's susceptibility to allosteric activation.

2.2.8. Conclusions

In this section we presented the NMR structures of the hGlyR-α1 TMD, the first structures for a mammalian anionic Cys-loop receptor TMD. Using NMR and electron microscopy

we demonstrated that the hGlyR-α1 TMD spontaneously forms pentameric Cl^- conducting channels. While the structures of the hGlyR-α1 TMD share an overall topology with previously solved structures of pLGICs, several unique features were observed which are potentially relevant to the allosteric modulation of the channel. These features include a shorter helix of the pore-lining TM2 with helical unwinding near the C-terminal end, a TM3 helical kink at A288, and a highly dynamic segment between S267(15') of TM2 and A288. The NMR structures of the hGlyR-α1 TMD provide valuable structural and dynamic templates for rationalizing dynamic modulation of anionic Cys-loop receptors and discovering novel therapeutic modulators.

CHAPTER 3

ANESTHETIC BINDING SITES IN NICOTINIC ACETYLCHOLINE RECEPTORS

3.1. ANESTHETIC SITES IDENTIFIED COMPUTATIONALLY

This section has been published as a full article in *J Phys Chem B* **114**: 7649-7655.

3.1.1. Background and Significance

The α7 and α4β2 nAChR subtypes are found in high abundance in the brain [8,9]. Despite high sequence homology (α7 has 62% and 57% sequence homology with α4 and β2, respectively), they exhibit substantial differences in their responses to general volatile anesthetics. The α4β2 nAChR is sensitive to inhaled general anesthetics, while α7 is considerably less sensitive [5,6].

The underlying cause for the different functional responses of α7 and α4β2 to general anesthetics remains unclear. Discovering the cause may advance the current understanding of anesthetic action on the α7 and α4β2 nAChR as well as homologous proteins. There are at least three possibilities that can contribute to the differences observed on α7 and α4β2. 1) Inhaled anesthetics interact with α4β2, but not with α7. 2) Anesthetics interact with both proteins, but in distinctive regions of the proteins and with different binding affinities. In this case, anesthetics may bind to functionally relevant regions in α4β2, while binding to functionally insensitive regions in α7. 3) Anesthetics act

similarly in both proteins, but α7 and α4β2 react differently to the perturbation of anesthetics due to their intrinsic structural and dynamic differences.

Complementary to experimental efforts, computational approaches provide meaningful predictions that can be substantiated by experimental evidence. Modeling, MD simulations, and normal mode analysis (NMA) have illustrated structural and dynamic features for nAChRs and predicted plausible channel gating mechanisms [129-133]. Computations have also provided insights for anesthetic binding to proteins and anesthetic effects on protein structures and dynamics [42,43,134-137].

In this section, we investigated how the inhaled general anesthetic halothane interacted with the α7 nAChR over 20-ns MD simulations on the closed- and open-channel α7 in the absence and presence of halothane molecules. In this section of the thesis we compare the computationally determined binding sites and energies for open- and closed-channel α7 with those previously determined for halothane binding in α4β2 [42,43]. Our computational model suggests that halothane binds to the α7 nAChR. The halothane binding sites in α7 were distributed in EC and TM domains as well as the EC/TM interface, similar to binding locations observed previously in α4β2 [42,43].

3.1.2. Methods

The open- and closed-channel α7 systems were prepared using the same method reported previously [138]. Briefly, the sequence of human α7 nAChR (P36544) was obtained from the ExPASy Molecular Biology Server (http://us.expasy.org) [139]. The closed-channel α7 structure was gen erated by homology modeling using the structure of *Torpedo marmorata* nAChR [1] as a template (PDB ID: 2BG9). The resulting closed-channel α7

model was energy minimized for 10,000 steps with a 500 kcal/mol/Å^2 harmonic restraint on its backbone atoms using NAMD 2.6 [91] and evaluated subsequently using the PROCHECK program [140]. The open-channel α7 was generated in the same way as we did previously for generating open-channel α4β2 nAChR [138]. Elastic-network NMA [141] was performed on the closed-channel α7 nAChR using the online *elNémo* server [142]. The lowest frequency eigenvectors, corresponding to a twist-to-open motion, were applied to the closed-channel α7 model through multiple cycles. In each cycle, heavy atoms of α7 experienced only small displacements, the model was energy minimized, and the pore radius was evaluated using the Hole program [92]. The final minimum pore radius at the hydrophobic girdle was 4.0 Å, which was close to the experimentally obtained value of 3.7 Å for the open-channel [143]. Two nicotine molecules were docked at the agonist-binding sites for open-channel α7. The choice of nicotine rather than other agonists was based on our comparative studies on α4β2 [42,43,138], in which nicotine was used as an agonist for the open-channel simulations because of its high affinity to α4β2 and the availability of the nicotine-bound AChBP crystal structure [30]. The open- and closed-channel α7 were separately immersed into a previously prepared water and lipids box [138,144] and energy-minimized for 50,000 steps with a harmonic restraint of 500 kcal/mol/Å^2 on protein backbones.

All MD simulations were performed using NAMD 2.6 [91] and CHARMM27 force-field parameters [145]. In order to be comparable with the simulations for α4β2 [42,43], the constant pressure of 1 atm and the constant temperature of 303 K (NPT ensemble) were also applied to the α7 simulations. Each open- and closed-channel system first went to a NPT equilibration with an initial harmonic restraint of 250 kcal/mol/Å^2 applied to the protein Cα

atoms. The restraint was gradually removed over a ~2 ns time period. The systems then went to unrestrained simulations for multiple ns before taking snapshots of the open- and closed-channel α7 for halothane docking. The docking to the α7 snapshots at four different time points (3.5, 4.5 5.5 and 6.5 ns) showed similarities (Figure 3.1.1 and Figure 3.1.2). Halothanes present in the snapshot at 5.5 ns were carried on for additional 20-ns simulations. The subsequent 20-ns MD simulations were performed on four individual systems: a closed channel without halothane, a closed channel with halothane, an open channel without halothane, and an open channel with halothane. Each halothane system underwent two additional replica simulations with different random seeds, yielding three statistically independent trajectories for each halothane system. The same protocols reported previously were used for the MD simulations [42,138]. Halothane parameters for docking and MD simulations were taken from our previous publication [146].

The initial halothane sites in α7 were identified using Autodock4 [147], through a Lamarckian genetic algorithm with a grid spacing of 0.375 Å. Structural snap shots of both closed- and open-channel α7 from the four previously mentioned time points were collected for halothane docking. We performed 500 independent halothane dockings on each of these structures. Based on the binding energies and occupancies from docking and similarity to the sites observed in *Torpedo marmorata* nAChR [41], five and four high halothane occupancy sites were determined for the open- and closed-channel α7, respectively. One halothane was manually placed at the interface of the EC and TM domains in the closed channel for the purpose of comparison with the open channel. Thus, five halothane molecules were present in both open- and closed-channel systems for MD simulations.

Halo-1_{closed} was identified with high occupancy near the agonist-binding site. A similar site (close to δ212) was also identified by photoaffinity labeling experiments on the *Torpedo marmarota* nAChR [41]. Halo-1_{open} was found in three different snapshots with high occupancy and low binding energy. Halo-2 was found with high occupancy across all four structures in the closed channel and in 3 snapshots of the open channel. This site is consistent with the γ111 site in *Torpedo marmarota* nAChR [41]. Halo-3 and halo-4 represent the EC/TM interfacial sites found across almost all snapshots for both open- and closed-channel α7 (only halo-4 was manually put in the closed-channel for comparison). These sites were also consistent with the δ228 site identified in *Torpedo marmarota* [41]. Halo-5 was found with high occupancy in all snapshots of the closed channel. But in the open channel, halo-5 was only observed in docking on a snapshot from 2.5 ns (data not shown) with occupancy of 105 of 500 and a binding energy of -3.35 kcal/mol. We purposely kept a halothane molecule in this location in the open-channel structure at 5.5 ns to test if it behaved similar or different from Halo-5_{closed}. Figure 3.1.1, Figure 3.1.2, Table 3.1.1, and Table 3.1.2 show and summarize halothane-docking results in the closed and open channels.

Halothane binding energies ($\Delta\Delta G_{binding}$) were calculated for each halothane site in both open- and closed-channel α7 using the Free Energy Perturbation (FEP) [148,149] implementation in NAMD-2.6 [91]. The same calculation protocol used previously for the α4β2 systems [42] was adopted in the calculations for α7 systems except that the time step was changed from 2 fs to 1 fs. The $\Delta\Delta G_{binding}$ is the result of subtracting the free energy of ligand water interactions ($\Delta G_{L,W}$) from that of ligand protein interactions ($\Delta G_{P,L}$).

VMD [86] was used for visualizing MD trajectories and generating figures.

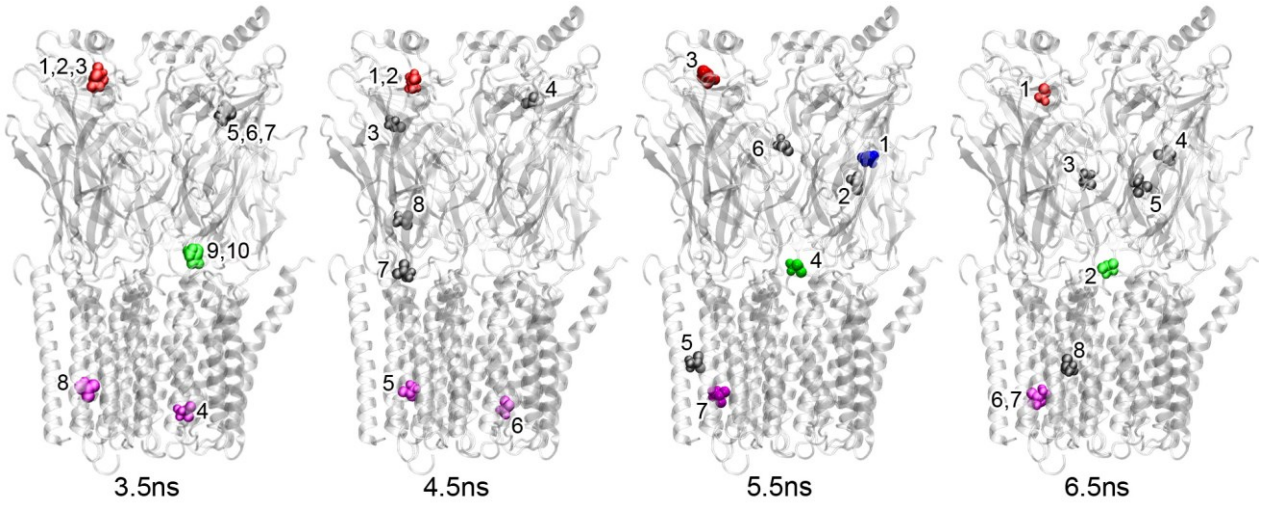

Figure 3.1.1. Halothane docking results for the closed-channel α7 nAChR. Docking was performed on structures taken from four different time points of unrestrained MD simulation. Note the similarities of halothane docking sites among four snapshot structures. Halothanes present in the snapshot at 5.5 ns are carried on for subsequent simulation. Colors of halothane at different sites are the same as that in the main text (i.e halo-1 is blue, halo-2 is red, halo-3 is green, and halo-5 is magenta). Halothanes colored in gray are those that appear in the docking results but are not included for further simulation. Halothanes are numbered the same as that in **Table 3.1.1**.

Table 3.1.1. Energies and Occupancies for Halothanes in Figure 3.1.1

	3.5 ns		4.5 ns		5.5 ns		6.5ns	
ID[c]	Energy[a]	Occupancy[b]	Energy[a]	Occupancy[b]	Energy[a]	Occupancy[b]	Energy[a]	Occupancy[b]
1	-3.67	280	-3.46	230	-3.62	148	-3.50	206
2	-3.66	101	-3.43	12	-3.57	37	-3.43	278
3	-3.65	1	-3.33	13	-3.4	154	-3.33	1
4	-3.55	66	-3.33	19	-3.29	126	-3.27	6
5	-3.52	11	-3.32	106	-3.28	10	-3.27	1
6	-3.49	1	-3.32	116	-3.23	1	-3.22	5
7	-3.48	4	-3.31	3	-3.22	24	-3.22	2
8	-3.42	33	-3.13	1			-3.20	1
9	-3.23	2						
10	-3.23	1						

[a] Energies in kcal/mol
[b] Occupancies based on 500 runs
[c] Halothanes are numbered according to Figure 3.1.1

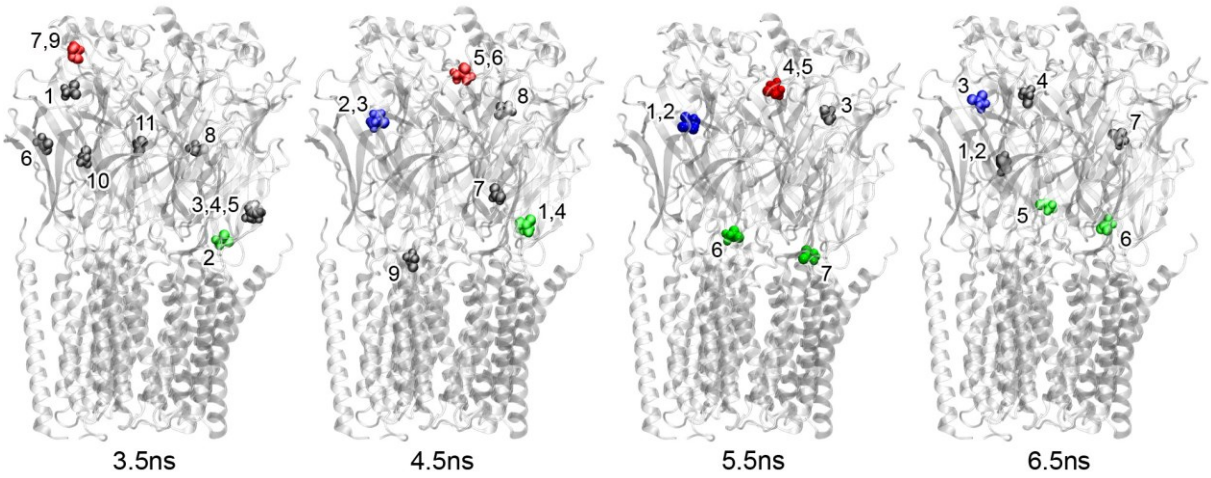

Figure 3.1.2. Halothane docking results for the open-channel α7 nAChR. Docking was performed on structures taken from four different time points of unrestrained MD simulation. Note the similarities of halothane docking sites among four snapshot structures. Halothanes present in the snapshot at 5.5 ns are carried on for subsequent simulation. Colors of halothane at different sites are the same as that in the main text (i.e halo-1 is blue, halo-2 is red, halo-3 is green). The two green halothanes represent equivalent sites in different subunits. Halothanes colored in gray are those that appear in the docking results but are not included for further simulation. Halothanes are numbered the same as that in **Table 3.1.2**.

Table 3.1.2. Energies and Occupancies for Halothanes in Figure 3.1.2

	3.5 ns		4.5 ns		5.5 ns		6.5ns	
ID[c]	Energy[a]	Occupancy[b]	Energy[a]	Occupancy[b]	Energy[a]	Occupancy[b]	Energy[a]	Occupancy[b]
1	-3.57	307	-3.4	88	-3.59	28	-3.50	206
2	-3.44	8	-3.37	259	-3.59	406	-3.43	278
3	-3.39	65	-3.34	37	-3.47	5	-3.33	1
4	-3.37	19	-3.34	9	-3.37	15	-3.27	6
5	-3.37	39	-3.32	22	-3.35	4	-3.27	1
6	-3.36	29	-3.3	15	-3.31	32	-3.22	5
7	-3.27	1	-3.26	66	-3.23	10	-3.22	2
8	-3.25	1	-3.26	1			-3.20	1
9	-3.25	1	-3.18	3				
10	-3.22	29						
11	-3.22	1						

[a] Energies in kcal/mol
[b] Occupancies based on 500 runs
[c] Halothanes are numbered according to Figure 3.1.2

3.1.3. Closed and Open-channel α7 Models

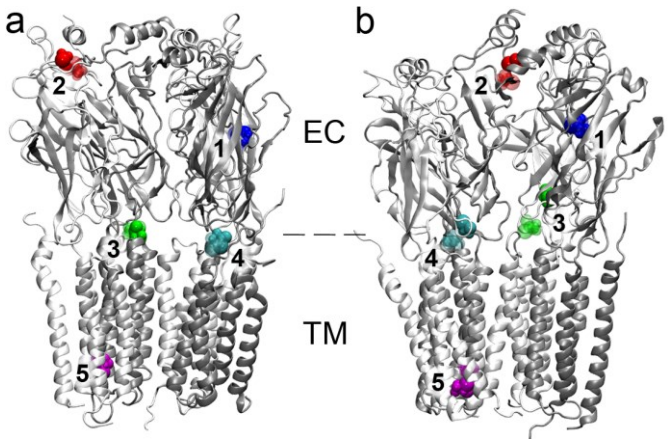

Figure 3.1.3. The closed- (a) and open- (b) channel structures of α7 at the end of 20-ns simulations. For clarity, the lipids and water molecules in the simulation systems are not shown. Five halothane-binding sites, labeled 1-5 for each system, at the beginning and end of the simulations are highlighted with transparent and solid halothane molecules in VDW format, respectively. EC and TM domains are labeled and the EC/TM interface is marked with a dash line.

The closed- and open-channel α7 models (Figure 3.1.3) were generated through the same strategy as used for previously constructing α4β2 nAChRs [138]. Subunit packing and channel integrity were maintained over the course of 20-ns of simulation. RMSD of backbone atoms reached plateaus gradually in both conformations and stabilized in the last 7 ns of the simulations. At the end of the simulations, the pore radius at the hydrophobic girdle was ~4.0 Å and ~2.2 Å for the open channel and closed channel, respectively (Figure 3.1.4). The constricting residues for the closed channel were L256 and to a lesser extent V252, in agreement with Law's α7 model [130]. Interestingly, the narrowest pore region (~3.0 Å radius) in our open-channel model occurred at residue T245, which is close to the IC end of the channel. In the narrow pore region, the hydroxyl group of T245 could interact effectively with an ion to facilitate partial desolvation of the

ion, and thus assist ion permeation through the pore. The pore profile with a wide-open EC entrance and a much narrower IC exit (presumably for Na^+) for the open-channel of α7 is quite similar to that found in the X-ray structure of GLIC [27].

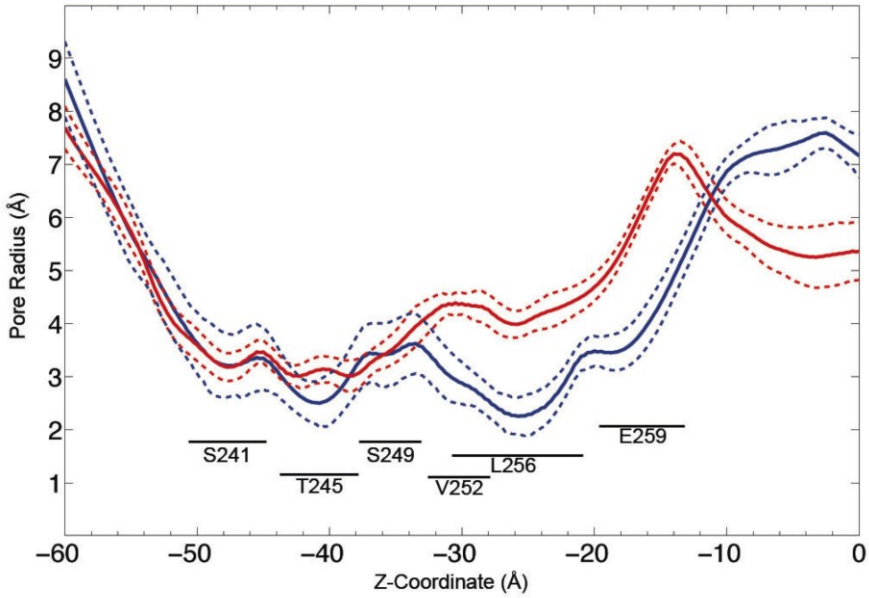

Figure 3.1.4. Pore radius profiles for the closed- (blue) and open- (red) channel α7 conformations at the end of 20-ns simulations. Plotted are the averages (solid) and standard deviations (dashed) of the pore radii calculated from 100 snapshots from the last 1 ns of simulation. The locations of pore lining residues are labeled.

3.1.4. Halothane in α7

Although previous experiments suggested that halothane had no functional impact on the α7 nAChR [5,6], we found multiple halothane binding sites in both the closed- and open-channel α7 nAChR (Figure 3.1.3). Most halothane molecules did not move significantly away from their initial positions during the simulations. The binding energies of halothane

molecules at their final sites of the first 20-ns simulations were calculated using the FEP method and summarized in Table 3.1.3.

Table 3.1.3. Binding energies and disassociation constants of halothane in closed- and open-channel α7 calculated using FEP based on the first simulation [148,149].

Site ID	*Binding Energy* (kcal/mol)		K_d (mM)	
	open	Closed	open	Closed
halo-1	-6.3	-3.1	2.9×10^{-2}	5.8
halo-2	-3.7	-2.7	2.1	11.3
halo-3	-5.3	-7.0	1.5×10^{-1}	8.9×10^{-3}
halo-4	-2.9	-6.8	8.1	1.2×10^{-2}
halo-5	-7.3	-8.7	5.4×10^{-3}	5.3×10^{-4}

Several features are noteworthy. First, halothane-binding sites sampled all representative regions of the α7 nAChR, including the EC and TM domains and the EC/TM interface. Second, most binding sites were at comparable locations in the closed- and open-channel α7 nAChR. Third, halothane binding energies varied significantly among individual sites. Halo-5, surrounded primarily by non-polar residues at the intracellular end of the TM domains, showed the lowest binding energy in both channel conformations. Halo-3 and halo-4 at the EC/TM interface exhibited lower binding energies in the closed channel than in the open channel. However, halo-1 and halo-2 in the ECD had lower binding energies in the open channel. Collectively, the variation in binding energies reflected differences in local binding environments.

Despite the existence of multiple halothane sites in α7, the pattern of halothane-binding sites in α7 did not show the five-fold symmetry that one might expect from a homopentamer, such as the α7 nAChR. This is understandable if one considers asymmetric motion in α7 [129,131,150]. Asymmetric anesthetic bindings in a highly symmetric

protein assembly were also observed in high-resolution X-ray structures of apoferritin complexed with anesthetics [135,151], in which subtle motion-induced changes at potential binding sites might differentiate one equivalent site from another.

3.1.5. Comparison of halothane binding between α7 and α4β2

Multiple halothane sites in the α4β2 nAChR were identified by our previous computational studies [42,43]. The existence of halothane binding sites in α4β2 was in good agreement with the finding that the channel function of the α4β2 nAChR could be inhibited by halothane [5,6]. In the case of the α7 nAChR, on which halothane showed no obvious impact in electrophysiology measurements [5,6], one might expect no significant halothane binding. However, our data suggested multiple binding sites in α7. Moreover, halothane binding energies in α7 were comparable with those in α4β2. One potential explanation for the discrepancy is that the halothane sites exclusive to α4β2 may hold primary responsibility for producing functional inhibition. It is, therefore, noteworthy that α4β2 had halothane binding sites in the TM domains toward the EC end, either between the α4 and β2 subunits or within a β2 subunit, with K_d values less than 0.2 mM [42,43], while equivalent sites did not exist in α7.

3.1.6. Conclusions

Our study revealed several important points regarding anesthetic binding to the α7 nAChR. First, lack of sensitive functional responses of the α7 nAChR to halothane in previous experiments is unlikely due to lack of halothane interaction with α7. Multiple halothane binding sites were observed in both closed- and open-channel α7. Some of the

sites have fairly high binding affinities. Second, the binding sites and affinities of halothane in α7 are dependent on the protein conformation. Overall halothane affinity was higher in the closed-channel α7, similar to previous observations of α4β2 [42,43]. Finally, while many of the sites observed in α7 and α4β2 overlapped, sites were observed at the EC end of the TMD in α4β2, which were not present in α7.

3.2. HALOTHANE AND KETAMINE BINDING SITES IN α4β2 DERIVED BY NMR

This section has been published as a full article in *Biochim Biophys Acta* **1828** (9): 398-404.

3.2.1. Background and Significance

Cys-loop receptors, including nAChRs, are important targets of general anesthetics [152,153]. Among the many nAChR subtypes, the α4β2 nAChR is one of the most abundant subtypes in the brain [8]. It is involved in memory [16], nociception [17], and the autonomic response [18]. It is highly sensitive to a variety of general anesthetics. Its current is inhibited by both volatile and intravenous general anesthetics at clinically relevant concentrations [5,6,154].

To reveal the underlying mechanism of anesthetic inhibition of a channel protein, an essential task is to identify where anesthetics bind to the protein. Mutagenesis has been widely used to determine residues showing different functional responses to anesthetics before and after mutations [55,155,156]. Such an approach is useful, but it is difficult to differentiate direct binding from allosteric action. Photoaffinity labeling has

emerged as a powerful tool for identifying specific protein residues participating in anesthetic binding [41,153,157-160]. Analogues of halothane [41], etomidate [75,159,161], and a neurosteroid [157] have been used in photoaffinity labeling studies of the *Torpedo* nAChR or the $GABA_A$ receptor. Multiple anesthetic binding sites were identified in the TM domains and other regions of these receptors. Despite considerable progress in developing new anesthetic analogues for photolabeling [162-164], the choices of anesthetics for photolabeling are still limited. In addition, large hydrophobic patches within the TMD often hinder amino acid sequencing and have made it difficult to determine specific photolabeled residues in some channel proteins. X-ray crystallography can offer high-resolution structural information for anesthetic binding. A critical issue is whether a high quality crystal is attainable for the protein of interest. Structural determination of eukaryotic Cys-loop receptors remains a great challenge, but recent successes on structures of prokaryotic homologues are encouraging [26-29]. Crystal structures of the ligand-bound ELIC [120,165] and the anesthetic desflurane- or propofol-bound GLIC [106], shed light on molecular recognition of general anesthetics in Cys-loop receptors. NMR spectroscopy is yet another powerful technique for structure determination of ion channels [36,66,111,166] and probing protein-ligand interactions at the atomic level. Using NMR, we have identified specific sites of anesthetic interaction with the TM domains of several proteins [93,113,167-171].

In this study, we used NMR spectroscopy to examine the plausible binding sites of the volatile general anesthetic halothane and the intravenous general anesthetic ketamine within the TM domains of the α4β2 nAChR. We previously determined the structures of the entire TM domains of the α4 and β2 nAChRs in LDAO detergent micelles

by solution NMR [36]. The high-resolution structure of the α4β2 TMD discussed in Section 2.1 provides an excellent platform for investigating anesthetic binding sites that may be responsible for anesthetic inhibition of the α4β2 nAChR. The knowledge of anesthetic binding sites within the nAChR TM domains is essential for solving the mystery of anesthetic modulations of the α4β2 nAChR and other Cys-loop receptors.

3.2.2. Methods

Sample Preparations

Expression and purification of the human α4 and β2 nAChR TM domains as well as the NMR sample preparation were reported in detail recently [36]. The same protein expression and purification protocols were used for the current study. Each NMR sample contained 0.25-0.3 mM protein, 1-2 % (40-80 mM) LDAO detergent, 5 mM sodium acetate pH 4.7, 10 mM NaCl, and 20 mM 2-mercaptoethanol to prevent disulfide bond formation. 5% D_2O was added to the samples for deuterium lock in NMR measurements. To keep adequate NMR spectral resolution, two types of the NMR samples were prepared for investigating anesthetic binding. One is β2(α4), in which β2 is ^{15}N-labeled (NMR observable) and mixed with the unlabeled α4 (invisible in ^{15}N NMR) in a 3:2 molar ratio. Another type is α4(β2) that has α4 ^{15}N-labeled and mixed with unlabeled β2 in a 3:2 molar ratio. In these individually labeled α4β2 samples, α4 and β2 retained their assembling interfaces and gained better NMR spectral resolution. The anesthetics ketamine or halothane were titrated to the samples using a micropipette or a gas-tight microsyringe, respectively. The ketamine concentration in the NMR samples was calculated based on the concentration

of a stock solution. The halothane concentration was quantified based on ^{19}F NMR using the method reported previously [170].

NMR data acquisition, processing, and analysis

NMR spectra were acquired on Bruker Avance 600, 700, or 800 MHz spectrometers at 45 ºC. Each spectrometer was equipped with a triple-resonance inverse-detection cryoprobe, TCI (Bruker Instruments, Billerica, MA). ^{1}H-^{15}N TROSY-HSQC spectra were acquired for each sample before and after adding anesthetics. Concentrations of halothane and ketamined used for the NMR experiments were up to 8 and 0.3 mM, respectively. Spectral windows of 13 ppm (1024 data points) in the ^{1}H dimension and 22 or 24 ppm (128 data points) in ^{15}N dimension were used. One second relaxation delay was used. The specific α4 and β2 residues affected by anesthetic binding were identified based on chemical shift changes induced by anesthetics. Since halothane has a distinct proton resonance that is suitable for saturation transfer used to determine halothane binding sites, we also performed 2D saturation transfer experiments using a modified HSQC pulse sequence [168] on the β2(α4) and α4(β2) samples containing ~2.0 mM halothane that has a distinct proton resonance. The spectra were acquired in an interleaved fashion with on- and off-^{1}H resonance frequencies of 6.48 ppm (the halothane proton) and 15 ppm (blank), respectively. The selective saturation was achieved using an IBURP2 pulse train (50 ms Gaus1.1000-shaped or rectangular pulses with an interpulse delay of 4 μs). A total saturation time was one sec and a relaxation delay was 1.5 sec. The 1D saturation transfer difference experiments [172] were performed to confirm that the saturation parameters used in 2D experiments were chosen properly. The ^{1}H chemical

shifts were referenced to the DSS resonance at 0 ppm and the ^{15}N chemical shifts were indirectly referenced [78].

NMR data were processed using NMRPipe 4.1 and NMRDraw 1.8 [82], and analyzed using Sparky 3.10 [83]. Each processed spectrum had 4096 × 512 data points. ^{1}H and ^{15}N chemical shift assignments for the α4 and β2 TM domains after addition of anesthetics were referenced to the previous assignments for the same proteins without drugs [36]. The published pentameric models of α4β2 and the MATLAB® programming environment were used to analyze interactions between anesthetics and α4β2. Chemical shifts and peak intensities in the NMR spectra were measured using Sparky 3.10 [83].

Visualization of anesthetics in the α4β2 nAChR

To assist visualizing anesthetics in the NMR identified binding sites, we performed targeted docking of halothane or ketamine to our previously reported α4β2 model. The targeted docking kept only those sites consistent with the NMR results. Docking was performed with Autodock4 [147] using a Lamarckian genetic algorithm with a grid spacing of 0.402 Å. For each intra-subunit site suggested by the NMR data, 250 independent anesthetic dockings were performed within a cube covering ~9000 $Å^3$ located at either the EC or IC end of the TMD. For each inter-subunit site, 500 independent anesthetic dockings were performed within a ~21x 21 x 42 Å rectangular prism covering the length of the inter-subunit interface.

3.2.3. Multiple halothane interaction sites in the α4β2 nAChR

Halothane bound to inter- and intra-subunit cavities of the α4β2 TM domains. As exhibited in the ^{1}H-^{15}N HSQC spectra in Figure 3.2.1, the majority of residues were not affected when 2mM halothane was added to either the α4(β2) or the β2(α4) samples. However, some residues had obvious changes in chemical shift. Full assignments of the NMR spectra showing halothane effects are provided in the online supporting material of the published manuscript [39]. Direct interactions between halothane and α4β2 were further demonstrated in 2D saturation transfer experiments [173,174] (**Figure 3.2.2**). After the residues showing changes either in chemical shift or saturation transfer were mapped onto the structure of α4β2 (Figure 3.2.3), the halothane interaction sites became apparent. The β2 subunit has two intra-subunit halothane binding sites near the EC and IC ends of the TMD. The closeness of hydrogen atoms of halothane to Y212 and V262 (site #1 in Figure 3.2.3) and to T224 and F231 (site #2) facilitated the observed saturation transfer (**Figure 3.2.2**). The α4 subunit also has an intra-subunit halothane site (#3) near the IC end of the TMD. Halothane near the EC end of the α4 TMD (#4) more or less resided between intra- and inter-subunit site, where residues I268 and N221, L222 of α4 and K260 and V262 of β2 line the cavity. It appears that #4 is open for halothane to sample both intra- and inter-subunit cavities. Another inter-subunit site for halothane (#5) is supported by I450 of β2 and L283 of α4, where saturation transfer was observed (**Figure 3.2.2**).

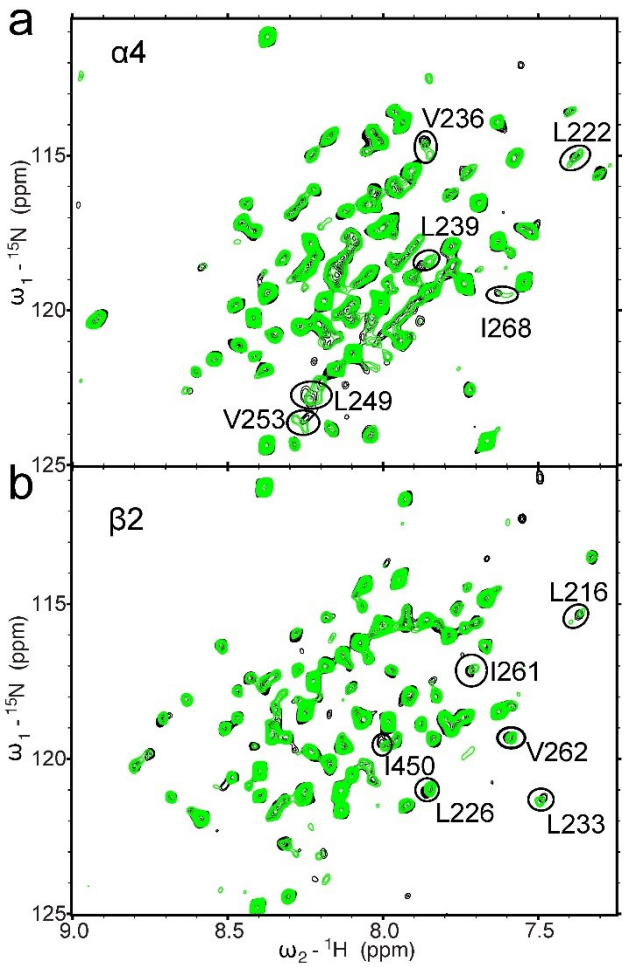

Figure 3.2.1. NMR spectra of the α4β2 nAChR TMD in the absence (black) and presence (green) of 2 mM halothane. (**a**) α4(β2), where only α4 is ^{15}N-labeled; (**b**) β2(α4), where only β2 is ^{15}N-labeled.. Peaks displaying significant changes in chemical shift are circled.

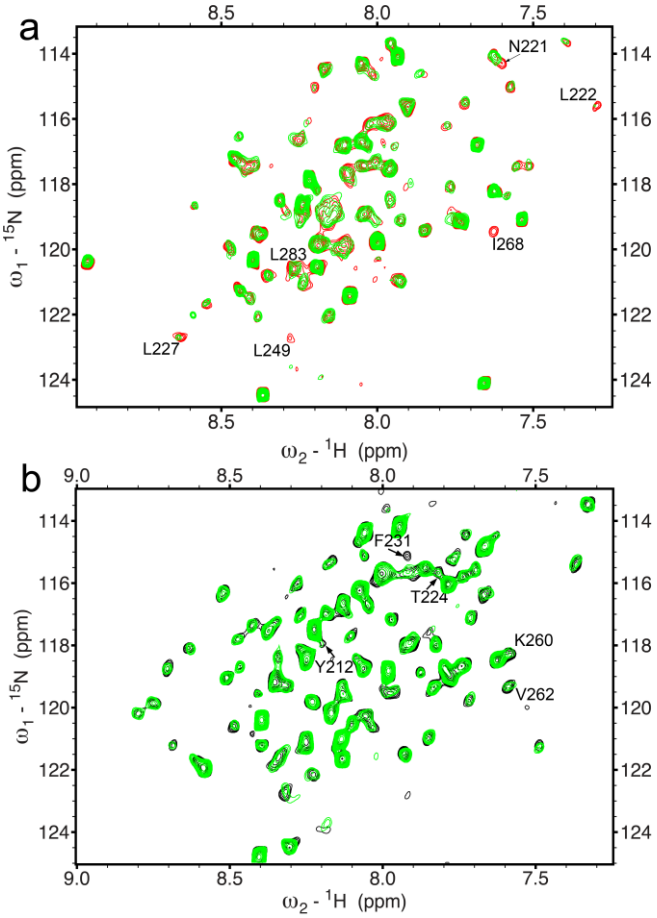

Figure 3.2.2. The 2D saturation transfer experiment showed specific interactions between halothane and residues of α4β2. (**a**) Overlay of the α4(β2) spectra with (green) and without (red) saturation of the proton resonance of halothane (2 mM). (**b**) Overlay of the β2(α4) spectra with (green) and without (black) saturation of the proton resonance of halothane (2 mM). The labeled resonance peaks showed significant intensity decrease when the proton resonance of halothane was saturated.

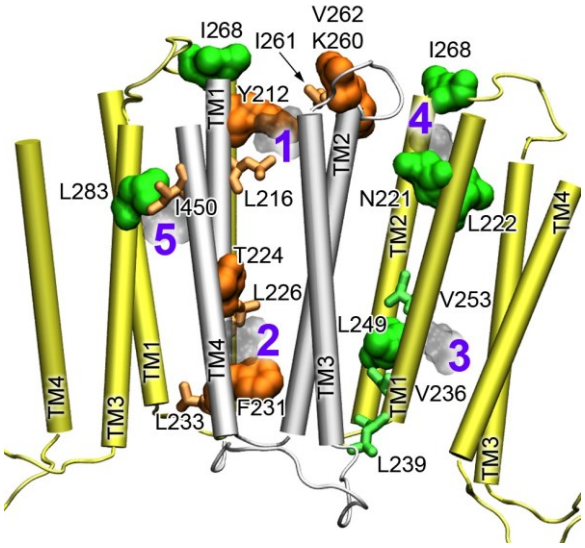

Figure 3.2.3. Multiple halothane-binding sites in the α4β2 nAChR. The TM domains of α4 and β2 are colored in yellow and silver, respectively. Residues of α4 (green) and β2 (orange) are highlighted in the surface presentation if they show direct interactions with halothane in the 2D saturation transfer experiments or in the stick presentation if they show changes in chemical shift upon halothane binding. The docked halothane molecules are numbered and shown in light gray. Note the inter-subunit sites, #4 and #5.

Collectively, both α4 and β2 have intra-subunit binding sites for halothane. The intra-subunit sites near the EC end and the IC end are homologous to the anesthetic site identified in the X-ray structures of GLIC [106] and a neurosteroid photolabeling site in the β3 subunit of the $GABA_A$ receptor [157], respectively. In addition to the intra-subunit sites, our NMR data revealed existence of inter-subunit sites for anesthetic binding. The inter- and intra-subunit sites identified at the EC end of the TMD are analogous to sites identified in our previous computational studies [42,43].

3.2.4. Ketamine interaction sites in the α4β2 nAChR

Compared to volatile anesthetics, such as halothane, the intravenous anesthetic ketamine inhibits the function of the α4β2 nAChR at a lower concentration [45]. We added only 80 μM ketamine to the α4(β2) or β2(α4) samples and observed notable changes in chemical shift for several residues in ^{1}H-^{15}N HSQC spectra (Figure 3.2.4) Full assignments of the NMR spectra showing ketamine effects are provided in the online supporting material of the published manuscript [39]. Severe overlapping of proton signals of ketamine and protein prevented a reliable result from saturation transfer difference experiments. Thus, the ketamine sites were determined based on chemical shift perturbation. Two ketamine-binding sites emerged when the ketamine-perturbed residues were mapped onto the NMR structure of α4β2 (Figure 3.2.5). One is reminiscent of the intra-subunit halothane site near the EC end of the TMD in β2 (Figure 3.2.3). Another is located near the IC end of the TMD between β2 and α4, where ketamine contacts I287 of β2 and V234 of α4. Ketamine perturbation to these residues propagated to other more remote residues (V283 and K246) and caused changes in their chemical shifts.

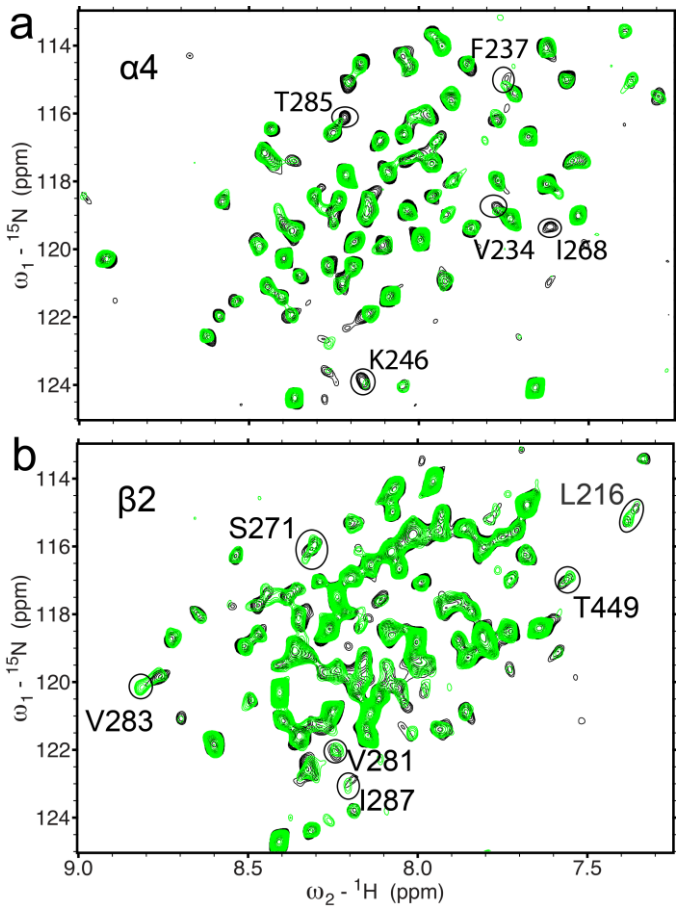

Figure 3.2.4. NMR spectra of the α4β2 nAChR TMD in the absence (black) and presence (green) of 80 μM ketamine. (**a**) α4(β2), where only α4 is ^{15}N-labeled; (**b**) β2(α4), where only β2 is ^{15}N-labeled. Peaks displaying significant changes in chemical shift are circled.

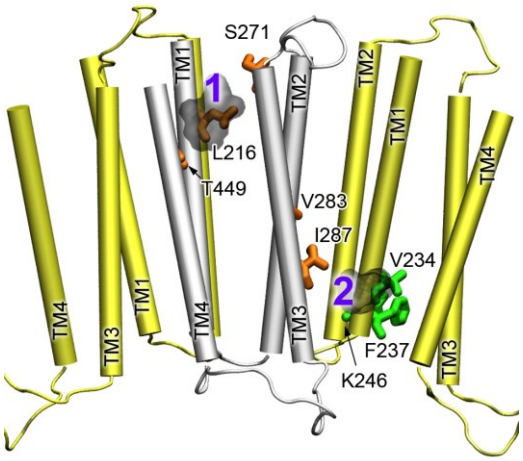

Figure 3.2.5. Ketamine-binding sites in the α4β2 nAChR. The TM domains of α4 and β2 are colored in yellow and silver, respectively. The residues of α4 and β2 showing changes in chemical shift upon ketamine binding are highlighted in green and orange sticks, respectively. The docked ketamine molecules are numbered and shown in light gray.

3.2.5. A common general-anesthetic binding site near the EC end of the TMD

Both the inhalational anesthetic halothane and the intravenous anesthetic ketamine have multiple interaction sites in the TM domains of the α4β2 nAChR. This finding is in accord with previous computational predictions [42-44,175,176] and experimental observations [41,158,159,177] on the α4β2 nAChR and its homologous proteins.

Among different sites, the intra-subunit binding site near the EC end of the TM domain (#1 in Figure 3.2.3 and Figure 3.2.5) has been most substantiated by experiments on several homologous proteins. Photo-affinity labeling of [^{14}C] halothane to the *Torpedo* nAChR was identified on residue δ-Y228 [41], which is homologous to Y212 of β2 lining halothane site #1 (Figure 3.2.3). Fluorescence quenching experiments suggested halothane binding to an equivalent site in GLIC [177]. Furthermore, crystal structures of GLIC in complex with the anesthetics desflurane and propofol revealed the intra-subunit

anesthetic binding site [106] that is in remarkable agreement with our NMR identified site for halothane or ketamine in the β2 subunit (Figure 3.2.6). It is intriguing to see that in the absence of the ECD, the TMD alone presents the same anesthetic binding site as the intact homologous proteins. Such a finding indicates that the NMR structures of the α4β2 TM domains [36] well represent the same domains in the intact protein. Halothane and ketamine have very different molecular volumes and shapes. Their binding to the EC end of the α4β2 nAChR TMD not only supports the notion that the site is a common anesthetic binding site for pLGICs [106], but also demonstrates the flexibility of the cavity to accommodate different anesthetics.

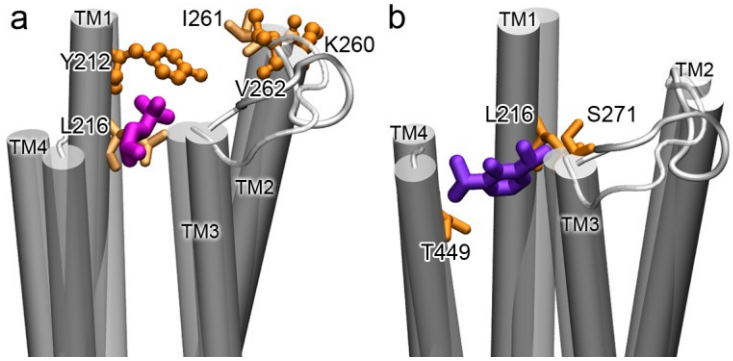

Figure 3.2.6. Comparisons of the intra-subunit anesthetic binding sites within the β2 subunit (silver) with the crystal structures of the anesthetic-bound GLIC (white, transparent). (**a**) The NMR determined residues showing halothane cross-saturation (orange ball and stick representation) as well as changes in chemical shift (orange sticks) are in remarkable agreement with the X-ray determined binding position for desflurane (magenta). (**b**) Likewise, residues showing changes in chemical shift in response to ketamine binding agree well with the binding position of propofol (purple) in GLIC.

3.2.6. Additional anesthetic binding sites

Inter-subunit halothane binding sites at the interface of α4 and β2 (#4 and #5 in Figure 3.2.3) are almost at the same height as the intra-subunit halothane site at the upper part

of the TMD. Several residues lining these sites were implicated previously as anesthetic-labeling residues in homologous proteins. L283 at the inter-subunit halothane-binding site is homologous to A288 of the α1 glycine receptor, where the site for alcohol and anesthetic action was rationalized [55,178]. Although the X-ray structures of GLIC bound with desflurane or propofol revealed only the intra-subunit anesthetic binding site, the study recognized the possibility of anesthetic migration from intra- into inter-subunit cavities [106]. The NMR identified halothane sites (#4 and #5) in Figure 3.2.3 add compelling evidence for anesthetic binding to the inter-subunit cavities. Ketamine, however, did not appear in the inter-subunit cavities at the upper part of the TMD. The larger size of ketamine may have prevented the molecule from occupying both intra- and inter-subunit cavities.

Another discrete set of intra- or inter-subunit cavities for anesthetic binding was found at the IC end of the TM domains. Halothane or ketamine binding to this region of the α4β2 nAChR was observed for the first time, but halothane binding to the homologous region in GLIC (W213 and W217) was detected previously using fluorescence quenching [177]. The region at the IC end of the TMD was also observed for cholesterol binding in the *Torpedo* nAChR [179]. Neurosteroids modulate $GABA_A$ receptors via binding to the TM domains of the receptors [155,180]. A neurosteroid-binding site at the IC end of the TMD was recently indentified [157], highlighting the importance of this region in drug binding and modulation of channel function.

It is worth noting that anesthetic binding is not restricted to the TMD. Anesthetics may also bind to cavities in the ECD. A recent crystal structure of GLIC in complex with ketamine shows that ketamine binds to an inter-subunit cavity in the ECD and the ketamine binding inhibits GLIC current [47]. For the α4β2 nAChR TMD, in the absence of

the ECD, the channels formed exhibit spontaneous opening and closing [36]. The degree to which anesthetics increase the channel closing probability and which binding site plays the most critical role in channel inhibition need to be investigated in future studies.

3.2.7. Conclusions

The study revealed multiple anesthetic binding sites in the TM domains of the α4β2 nAChR. The identified intra-subunit halothane and ketamine sites near the EC end of the TM domains are reminiscent of the previously reported site on homologous proteins [41,106], supporting the notion that the site identified is a common anesthetic site. The inter-subunit sites near the EC end of the TM domains were observed for halothane but not for ketamine. It is noteworthy that both intra- and inter-subunit binding sites at the EC end of the TMD were identified in previous computational studies [42,43]. The sites near the IC end of the TM domains were least documented for anesthetic binding in the literature. The finding of halothane and ketamine at these sites in our NMR study adds more weight to this region.

3.3. HALOTHANE AND KETAMINE BINDING SITES IN α7 DERIVED BY NMR

This section has been accepted for publication as a full article in *Biochim Biophys Acta*.

3.3.1. Background and Significance

The α7 nAChR is one of the most abundant nAChR subtypes in the brain [3]. High expression levels of the α7 nAChR have been observed in brain regions involved in learning, memory, and cognition [63,64]. Therefore, the α7 nAChR is a viable target for therapeutics to regulate processes impaired in schizophrenia, Alzheimer's disease, and other neurological disorders [65,181].

Unlike the α4β2 nAChR discussed in the previous section, which is highly sensitive to the general volatile anesthetic halothane, the α7 nAChR is insensitive to halothane [5,6]. Despite this discrepancy in sensitivities, our previous computational study identified halothane-binding sites in α7, suggesting that the insensitivity of α7 to halothane is unlikely due to the lack of halothane binding [44]. For the intravenous anesthetic ketamine the scenario is somewhat reversed, where the α7 nAChR is more sensitive to ketamine inhibition than the α4β2 nAChR [45,46].

In this study we determined binding sites for the volatile anesthetic halothane and the intravenous anesthetic ketamine in the α7 nAChR TMD using NMR spectroscopy. The high-resolution structure of the α7 TMD discussed in the previous chapter was used as the platform for investigating anesthetic binding sites within the α7 nAChR TMD. As predicted by the previous computational project we identified specific halothane binding sites in the α7 TMD. Identification of anesthetic binding sites for both halothane and

ketamine provides insights into understanding the mechanism anesthetic modulations for nAChRs and other Cys-loop receptors.

3.3.2. Methods

Sample preparations

The human α7 nAChR TMD for the NMR study contained 137 residues (Figure 2.1.1). The same protocol as reported previously [36] was used for the α7 expression and purification. The protein was expressed in *E. coli* Rosetta 2(DE3) pLysS (Novagen) at 15 °C for three days using the Marley protocol [76]. The protein was purified in LDAO using his-tag affinity column before and after cleavage of the his-tagged region. Each NMR sample contained 0.25-0.3 mM α7, 1-2 % (40-80 mM) LDAO detergent, 5 mM sodium acetate at pH 4.7, 10 mM NaCl, and 20 mM 2-mercaptoethanol to prevent disulfide bond formation. 5% D_2O was added for deuterium lock in NMR experiments. The anesthetics ketamine (80-240 μM) or halothane (0.7-5.5 mM) were titrated into the samples using a micropipette or a gas-tight microsyringe, respectively. The concentration of the volatile anesthetic halothane was quantified based on ^{19}F NMR using the method reported previously [170].

NMR spectroscopy

NMR spectra were acquired on Bruker Avance 600 MHz spectrometers at 45 ºC using triple-resonance inverse-detection cryoprobes (Bruker Instruments, Billerica, MA). ^{1}H-^{15}N TROSY-HSQC spectra were acquired in the absence and presence of the anesthetics halothane or ketamine. Direct contacts of halothane with the α7 TMD were determined

by STD spectra [172]. 2D saturation transfer spectra [168] were acquired in the presence of 3.2 mM halothane in an interleaved fashion with on- and off-^{1}H resonance frequencies of 6.48 ppm (the halothane proton frequency) and 25 ppm (blank), respectively. The selective saturation was achieved using an IBURP2 pulse train (50 ms Gaus1.1000-shaped with an interpulse delay of 4 μs). The total saturation time was 2 s and a recycle delay was 3 s. The ^{1}H chemical shifts were referenced to the DSS resonance at 0 ppm and the ^{15}N and ^{13}C chemical shifts were referenced indirectly [78].

NMR data were processed using NMRPipe 4.1 and NMRDraw 1.8 [82] and analyzed using Sparky 3.10 [83]. ^{1}H, ^{15}N, and ^{13}C chemical shift assignments were performed manually.

Visualization and molecular docking of anesthetics in the α7 nAChR

To assist with visualizing halothane- and ketamine-binding sites identified by NMR experiments, we performed targeted anesthetic docking to the α7 NMR structures. The targeted docking kept only those sites consistent with the NMR results. Docking was performed with Autodock4 [147] using a Lamarckian genetic algorithm with a grid spacing of 0.375 Å. For each binding site suggested by NMR, 250 independent anesthetic dockings were performed within a cube covering ~6600 Å^{3} located at the IC end of the TMD. Each docking calculation used an initial population size of 500.

3.3.3. Halothane binding site in the human α7 nAChR TMD

To identify residues that directly interact with halothane, we performed 2D saturation transfer NMR experiments. In these experiments, spectra for the α7 nAChR TMD in the

presence of halothane were acquired in an interleaved fashion with ^{1}H saturation frequencies at 6.48 ppm (halothane proton) and 25 ppm (blank), respectively. When halothane was saturated, residues showing substantial decrease in their peak intensities should be in close contact with halothane (Figure 3.3.1a). These residues include F230 in TM1, K239 in TM2, and F453 and C449 in TM4. The full spectra of the 2D saturation transfer experiments are provided in the online supporting material of the manuscript [37].

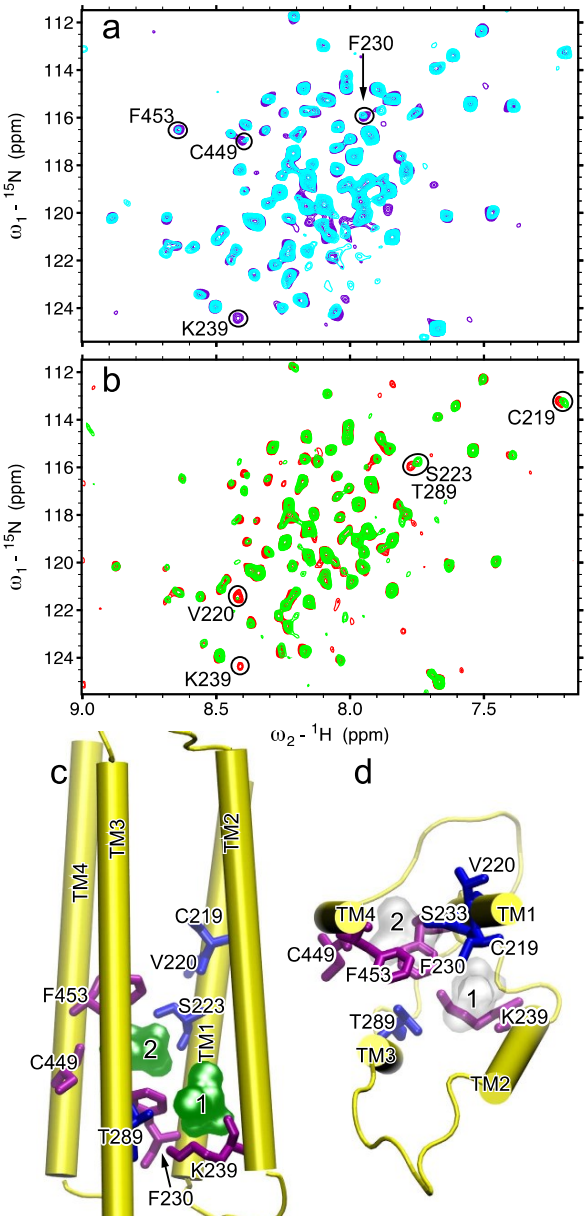

Figure 3.3.1. Halothane binding sites in the α7 nAChR TMD. (**a**) Overlay of 2D saturation transfer NMR spectra of α7 acquired with ^{1}H saturation frequency on (cyan) and off (purple) the proton resonance of halothane (3.2 mM). Residues showing considerable decreases in their peak intensities upon saturation of the halothane signal are labeled. (**b**) Overlay of ^{1}H-^{15}N TROSY-HSQC spectra of α7 in the absence (red) and the presence (green) of halothane (1.7 mM). Residues showing significant changes in chemical shift or relative peak intensity are labeled. (**c**) Side and (**d**) top views of the α7 structure highlighting the residues affected by halothane in (a) and (b) using purple and blue sticks, respectively. Two halothane molecules are shown in silver surface.

^{1}H-^{15}N TROSY HSQC spectra of α7 were acquired in the absence and presence of halothane (Figure 3.3.1b). Full assignments of the NMR spectra showing halothane effects are provided in the online supporting material of the published manuscript [37]. After the addition of halothane residues C219, V220, S223 of TM1, K239 of TM2, and T289 of TM3, were noted to show changes observable in the HSQC spectra. When these residues along with those identified in saturation transfer experiments were mapped onto the α7 structure, halothane binding to an intra-subunit cavity became clear (Figure 3.3.1c). The cavity is large enough to host two halothane molecules. This site is similar to one of the sites observed in the α4β2 nAChR [39]. However, unlike α4β2, α7 does not have halothane bound to the EC end of the TMD. The different binding sites may account for high functional sensitivity of the α4β2 nAChR and low functional sensitivity of α7 nAChR to halothane [5,182].

3.3.4. Ketamine binding sites in the human α7 nAChR TMD

Because the ketamine signal overlaps with the α7 signal in the ^{1}H spectra, the saturation transfer experiments could not be performed. Thus, we compared the α7 ^{1}H–^{15}N TROSY HSQC spectra in the absence and presence of ketamine to identify ketamine binding sites. Residues showing significant changes in the spectra after the addition of ketamine are highlighted (Figure 3.3.2a) and mapped onto the α7 structure (Figure 3.3.2b). Full assignments of the NMR spectra showing ketamine effects are provided in the online supporting material of the manuscript [37]. Most residues affected by ketamine are located in the lower half of the TMD, similar to the case for halothane (Figure 3.3.1c). It is noteworthy that the binding sites for ketamine and halothane largely overlap, but each

drug perturbed different residues within the relatively large cavity near the IC end of the α7 TMD. For example, F453, S285, I217, and L248 displayed chemical shift changes upon addition of ketamine, yet similar changes for these residues were not observed when halothane was added to the sample (Figure 3.3.1b). Conversely, C219, S223, and T289 showed chemical shift changes upon the addition of halothane, but not ketamine. Only a single ketamine molecule can fit into the cavity because of the larger molecular volume of ketamine. In contrast, the cavity can host two halothane molecules simultaneously.

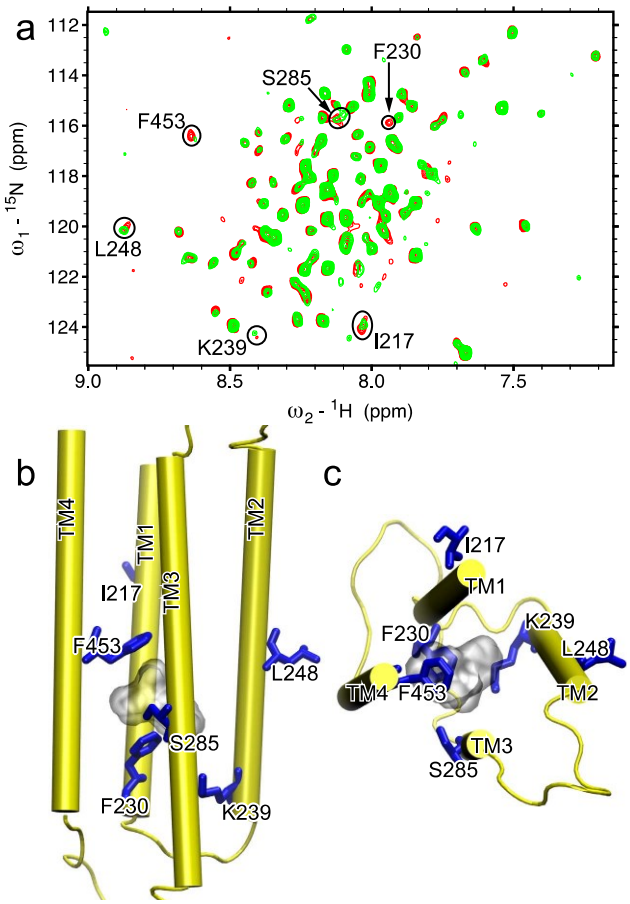

Figure 3.3.2. Ketamine binding site in the α7 nAChR TMD. (**a**) Overlay of ^{1}H-^{15}N TROSY-HSQC spectra of α7 in the absence (red) and the presence (green) of 80 μM ketamine. Residues involved in ketamine binding demonstrated significant changes in chemical shift or peak intensity. They are highlighted in circles and labeled with the one-letter amino acid code and the sequence number. (**b**) Side and (**c**) top views of the α7 structure highlighting the residues (blue sticks) perturbed by ketamine (gray surface) binding.

3.3.5. Conclusions

In this section we revealed the sites of binding for anesthetics ketamine and halothane in the TMD of the α7 nAChR. In contrast to our previous observations for the α4β2 nAChR TM domains, neither anesthetic binding was observed to bind at the EC end of the α7 nAChR TMD. Rather, anesthetics halothane and ketamine were observed to bind to an

intra-subunit cavity located at the IC end of the α7 TMD. This result is consistent with our previous computational prediction [44], where halothane was observed to bind at the IC end of the α7 TMD, but was not observed to bind at the EC end of the α7 TMD. Our finding here provides experimental evidence for anesthetic binding in α7 similar to that observed in our computational study [44].

CHAPTER 4

FUNCTIONALLY RELEVANT ANESTHETIC BINDING SITES

4.1. COMPUTATIONAL DETERMINANTS OF ANESTHETIC SENSITIVITY

This section has been published as a full article in *J Phys Chem B* **114**: 7649-7655.

4.1.1. Background and Significance

The α7 and α4β2 nAChRs show distinct sensitivities to the general volatile anesthetic halothane. The α4β2 nAChR is sensitive to halothane, while α7 is insensitive [5,6]. The underlying cause for these different functional responses has remained unclear. As has been discussed, at least three scenarios could produce the differences observed between α7 and α4β2. (1) Halothane interacts with α4β2, but not with α7. (2) Halothane interacts with both proteins, but in distinct regions. (3) Halothane binds to similar regions in both proteins, but α7 and α4β2 react differently to the anesthetic perturbation. As discussed in Chapter 2, scenario 1 is unlikely as both computational and experimental results suggest that halothane binds to α7. As the previous studies show the presence of both distinct and overlapping halothane binding sites between α7 and α4β2, scenarios 2 and 3 are both still valid.

In this section of the thesis, we continued our previous computational study to investigate how halothane binding affected the closed- and open-channel α7 nAChR over 20-ns MD simulations. To determine why α7 is much less sensitive than α4β2 to

anesthetic inhibition, the effects of halothane on the α7 structure and dynamics were compared with the data from previous MD simulations on α4β2 [42,43]. The correlated motion between EC and TM domains, particularly at the EC/TM interface, was found resilient to halothane perturbation in α7 and α4, but not in β2. Because of its unique EC/TM interface, the β2 subunits may bring the α4β2 nAChR to react more sensitively to halothane disturbance. The importance of the interface of the EC/TM interface to channel function was revealed by MD simulations and various experiments [183-185]. Dynamic susceptibility to halothane perturbation in the β2 subunit has been perceived as a reason why α4β2 is functionally more sensitive to halothane than α7.

4.1.2. Methods

Setup of MD simulations is described previously in section 3.1.2. Below are details for computational analyses of the simulation systems discussed in this section.

The Gaussian network model (GNM) [186,187] was used to analyze if halothane had any effect on the global dynamics of the α7 nAChR. Cα atoms represented residues and the interactions were cutoff at 10 Å. The five slowest modes of the GNM calculations on the structures after 20-ns MD simulations were included in the data analysis.

The pore radius profiles were obtained using the HOLE program [92] with a step size of 0.25 Å along the pore axis. Average profiles for both open- and closed- channel α7 were calculated using 100 frames from the last 1-ns simulation. The water profiles within the pore at each simulation time point were calculated by counting the number of water molecules within 2.5 Å windows along the pore axis. Each reported water profile resulted from the average of profiles at 100 time points over the last 1 ns of simulation.

The VMD program [86] was used for visualizing MD trajectories, generating figures, and calculating RMSD and root mean square fluctuation (RMSF). RMSF was calculated on the data sampling the last 7 ns simulations of the α7 systems. For comparison, the same data analysis was also performed on the α4β2 data acquired previously [42,43].

4.1.3. Differences of halothane behavior in α7 and α4β2.

Multiple halothane sites in the α4β2 nAChR were identified by our previous computational studies [42,43]. The existence of halothane binding sites in α4β2 is in good agreement with the finding that the channel function of the α4β2 nAChR could be inhibited by halothane [5,6]. In the case of the α7 nAChR, on which halothane showed no obvious impact in electrophysiology measurements [5,6], one might expect no significant halothane binding. However, our data suggested multiple binding sites in α7. Moreover, halothane binding energies in α7 were comparable with those in α4β2.

How can halothane molecules act on α7 differently from α4β2 to induce different functional impacts? First, the halothane sites exclusive to α4β2 may hold primary responsibility for producing functional inhibition. α4β2 had halothane binding sites in the TM domains toward the EC end, either between the α4 and β2 subunits or within a β2 subunit, with K_d values less than 0.2 mM [42,43], while equivalent sites did not exist in α7. Second, it is possible that different functional responses may result from intrinsic differences in the structural and dynamic properties of α7 and α4β2 to similar halothane bindings. Our previous studies demonstrated that a halothane-binding site similar to halo-3 or halo-4 in Figure 3.1.3 could elicit considerable structural and dynamic changes in β2,

but not in α4 [42,43]. If α7 is similar to α4 in its structural and dynamic responses to halothane binding, insensitive functional response to halothane binding in α7 should be anticipated.

4.1.4. Distinct response of the EC/TM interfacial structure and dynamics to halothane binding between α7 and β2.

Interactions of the TM2-TM3 linker with the Cys loop and the β1-β2 linker at the EC/TM interface are critical for propagating signals of agonist binding in the EC domain to channel gating in the TM domains [138,188-192]. We found previously that such interactions in β2 were much more susceptible to halothane perturbation than those in α4 [42,43]. In this study, we noticed that α7 more closely resembled α4, bearing similar resilience to halothane binding at the EC/TM interface.

Figure 4.1.1 compares representative EC/TM interfacial structures of the α7, α4, and β2 subunits in the open-channel conformations in the absence and presence of halothane at the end of 20-ns simulations. The interactions between the EC and TM domains are dominated by hydrophobic contacts. Although some halothane molecules were initially docked at the EC/TM interface in α7 and α4, they moved away during the simulations (Figure 4.1.2) and made no strong impact to the interfacial interaction. In contrast, the hydrophobic interaction in the same region of the β2 subunit was disrupted by polar contacts (Figure 4.1.1c) and salt bridges (R48 and D268 or D140 and K274) [138], creating a more amphiphilic environment. A halothane molecule moved between the Cys loop and TM2-TM3 linker of the β2 subunit, weakened the interfacial interactions, and consequently generated a wide gap between the EC and TM domains (Figure 4.1.1f). Our early experiments proved that anesthetics prefer an amphiphilic environment to a

hydrophilic region [113,193,194]. Thus, it is understandable why we did not observe the same halothane binding and subsequent effect in either α7 or α4 as that in β2.

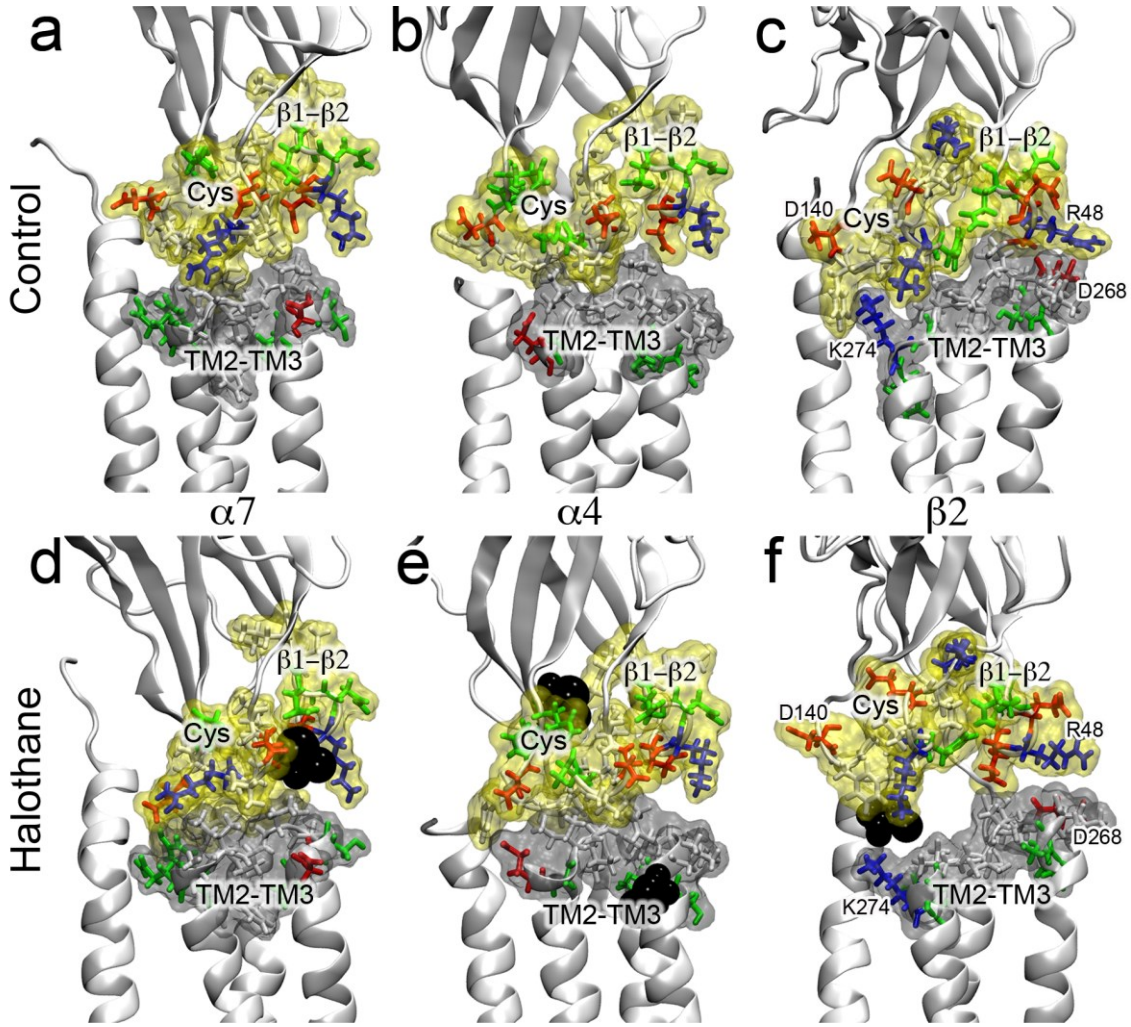

Figure 4.1.1. Residue packing at the EC/TM interface of the open-channel conformations of α7 (a and d), α4 (b and e), and β2 (c and f) in the absence (a, b, and c) and presence (d, e, and f) of halothane (black, VDW). The residues are colored according to their types, white: nonpolar; green: polar; red: acidic; blue: basic. The residues in the TM2-TM3 linker are highlighted in grey shadow, the residues in the β1β2 loop and the Cys-loop are covered with transparent yellow surface. Nonpolar contacts dominate the interaction at the EC/TM interfaces of all three subunits. Unlike α7 and α4, β2 could form salt bridges between K274 and D140 or R48 and D268. Halothane at the β2 EC/TM interface introduced a sizeable gap that interrupted the correlated motion between the EC and TM domains.

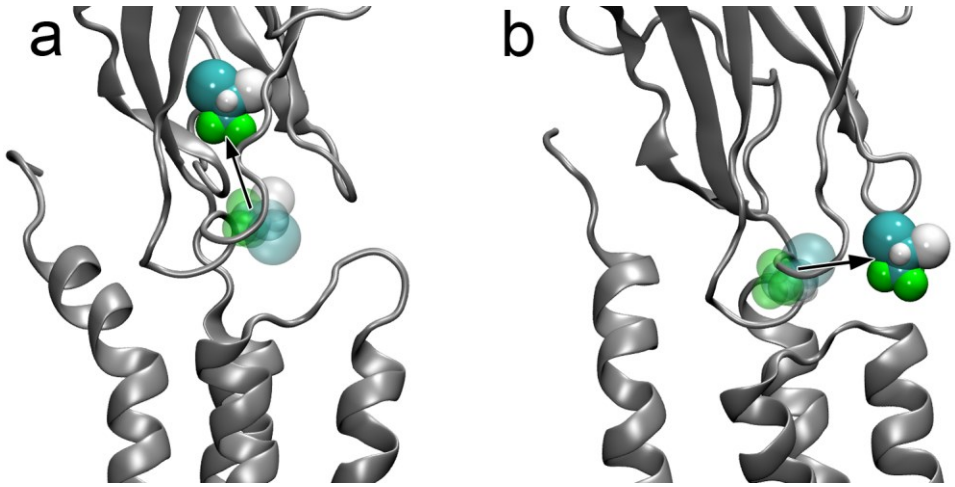

Figure 4.1.2. The initial and final sites of halo-3$_{open}$ (a) and halo-4$_{open}$ (b) over a 20-ns simulation. Both halothanes are initially (transparent) docked behind the Cys loop, but each moved away from their initial locations at the end (solid) of the simulation. Note that halo-3$_{open}$ migrated up into the ECD, while halo-4$_{open}$ migrated toward the pore.

The cross-correlation maps in Figure 4.1.3 integrated all GNM modes that demonstrated motional dependency between α7 residues in the absence and presence of halothane. For comparison, the corresponding maps of β2 were included in Figure 4.1.3. In the control systems, the Cys loop and the β1-β2 linker were strongly correlated with the TM2-TM3 linker in both α7 and β2 subunits, indicating the capacity of these contact points within the EC/TM interface to act as the actuation points for propagating signal from the agonist binding site to the channel gate. In the presence halothane, the correlations between these loops and linkers remained almost the same in α7, but diminished in β2. Insensitivity of correlated motion of α7 to halothane was substantiated by the results from the other trajectories as well. Such a sensitive response of β2 and an insensitive response of α7 to halothane appeared consistent with halothane induced functional responses of α7 and α4β2 [5,6].

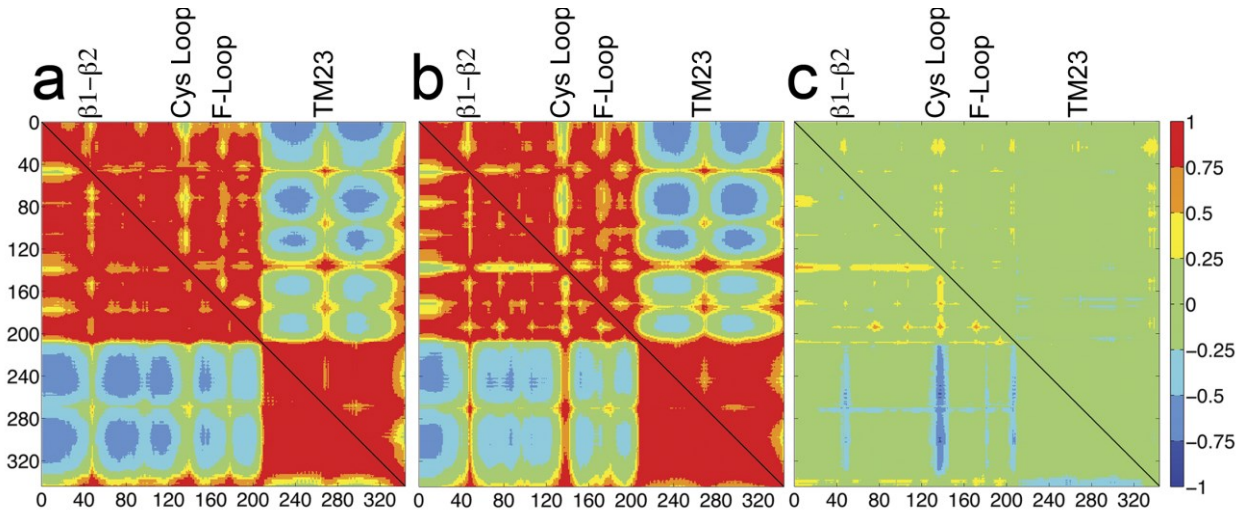

Figure 4.1.3. Cross correlation maps for the open-channel α7 (upper right panels) and β2 (lower left panels) nAChRs. Cross correlation maps were generated from the 5 lowest frequency modes of GNM analysis for the halothane (**a**) and control (**b**) systems**.** The difference (c) between the halothane and control systems (a minus b) shows that α7 displays limited changes in the correlated motion, but β2 has a substantial decrease (blue) in its correlated motion between the Cys loop and the TM domains.

The data presented in Figure 4.1.1 and Figure 4.1.3 were from the open-channel systems. One may wonder what happened to the closed-channel α7. Interestingly, overall higher binding affinity of halothane in the closed-channel conformation did not produce a profound effect on the structure and correlated motions of the α7 subunit. A similar phenomenon was also observed in the closed-channel α4β2, where halothane had higher affinity in the closed system and produced less structural and dynamical consequences on the α4β2 than that in the open system [42,43]. Taken together, these results suggest that high binding affinity of anesthetics may not be sufficient to assure functional changes in these receptors.

4.1.5. Conclusions

Our study revealed two important points regarding anesthetic action on α7 nAChR. First, lack of sensitive functional responses of the α7 nAChR to halothane in previous experiments was unlikely due to lack of halothane interaction with α7. Second, halothane binding to α7 did not induce profound changes in the structure and dynamics of α7 that could be related to the channel function. This is probably the most distinctive difference between α7 and α4β2. The favorable interaction between halothane and the amphiphilic EC/TM interface of the β2 subunit brings about changes in dynamics at this interface. These changes may be the reason why α4β2 is functionally more sensitive to halothane than α7.

It is worth noting that the previous experiments of anesthetic sensitivity on α7 were performed on the recombinant homomeric α7 nAChR [6,195], as reflected in our homopentameric α7 structural models. But in nature, α7 could also form heteromeric functional channels with other types of subunits. The α7 and β2 subunits of nAChR were found co-expressed within individual interneurons, signifying a possibility of the α7 and β2 co-assembled nAChR [196]. Co-expression of the rat α7 and β2 in *Xenopus laevis* oocytes resulted in functional nAChR channels with lower agonist sensitivity to and slower desensitization rate than the recombinant homomeric α7 nAChR [7]. Based on what has been found in our computational study, we predict that halothane will inhibit the function of the α7β2 nAChR, as it does to the α4β2 nAChR.

4.2. FUNCTIONALLY RELEVANT SITE FOR VOLATILE ANESTHETIC ISOFLURANE BINDING

This section has been published as a full article in *J Biol. Chem.* (2013).

4.2.1. Background and Significance

Neuronal nAChRs are composed of α (α2 – α10) and β (β2 – β4) subunits and assemble to form either homo- or hetero-pLGICs. The α7 subunit mainly forms homo-pLGICs, but it can also assemble with β2 or β3 subunits to form hetero-pLGICs [7,197,198]. nAChRs have been implicated in general anesthesia and play roles in memory [16], nociception [17], and the autonomic response [18]. Different subtypes of nAChRs show distinct sensitivities to general anesthetics [5,6,199], even though they share high sequence homology. For instance, the α7 nAChR is insensitive to volatile anesthetics at clinically relevant concentrations, while the α4β2 nAChR is hypersensitive [5,6].

Previously, we investigated potential causes for different sensitivities of the α4β2 and α7 nAChRs to volatile general anesthetics using MD simulations [42-44]. While multiple anesthetic binding sites were observed in α7, α4, and β2 subunits, anesthetic binding to a site at the interface between EC and TM domains of β2 produced a profound change in protein dynamics that was likely to affect channel function. On the basis of the simulation results, we proposed that the susceptibility to anesthetic perturbation in β2, but not in α7, underlies the functional sensitivity of α4β2 and insensitivity of α7 to volatile anesthetics [44]. We also predicted that unlike α7, α7β2 would be sensitive to volatile anesthetics due to the involvement of β2 [44].

In the present study, we revealed different functional responses of the α7β2 and α7 nAChRs, expressed in neurons and *Xenopus laevis* oocytes, to the anesthetic isoflurane. We also determined the binding sites and dynamic effects of isoflurane on both the α7 and β2 nAChR TM domains using NMR, validated the functional relevance of the identified isoflurane site via point mutations and subsequent functional measurements, and rationalized potential causes underlying the insensitivity of the α7 channel and the hyper-sensitivity of the α7β2 channel to isoflurane. The study provides compelling evidence that isoflurane binds to both α7 and β2, but at different locations. More importantly, isoflurane binding induced pronounced dynamics changes in β2, particularly for the channel gate residue L249(9'). In contrast, isoflurane binding to α7 did not generate the same dynamics changes. The study conveys a message that only those sites being able to modulate protein dynamics upon anesthetic binding will produce functional effects.

4.2.2. Methods

Electrophysiology measurements

Neuron dissociation and patch clamp whole-cell current recordings were performed as reported previously [197]. Briefly, several 400-μm coronal slices from postnatal Wistar rats (2-3 weeks old) containing the ventral diagonal band (VDB) or the ventral tegmental area (VTA) were cut in cold (2-4°C) artificial cerebrospinal fluid (ACSF). The slices were incubated for at least one hour in oxygenated ACSF at room temperature (22 ± 1°C). Thereafter, the slices were treated with pronase (1 mg/6 mL) at 31°C for 30 min. The medial septum/diagonal band or VTA region was micropunched out from the slices using

a well-polished needle. Each punched piece was then dissociated mechanically using several fire-polished micro-Pasteur pipettes in a 35-mm culture dish filled with well-oxygenated, standard external solution (150 mM NaCl, 5 mM KCl, 1 mM $MgCl_2$, 2 mM $CaCl_2$, 10 mM glucose, and 10 mM HEPES; pH 7.4 with Tris-base). The separated single cells usually adhered to the bottom of the dish within 30 min. Human α7-nAChR was expressed heterologously in transfected SH-EP1 human epithelial cells as described in details previously [200].

Functional measurements were performed using perforated patch whole-cell recordings coupled with a two-barrel drug application system [197]. After the formation of whole-cell configuration, an access resistance less than 30 MΩ was acceptable for voltage-clamp recordings. The series resistance was not compensated in the experiments using dissociated neurons. Data were filtered at 2 kHz, acquired at 11 kHz, and digitized on-line (Digidata 1322 series A/D board; Axon Instruments, Foster City, CA). All experiments were done at room temperature (22 ± 1°C). Clampex 9.2 (Axon Instruments) was used for data acquisition, and Prism 3.0 (*Prismsoft Inc.*) was used for graphics and statistical calculation. For statistical analysis of multiple groups of data, one-way or multivariate ANOVA followed by appropriate test was applied. $p < 0.05$ was considered significant, and data were represented as mean ± SE.

To ascertain the different sensitivity of α7β2 and α7 to isoflurane observed in neurons, we also used *Xenopus laevis* oocytes for channel expression and functional measurements. The plasmids encoding human α7 and β2 nAChRs for oocyte expression were gifts from Prof. Lindstrom's lab at the University of Pennsylvania and Prof. Henry Lester's lab at the California Institute of Technology, respectively. To reconcile the

structural and functional data, we constructed two mutants (α7-M22'V and α7β2-V22'M) for functional measurements in oocytes. The mutations were introduced by QuikChange Lightning Site-Directed Mutagenesis Kit (Agilent) and confirmed by DNA sequencing. cRNAs were synthesized for α7 and α7-M261V(M22'V) with the mMessage mMachine SP6 kit (Ambion), and for β2 and β2-V22'M with the mMessage mMachine T7 kit (Ambion). The cRNAs were purified with Rneasy Kit (Qiagen).

Channel functions of *Xenopus laevis* oocytes (stage 5-6) expressing native and mutant nAChRs were measured by two-electrode voltage clamp experiments. For making α7β2, the RNAs of α7 and β2 were injected to each oocyte in a 1:1 ratio with a total of 25 ng. The injected oocytes were maintained at 18˚C in a modified Barth's solution [120]. After expressed for 24 to 36 hrs, the oocyte in a 20-μL recording chamber (Automate Scientific) and the ND96 buffer [81] was clamped with an OC-725C Amplifier (Warner Instruments) to a holding potential of -60 mV, and currents elicited by acetylcholine and modulated by 50-μM isoflurane were recorded. The collected data were processed using Clampex 10 software (Molecular Devices).

NMR experiments

NMR samples of the TM domains of the α7 and β2 human nAChRs were prepared using the protocols as reported in detail previously [36]. Each NMR sample at pH 4.7 contained 0.25-0.3 mM protein, 40-60 mM LDAO detergent, 5 mM sodium acetate, 10 mM NaCl, 20 mM 2-mercaptoethanol to prevent disulfide bond formation, and 5% D_2O for deuterium lock in NMR measurements. The anesthetic isoflurane was titrated into the samples using

a gas-tight microsyringe. The isoflurane concentration was quantified based on ^{19}F NMR using the method reported previously [170].

All NMR spectra were acquired on a Bruker Avance 600 MHz spectrometer, which was equipped with a triple-resonance inverse-detection TCI cryoprobe (Bruker Instruments, Billerica, MA). ^{1}H-^{15}N TROSY-HSQC spectra were acquired with one-second relaxation delay for each sample before and after adding isoflurane. Spectral windows were typically 13 ppm (1024 data points) in the ^{1}H dimension and 22 ppm (128 data points) in ^{15}N dimension. The ^{1}H chemical shifts were referenced to the DSS resonance at 0 ppm and the ^{15}N chemical shifts were indirectly referenced [78].

The collected NMR data were processed using NMRPipe 4.1 and NMRDraw 1.8 [82], and analyzed using Sparky 3.10 [83]. Each processed spectrum had 4096 $\times$ 512 data points. ^{1}H and ^{15}N chemical shift assignments for the α7 and β2 TM domains in the presence of isoflurane were referenced to the previous assignments for the same proteins without drugs [36]. Chemical shifts and peak intensities in the NMR spectra were measured using Sparky 3.10 [83].

Visualization of isoflurane binding and calculation of cavity volumes and angles between TM2 and TM4

To assist visualizing isoflurane-binding sites identified by NMR experiments, we performed docking of isoflurane to NMR structures of the α7 and β2 TM domains. The targeted docking kept only those sites consistent with the NMR results. Docking was performed with Autodock4 [147] using a Lamarckian genetic algorithm with a grid spacing of 0.375 Å. For each intra-subunit binding site suggested by the NMR data, 250

independent anesthetic dockings were performed within a cube covering ~6600 Å^3 using an initial population size of 500.

The sizes of inter-subunit cavities for isoflurane binding were calculated using the POVME algorithm [201]. A grid encompassing the cavity in each of the 20 NMR structures of α7 or β2 was generated with 0.5-Å grid spacing. The algorithm output the grid points defining the cavity, which represent a subset of the total cavity points. Using MATLAB®, we determined the frequency that each point was observed in the bundle of twenty NMR structures for α7 or β2. Points shown from at least five structures were used for highlighting the cavity in Figure 4.2.3. Reported cavity volumes are the mean ± standard error of the volumes calculated for the 20 NMR structures.

The VMD program [86] was used for visualizing molecular structures and generating figures.

The angles between TM2 and TM4 helices near the EC end of the TM domain were calculated for each of 20 structures for β2 or α7. Vectors were fit to backbone atoms of TM2 (residues from K260 to L249 in β2 and from E259 to L248 in α7) and TM4 (residues from L454 to F443 in β2 and from M466 to V455 in α7). Angles were calculated using the cross product of the two vectors. The values reported are the mean difference between the β2 and α7 angles ± the pooled standard error SE_P,

$SE_p = S_p\sqrt{\frac{1}{n_1}+\frac{1}{n_2}}$ where $S_p = \sqrt{\frac{(n_1-1)s_1^2+(n_2-1)s_2^2}{n_1+n_2-2}}$, n_1 and n_2 represent the two sample sizes, and s_1 and s_2 represent the two standard deviations.

4.2.3. The α7β2 nAChR is much more sensitive to isoflurane inhibition than the α7 nAChR

Previous pharmacological, cell biological and single cell RT-PCR studies confirmed the expression, localization, and assembly of α7β2 nAChRs in VDB neurons [197]. We used the same dissociated VDB neurons to test functional responses of α7β2 nAChRs to the volatile anesthetic isoflurane. As shown in Figure 4.2.1, the inward currents were generated by application of 10 mM choline, an agonist for α7-containing nAChRs, in acutely dissociated neurons from mouse VDB at a holding potential of −60 mV. The peak currents were significantly reduced by 10 μM isoflurane after 2 min of isoflurane pre-incubation. Isoflurane pre-incubation reduced the maximal choline-induced activation by 37 ± 8%. The EC_{50} and Hill coefficient had no significant changes ($p = 0.58$) in the absence (3.8 ± 0.3 mM; 1.35 ± 0.32) and presence (4.1 ± 0.5 mM; 1.23 ± 0.18) of 10 μM isoflurane, suggesting that isoflurane inhibition occurs in a non-competitive manner (Figure 4.2.1a). Isoflurane inhibition of α7β2-nAChR-mediated whole-cell current in acutely dissociated neurons from mouse VDB was concentration dependent with an IC_{50} of 11.7 ± 1.6 μM (Figure 4.2.1b), less than 0.1 MAC (Minimum Alveolar Concentration) in human [154,202]. We measured isoflurane inhibition by using a repeated application protocol, in which choline was applied at 2 min-intervals in the continuous presence of 10 μM isoflurane. Isoflurane progressively inhibited α7β2 currents. Reversibility of isoflurane inhibition was demonstrated by the current recovery after 4 min of isoflurane washout. In contrast to α7β2, the homomeric α7 expressed either in neurons dissociated from ventral tegmental area (VTA) [203] or in the SH-EP1 cells [200] are not sensitive to 10 μM isoflurane (Figure 4.2.1c and d). This is consistent with an IC_{50} of ~600 μM (~2 MAC) for the human

α7 nAChR reported previously [204]. Different sensitivities to isoflurane inhibition were also observed in the recombinant α7β2 and α7 nAChRs expressed in *Xenopus laevis* oocytes. Representative current traces obtained from oocytes (Figure 4.2.1e and f) echo the message conveyed by the results from the dissociated neurons (Figure 4.2.1a-d). In addition, we found that a swap of residue 22' between α7 and β2 had a dramtic impact on isoflurane inhibition (Figure 4.2.1g and h). While α7 is insensitive to isoflurane inhibition, the mutant α7-M261(22')V showed 39±7% (n=6) isoflurane inhibition, similar to that (46±3%, n=4) observed on α7β2. Conversely, the mutant α7β2-V262(22')M, similar to α7, showed a lower sensitivity to isoflurane inhibition (12±2%, n=4). Altogether, these data suggest an indispensible role of β2 and importance of its residue V262(22') in isoflurane inhibition.

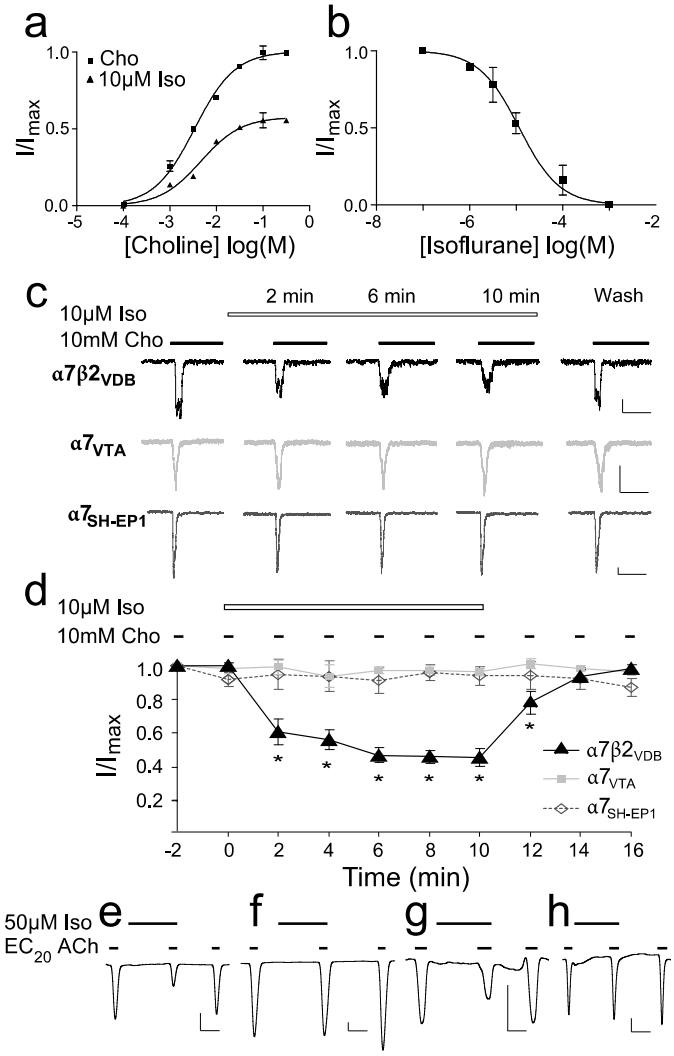

Figure 4.2.1. Isoflurane inhibited function of the α7β2 but not α7 nAChRs. (**a**) The α7β2 nAChRs expressed in VDB neurons were non-competitively inhibited by 2 minutes pre-incubation with 10 μM isoflurane. EC_{50} of choline and Hill coefficients show no significant differences in the absence and presence of isoflurane. (**b**) Isoflurane inhibited α7β2 with an IC_{50} of 11.7 ± 1.6 μM. Fractional currents were obtained from the mean peak currents elicited by 10 mM choline (~EC_{70}). The error bars are standard errors (n=6). (**c**) Representative whole-cell current traces for α7β2 expressed in VDB neurons, native α7 in VTA neurons and heterologously human α7 nAChRs in the SH-EP1 cells. The vertical and horizontal scales represent 50 pA and 250 ms, respectively. (**d**) Normalized mean (± SE) peak current responses of α7β2 and α7 expressed in various cells to the prolonged choline stimulation in the presence of 10 μM isoflurane (n=6). Isoflurane inhibited choline-induced currents in α7β2, but not in α7. (**e**)-(**h**): Representative current traces for (**e**) α7β2, (**f**) α7, (**g**) the α7-M22'V mutant, and (**h**) the α7β2-V22'M mutant expressed in *Xenopus* oocytes. The currents were elicited by acetylcholine at the EC_{20}, modulated by isoflurane (50 μM), recorded by two-electrode voltage clamp at – 60mV. The vertical and horizontal scales represent 25 nA and 1 min, respectively.

4.2.4. β2 and α7 have different isoflurane binding sites in their TM domains.

We investigated the binding sites of isoflurane in the TM domains of β2 and α7 nAChRs using high resolution NMR. As shown in the ^{1}H-^{15}N TROSY HSQC spectra (Figure 4.2.2a and b), the presence of 1.3 or 1.6 mM isoflurane perturbed a number of residues in β2 or α7 nAChRs, respectively. The residues with either more than 40% intensity change or a combined chemical shift change [205] greater than 15 ppb (β2) and 10 ppb (α7) were mapped onto NMR structures of the β2 or α7 TM domains (Figure 4.2.2c and d). Intra-subunit pockets for isoflurane binding were found in the NMR structures of β2 and α7, but at different sites: the one in α7 is close to the intracellular end of the TM domain; the one in β2 is at the EC end of the TMD, which is also the site for halothane and ketamine binding [39]. Moreover, this anesthetic site in β2 is homologous to the previously identified anesthetic site in GLIC [106], ELIC [206], and the *Torpedo* nAChR [41]. The isoflurane site in α7 is homologous to a halothane binding site at the IC end of the β2 TMD identified by NMR, and coincides with one of the halothane sites in α7 predicted by our previous MD simulations [44].

Some residues, including the channel gate residue L249(L9') in β2, showed significant changes upon the addition of isoflurane, but are structurally remote from the cluster of residues defining the binding pocket. Their changes likely result from allosteric effects rather than direct contact with isoflurane. It is also worth noting that several pore-lining residues in β2, but not α7, showed greatly reduced intensity upon the addition of isoflurane, indicative of motional changes for these residues.

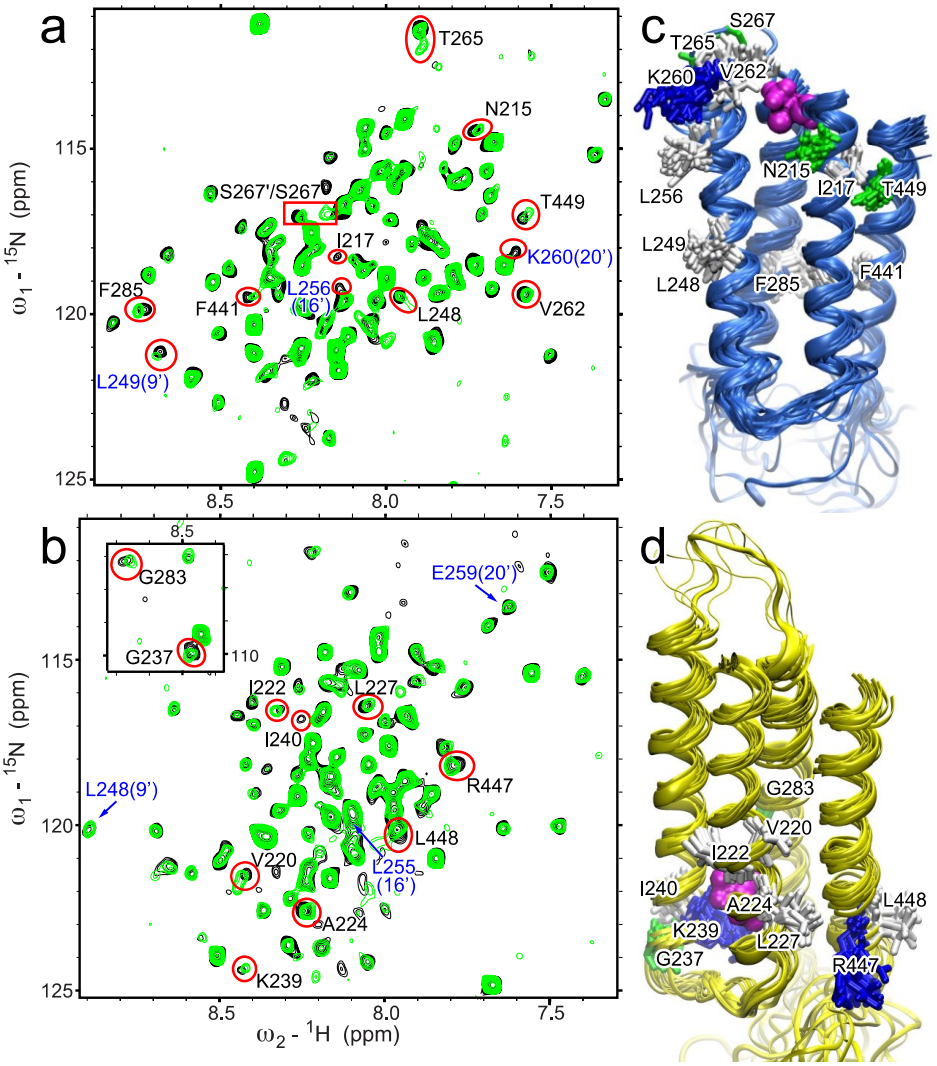

Figure 4.2.2. Isoflurane binding to the TM domains of β2 and α7. ^{1}H-^{15}N TROSY-HSQC spectra of (**a**) β2 and (**b**) α7 in the presence (green) and absence (black) of 1.3 or 1.6 mM isoflurane, respectively. Residues showing significant changes in chemical shift or peak intensity are labeled and highlighted in red. Residues labeled in blue are pore-lining residues. (**c**) The bundle of 20 NMR structures of the β2 TMD mapped with residues highlighted in red in (a). (**d**) The bundle of 20 NMR structures of the α7 TMD mapped with residues highlighted in red in (b). Residues are colored based on residue type: green – polar, white – nonpolar, and blue – basic. Docked isoflurane is shown in magenta surface.

4.2.5. A smaller intra-subunit pocket excludes isoflurane binding to the EC end of the α7 TMD.

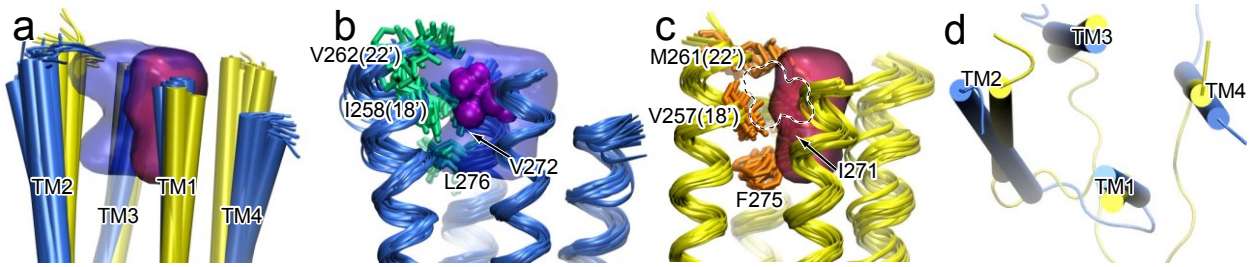

Figure 4.2.3. The intra-subunit cavity at the EC end of the TMD in β2, but not in α7, can accommodate isoflurane binding. (**a**) Alignment of 20 NMR structures with the lowest target function for β2 (blue) and α7 (yellow), and the cavities of β2 (blue) and α7 (red), outlined by grid points present in at least five of the 20 structures. Residues highlighted with the side chain bundles (shown in stick representation) in (**b**) β2 and (**c**) α7 have primary responsibility for the different cavity volumes. Note that in β2, the cavity can accommodate isoflurane (purple surface), but the cavity in α7 (dotted outline) cannot do the same. (**d**) The top view of the lowest target function structures of β2 (blue) and α7 (yellow) shows different orientations of TM helices.

To determine why isoflurane binds to the EC end of the TMD in β2 but not in α7, we examined the pocket in this region based on NMR structures of the β2 and α7 TM domains. Mostly hydrophobic residues and a few hydrophilic residues from four TM helices line the intra-subunit pocket near the EC end of the TM helices in both β2 and α7. The average cavity volumes are 179 ± 12 $Å^3$ and 122 ± 10 $Å^3$ for β2 and α7, respectively (Figure 4.2.3). The differences in cavity volume primarily result from tighter packing of four helices in the region of α7 and greater side chain volume of several cavity-lining residues in α7, such as α7-M261(22') vs. β2-V262(22'), α7-I271 vs. β2-V272, and α7-F275 vs. β2-L276. The differences in isoflurane inhibition made by these residues were

evident in functional measurements of the mutants α7-M261(22')V and α7β2-V262(22')M (Figure 4.2.1g and h). Helical tilting differences (6.7 ± 1.3°), measured by angles between TM2 and TM4 (Figure 4.2.3d), also contribute to different cavity volumes at the EC end of the TMD between β2 and α7. Both the inward helical tilting of α7 and the more bulky M22' side chain in α7 contribute to a smaller cavity. Furthermore, orientations of side chains also affect the cavity volumes. For the residues in TM3, both side chains of β2-V272 and β2-L276 are oriented away from the cavity, while the equivalent residues α7-I271 and α7-F275 are oriented towards the cavity. A smaller cavity in the EC end of the TMD in α7 has reduced the probability of isoflurane binding to the region, considering that isoflurane has a volume of 144 $Å^3$ [207].

4.2.6. Isoflurane modulates the dynamics of α7 and β2 differently.

One of the most striking differences between α7 and β2 is that upon isoflurane binding, α7 retained a single signal for each residue in the NMR spectra, but β2 showed classic examples of two-site chemical exchange [208,209] for several residues, including the channel gate residue L249(9') and V262(22') lining the isoflurane-binding pocket in β2. As shown in Figure 4.2.4, in the absence of isoflurane (black), each of these β2 residues showed a single peak in the NMR spectrum. After adding 1.3 mM isoflurane (red), an additional peak became observable for L248 and T265 (denoted as L248' and T265', respectively). When the isoflurane concentration was increased to 3 mM (cyan), L249 and V262 also showed additional peaks. The combined chemical shift change between each pair of peaks (A-B or A'-B), $\Delta\omega_{H+N} = [(\Delta\omega_H^2 + \Delta\omega_N^2)]^{1/2}$, is 32, 27, 37, 32 Hz for L248, L249, V262, and T265 of β2, respectively. Based on the consensus from many previous studies [208-

[210], the occurrence of two distinct peaks for a residue indicates a slow exchange with $k_{ex} << 2\pi\Delta\omega_{H+N} \sim 200s^{-1}$.

Conformational exchange among β2 residues also shows some differences. For residues L248 and T265, peak A remained at 20 Hz line width and the same resonance frequency in the absence and presence of isoflurane, indicating a possibility that slow conformational exchange with an extremely low population for the second conformation (peak B) already existed in the absence of isoflurane. Isoflurane shifted the equilibria between the two conformations. Indeed, the population of conformation B, $p_B = 1-p_A$, increased from 0 to ~0.3 and more than ~0.5 when isoflurane was increased from 0 to 1.3 and 3 mM. Overall, L248 and T265 fit well to the scheme of slow exchange between two conformations [208-210]. In the case of L249 and V262, however, a single peak with a broader line width in the ^1H dimension was observed in the presence of 0 mM (L249, 21 Hz; V262, 17 Hz) and 1.3 mM isoflurane (L249, 19 Hz; V262, 16 Hz), but two narrower peaks (L249, 16 and 12 Hz; V262, 14 and 12 Hz) were observed in the presence of 3 mM isoflurane. The results suggest that L249 and V262 were likely in an intermediate exchange regime [208,209] before exposed to 3 mM isoflurane. In addition to slower exchange between A' and B conformations, the increased isoflurane concentration also shifted peak A' from peak A by 14 and 11 Hz for L249 and V262, respectively (Figure 4.2.4). This is not unexpected, considering that multiple conformers with subtle differences can co-exist in a functional state [211,212].

The sensitivity of β2 and insensitivity of α7 to the dynamics modulation by isoflurane are in good agreement with their distinctly different functional responses to isoflurane inhibition.

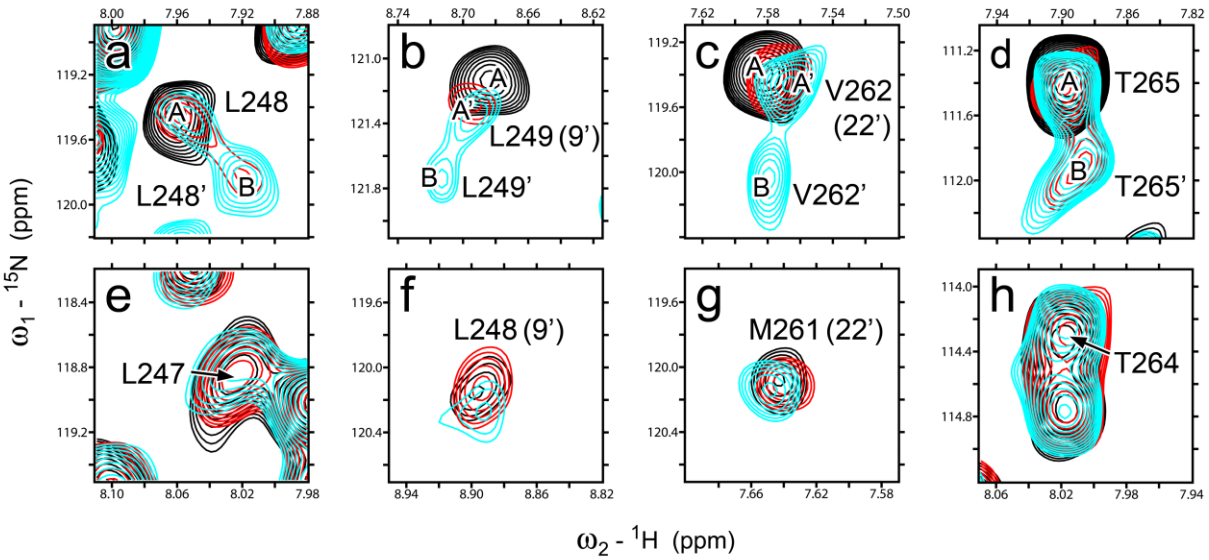

Figure 4.2.4. Different dynamics responses of β2 and α7 to isoflurane modulation. Overlay of NMR spectra for individual residues in (**a**)-(**d**) β2 and (**e**)-(**h**) α7 in the presence of isoflurane: 0 mM (black), 1.3 mM for β2 and 1.6 mM for α7 (red), 3.0 mM for β2 and 3.3 mM for α7 (cyan). Note that none of the α7 residues show an additional conformation over the isoflurane concentration range used in the experiments. The peaks representing the different conformations for β2 are labeled A, A', and B.

4.2.7. Discussion

Our functional data substantiate the previous prediction [44] that, unlike the α7 nAChR, the α7β2 nAChR is sensitive to anesthetic inhibition. The result highlights the role of β2 in functional modulation by volatile anesthetics and supports our hypothesis that β2 is primarily responsible for the difference of anesthetic susceptibility between α4β2 and α7 [44]. More importantly, the result conveys the message that two or three subunits susceptible to anesthetics, such as β2 in α7β2, are sufficient to produce functional effects. The message is consistent with the notion obtained from MD simulations of anesthetic propofol action in GLIC [62].

Why is β2 more susceptible to volatile anesthetics than α7? This key question has been addressed by our NMR experiments from three aspects. First, β2 and α7 show some structural differences in their TM domains, even though they share a common scaffold. The most notable difference lies in the size of an intra-subunit cavity near the EC end of the TMD that is large enough in β2, but not in α7, to accommodate isoflurane binding. Second, the structural difference leads to different binding locations for isoflurane, which binds to the cavity at the EC end of the TMD in β2 but to a pocket located at the IC end of the TMD in α7. Finally, differences in their structures and isoflurane-binding sites may have contributed to different dynamics responses of β2 and α7 to isoflurane binding. Only in β2 were isoflurane-induced changes in conformational populations and motion on the μs-ms timescale observed. The combined effects from structures, anesthetic binding sites, and dynamics modulations may have contributed to the functional differences between β2 and α7.

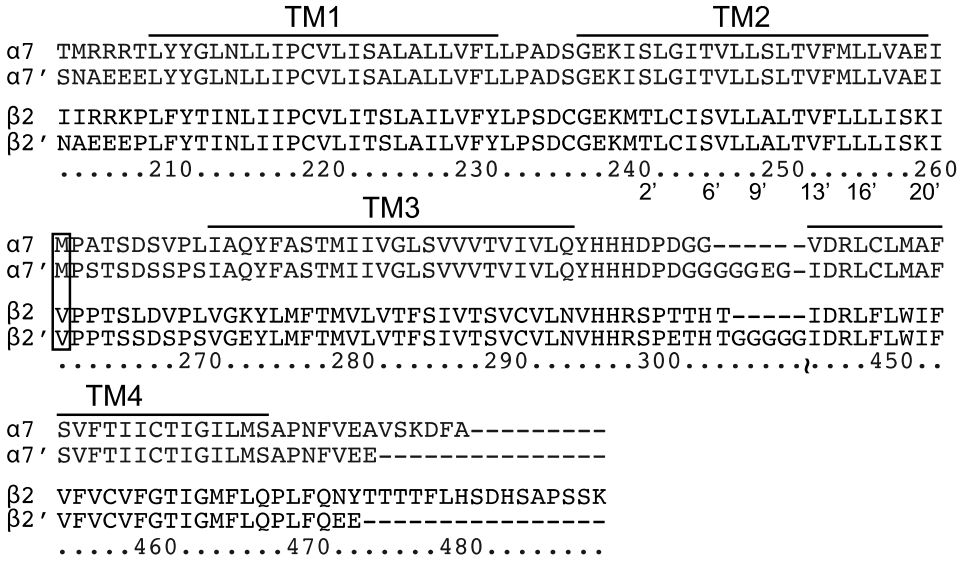

Figure 4.2.5. Sequence alignments for TM domains of human α7 and β2 nAChRs. Sequences of the constructs used for NMR samples, α7' and β2', are aligned with their respective native sequences. Note that only a few terminal and loop residues were changed to increase the stability of NMR samples. The labeled sequence numbers are for the α7 nAChR. The pore lining residues are labeled using the conventional prime numbering. Residues in the box were mutated in the study.

The sequence identity between β2 and α7 is high, ~50% for the TM domain and close to 65% for the pore-lining TM2 helix. Their sequence homology is even higher (Figure 4.2.5). Our results demonstrate that variation in a small number of residues is sufficient to make differences in protein structures, drug binding sites, and functional responses to drug binding. The functional significance of such small changes in structure highlights the necessity of solving individual protein structures, even for highly homologous proteins. In the case of β2 and α7, the homologous cavity-lining residues β2-V22' and α7-M22' make a notable difference for their respective cavities, isoflurane binding, and isoflurane inhibition. Indeed, a single α7-M22'V mutation markedly increase the channel sensitivity to isoflurane and the α7β2-V22'M mutation had a reverse effect.

This result is consistent with the diminished sensitivity to volatile anesthetics observed previously for the I22'M mutation in the α3 containing nAChR [195]. A larger volume and extended side-chain conformation of M22' can effectively reduce the cavity volume and obstruct drug binding. Moreover, methionine may also stabilize the TM2 helix and make it more resilient to structural and dynamic perturbation introduced by anesthetic binding. Previous studies using unnatural amino acid substitutions have shown that residues with un-branched side chains, such as methionine and alanine, have a more stabilizing effect on α helices than branched amino acids, such as valine and isoleucine [213]. Similarly, β2-S19' and α7-A19' could also make dynamics differences to the TM2 helix. Alanine is a natural helix promoter [214], while serine and threonine often disrupt α-helices due to backbone to side chain hydrogen bonds [125,215]. Our previous NMR study noted heightened conformational dynamics at the EC end of TM2 for the glycine receptor, which is uniquely rich with serines in this region compared to other pLGICs [38]. Contributions to the anesthetic binding site from two pairs of residues in TM3, β2-L276/α7-F275 and β2-V272/α7-I271, should also not be under estimated. Mutation on the homologous residue in GLIC was found to significantly affect the channel's susceptibility to the anesthetics desflurane and propofol [106].

The anesthetic binding site at the EC end of the TMD, as revealed for isoflurane in β2, is probably a common site in pLGICs for anesthetics. Using NMR, we found that anesthetics halothane and ketamine bound to the same site in β2 [39]. The site is also consistent with one of the halothane sites identified by photo-affinity labeling in the *Torpedo* nAChR [41] and by fluorescence quenching in GLIC [177]. The anesthetics desflurane and propofol were found in the homologous site in the crystal structures of

GLIC bound with these anestethics [106]. Functional and mutation studies on the α7/α3 nAChR chimeras also underscored the importance of the cavity to inhibition by the volatile anesthetic halothane [195]. In contrast, anesthetic binding to the IC end of the TMD, as observed for isoflurane in α7 in this study, is less effective to perturb channel function. Isoflurane inhibits α7 only at concentrations higher than those used clinically [204].

Our results provide evidence that functional insensitivity of α7 to volatile anesthetics is not due to lack of anesthetic binding, at least in the case of isoflurane. The hypersensitivity of α7β2 and insensitivity of α7 suggest that the EC end of the TMD plays a critical role for channel gating in pLGICs. Increasing the rigidity of residues at the EC end of the TMD can make the channel less responsive to activation signals. Many previous studies support this notion. Increasing helical flexibility at the EC end of TM2 of the nAChR was found to increase the receptors' sensitivity to agonist more than tenfold [57]. Disulfide bond trapping experiments on the $GABA_A$ receptor [216] and EPR experiments on GLIC [58] also support heightened dynamics at the EC end of TM2 during channel gating. Our previous work on the glycine receptor suggested that increasing or decreasing the conformational dynamics at the EC end of TM2 could respectively increase or decrease the channel's susceptibility to allosteric modulation [38]. Thus, it is conceivable that changing dynamics of the EC end of the TMD, either via drug binding or point mutations, is a common mechanism to modulate functions of pLGICs.

4.2.8. Conclusions

The general volatile anesthetic isoflurane binds to an intra-subunit cavity at the EC end of the TMD, similar to the binding site observed for halothane. Mutagenesis and functional

measurements confirmed that this site is the functionally relevant site for isoflurane, and likely other general volatile anesthetics. Our study not only highlights the importance of the anesthetic binding site, but also emphasizes the role of channel dynamics in anesthetic action. Although β2 and α7 have high sequence homology, the dynamics and subtle structural differences are sufficient to affect anesthetic binding as well as functional consequences. Anesthetic binding is necessary but not sufficient to produce a functional consequence. Only the binding that modulates dynamics of pore-lining residues, such as that at the EC end of the β2 TMD, can impact function.

4.3. FUNCTIONALLY RELEVANT SITES FOR INTRAVENOUS ANESTHETIC KETAMINE BINDING

This section is based on manuscripts published in *Structure* **20**(9): 1463-1469 and recently accepted for publication in *Biochim Biophys Acta*.

4.3.1. Background and Significance

In previous sections, it was determined that general volatile anesthetics, such as halothane or isoflurane, bound to an intra-subunit cavity at the EC end of the β2 TMD, but only bound to a cavity located at the IC end of the TMD in α7. Subsequent functional experiments validated that functional insensitivity of α7 to volatile general anesthetics resulted from the lack of anesthetic binding to the EC end of the TMD, suggesting that the site observed in β2 is the functionally relevant site for volatile general anesthetics. But what about the functionally relevant site for the intravenous general anesthetic ketamine?

With respect to inhibition by ketamine the α7 nAChR is more sensitive than the α4β2 nAChR [45,46]. The IC_{50} values of ketamine for the α7 and α4β2 nAChRs are ~20 μM and 50-72 μM [45,46], respectively.

In this section of the thesis we rationalize the potentially relevant sites for anesthetic ketamine binding within the α7 nAChR TMD. Our results indicate two potentially relevant anesthetic binding sites for ketamine in the α7 nAChR: one in the TMD, and the other in the ECD. NMR data indicate that ketamine binds to an intra-subunit binding site located at the IC end of the α7 TMD. Functional measurements showed that the α7 nAChR TMD used in the NMR experiments was inhibited by ketamine. We also observed that ketamine, but not halothane, binding to the α7 nAChR TMD could perturb the channel gate residue L248(9'), affirming our previous conclusion that only those sites that can affect channel dynamics will produce functional effects. Crystal structures of GLIC, a bacterial homologue of the α7 nAChR, co-crystallized with ketamine show ketamine binding in the ECD. Functional measurements showed that ketamine could inhibit GLIC and that the crystallographically determined binding site was functionally relevant.

4.3.2. Ketamine action site in the α7 nAChR TMD

In the previous section we noted that isoflurane bound to an intra-subunit site at the EC end of β2 but not α7. Rather isoflurane binding was noted at the IC end of the α7 TMD. These results were consistent for halothane binding, where halothane could bind at the EC end of the TMD in β2 (Figure 3.2.4), but was only found to bind to an intra-subunit cavity towards the IC end of the TMD in α7 (Figure 3.3.1). As the β2, not the α7, subunit

is sensitive to volatile anesthetics it was deduced that the anesthetic binding site at the EC, not the IC, end of the TMD was the functionally relevant binding site for general volatile anesthetics.

In the case of the intravenous anesthetic ketamine binding to the α7 nAChR, ketamine binding was observed to occupy the intra-subunit cavity at the IC end of the α7 nAChR TMD as halothane (Figure 3.3.2). However, while α7 is insensitive to halothane, it is sensitive to ketamine. Indeed, our functional experiments on the α7 TMD show that ketamine could inhibit the α7 nAChR TMD alone, even in the absence of the ECD (Figure 2.1.12). It is possible that with its larger molecular size, ketamine can accomplish what halothane and other volatile anesthetics cannot. While ketamine and halothane share the same binding cavity, the residues they affect in that cavity are different. Residues F453, S285, I217, and L248 displayed chemical shift changes upon addition of ketamine, but not halothane (Figure 3.3.1B). In contrast, residues C219, S223, and T289 showed chemical shift changes upon the addition of halothane, but not ketamine. Differences in affected residues could result in differences in functional effects. Supporting evidence for such a possibility includes that ketamine, but not halothane, changed the chemical shift of the pore-lining residue L248 (L9') (Figure 3.3.2). L9' is a key residue in the channel gate. Its chemical shift change signifies perturbation to the channel gate, which will most likely generate a functional consequence. This finding provides further support for our hypothesis in the previous section that only the anesthetic binding that can affect the channel gate will produce a functional result.

4.3.3. Ketamine action site in the α7 nAChR ECD

While the NMR data discussed above suggest that the functionally relevant site for ketamine inhibition of the α7 nAChR is located in the TMD, it is worth noting the possibility of an additional site located in the ECD. Such a site has been suggested by our X-ray crystallographic studies on GLIC, a bacterial homologue of the α7 nAChR.

The ECD of GLIC shows a similar architecture to the EC domains of nAChRs determined by cryo-EM [1] and X-ray crystallography [32]. Furthermore, ketamine can inhibit the function of GLIC at concentrations similar to those observed for the α7 and α4β2 nAChRs [45-47]. Co-crystallization of GLIC with ketamine, shows ketamine binding to an amphiphilic inter-subunit cavity located in the ECD (Figure 4.3.1). In this cavity, ketamine forms favorable electrostatic interactions with hydrophilic residues, in addition to VDW interactions with some hydrophobic residues. On one side of the cavity, the chloro group of ketamine points to the positively charged amine of K183 of β10 and the phenyl ring faces F174 and L176 of loop C. On another side of the cavity, the aminium of ketamine makes electrostatic interactions with side chains of N152, D153, and D154 of the β8-β9 loop (loop F). The carbonyl group of ketamine can potentially form a hydrogen bond with the hydroxyl group of Y23 on β1. K183 of the principal side carries a positive charge on its side chain whereas the side chains of D153 and D154 of the complementary side are likely negatively charged. Thus, electrostatic interactions contribute significantly to stabilizing ketamine binding (Figure 4.3.1).

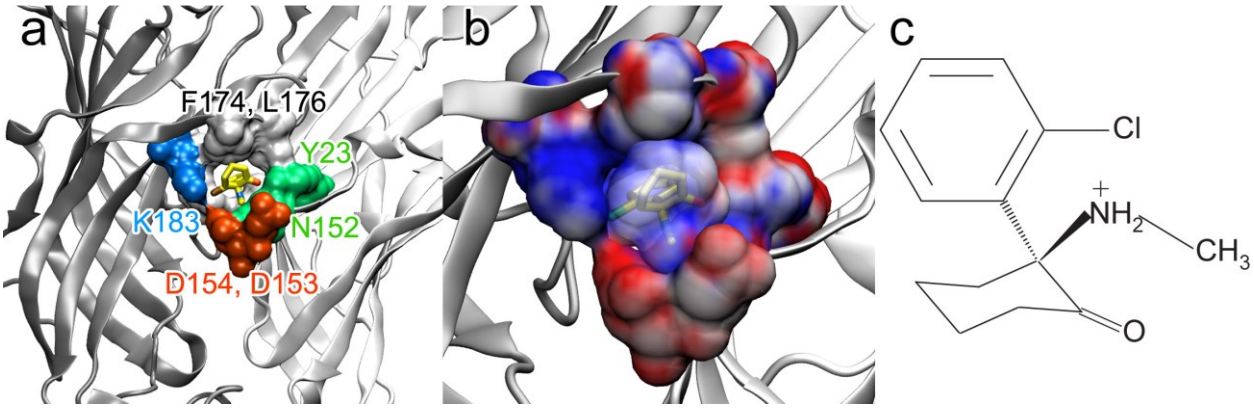

Figure 4.3.1. Amphiphilic ketamine-binding cavity in the GLIC ECD. a) The labeled polar and hydrophobic residues are within 3.0 Å of ketamine and those unlabeled hydrophobic residues (colored in white) are within 4 Å of ketamine. **b**) Electrostatic potentials mapped to the molecular surfaces for ketamine (transparent) and residues within 3.0 Å of ketamine (solid). Potentials were calculated using the APBS plugin in VMD. The scale of the potential is from +15 kT/e (blue) to -15 kT/e (red). **c**) Structure of protonated ketamine.

From the modeled structures of the α7 and α4β2 nAChRs [44,138], it is notable that both proteins have a pocket similar to the ketamine pocket in GLIC, where several acidic residues are on one side of the pocket (Figure 4.3.2). Similar to the electrostatic stabilization observed in the GLIC-ketamine crystal structure, these negatively charged residues could attract ketamine and stabilize the ketamine binding in the nAChRs. A greater number of negatively charged residues in the pocket of α7 than α4β2 nAChRs seem to be consistent with the observation that the α7 nAChR is more sensitive to ketamine inhibition than the α4β2 nAChR [45].

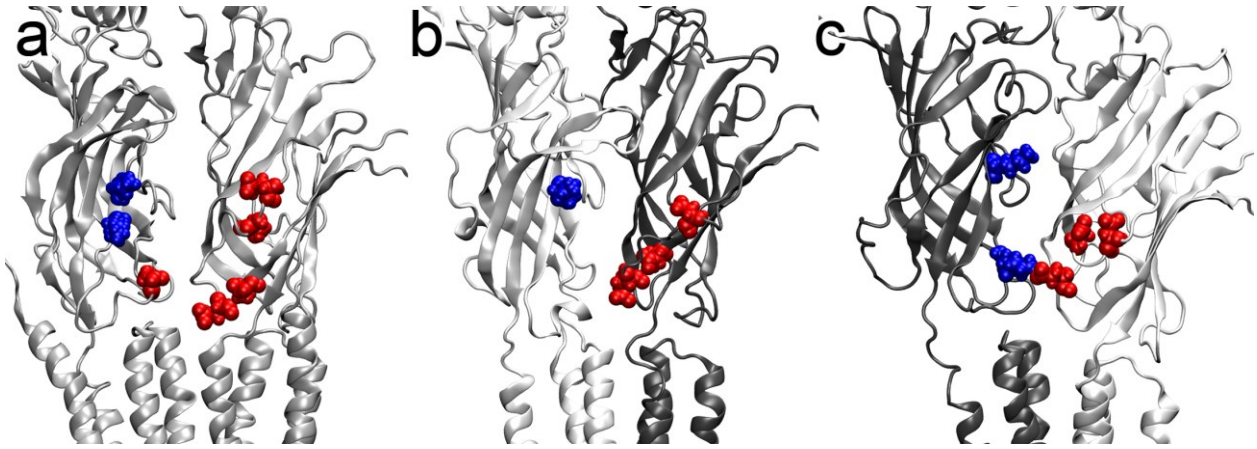

Figure 4.3.2. Interfacial cavities in nAChRs homologous to the ketamine-binding cavity in GLIC. (**a**) α7; (**b**) α4 (white)-β2 (gray); (**c**) β2 (gray)-α4 (white). Basic and acidic residues are colored in blue and red, respectively. A greater number of acidic residues in the pocket of the α7 nAChR may benefit the binding of the positively charged ketamine. Functional measurements indeed showed that inhibition of ketamine was more effective on α7 than on α4β2 nAChRs [45].

The ketamine-binding site observed in GLIC partially overlaps with the extended interaction surface of antagonists in Cys-loop receptors [31,217], suggesting that ketamine inhibition may occur via a similar mechanism as competitive antagonists inhibit functions of nAChRs. Additionally, the functional relevance of the identified ketamine site in GLIC was validated in electrophysiology measurements by mutating N152 in the binding pocket to cysteine and subsequently labeling the site with 8-(chloromercuri)-2-dibenzofuransulfonic acid (CBFS) to mimic anesthetic binding [47]. While these results validate the functional relevance of this site for GLIC are they valid for the nAChRs. In functional measurements on the α7 nAChR, labeling of α7-S188C (the residue homologuous to N152C in GLIC) using an analogue of the α7-specific antagonist methyllycaconitine (MLA) demonstrated that this site could be responsible for α7 inhibition by MLA [218]. Both GLIC and α7 show similar inter-subunit binding cavities, containing a

number of acidic residues that could stabilize binding of positively charged ketamine. Furthermore, functional measurements demonstrated that covalent labeling at homologous sites in GLIC and α7 lining this inter-subunit cavity could result in functional inhibition. Taken together, these data suggest that ketamine binding to the α7 EC domain likely contributes to functional inhibition of the α7 nAChR.

4.3.4. Conclusions

Functional measurements show that ketamine can inhibit ivermectin-elicited currents of the α7 nAChR TMD injected into *Xenopus laevis* oocytes. Our NMR results on the same α7 TMD show ketamine binding to an intra-subunit cavity at the IC end of the TMD. Since this was the only site observed for ketamine binding to the α7 TMD, it is likely the site responsible for ketamine inhibition of the α7 TMD. NMR results also demonstrated that ketamine, but not halothane, could perturb the channel gate residue L9', consistent with the sensitivity or insensitivity of α7 to ketamine or halothane, respectively. The finding supports our hypothesis that only the binding that can affect pore-lining residues, can impact function. In addition to anesthetic sensitivity at a site in the TMD, our study on GLIC suggests that anesthetic binding to the ECD may also contribute to ketamine inhibition. It is likely that Ketamine binding to the TMD as well as the ECD can both contribute to functional inhibition of the α7 nAChR [45,46,104].

CHAPTER 5

MECHANISMS OF ALLOSTERIC MODULATION

5.1. SIGNALLING PATHWAYS OF AGONIST-INDUCED ACTIVATION

This section has been published as a full article in *PLoS One*. **8** (5): e64326.

5.1.1. Background and Significance

Vertebrate pLGICs regulate ionic conductance in nerve cells and play an important role in fast synaptic signal transduction [25,219]. They are formed by five homologous or identical subunits assembled around the central channel axis. Agonist binding to the orthosteric site in the ECD allosterically triggers conformational changes to allow ions to pass through the cell membrane. How the agonist-binding signal in the ECD is propagated to a remote channel region in the TMD has been studied extensively on nAChRs in the past [52,188,220,221]. It remains an open subject for investigation as to whether there are common activation or deactivation signal pathways shared by all pLGICs.

GLIC is a cationic homo-pLGIC [222]. Crystal structures of GLIC [27,28] show a common scaffold with vertebrate pLGICs, such as nAChRs [1], except without an IC domain. Opening of the GLIC channel is triggered by extracellular protons [222], but it is unclear which titratable residues are responsible for GLIC activation. Similar to nAChRs [223], GLIC is reversibly inhibited by general anesthetics in a concentration dependent manner [47,106,224]. Recent X-ray crystallographic studies revealed anesthetic binding sites not only

in the upper part of the TMD within each subunit [106], but also at the interface of two adjacent subunits in the ECD [47]. The high resolution structures and well defined anesthetic binding sites provide the opportunity to critically examine how perturbations on titratable residues of GLIC modulate the functional status of the channel and how anesthetic binding allosterically inhibits GLIC currents without blocking the channel.

Introducing a Markovian process into coarse-grained models has offered opportunities to assess signal propagation in proteins [48,49,225-229]. The PMT model [48] is particularly effective for probing how different parts of a macromolecular machine respond to signal perturbation that is either due to ligand binding or site-specific mutations. It characterizes the dynamic response of all residues in the protein over the time course from the initial perturbation to equilibrium. It can identify key signal-mediating residues that can be readily validated experimentally [52,188,220,221].

In this section, we investigated signal transmission in GLIC from the EC domain to the TMD of GLIC upon two different stimuli. The first one is at the C loop region, where residues E177, D178, and R179 potentially form salt bridges with residues K148 and D91 at the complementary site of an adjacent subunit. We performed mutations (D91N, E177Q, and D178N, termed the NQN mutation) to remove the potential of salt bridges. Perturbation to GLIC due to the NQN mutation was evidenced in our crystal structure and functional measurements as presented below. The second perturbation site at the ECD is below the C loop, where the anesthetic ketamine was found to bind to an existing inter-subunit pocket and inhibit GLIC current in a concentration dependent manner [47]. While the functional relevance of these perturbation sites is proven, it needs to be further clarified how the perturbation signal propagates from the ECD to the channel gate. Here

we used the PMT model to identify crucial signaling paths within a subunit and between adjacent subunits of GLIC. The resulting information will facilitate our understanding of the mechanisms of allosteric action in pLGICs.

5.1.2. Methods

PMT calculations

PMT calculations were performed on the pentameric GLIC using the online server (http://gila-fw.bioengr.uic.edu/lab/tools/pmtmodel/). Details of the PMT model were provided in the previous publication [48]. Briefly, the Markovian transition model [49] was used to investigate how a given perturbation is transmitted through a protein network over time. At each time step, the perturbation is transmitted from residue i to residue j with a probability m_{ij}, an element in the Markovian transition matrix $\mathbf{M} = \{m_{ij}\}_{N\times N}$, where N is the total number of residues in the protein and $\sum_i m_{ij} = 1$. Each residue is represented as a single node in the model. The m_{ij} values are computed from the atomistic (no hydrogens) structure according to $m_{ij} = n_{ij}/\sum_i m_{ij}$, where n_{ij} is the number of atom-atom contacts between residues i and j. Two atoms from different residues are considered in contact if the Euclidean distance between the two atoms is ≤ 4.5 Å, the cutoff that consistently displayed the fastest signal propagation for all tested perturbation sites [48,49]. The initial perturbation, $\boldsymbol{p}(0)$, is defined by a set of probabilities $\{p_i(0)\}_N$, where $p_i(0)$ is the probability mass located at node i at time $t = 0$. The signal distribution at time t is defined by a vector $\boldsymbol{p}(t) = [p_1(t), \ldots, p_N(t)]$. The probability flow, which depends on both $\mathbf{M}$ and $\boldsymbol{p}(0)$, provides clues to the signal transduction within the protein under a particular stimulus. The final

distribution at equilibrium, $\boldsymbol{p}(\infty)$, depends only on **M,** not on $\boldsymbol{p}(0)$. The master equation describing time-dependent transmission of perturbation is

$$\frac{d\boldsymbol{p}(t)}{dt} = \mathbf{R}\boldsymbol{p}(t) \qquad (5.1)$$

where **R** = **M** – **I**, and **I** is the identity matrix. The Krylov subspace method [230] was used for computing each $\boldsymbol{p}(t)$.

The top elementary (or fundamental) signal paths of the highest probability were further elucidated using Yen's algorithm [50] implemented in MATLAB® (http://www.mathworks.com/matlabcentral/fileexchange/32513-k-shortest-path-yens-algorithm). Briefly, for Yen's algorithm, we transformed the Markov transition matrix, **M,** in the PMT model to a "cost" matrix by computing the element-wise inverse of **M**. Yen's algorithm computes the summed cost for transitions between node *i* and node *j*. The cost of each transition corresponds to element *i,j* in the cost matrix. The sequence of nodes that minimizes the cost between the specified starting and ending nodes was determined. The lower the cost is, the higher the probability of the signal path will be.

All the data were processed using MATLAB7.10 (The MathWorkds Inc.). VMD was used to render protein images [86].

The initial perturbation sites were chosen based on our crystal structures and functional measurements of GLIC reported previously (PDB ID: 4F8H) [47] and reported below.

Free energy calculations for the subunit interface

To compare the stability of the subunit interface before and after the NQN mutation in GLIC, we calculated free energy changes for the subunit interface in the crystal structures

of the wild type GLIC and the NQN mutant GLIC using the PISA online server (http://www.ebi.ac.uk/msd-srv/prot_int/pistart.html) [231].

Protein preparation, crystallization, and structure determination

The NQN (D91N, E177Q, and D178N) mutation to remove potential salt bridges between the C loop and the complementary side of the adjacent subunit was achieved using site-directed mutagenesis on GLIC with the QuikChange Lightning Kit (Stratagene, Santa Clara, CA) and confirmed by DNA sequencing. The GLIC mutant was expressed in Rosetta(DE3)pLysS (Novagen) and purified as reported in details previously [27,28,47]. The pentameric GLIC-NQN mutant in 0.01% (w/v) *n*-tetradecyl-β-D-maltoside from a final purification using SEC was concentrated to ~10 mg/mL and used for crystallization.

The crystallization and cryo-protection conditions used for the GLIC-NQN mutant were the same as those used previously for GLIC and the GLIC-ketamine complex [47]. The X-ray diffraction data were acquired on beamline 12-2 at the Stanford Synchrotron Radiation Lightsource and processed using the XDS program [232]. The initial structure was solved by molecular replacement using the GLIC-ketamine structure (PDB ID: 4F8H) as the starting model. The NQN mutations were made manually on the model with COOT [233]. Phenix (version: 1.8.1) [234] was used for structure refinement. Six detergent and ten lipid molecules were built into well-defined extra electron densities after initial refinement runs. Oxalate molecules degraded from PEG reagents, acetate ions from the crystallization solution, and water molecules were built into the electron densities at the final stages of the refinement with COOT [233]. Non-crystallographic symmetry (NCS) restraints were applied for five subunits in each asymmetric unit. The stereochemical quality of the model was checked with PROCHECK [140] and MolProbity [235]. Crystal

structure analysis was performed using Phenix and CCP4 [236]. PyMOL [237] and VMD [86] programs were used for structural analysis and figure preparation.

Functional measurements of the NQN Mutant

For functional measurements of the NQN mutant, the site-directed mutagenesis was introduced to GLIC in the pTLN vector for expression in *Xenopus laevis* oocytes and confirmed by DNA sequencing. The plasmid DNA was linearized with MluI enzyme (New England BioLabs, Ipswich, MA). Capped complementary RNA was transcribed with the mMESSAGE mMACHINE SP6 kit (Ambion, Austin, TX) and purified with the RNeasy kit (Qiagen, Valencia, CA). The defolliculated stage V-VI oocytes were injected with cRNA (10-25 ng/each) and maintained at 18°C in Modified Barth's Solution (MBS) containing 88 mM NaCl, 1 mM KCl, 2.4 mM $NaHCO_3$, 15 mM HEPES, 0.3 mM $Ca(NO_3)_2$, 0.41 mM $CaCl_2$, 0.82 mM $MgSO_4$, 10 µg/mL sodium penicillin, 10 µg/mL streptomycin sulphate, 100 µg/mL gentamycin sulphate, pH 6.7. Two-electrode voltage clamp experiments were performed on oocytes expressing the NQN mutant at room temperature 16-40 hours after the injection, using a model OC-725C amplifier (Warner Instruments) and a 20-µl recording chamber (Automate Scientific). Oocytes were perfused with ND96 buffer (96 mM NaCl, 2 mM KCl, 1.8 mM $CaCl_2$, 1 mM $MgCl_2$, 5 mM HEPES, pH7.4) and clamped to a holding potential of –40 or –60 mV. The ND96 buffer at the lower pH was prepared with the addition of 5 mM MES and HCl. Data were collected and processed using Clampex 10 (Molecular Devices). The data were fit by least squares regression to the Hill Equation using Prism software (Graphpad). The same software was also used for statistic analysis using extra sum-of-squares F-test.

5.1.3. Two functionally relevant sites at the EC domain of GLIC

Two functionally relevant sites at the ECD of GLIC (Figure 5.1.1a) were chosen for investigating how perturbation signals are transmitted from the ECD to the channel gate.

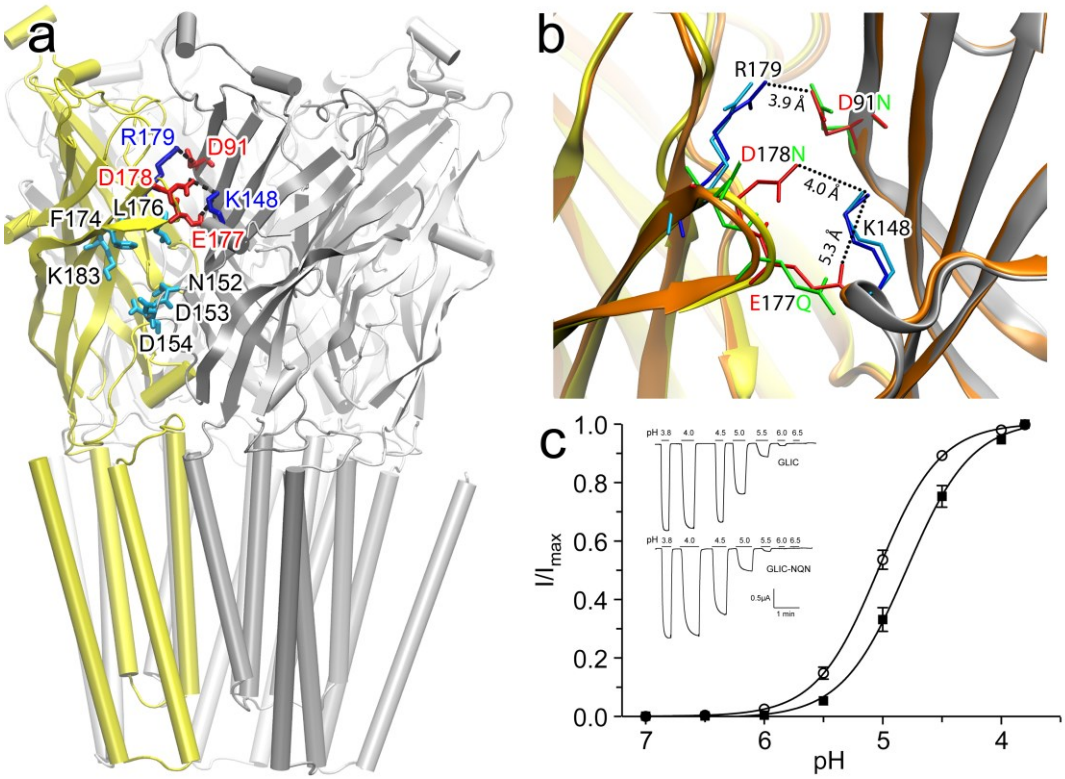

Figure 5.1.1. Functionally relevant sites in the EC domain of GLIC. (**a**) Residues for the NQN mutation (D91N; E177Q; D178N) and the complementary basic residues (R179 and K148) for salt bridge formation are highlighted in red and blue, respectively. Residues involved in the ketamine binding site (F174, L176, K183; N152, D153, D154) are highlighted in cyan. (**b**) The C loop region of the crystal structure of the NQN mutant (orange), showing an outward movement of the C loop in comparison with the wild type GLIC (yellow and gray) due to removal of salt bridges in the mutant. R179 and K148 are shown in blue and cyan sticks for GLIC and the NQN mutant respectively. D91N, E177Q, and D178N are shown in red and green sticks, before and after the mutation, respectively. The salt bridge distances in GLIC are highlighted. Note the enlarged gap after the mutation. No hydrogen bonds could be formed for the mutated residues. (**c**) Two-electrode voltage clamp measurements on *Xenopus laevis* oocytes expressing the NQN mutant (solid square) and the wild type GLIC (open circle). The half maximal effective concentrations (EC_{50}) for the mutant and GLIC are pH 4.80 ± 0.03 (n = 13) and 5.04 ± 0.02 (n = 10), respectively. The EC_{50} difference between the wild type GLIC and the NQN mutant is statistically significant ($p < 0.0001$). Error bars represent standard error from the mean. The inserts are the representative traces for GLIC and the NQN mutant.

One site is at the C loop region, where the inter-subunit salt bridges (E177-K148, D178-K148, and R179-D91) are observed in the crystal structures of the open-channel GLIC [27,47]. In order to understand the functional role of these salt bridges, we performed the NQN mutation (D91N, E177Q, D178N) to eliminate the salt bridges, crystallized the NQN mutant, and solved its structure (PDB ID: 4IRE) to a resolution of 3.19 Å (Table 5.1.1). The overall structures of the NQN mutant and GLIC are nearly the same (RMSD ~ 0.5 Å) and show an open channel conformation. However, the C loop of the NQN mutant shows an outward movement and the interfacial gap in the C loop region, measured by side chain displacement of D178N, widens 3 Å (Figure 5.1.1b). The NQN mutation removed the salt bridges but did not generate hydrogen bonds. To compare the conformational stability before and after the mutation, we calculated free energies for the inter-subunit interface in the crystal structures of the wild type GLIC and the NQN mutant. The resultant free energies of –29 kcal/mol and –26 kcal/mol for GLIC and the NQN mutant, respectively, suggest that removing the salt bridges at the subunit interface destabilized the open channel conformation. Functional measurements of the wild type GLIC and the NQN mutant provide results consistent with the free energy calculations. The mutation shifted the EC_{50} from pH 5.0 in the wild type GLIC to pH 4.8 in the NQN mutant (Figure 5.1.1c). Statistical analyses confirmed that the EC_{50} difference between the wild type GLIC and the mutant was significant with $p < 0.0001$. Apparently, more protons are required for channel activation to compensate for destabilization of the open-channel conformation due to the absence of the inter-subunit salt bridges.

Table 5.1.1. Data collection and refinement statistics

Data collection and process	
Beamline	SSRL BL12-2
Wavelength (Å)	0.9795
Space group	C2
Unit cell (Å)	182.0, 133.6, 161.4
β (°)	102.6
Resolution (Å)	29.86-3.19 (3.36-3.19)
R_{merge}(%)[a]	6.8 (70.7)
Completeness (%)[a]	97.5 (92.9)
<I/σ>[a]	14.0 (1.8)
Unique reflections[a]	61417 (9335)
Redundancy[a]	3.8 (3.7)
Refinement statistics	
Resolution (Å)	29.86-3.19
No. Reflections (test set)	61291 (999)
R_{work}/R_{free}	0.204/0.243
Non-H protein (ligand) atoms	12686 (754)
<B-factors> (Å^2)	
Protein	87.3
Detergents	107.5
Lipids	121.0
Solvent	93.5
R.M.S. Deviations	
Bond lengths (Å)	0.009
Bond angles (degrees)	1.3
Rotamer outliers (%)	5.3
Ramachandran outliers (%)	0.19
Ramachandran favored (%)	97.17
PDB ID	4IRE

[a]Values in the parentheses are for highest-resolution shell.

The other relevant location is the ketamine-binding site [47], which we identified previously in a 2.99-Å resolution X-ray structure of the GLIC-ketamine complex (PDB ID: 4F8H). Ketamine binds to an inter-subunit cavity, which is lined by residues F174, L176 and K183 on the principal side and N152, D153 and D154 on the complementary side. The ketamine binding site is partially overlapped with the homologous antagonist-binding site in pLGICs. The functional relevance of the ketamine site was determined by profound

changes in GLIC activation upon cysteine substitution of the cavity-lining residue N152. The functional relevance was also evidenced by changes in ketamine inhibition upon the subsequent chemical labeling to N152C.

These structural and functional data highlight the functional relevance of the two sites and provide the experimental basis for initial perturbation in PMT calculations as presented below.

5.1.4. Time-dependent transmission of perturbation initiated at the NQN mutation site and the ketamine-binding site

To reveal the allosteric signaling pathway in GLIC, we placed an initial perturbation of uniform strength on residues shown in Figure 5.1.1a for the NQN mutation or ketamine binding within the PMT model. The time-dependent probability flux, defined in Equation (5.1), was calculated for each selected scenario of initial perturbation site (Figure 5.1.2). The pertubation originated from the NQN mutation site was transmitted immediately to Y23, L103, R133, and K148. Among them, R133 and K148 form intra- and inter-subunit salt bridges with D178 and E177, respectively. The perturbation at the ketamine binding site was transmitted to a cluster of residues in β1 (Y23, I25, E26) and β6 (L130, I131, R133). These residues are mostly in close contact with the perturbed sites. As time proceeds, increasing numbers of residues in the ECD experience the positive probability flux (colored red in Figure 5.1.2). The positive probability flux occured in the TMD when most residues in the ECD experienced the negative probability flux (signal moved away, colored blue in Figure 5.1.2).

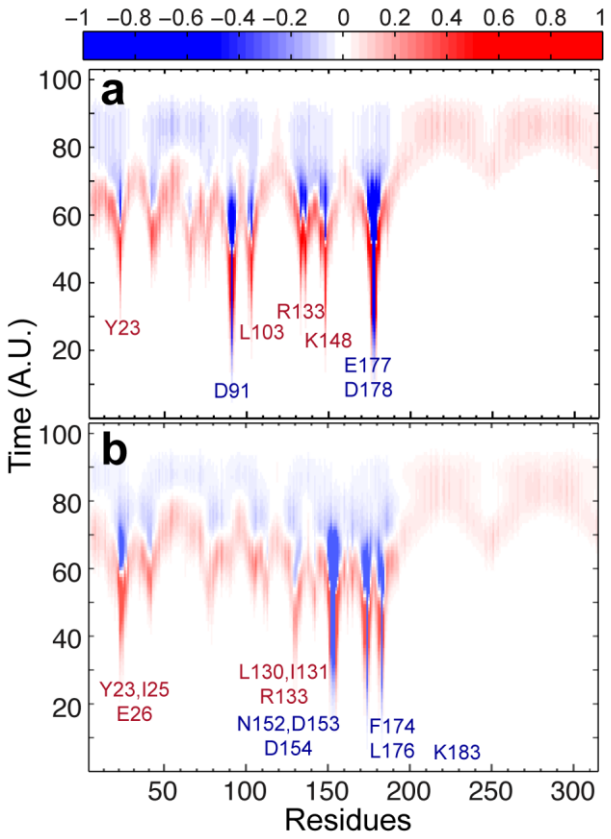

Figure 5.1.2. Trajectories of the probability flux over time for each residue upon different initial perturbations. (**a**) Initial perturbation at the NQN mutation site; (**b**) initial perturbation at the ketamine-binding site. The color denotes the normalized intensity of the probability flux. See Equation **(5.1)** in the Methods section. The positive and negative signs describe the net signal flow into and out of the residue, respectively. The time axis is in arbitrary unit. The initially perturbed and immediately affected residues are labeled in blue and red, respectively.

The two initial perturbation sites share similar overall patterns of the probability flux in the TMD. The signals reached pre-TM1, the TM2-TM3 linker, and the C-terminus of TM4 before they propagated to other parts of the TMD. The residues immediately affected by the perturbation in the ECD were clearly identified, but specific signaling paths became obscured as the signal diffused through the protein. To trace the paths between the

initially perturbed residues and the channel gate residue I233 (also named 9', a commonly presumed hydrophobic gate residue), we used Yen's algorithm [50] that outputs the most likely paths based on the probabilities stored in the Markovian transmission matrix. The pore-lining residues other than 9' were also tested as target residues and produced the same paths as observed for the target 9'. There were a total of three and six initially perturbed residues for the NQN mutation site and ketamine-binding site, respectively. For each of the perturbed residues involved in the NQN mutation site (D91, E177, D178) and ketamine binding site (N152, D153, D154, F174, L176, K183), 10 signal paths with the highest probability were determined using Yen's algorithm [50]. The signal starts at the perturbed residue and ends at the channel gate residue I233. For completeness, three scenarios following each perturbation were considered, assume all signals start in subunit B: (1) signal starts and ends within subunit B; (2) signal starts in subunit B and ends in subunit A; (3) Signal starts in subunit B and ends in subunit C. In total, 270 paths were obtained (9 initial perturbations, 10 paths of highest probability for each perturbation, 3 different scenarios for the ending point). Many of the observed signal pathways are degenerate. However, the emerged pathways of the highest probability for signal transduction from the ECD to the channel pore in our analysis (Table 5.1.2) reveal the involvement of two critical regions. The first one is the β1-β2 loop (also named loop 2) that couples with the C-terminus of TM2 (Figure 5.1.3a and d). The second one is pre-TM1 that often mediates signaling between subunits (Figure 5.1.3b, e, and f).

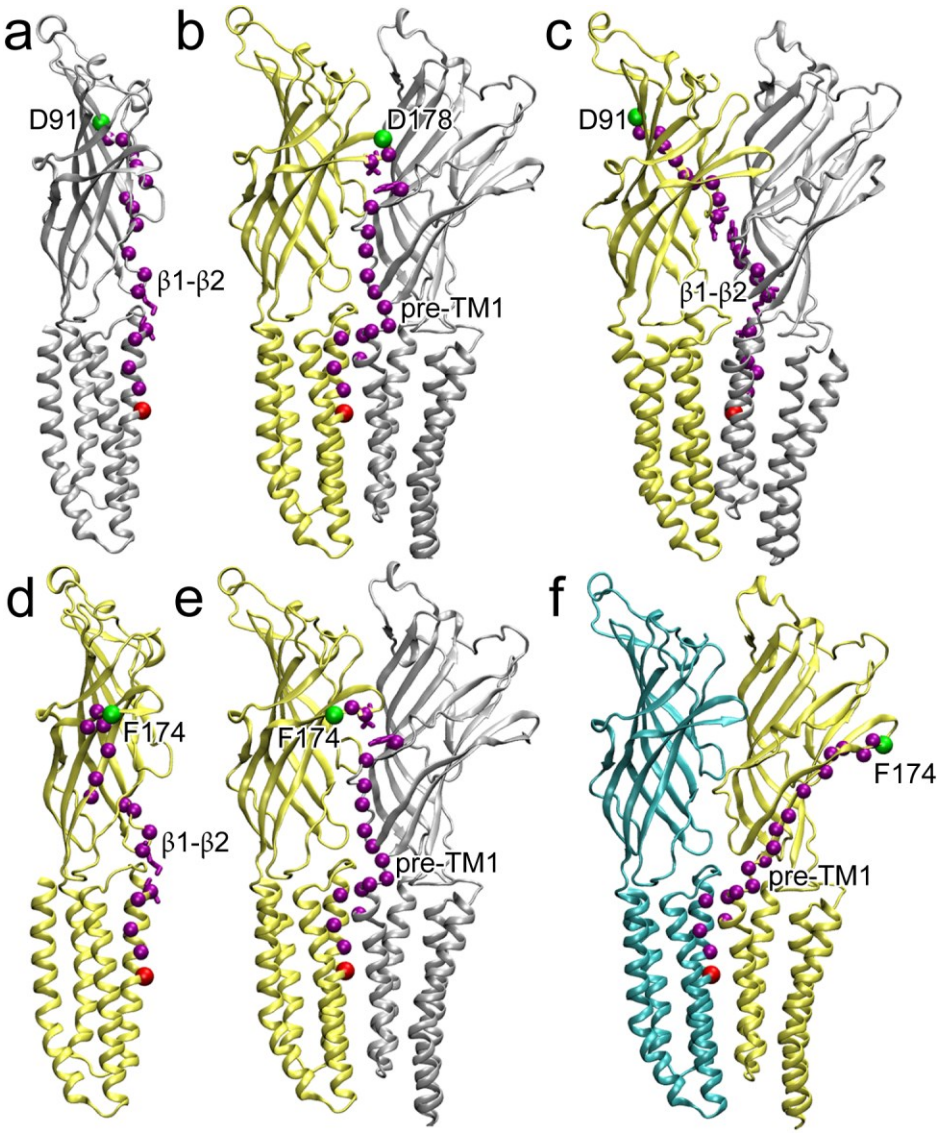

Figure 5.1.3. Paths with the highest probability to reach the channel gate (I233; 9') under different initial perturbations in GLIC. (**a**) The path within a subunit upon perturbation to D91 of the NQN mutation; (**b**) the path between D178 of the NQN mutation site and I233 (9') of the same subunit showing an inter-subunit pathway; (**c**) the path between D91 of subunit B and I233 (9') of subunit A; the perturbation to F174 of the ketamine binding site shows both (**d**) intra- and (**e**) inter-subunit paths for signal starting and ending in subunit B; (**f**) the path between F174 of subunit B and I233 (9') of subunit C. The perturbation starting and ending points are shown in green and red spheres, respectively. The pathways are highlighted in purple spheres. Subunits A, B, and C are colored silver, yellow, and cyan, respectively. All calculations were performed using Yen's algorithm [50].

Table 5.1.2. Highest probability paths for each residue in the NQN mutation site (D91, E177, D178) and ketamine binding site (N152, D153, D154, F174, L176, K183)

	β1-β2 Loop	Pre-TM1
Subunit B to subunit B		
D91	V90, V89, D88, A87, D86, S107, A108, R109, **T36, A34, K33**, T244, E243, N239, I236, I233	N/A
D178	E177, L176, Y23, N152, V155, F156, P113, L114, **E35, A34, K33**, T244, E243, N239, I236, I233	E177, L176, Y23, N152, V155, F156, T158, G159, **Q193, Y194, F195, S196, N**200, E243, N239, I236, I233
E177	L176, Y23, N152, V155, F156, P113, L114, **E35, A34, K33**, T244, E243, N239, I236, I233	L176, Y23, N152, V155, F156, T158, G159, **Q193, Y194, F195, S196, N**200, E243, N239, I236, I233
N152	V155, F156, L157, **L30, D31, K33**, T244, E243, N239, I236, I233	N/A
D153	D154, F156, L157, **L30, D31, K33**, T244, E243, N239, I236, I233	N/A
D154	F156, L157, **L30, D31, K33**, T244, E243, N239, I236, I233	N/A
F174	N173, A172, K183, Y129, H127, L126, **F37, T36, A34, K33**, T244, E243, N239, I236, I233	A175, L176, Y23, N152, V155, F156, T158, G159, **Q193, Y194, F195, S196, N**200, E243, N239, I236, I233
L176	Y23, N152, V155, F156, P113, L114, **E35, A34, K33**, T244, E243, N239, I236, I233	Y23, N152, V155, F156, T158, G159, **Q193, Y194, F195, S196, N**200, E243, N239, I236, I233
K183	Y129, H127, L126, **F37, T36, A34, K33**, T244, E243, N239, I236, I233	N/A
Subunit B to subunit A		
D91	V90, V89, D88, A87, D86, R85, A84, N83, E82, Y28, S29, **L30**, **D31, K33**, T244, E243, N239, I236, I233	N/A
D178	E177, L176, Y23, L24, I25, E26, C27, Y28, S29, **L30**, **D31, K33**, T244, E243, N239, I236, I233	N/A
E177	L176, Y23, L24, I25, E26, C27, Y28, S29, **L30**, **D31, K33**, T244, E243, N239, I236, I233	N/A
N152	V155, F156, L157, L**30, D31, K33**, P247, K248, N245, T244, E243, N239, I236, I233	N/A
D153	D154, F156, L157, L**30, D31, K33**, P247, K248, N245, T244, E243, N239, I236, I233	N/A
D154	F156, L157, L**30, D31, K33**, P247, K248, N245, T244, E243, N239, I236, I233	N/A
F174	A175, L176, Y23, L24, I25, E26, C27, Y28, S29, **L30**, **D31, K33**, T244, E243, N239, I236, I233	N/A

L176	Y23, L24, I25, E26, C27, Y28, S29,, **L30**, **D31, K33**, T244, E243, N239, I236, I233	N/A
K183	Y129, N80, V81, E82, Y28, S29, **L30**, **D31, K33**, T244, E243, N239, I236, I233	N/A
Subunit B to subunit C		
D91	V90, V89, D88, R105, V79, N80, V110, F37, **T36, E35, A34, K33,** T244, E243, N239, I236, I233	N/A
D178	E177, L176, Y23, N152, V155, F156, P113, L114, **E35, A34, K33**, T244, E243, N239, F238, I236, I233	R179, R133, V132, I131, L130 Y129, H127, T125, Q124, S123, D122, F121, **Y194, F195, S196,** N200, E243, N239, I236, I233
E177	L176, Y23, N152, V155, F156, P113, L114, **E35, A34, K33**, T244, E243, N239, F238, I236, I233	L176, Y23, N152, V155, F156, T158, G159, Q**193, Y194, F195, S196**, **N**200, E243, N239, F238, I236, I233
N152	V155, F156, T158, P113, L114, **E35, A34, K33,** T244, E243, N239, I236, I233	V155, F156, T158, G159, **Q193, Y194, F195, S196**, N200, E243, N239, I236, I233
D153	D154, F156, T158, P113, L114, **E35, A34, K33,** T244, E243, N239, I236, I233	D154, F156, T158, G159, **Q193, Y194, F195, S196**, N200, E243, N239, I236, I233
D154	F156, T158, P113, L114, **E35, A34, K33,** T244, E243, N239, I236, I233	F156, T158, G159, **Q193, Y194, F195, S196**, N200, E243, N239, I236, I233
F174	N/A	N173, A172, P171, K170, V168, A167, T166, F165, S164, E163, I162, D161, **Q193, Y194, F195, S196**, N200, E243, N239, I236, I233
L176	Y23, N152, V155, F156, P113, L114, **E35, A34, K33**, T244, E243, N239, F238, I236, I233	Y23, N152, V155, F156, T158, G159, Q**193, Y194, F195, S196**, **N**200, E243, N239, F238, I236, I233
K183	N/A	Y129, H127, T125, Q124, S123, D122, F121, **Y194, F195, S196**, N200, E243, N239, I236, I233

*Residues colored black, red, and green belong to subunits B, A, and C, respectively.
*Residues in the β1-β2 loop or pre-TM1 are highlighted in bold

5.1.5. The paths via the β1-β2 loop

Paths involving the β1-β2 loop can be either within a subunit or between adjacent subunits. For the intra-subunit signaling path, the perturbation signals resulting from the NQN mutation and ketamine binding initially travel via different routes, but eventually emerge at the β1-β2 loop, and further propagate along the same path to the channel gate. For example, as shown in Figure 5.1.3a and d, the initial perturbations at D91 and F174 have two respective paths at the beginning: (i) D91, V90, V89, D88, A87, D86, S107, A108, R109→ T36 of the β1-β2 loop; and (ii) F174, N173, A172, K183, Y129, H127,

L126→ F37 of the β1-β2 loop. Once the signal reached the β1-β2 loop, the rest of the path follows: F37, T36, A34, K33, T244, E243, N239, I236, I233(9').

Assuming perturbations start in subunit B, inter-subunit paths involving the β1-β2 loop are observed for signals ending in either subunit A or subunit C. We note variations in the signal path when the initially perturbed residue or the ending subunit are varied (Table 5.1.2), but the involvement of the β1-β2 loop was observed in 66% of 270 paths identified by Yen's algorithm.

The important role of the β1-β2 loop in the channel function has been well documented by experimental studies. Mutagenesis in the mouse α1 subunit of nAChR and subsequent single channel electrophysiology measurements in the nAChR by Auerbach's group showed that residues in the β1-β2 loop, homologous to GLIC D32 (α1-E45) and K33 (α1-V46), are critical for channel gating [189,238]. Sine's group also found the critical role of α1-E45 and α1-V46 in the channel gating of the human nAChR [221]. Furthermore, residues at the C-terminus of TM2 of the mouse nAChR, homologous to GLIC E243 (α1-V261) and T244 (α1-E262), were found in the same gating block (Φ ~ 0.8) as the residues in the β1-β2 loop [51]. They are significantly coupled to channel gating [51]. More comparisons between our model predictions and experimental data on nAChR are provided in a specific section below.

5.1.6. The paths via pre-TM1

The paths involving pre-TM1 were not observed as frequently as those involving the β1-β2 loop, but the significant occurrences of these paths (34% of the paths identified) make them worth noting. Unlike the β1-β2 loop that occurs in the signaling pathways both within

a subunit and between adjacent subunits, pre-TM1 occurs exclusively in pathways across adjacent subunits. Assuming all perturbations start in subunit B, there are at least two types of paths involving pre-TM1. First, the initial perturbation signal (such as L176) traveled across subunit B, passed the pre-TM1 in the adjacent subunit A (Y23, N152, V155, F156, T158, G159, **Q193, Y194, F195, S196,** N200), and then propagated to the channel gate in subunit B (E243, N239, I236, **I233**), such as shown in Figure 5.1.3b and e. Second, the initial perturbation signal traveled through pre-TM1 of subunit B (F174, N173, A172, P171, K170, V168, A167, T166, F165, S164, E163, I162, D161, **Q193, Y194, F195, S196**, N200) before reaching TM2 and the channel gate of subunit C (E243, N239, I236, I233), such as shown in Figure 5.1.3f. Additional high probability paths involving pre-TM1 between a perturbed residue and the channel gate are provided in Table 5.1.2.

The involvement of pre-TM1 in signaling paths between the ECD and the channel gate is not unexpected. Pre-TM1 covalently links the EC and TM domains. The functional contribution of pre-TM1 has been recognized in the past. However, the contribution was often attributed to the coupling with other loops at the EC/TM interface[185,221,239-241]. Mutagenesis, single-channel kinetic analyses, and thermodynamic mutant cycle analyses on the nAChR revealed energetic coupling among residues from pre-TM1, the Cys-loop, and the TM2–TM3 linker [185]. Specific interactions between pre-TM1 and the β1-β2 loop are shown in crystal structures of the mouse *α*1 nAChR ECD [32] and GLIC [27,28]. The functional coupling of pre-TM1 with the loop β1-β2 has been demonstrated in several experimental studies[185,239,241]. It was proposed that the coupling of pre-TM1 to the TM2–TM3 linker constitutes a principal transduction pathway [221,240]. Our analysis here reveals

a novel coupling mode of pre-TM1, in which pre-TM1, in conjunction with the C-terminal end of TM1, can directly transduce signals to TM2 and the channel gate of the adjacent subunit. This newly identified coupling is more direct and probably more effective for pre-TM1 to convey signals from the ECD to the channel gate. In addition, since the coupling is between adjacent subunits, it facilitates communications and cooperative action among subunits.

It is worth noting that among all four TM helices, the TM2 conformation is the most sensitively correlated to the channel state as indicated in the crystal structures [27,211] and in MD simulations [62]. The TM1 conformation is the second most sensitive to the channel state [27,211,242]. The direct coupling of pre-TM1 N200 with TM2 E243 of the neighboring subunit may alter the TM2 tilting angles and induce a conformational change.

5.1.7. Why only the β1-β2 loop and pre-TM1

Four regions from the EC domain (β1-β2, β8-β9, β10, and the Cys-loop) and two regions from the TM domain (pre-TM1 and the TM2-TM3 linker) comprise the coupling interface between the EC and TM domains of GLIC and other pLGICs. Previous studies on Cys-loop receptors have shown that these regions, either individually or in combination, mediate the transduction of agonist binding to channel gating [52,185,188,221,239,240,243,244].

In the context of the PMT model, paths to TM2 through either the β1-β2 loop or pre-TM1 have higher probabilities than paths through other loops, such as the Cys-loop and the TM2-TM3 linker. While these loops were not detected in the highest probability paths, this does not imply that such loops are not important. The PMT model has a limitation in that it only considers the number of atom-atom contacts for the probability of

passing a signal from one residue to another. Consequently, Van der Waals interactions are weighted more heavily than Coulombic interactions. For Cys-loop receptors, the importance of salt bridges at the interface of the EC and TM domains has been well-documented [44,221,243]. Thus, our results should not be interpreted to rule out the functional contribution of the Cys-loop and the TM2-TM3 linker. Rather, these results explicitly demonstrate the importance of the β1-β2 loop and pre-TM1 in the signaling pathways.

5.1.8. The signaling pathway within the muscle-type nAChR

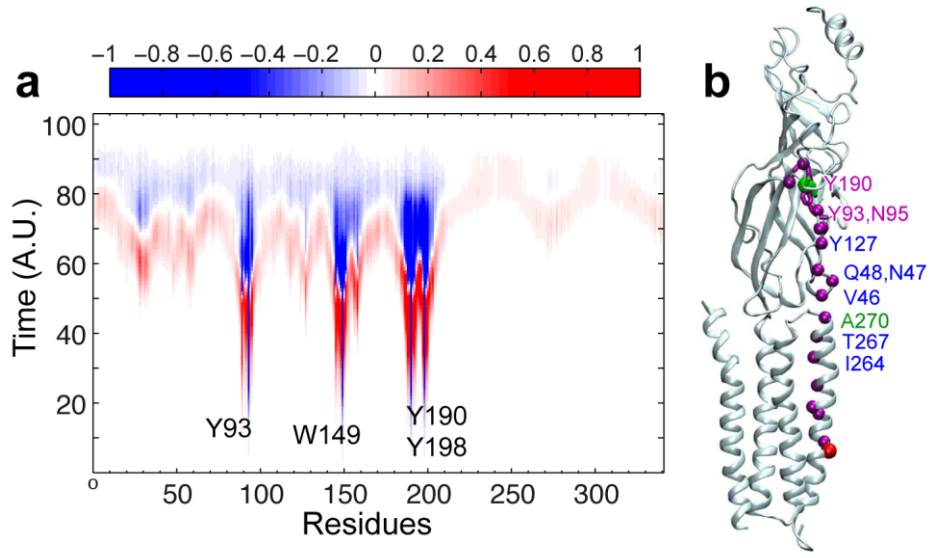

Figure 5.1.4. Trajectory of the probability flux and the highest probability path in nAChR (PDB ID: 2BG9). (**a**) Trajectory of the probability flux over time for each residue of the α1 nAChR upon perturbation to the agonist-binding site (Y93, W149, Y190, and Y198). The color denotes the normalized intensity of the flux. Positive and negative signs describe the net signal flow into and out of the residue, respectively. (**b**) The signaling path with highest probability between Y190 of the C loop and the pore-lining residue L251 (9') in the α1 nAChR. Perturbation starting and ending points are shown in green and red spheres, respectively. Residues comprising the path are shown in purple spheres. The labeled residues were identified previously in the mutagenesis and functional studies for transferring energy from the extracellular domain to the channel gating [51,184,189,238,245,246].

The results from the PMT model depend heavily on the protein structure. Therefore, what we observed on GLIC is expected to be applicable to the homologous Cys-loop receptors. To confirm this is the case, we performed the same calculations on the muscle-type nAChR (PDB ID: 2BG9). The advantage of using the muscle-type nAChR is not only the availability of the structure, but also the availability of extensive

experimental data [51,184,185,189,221,239,245,246]. The initial perturbation was placed at the agonist binding site, namely residues α1-Y93, α1-W149, α1-Y190, and α1-Y198 (Figure 5.1.4). The results from Yen's algorithm show that these residues in the binding site are well coupled, as they pass signal to each other along the highest probability paths. Thus we examined the representative pathway between Y190 and L251 (L9').

Despite the inclusion of adjacent subunits in the calculations, the initial perturbation signal traveled only through an intra-subunit path via the β1-β2 loop to reach the channel gate. More interestingly, when the path was constrained between Y190 and the channel gate of either adjacent subunit, the signal still traveled to TM2 within the same subunit before ending at the channel gate residue of the adjacent subunit. This is presumably due to tighter TM2 helical packing in the closed-channel nAChR structure versus the open-channel GLIC structure. The intra-subunit path for the nAChR is similar to the intra-subunit path observed for GLIC (Figure 5.1.3a and d). Furthermore, residues along the pathway were previously suggested for signal propagation in experimental studies (Figure 5.1.4b) [51,184,189,238,245,246]. The observed pathway is well supported by experimental data.

5.1.9. Conclusions

Using the PMT model in combination with Yen's algorithm, we revealed multiple pathways for signal transduction from the ECD to the channel gate. While the EC/TM interfacial structural elements (such as the Cys-loop, the β1-β2 loop, pre-TM1, and the TM2-TM3 linker) are expected to play roles in the signal transduction, we only found the β1-β2 loop or pre-TM1 in the signal transduction pathways of the highest probability upon different perturbations to the ECD. Paths involving the β1-β2 loop can be either within a subunit or

between adjacent subunits, but paths involving pre-TM1 are exclusively between adjacent subunits. In the past, signaling involving pre-TM1 has been attributed to pre-TM1 coupling with other loops at the EC/TM interface. Our data suggest that pre-TM1 can directly couple with TM2 of the adjacent subunit, providing a new insight into the allosteric signaling mechanisms of pLGICs.

5.2. THE RELATIONSHIP BETWEEN DYNAMICS AND ALLOSTERIC MODULATION

This section of the Thesis is based on publications in *Structure* **21** (10): 1-8, *J Phys Chem B* **114**: 7649-7655, *Biochim Biophys Acta* **1828** (9): 398-404, and *J Biol. Chem.* (2013) and a manuscript recently accepted for publication in *Biochim Biophys Acta*.

5.2.1. Background and Significance

The precise mechanisms of allosteric modulation within Cys-loop receptors are currently unknown. Our NMR study on the glycine receptor TMD showed unique dynamics at the EC end of the TMD that could be related to channel function [38]. Other studies have also shown that dynamics at the EC end of TM2 is important to channel gating [57,58]. Our structural study of the hGlyR-α1 TMD also suggested that mutations affecting anesthetic sensitivity more likely affected the intrinsic gating dynamics than specific anesthetic binding [38]. In support of this theory, several past studies have shown that mutations affecting anesthetic modulation often concurrently affect the intrinsic gating dynamics of the channel [54-56]. Our NMR studies on the neuronal nAChRs also provide support for the

involvement of dynamics in allosteric modulation and suggest that only the ligand binding that can affect the channel dynamics will produce the functional effect.

In this section we explore the relationship between dynamics and allosteric modulation. Our study on the hGlyR-α1 TMD identified dynamics at the EC end of the TMD that could be related to channel gating. Further support for the role dynamics in allosteric modulation was observed in both our computational MD results and experimental NMR results. The results show significant changes to channel dynamics in channels affected by anesthetics. The results presented here provide compelling evidence for the importance of dynamics in allosteric modulation. Our findings present a significant achievement towards understanding the mechanism of allosteric modulation in Cys-loop receptors.

5.2.2. Channel gating and dynamics in the hGlyR-α1 TMD

Dynamic characteristics of the TM2 and TM3 helices near the TM2-TM3 linker can be observed both in the bundle of structures (Figure 2.2.5), and directly in the high-resolution NMR spectra. In the spectra, two sets of NMR peaks are identifiable for several residues near the TM2 C-terminus, including S268(16'), G269(17'), and S270(18') (Figure 2.2.7a). The data suggest that at least two conformations coexist in this region and undergo slow exchange on the μs timescale. A similar minor conformation was also observed in an extended TM2 segment of GlyR [124] and in the TM2-TM3 construct in lipid bicelles [121]. The NMR structures determined in the present study are associated with the major peaks. The structure in the minor conformation could not be determined because of insufficient NOESY connectivity. A considerable degree of conformational flexibility in the region of

the TM2 and TM3 helices near the TM2-TM3 linker is also evident in the backbone dynamics, as measured by the ^{15}N relaxation parameters (R_1 and R_2) and ^{15}N-{^1H} hetNOE of the major peaks. The segment from S267 (S15') in TM2 to K276 (K24') in the TM2-TM3 linker, and residues involved in the TM3 helical kink show smaller hetNOE and R_2 values and relatively higher R_1, suggesting high flexibility in the region [38].

The conformational dynamics near the EC end TM2 shows two conformations for R271(19'), with a smaller population in a more extended helix and a larger population in an unwound conformation. Consequently, instead of facing the pore, R19' in some structures is mostly tangent to the pore, where R271(19') experiences a more hydrophobic environment. Indeed, such conformational flexibility was noted previously by tethering a rhodamine fluorophore to R271C [126], suggesting that conformational flexibility at the EC end of the pore is related to channel function. Ester substitution is expected to weaken the backbone hydrogen bonds and increase the flexibility of the pore-lining TM2 helix. Single-point amide-to-ester mutations at 13', 16', or 19' of nAChR increased the receptor's sensitivity to agonist more than tenfold [57]. A more recent study using electron paramagnetic resonance spectroscopy also observed greater conformational changes at the EC end of TM2 upon agonist binding [58].

The high flexibility of the TM2 C-terminus of hGlyR-α1 is likely coupled with the structural flexibility near the N-terminal helix of TM3. A helical kink (I285-A288) divides the TM3 domain into two α-helical segments: one from V277 to D284 and the other from V289 to V307 (Figure 2.2.5a and Figure 2.2.6). While the TM3 helices in the crystal structure of the GluCl and ivermectin complex show no kink [29], the kink may exist in the absence of ivermectin. When we aligned the TM structures of GluCl and hGlyR-α1, it

became clear that ivermectin partially overlapped with the kink observed in the NMR structure (Figure 2.2.7b), suggesting that ivermectin binding may have stabilized a straight helical conformation and that without ivermectin the flexibility would make it much more challenging to obtain high quality GluCl crystals for X-ray structure determination.

S267 and A288 mark the two ends of a dynamic region of the channel in our hGlyR-α1 TMD structures (Figure 2.2.7c). Intriguingly, mutations S267Y and A288W in the hGlyR-α1 TMD were found to substantially reduce general anesthetic and alcohol potentiation of GlyR responses [55]. Mutations at S267 showed that ethanol modulation was correlated with the volume but not the polarity or hydropathicity of the substituting side chains, suggesting that S267 itself is not directly involved in alcohol binding [128]. These functional consequences may result from the reduced conformational flexibility in the region due to bulky substitution at the S267 position. In fact, our previous NMR study demonstrated that the S267Y mutation increased the α-helix length at the TM2 C-terminus [111]. Mutation of A288 to an amino acid with a different size can also alter conformational flexibility in the region with functional consequences. Indeed, A288F and A288G have opposite functional impacts, with the former reducing and the latter increasing glycine-induced channel activation [54]. It is unlikely that glycine binding is affected by the mutations because the orthosteric agonist-binding site in the ECD is remote from A288. The changes in conformational flexibility due to mutations alter the channel's susceptibility to allosteric activation.

5.2.3. Effects of halothane on dynamics of α7 and α4β2 in MD simulations

Molecular simulations have shown a link between anesthetic effects on protein dynamics and the ability of the drug to modulate channel function. In previous sections we showed that cross-correlation maps from GNM analyses revealed correlations between the Cys-loop and the β1-β2 linker with the TM2-TM3 linker were unaffected by halothane in α7, but were diminished by halothane in β2 (Figure 4.1.3). Given the importance of interactions between these loops for propagating agonist binding signals in the ECD to channel gating in the TMD [138,188-192], a sensitive response of β2 and an insensitive response of α7 to halothane to correlated motions at the EC/TM interface is consistent with halothane induced functional responses of α7 and α4β2 [5,6].

Differences in halothane affects to local motion were also observed between α7 and α4β2. To assess whether halothane affected the local motion of α7, we calculated C_α RMSF for the closed- and open-channel α7 in both the control and halothane systems. For comparison, the same RMSF analysis was also performed on the previous α4β2 simulation data. As expected, residues in large loops and linkers, particularly at the N- and C-termini, show greater RMSF values than residues in helices or β sheets. Because of this terminal effect, residues at the N- and C-termini were excluded in our examination of halothane's effect on the RMSF. For a clear illustration of RMSF changes between the halothane and control systems, the average ratios of the backbone RMSFs of each subunit type in the halothane system to the control system were calculated. As shown in Figure 5.2.1, the average RMSF ratios for the majority of residues have values close to one, indicating that the motion of these residues on the ps-ns time scale was almost unaffected by halothane. The elevated ratios around residues 305 to 307 were due to the

disconnection between TM3 and TM4. The significant changes in the RMSF ratios of the halothane system to the control system were observed in the A- and F-loops of the β2 subunit, but the changes did not occur to α7 and α4. Interestingly, for most residues in the F-loop, their RMSF changes between the control and halothane systems are comparable to the changes between the open and closed channels (Table 5.2.1). Thus, halothane affected the RMSF of these residues in a way as if to shift an open-channel conformation to a closed channel conformation. It is known that the F-loop is important for coupling agonist binding to channel gating [188,247]. Mutations in the homologous loops in the δ and ε subunits have been shown to cause a dramatic decrease in channel conductance [248]. The ability of halothane to change the RMSF of the F-loop in α4β2 but not in α7 might be another source differentiating halothane functional impact on α4β2 from α7.

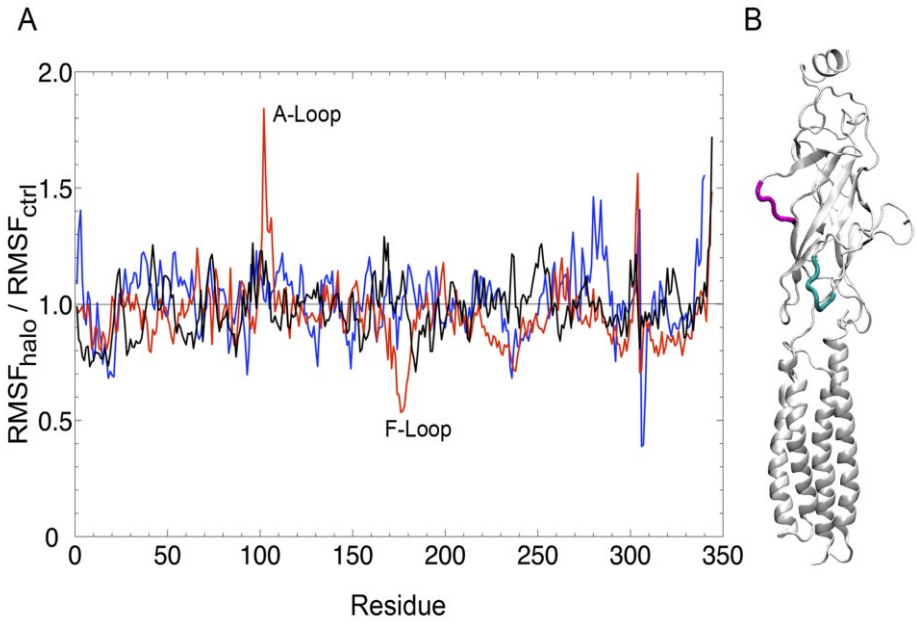

Figure 5.2.1. Changes in RMSF between halothane and control systems for the open-channel α7 and α4β2. (**A**) The ratio of the RMSFs in the presence and absence of halothane for the open-channel α7 (black) and α4β2 (α4-blue and β2-red)**.** The RMSF was calculated using the data from the last 7-ns simulation of each system and averaged for the same type of subunits. Ratios close to 1 indicate that the flexibility of residues in both control and halothane systems are nearly identical. Two significant changes in the present of halothane are observed in A-loop and F-loop of β2. The large variations around residues 305 to 307 were due to the ending residues of TM3 and TM4. (**B**) The residues around the A-loop (magenta) and F-loop (also referred to as β8-9 loop) in the β2 subunit showed a large RMSF increase and decrease in the halothane systems, respectively.

Table 5.2.1. RMSF difference values for residues in the F-loop of a β2 subunit in the open-channel conformation.

Residue	Halothane – Control	Closed – Open
175	-2.6 Å	N/A
176	-2.6 Å	N/A
177	-3.1 Å	-2.6 Å
178	-3.9 Å	-3.8 Å
179	-3.5 Å	-3.6 Å
180	-2.9 Å	-2.9 Å

*Only the RMSF differences of a magnitude greater than 2 Å are shown

5.2.4. Effects of halothane and ketamine on dynamics of the α4β2 nAChR TM domains

Motional characteristics of proteins are often reflected in peak intensities of residues in the NMR spectra [66,249]. Residues at the N- and C-termini as well as exposed loops experience fast motions (on the ps-ns timescale) and have higher signal intensities than residues in helices. Residues in the TM helices have weaker intensity due to restricted motion or broadening due to conformational-exchange on the μs-ms timescale [250].

Upon addition of anesthetics, changes in motion or conformational exchange for residues in α4β2 were evident in the NMR spectra. The most remarkable change is splitting of single peaks into double peaks (for example, V236 and L222 of α4; Figure 5.2.2A). The visibly separated double peaks could result from either a decrease in the rate of conformational exchange or a shift in the conformational distribution [251]. In the first scenario, a single NMR signal was detected when the exchange rate between the two conformations was faster than the NMR detection time scale. The single peaks became double peaks when anesthetics slowed down the exchange rate. The observed double peaks of V253 and L222 belong to this scenario. For shifting conformation equilibria by anesthetics, V236 of α4 gave a good example. In the second scenario, V236 had two populations (75% vs. 25%) with distinct resonance frequencies in the absence of halothane. The major peak shifted and its peak intensity dropped in an anesthetic concentration dependent manner. Conversely, the minor peak had less change in chemical shift but its intensity increased so that the two conformations became almost equal populated in the presence of 2 mM halothane. Thus, anesthetics have either decreased conformational exchange rates or shifted conformation equilibria.

In addition to the change in peak splitting, we observed increased and decreased signal intensities for some residues. When we highlight these residues in the structures of α4 and β2 (Figure 5.2.2), several features become clear. Most residues in the vicinity of anesthetic binding sites experienced dynamic changes. However, dynamic changes induced by anesthetics could extend beyond the binding sites, such as the case of dynamical changes at the upper helical region of α4 when ketamine bound to the inter-subunit site close to the IC end of the TMD. It is also noticeable that loop residues of fast motion and high NMR signal intensities are not affected by anesthetics, but residues at junctions of helices and loops (V262 and S271 of β2 and I267, I268, S277 of α4) are susceptible for dynamical modulation by anesthetics. This observation is consistent with a previous NMR study on another membrane protein [167].

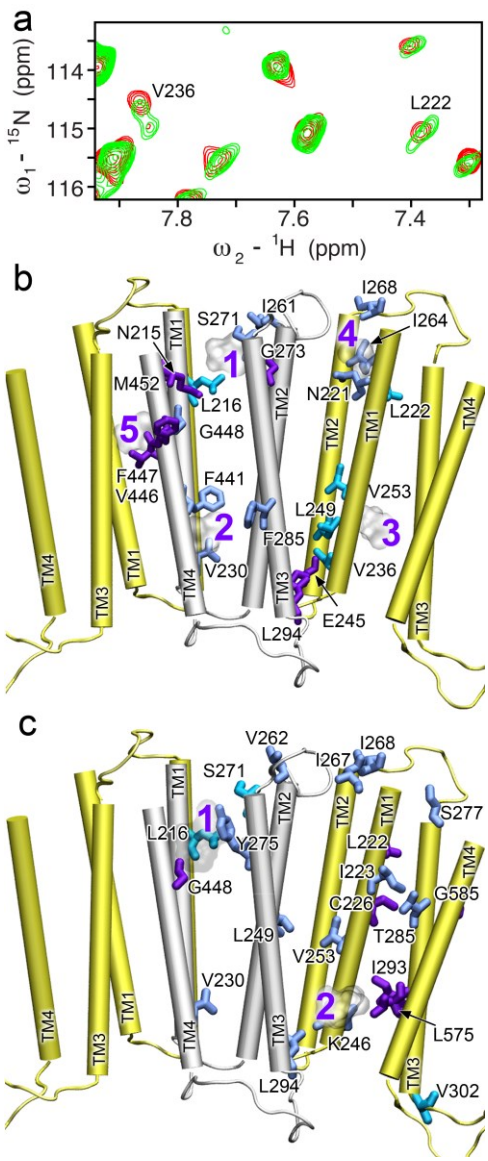

Figure 5.2.2. Anesthetics changed dynamics of residues in the α4β2 TM domains. (**a**) A representative expanded region of the ^{1}H-^{15}N TROSY-HSQC spectra for α4(β2) in the absence (black) and presence (red) of 2 mM halothane. Note the peak splitting for L222 and V236, indicative of slow exchange. (**b**) Residues experienced dynamics changes upon halothane binding are highlighted on the α4 (yellow) and β2 (silver) structures. (**c**) Residues experienced dynamics changes upon ketamine binding are highlighted on the α4 (yellow) and β2 (silver) structures. Three scenarios of dynamics changes are included in both (b) and (c): residues exhibiting peak splitting (cyan), decreases in peak intensity (blue), and increases in peak intensity (purple). Halothane and ketamine are shown in ghost representation to assist viewing each binding site.

Conformational changes in the TM domains of the α4β2 nAChR constitute different functional states of the ion channel. Our NMR data show that anesthetic sites at the EC end of the TM domains are virtually located behind the channel gate, while the sites at the IC end of the TM domains are adjacent to the ion selectivity filter. Both locations are crucial to channel function [106,252,253]. Conformational changes in these regions can affect transitions between different states of ion conductivity through channels.

Anesthetic modulation on channel motion was evidenced by changes of NMR signal intensities upon adding anesthetics, as well as peak splitting of the α4 and β2 residues at the EC and IC ends of the TM domains. Although changes in peak intensities alone could not tell whether anesthetics made conformational exchanges slower or faster, peak splitting unambiguously indicated a decrease in the conformational exchange rate on a μs-ms timescale [250]. Anesthetic occupancy of the α4β2 cavities may have reduced the degrees of freedom of interacting side chains and the attached backbone atoms, consequently resulting in decrease of exchange rate. For the same reason, anesthetic binding stabilized the original sub-conformation, shifted the conformational equilibria, and changed the population distribution of different conformations. The same trend of decrease in conformational exchange rates caused by anesthetics was also observed on other proteins [93,168]. The results support the notion that multiple conformers coexist dynamically in ion channel proteins and general anesthetics can shift the equilibrium among different conformation states [134].

It is also imperative to know that dynamics changes occurred not only to residues adjacent to anesthetics, but also to residues remote from the anesthetic binding sites. The observation is in accord with the consensus of allosteric mechanisms of signal

transduction [254]. Propagation of local anesthetic perturbation to remote sites, especially to the junctions of helices and loops, can lead functional consequences. Although ketamine does not bind near I267, I268, and S277 of α4, the observed motion changes in these residues are likely to affect communication between the EC and TM domains in the agonist-elicited channel activations [131,185].

5.2.5. Effects of halothane and ketamine on dynamics of the α7 nAChR TMD

Upon adding anesthetics to α7, relative amide peak intensities of some residues increased or decreased in the α7 NMR spectra (Figure 5.2.3), indicating changes in protein dynamics [36,66,249]. Residues lining the binding site for halothane or ketamine tended to experience intensity decrease, while residues distant from the binding sites had intensity decrease and increase (Figure 5.2.4). Among residues whose intensity changed more than 25%, halothane binding decreased intensity for 7 out of 10 residues; those in TM2 and TM3 decreased exclusively. In contrast, 6 out of 11 residues having more than 25% intensity changes in response to ketamine binding experienced peak intensity increase. Another notable difference between halothane and ketamine binding is the number of residues in TM4 affected by ketamine (R447, F453, S447, I458, and T461) and halothane (C449). The profound perturbation to TM4 is expected to introduce functional consequences [255-257]. The role of TM4 in Cys-loop receptor-lipid interactions as well as in nAChR function has been established [255-258].

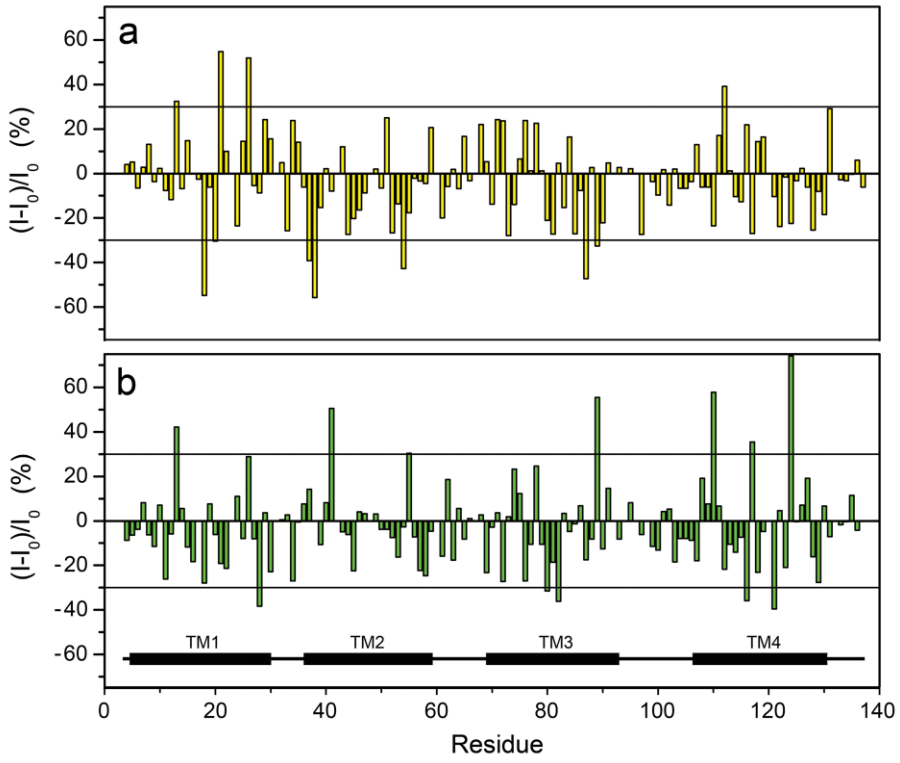

Figure 5.2.3. Anesthetics modulate backbone dynamics of the α7 nAChR TMD. Relative changes in peak intensity of the α7 TMD induced by (**a**) halothane (1.7 mM) and (**b**) ketamine (80 μM) versus the residue number. Residues significantly affected by halothane included L13, S21, L26, and C112 (peak intensity increased) as well as V18, I20, K37, I38, L54, T87, and I89 (peak intensity decreased). The ketamine binding affected the following residues: L13, G41, I89, R110, S117, and T124 (peak intensity increased) as well as F28, V80, L82, F116, and I121 (peak intensity decreased). To convert the numbering in this figure to the numbering for the full-length α7 nAChR, add 202 for residues labeled 1 to 102 and add 337 for residues labeled 103 to 137.

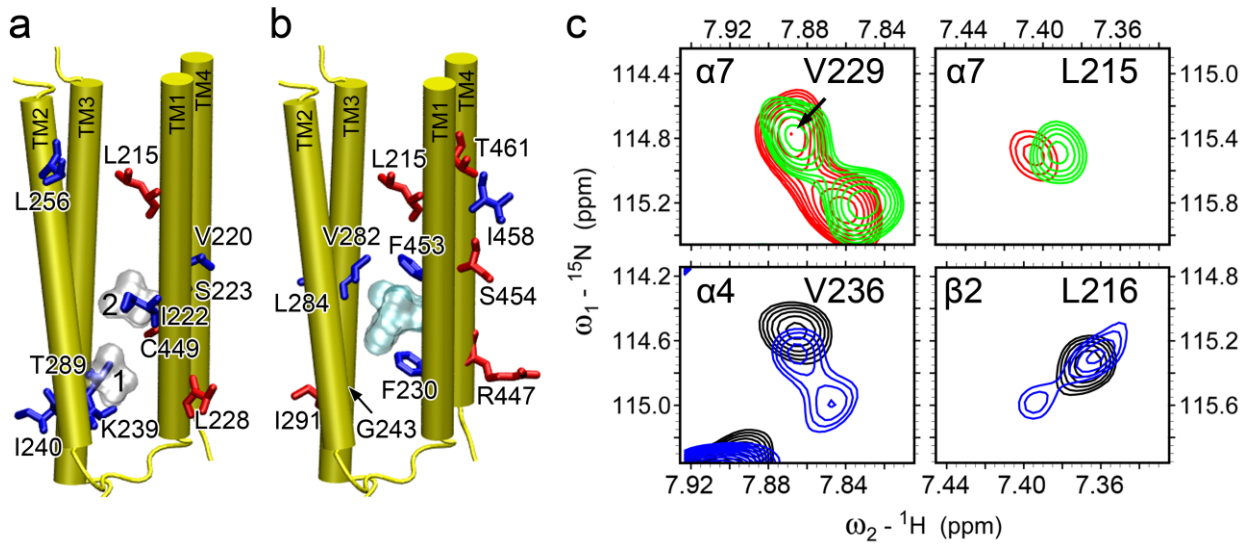

Figure 5.2.4. Anesthetic effects on backbone dynamics of the α7 nAChR TMD. Residues, whose relative peak intensity increased (red) or decreased (blue) upon the addition of (**a**) halothane (silver surface) and (**b**) ketamine (cyan surface) binding, are highlighted in the α7 structure. (**c**) Representative regions of ^{1}H-^{15}N TROSY-HSQC spectra in the absence (red or black) and presence (green or blue) of halothane. α7-V229 (top, left) is equivalent to α4-V236 (bottom, left); α7-L215 (top, right) is equivalent to β2-L216 (bottom, right). Note the halothane-induced peak splitting in α4-V236 and β2-L216, a sign of decrease of conformational exchange rates by halothane. Such changes were not observed in α7.

Peak splitting was observed previously in NMR spectra of the α4β2 nAChR TMD in the presence of anesthetics [39]. The splitting likely indicates a shift of conformational exchange from intermediate (or fast) to slow time scale. It is noteworthy that the splitting observed on α4β2 did not occur on α7 (Figure 5.2.4c). Neither halothane nor ketamine was able to drive α7 into slow conformational exchange mode as they did on α4β2.

The α7 nAChR, unlike the α4β2 nAChR, has distinct low functional sensitivity to volatile anesthetics, such as halothane [5,182]. The α7 nAChR does not have a binding site for halothane at the EC end of the TMD as revealed previously for α4β2 [39]. Furthermore, we have disclosed an association of anesthetic modulation on channel dynamics and

channel function (Figure 5.2.4). Comparisons of structural, dynamics, and anesthetic binding information between α7 and α4β2 offer a clue for reasoning why α7 is insensitive to halothane and other volatile anesthetics. As discussed in chapter 3, halothane binds to α7, but the binding to the IC end of the TMD did not effectively modulate dynamics of channel residues as it did in α4β2 (Figure 5.2.4), where more profound dynamics changes were observed. These results suggest a plausible association between dynamics modulation and functional modulation by anesthetics. Anesthetic binding would not produce functional impact unless the binding can significantly alter channel motions coupled with functions.

Comparisons of halothane sites in α7 with those in the α4β2 nAChR [39] and distinct dynamic responses of these receptors to halothane binding convey an important message, that is, effective functional modulation occurs only when the binding of anesthetics, or any modulators, induces dynamics or conformational changes in the channel pore.

5.2.6. Isoflurane effects on the dynamics of α7 and β2 subunits

Peak intensities of residues in the ^{1}H-^{15}N HSQC spectra can reveal backbone motional characteristics of proteins [39,66,249]. Terminal and loop residues usually experience fast motion on the ps-ns timescale and show relatively high peak intensities. In contrast, residues in the TM helices often show weaker or invisible signals due to restricted motion or conformational exchange on the μs-ms timescale [250]. α7 and β2 exhibit similar motional characteristics in their respective ^{1}H-^{15}N HSQC spectra in the absence of isoflurane (Figure 5.2.5). However, they respond differently to the addition of isoflurane.

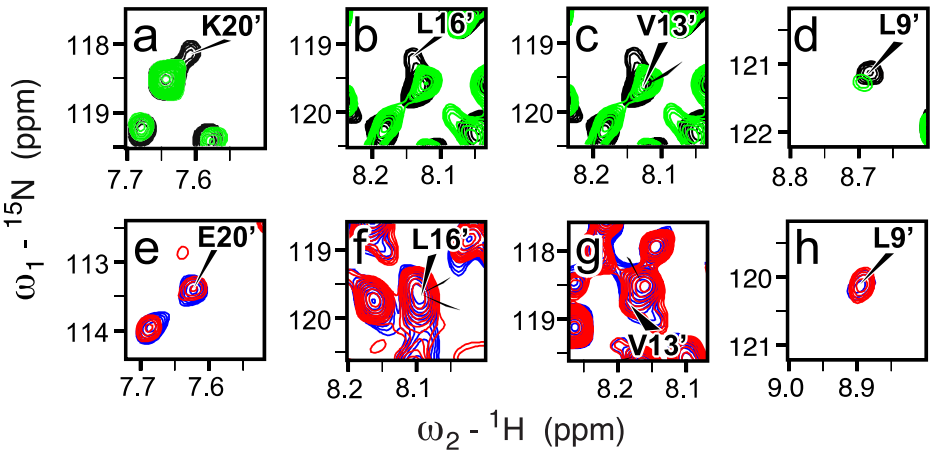

Figure 5.2.5. Pore-lining residues show more profound dynamics changes in β2 than in α7. (**a**)-(**d**) Excerpts of the ^{1}H-^{15}N TROSY-HSQC spectra for the β2 pore lining residues in the presence (green) and absence (black) of 1.3 mM isoflurane. (**e**)-(**h**) Excerpts of the ^{1}H-^{15}N TROSY-HSQC spectra for the α7 pore lining residues in the presence (red) and absence (blue) of 1.6 mM isoflurane. The presence of isoflurane significantly decreased peak intensities of the β2 pore-lining residues K20', L16' and L9'. V13' is difficult to be accurately assessed because of its peak overlap with another residue. In contrast, the homologous pore-lining residues of α7 exhibit no significant changes in the NMR spectra.

Figure 5.2.6 shows percentage changes of ^{1}H-^{15}N HSQC spectral peak intensities for residues in α7 and β2 in the presence and absence of isoflurane. α7 has a significant number of residues gaining more than 20% signal upon addition of isoflurane, while β2 has many more residues whose peak intensities decreased more than 20% due to isoflurane binding. Of particular note is the over 20% reduction of peak intensities for the β2 pore-lining residues (L9', L16', and K20') (Figure 5.2.6). V13' may also be affected to a similar degree, but the peak overlapping in the NMR spectrum limits the accuracy of its calculation (Figure 5.2.5). The data of relative intensity increase or decrease suggest that isoflurane largely facilitates the motion on α7, but slows down the motion of β2.

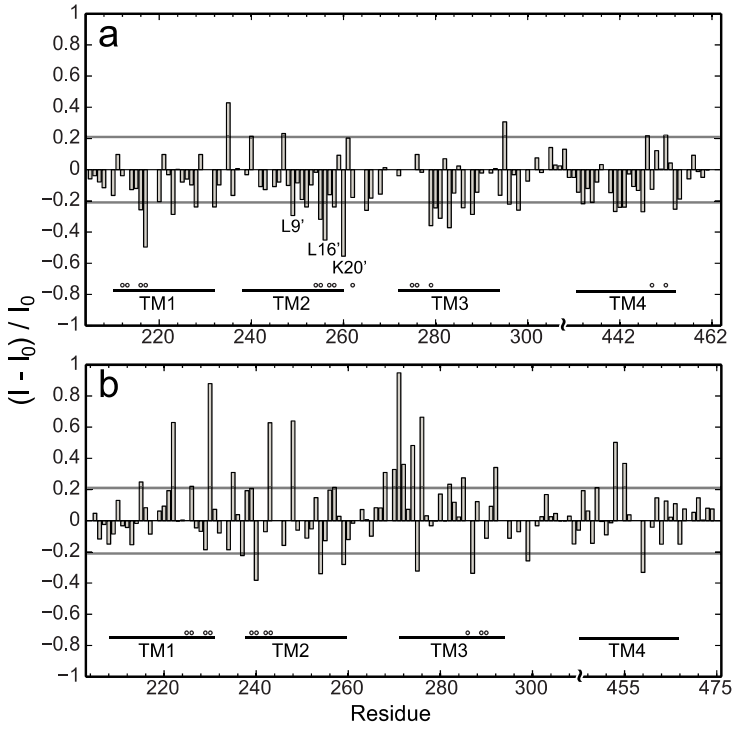

Figure 5.2.6. Different dynamics responses of β2 and α7 to isoflurane modulation. (**a**) β2 and (**b**) α7 have distinctly different patterns in percentage changes of NMR spectral peak intensity in the absence (I_0) and presence (I) of isoflurane. Residues lining the respective isoflurane-binding cavities in the β2 and α7 TM domains are marked with open circles.

One of the most striking differences between α7 and β2 is that upon isoflurane binding, α7 retained a single signal for each residue in the NMR spectra, but β2 showed classic examples of two-site chemical exchange [208,209] for several residues, including the channel gate residue L249(9') and V262(22') lining the isoflurane-binding pocket in β2. As shown in Figure 4.2.4, in the absence of isoflurane (black), each of these β2 residues showed a single peak in the NMR spectrum. After adding 1.3 mM isoflurane (red), an additional peak became observable for L248 and T265 (denoted as L248' and T265', respectively). When the isoflurane concentration was increased to 3 mM (cyan), L249 and V262 also showed additional peaks. The combined chemical shift change between each

pair of peaks (A-B or A'-B), $\Delta\omega_{H+N} = [(\Delta\omega_H^2 + \Delta\omega_N^2)]^{1/2}$, is 32, 27, 37, 32 Hz for L248, L249, V262, and T265 of β2, respectively. Based on the consensus from many previous studies [208-210], the occurrence of two distinct peaks for a residue indicates a slow exchange with $k_{ex} << 2\pi\Delta\omega_{H+N} \sim 200 s^{-1}$.

Conformational exchange among β2 residues also shows some differences. For residues L248 and T265, peak A remained at 20 Hz line width and the same resonance frequency in the absence and presence of isoflurane, indicating a possibility that slow conformational exchange with an extremely low population for the second conformation (peak B) already existed in the absence of isoflurane. Isoflurane shifted the equilibria between the two conformations. Indeed, the population of conformation B, $p_B = 1-p_A$, increased from 0 to ~0.3 and more than ~0.5 when isoflurane was increased from 0 to 1.3 and 3 mM. Overall, L248 and T265 fit well to the scheme of slow exchange between two conformations [208-210]. In the case of L249 and V262, however, a single peak with a broader line width in the ^1H dimension was observed in the presence of 0 mM (L249, 21 Hz; V262, 17 Hz) and 1.3 mM isoflurane (L249, 19 Hz; V262, 16 Hz), but two narrower peaks (L249, 16 and 12 Hz; V262, 14 and 12 Hz) were observed in the presence of 3 mM isoflurane. The results suggest that L249 and V262 were likely in an intermediate exchange regime [208,209] before exposed to 3 mM isoflurane. In addition to slower exchange between A' and B conformations, the increased isoflurane concentration also shifted peak A' from peak A by 14 and 11 Hz for L249 and V262, respectively (Figure 4.2.4). This is not unexpected, considering that multiple conformers with subtle differences can co-exist in a functional state [211,212].

The sensitivity of β2 and insensitivity of α7 to the dynamics modulation by

isoflurane are in good agreement with their distinctly different functional responses to isoflurane inhibition. Differences in their structures and isoflurane-binding sites may have contributed to different dynamics responses of β2 and α7 to isoflurane binding. Only in β2 were isoflurane-induced changes in conformational populations and motion on the μs-ms timescale observed. The combined effects from structures, anesthetic binding sites, and dynamics modulations may have contributed to the functional differences between β2 and α7.

5.2.7. Discussion

Computational results showed that halothane binding to α7 did not induce profound changes in the structure and dynamics of α7 that could be related to the channel function. The favorable interaction between halothane and the amphiphilic EC/TM interface of the β2 subunit brings about changes in dynamics at this interface. The insensitivity of α7 to halothane-induced dynamics changes may be the reason why α4β2 is functionally more sensitive to halothane than α7.

The respective sensitivity and insensitivity of β2 and α7 to dynamics modulation by volatile general anesthetics was affirmed by our NMR results. What makes β2 more susceptible to dynamics modulation than α7. We previously discussed in Chapter 4 that the β2-V22'M mutation could decrease the volume of the anesthetic binding cavity to prevent isoflurane from binding. However, methionine may also stabilize the TM2 helix and make it more resilient to structural and dynamic perturbation introduced by anesthetic binding. Previous studies using unnatural amino acid substitutions have shown that residues with un-branched side chains, such as methionine and alanine, have a more

stabilizing effect on α helices than branched amino acids, such as valine and isoleucine [213]. Similarly, β2-S19' and α7-A19' could also make dynamics differences to the TM2 helix. Alanine is a natural helix promoter [214], while serine and threonine often disrupt α-helices due to backbone to side chain hydrogen bonds [125,215]. Our study on hGlyR-α1 TM noted heightened conformational dynamics at the EC end of TM2, which is uniquely rich with serines in this region compared to other pLGICs [38].

Our results suggest that the EC end of the TMD plays a critical role for channel gating in pLGICs. Increasing the rigidity of residues at the EC end of the TMD can make the channel less responsive to activation signals. Many previous studies support this notion. Increasing helical flexibility at the EC end of TM2 of the nAChR was found to increase the receptors' sensitivity to agonist more than tenfold [57]. Disulfide bond trapping experiments on the $GABA_A$ receptor [216] and EPR experiments on GLIC [58] also support heightened dynamics at the EC end of TM2 during channel gating. Our work on the glycine receptor suggested that increasing or decreasing the conformational dynamics at the EC end of TM2 could respectively increase or decrease the channel's susceptibility to allosteric modulation [38]. Thus, it is conceivable that changing dynamics of the EC end of the TMD, either via drug binding or point mutations, is a common mechanism to modulate functions of pLGICs.

5.2.8. Conclusions

Past studies have shown that mutations affecting anesthetic modulation often concurrently affect the intrinsic gating dynamics of the channel [54-56], suggesting that the ability of anesthetics to modulate the channel is intrinsically related to the channel gating

dynamics. Our NMR studies on the neuronal nAChRs suggest that only the ligand binding that can affect the channel dynamics will produce the functional effect. Particularly, it was observed that isoflurane binding at the EC end of the TMD could substantially reduce dynamics for nearby residues in TM2 [40]. Other studies have shown that dynamics at the EC end of TM2 is important to channel gating [57,58]. The results suggest that binding to an intra-subunit site at the EC end of the TMD the anesthetic can limit dynamics at the EC end of TM2 and consequently make the channel more difficult to open. Only the binding that modulates dynamics of pore-lining residues, such as that at the EC end of the β2 TMD, can impact function. Our study emphasizes the role of channel dynamics in allosteric modulation.

5.3. THE IMPORTANCE OF ASYMMETRY TO ALLOSTERIC MODULATION

This section has been published as a full article in *J. Am. Chem Soc*. **35** (6): 2172-2180.

5.3.1. Background and Significance

Structural symmetry of a protein assembly results from its functional evolution [259-262]. The symmetry feature is often required to retain global structural stability and cooperative functionality [254,259,260,263]. Cys-loop receptors mediate fast synaptic signal transmission. Each Cys-loop receptor is comprised of five homologous subunits that form a pLGIC. For a homo-pLGIC, a fivefold symmetry around the central pore is assumed. Each subunit contains an ECD, a TMD of four TM helices (TM1 to TM4) with TM2 lining the pore, and an ICD that links TM3 and TM4. Agonist binding to the ECD induces channel opening

and allows ions to move through the pore. Despite the existence of five identical agonist-binding sites in a homo-pLGIC, occupancy of three nonconsecutive sites by agonists was found to induce maximal mean channel open time [59]. The maximum channel-gating efficacy could be reached when only three potential binding sites were occupied in the homomeric α1 GlyRs [60] and ρ1 $GABA_A$ receptors [61]. Skepticism remains as to whether asymmetric agonist binding induces spontaneous asymmetric conformational changes. In addition, it remains unclear whether ligands other than agonists also bind asymmetrically to these proteins to produce functional impact. Interestingly, an asymmetric intermediate conformation of a homo-trimeric transporter was captured recently in the crystal structure [264], indicating the involvement of asymmetric conformational change in biological function.

At pharmacologically relevant concentrations, general anesthetics potentiate anion-selective GlyRs and $GABA_A$ receptors, but inhibit cation-selective nAChRs and serotonin receptors [153,265]. Occupancy of a single binding site in the homo-pLGIC α1 GlyR by volatile anesthetics and alcohols was found to be sufficient to potentiate channel currents [266]. General anesthetics [224] and alcohols [56] also modulate the function of GLIC. Crystal structures of GLIC in complex with propofol or desflurane [106] reveal intra-subunit binding sites in the TMD of all five subunits (Figure 5.3.1). The structures of the anesthetic-GLIC complexes are virtually identical to the apo GLIC structure [27,106]. Propofol inhibits GLIC currents at concentrations used clinically [106,224]. A higher propofol concentration could completely close the GLIC channel and inhibit ion conductance [106,224]. Therefore, an apparently open channel structure of GLIC under symmetric anesthetic occupancy in the crystal structure seems incongruent with the potent inhibition

observed in the functional measurements. The relevance of the identified anesthetic site in the structure, however, is supported by functional studies on various mutants [106]. The question is whether inhibition of GLIC requires anesthetics to occupy all five subunits simultaneously or only a few subunits similar to channel activations by asymmetric agonist binding [59-61].

To address this apparent disagreement between structure and function, we performed multiple sets of MD simulations on the crystal structures of GLIC and the propofol-GLIC complex. The number of propofol molecules bound to GLIC was varied in different simulation systems by either keeping all five propofol molecules or deleting propofol from some of the subunits before the simulations. Two groups with distinct channel hydration states and conformations emerged over the course of MD simulations. GLIC with symmetric propofol occupancy in all five sites and the apo GLIC acted as one group, while GLIC with asymmetric propofol binding belonged to another group. The study suggests that symmetry of ligand binding has a profound effect on conformational transitions. Symmetry breaking by ligand binding facilitates conformational transitions. In general, symmetry breaking is a prevalent process in biology and symmetry breaking along well-defined axes is often linked to functional diversification on every scale [267]. The current simulation study along with previous knowledge of asymmetric agonist binding in activation of Cys-loop receptors [59-61,266] demand thorough characterizations of symmetry breaking by ligand binding in the functions of pLGICs, just as those characterized for many other biological systems [267].[267]

5.3.2. Methods

Crystal structures of the open-channel apo GLIC (PDB ID: 3EAM) and the open-channel propofol–GLIC complex (PDB ID: 3P50) were used for MD simulations. Crystal structures of the locally closed GLIC (PDB IDs: 3TLS and 3TLW) were used as references for the closed-channel conformations observed from the simulations. Five simulation systems were generated by varying the propofol occupancy in GLIC: (i) no propofol bound to GLIC (0PFL); (ii) five propofol molecules bound to GLIC (5PFL) as shown in the X-ray structure of the propofol–GLIC complex [106]; (iii) three propofol molecules bound to nonconsecutive subunits (3PFL); (iv) two propofol molecules bound to consecutive sites (2PFL); and (v) one propofol molecule bound to GLIC (1PFL). For each system, three parallel runs were performed using different seed numbers and each run lasted for 100 ns. Figure 5.3.1 shows all five systems and the propofol binding sites.

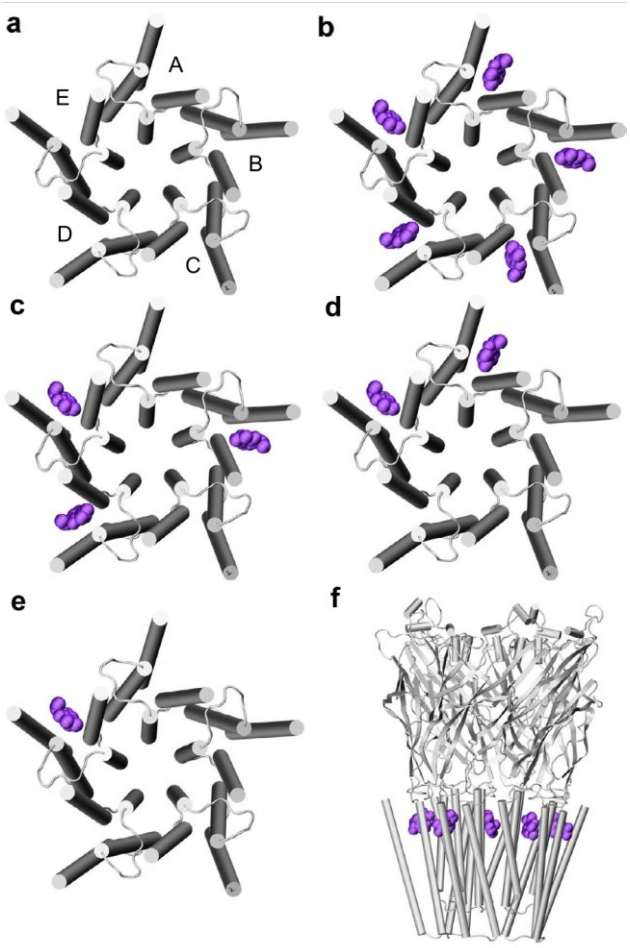

Figure 5.3.1. Propofol binding sites in different GLIC systems. Top views of the transmembrane domains of (a) 0PFL; (b) 5PFL; (c) 3PFL; (d) 2PFL; (e) 1PFL; and (f) a side view of 5PFL. Propofol is in VDW representation and colored in purple.

Protonation states of titratable residues in GLIC at pH = 4.6 were assigned based on the results reported by Bocquet et al. [27] Some modifications, including deprotonation of five H235 residues and two E222 residues, were made based on our recent calculations [268]. The TM domain of GLIC was inserted into a pre-equilibrated and solvated POPE/POPG (3:1) binary lipid mixture. Each simulation system has a hexagonal boundary condition of 104.6 Å × 104.6 Å × 129.8 Å, one GLIC, 167 POPE, 54 POPG, and approximately 23 700 TIP3 water molecules.

MD simulations were performed using NAMD 2.7b1 [91]. CHARMM27 force field with CMAP corrections (version 31) was used for protein, water, and lipids [145,269]. Propofol parametrization was done following the protocol of the CHARMM General Force Field (CGenFF) for drug-like molecules [270]. The details for propofol parameterization can be found in the online supporting material of the manuscript [62]. All simulation systems followed the same simulation protocol. Each system was energy minimized for 20 000 steps before equilibration for 2 ns, during which the backbone constraint on GLIC was gradually reduced from 10 kcal·mol^{-1}·Å^{-2} to zero. Each system underwent three runs up to 3 × 100 ns of unconstrained simulations under constant pressure (P = 1 bar) and temperature (T = 310 K) [271,272].

Periodic boundary conditions, water wrapping, hydrogen atoms constrained via SHAKE, and evaluation of long-range electrostatic forces via the Particle Mesh Ewald (PME) algorithm [273] were used in the simulations. Bonded interactions and short-range, nonbonded interactions were calculated every time step (2 fs). Electrostatic interactions were calculated every two time steps (4 fs). The cutoff distance for nonbonded interactions was 12 Å. A smoothing function was employed for the van der Waals interactions at a distance of 10 Å. The pair-list of the nonbonded interaction was calculated every 20 time-steps with a pair-list distance of 13.5 Å.

VMD [86] was used for visualization and most parts of data analysis. Unless otherwise specified, snapshots every 20 ps of the simulation trajectories (a total of 5000 snapshots) were used for data analyses for each 100-ns simulation. The number of water molecules (N_{water}) inside the hydrophobic gate region was obtained by counting water inside the pore between I233 (I9′) and I240 (I16′). The channel hydration state was

defined based on N_{water}: fully hydrated if $N_{water} \geq 10$, partially dehydrated if $0 < N_{water} < 10$ and fully dehydrated if $N_{water} = 0$. Ten water molecules inside the hydrophobic gate region are equivalent to 65% of the bulk water density and were used previously as a threshold in the evaluation of the channel hydration status [274]. A histogram of N_{water} was calculated based on the data from three 100-ns parallel runs for each system. Each run was named according to the duration of time that the channel remained hydrated. For example, the channel hydration time in the 5PFL system follows the order: 5PFL-1 > 5PFL-2 > 5PFL-3.

Orientation of the pore-lining TM2 helix was characterized by the radial (θ) and lateral (φ) tilting angles of the TM2 helices relative to the membrane normal, as defined in previous publications [176,183]. The same method as detailed previously [176] was used to calculate the radial and lateral tilting angles. For each system, distributions and histograms of the radial and lateral tilting angles were calculated for each channel hydration state and averaged over all five subunits in three replica simulations.

A normalized histogram for the joint events of (θ, φ) was used to estimate heterogeneity of the TM2 tilting angles using MATLAB. The joint Shannon entropy *S(i,j)* was calculated by [275]:

$$S(i,j) = \sum_{j=1}^{N} \sum_{i=1}^{N} p_{ij} \ln p_{ij} \qquad (5.2)$$

where p_{ij} is the joint probability of the event (θ_i, φ_j) obtained from the normalized histogram of the tilting angles, and N is the number of bins. For each system, the radial and lateral tilting angles were collected over all five subunits in three replica simulations. To generate the histogram, a bin size of 0.1° was used to sample angles ranging from −12° to 15° for

both θ and φ. Standard deviations of the entropies were estimated with the bootstrap method [276], using 100 sets of randomly sampled data points from the first 2600 × 3 snapshots for each system. The analysis of variance with posthoc Tukey HSD multiple comparison test between groups was performed using SPSS v20.

The anisotropic network model (ANM) [277] was used for structure-based analysis of GLIC dynamics. The Hessian matrix was built using all Cα atoms and a pairwise interaction cutoff of 15 Å. The 10 lowest frequency modes of ANM were calculated and visualized using ProDy [278].

The force, resulting from VDW and electrostatic interaction of propofol with GLIC, was calculated in x, y, z directions using the pairInteraction module implemented in NAMD 2.7b1 [91]. Residues within 5 Å of propofol were selected in the calculations. To quantify the primary component of the force, we performed principal component analyses (PCA) on the force trajectory (5000 frames over 100 ns) using MATLAB. For visualization, the principal component of the force is presented within the context of the GLIC structure. Each principal component was scaled by its eigenvalue and multiplied by the inverse of the eigenvector matrix. Each resultant vector was then centered on the propofol position and plotted.

For statistical analyses of the channel opening probability, we categorized a channel as “open” if the number of water molecules inside the channel gate is equal to or greater than 10; otherwise, the state of the channel is labeled as “closed”. We pooled all 3 replicated simulations for each system (snapshots every 0.5 ns of the simulation trajectories were used) and represented the number (X) of simulation snapshots that assumed an open state using a binomial distribution: $X \sim \mathrm{Bin}(N, p)$, where N is the total

number of simulation snapshots and *p* is the channel opening probability. The estimate of the channel open probability ($\hat{p}$), confidence interval for $\hat{p}$, the adjusted confidence interval for comparing two estimated channel opening probabilities, ($\tilde{p}_1 - \tilde{p}_2$), and therein the p-value were derived using an R language script and the methods described by Agresti and Caffo [279]. The open-channel probability was estimated by $\hat{p} = X/N$, the confidence interval for the estimate of channel opening probability is $\hat{p} \pm z_{\alpha/2}[\hat{p}(1 - \hat{p})/N]^{1/2}$, and the adjusted confidence interval for the estimated difference between two channel opening probabilities is

$$(\tilde{p}_1 - \tilde{p}_2) \pm z_{\alpha/2}\sqrt{\frac{\tilde{p}_1(1-\tilde{p}_1)+\tilde{p}_2(1-\tilde{p}_2)}{N+3}};\ \text{where}\ \tilde{p}_i = (X_i+1)/(N+2).$$

5.3.3. Asymmetric Propofol Binding Increased the Probability of Channel Dehydration

The channel hydration status is strongly related to the ion conductance. Ions cannot pass through a dry channel even if the pore is not yet geometrically closed [280]. An evolution from a fully hydrated to a completely dehydrated channel in simulations signifies a transition of the channel functional state. The GLIC crystal structures used for our simulations, in the absence and presence of propofol, have the same open-channel conformation [27,28,106]. At the beginning of all simulations, the GLIC channel was fully hydrated. Over the course of the simulations, GLIC exhibited only a small deviation from the crystal structure. The Cα RMSD of the overall protein and the TM domain reached a plateau after 5–8 ns. The RMSDs remained under 2 Å for the TM domain thereafter. The duration of the fully hydrated state, however, varied by runs, particularly by systems. As

shown in Figure 5.3.2a, 5PFL-1 remained full hydration almost for the entire 100 ns, while 5PFL-2 and 5PFL-3 were fully hydrated for 65 and 50 ns, respectively. The system with no propofol, 0PFL, showed almost the same results. In contrast, 3PFL, 2PFL, and 1PFL experienced much more rapid and extended channel dehydration.

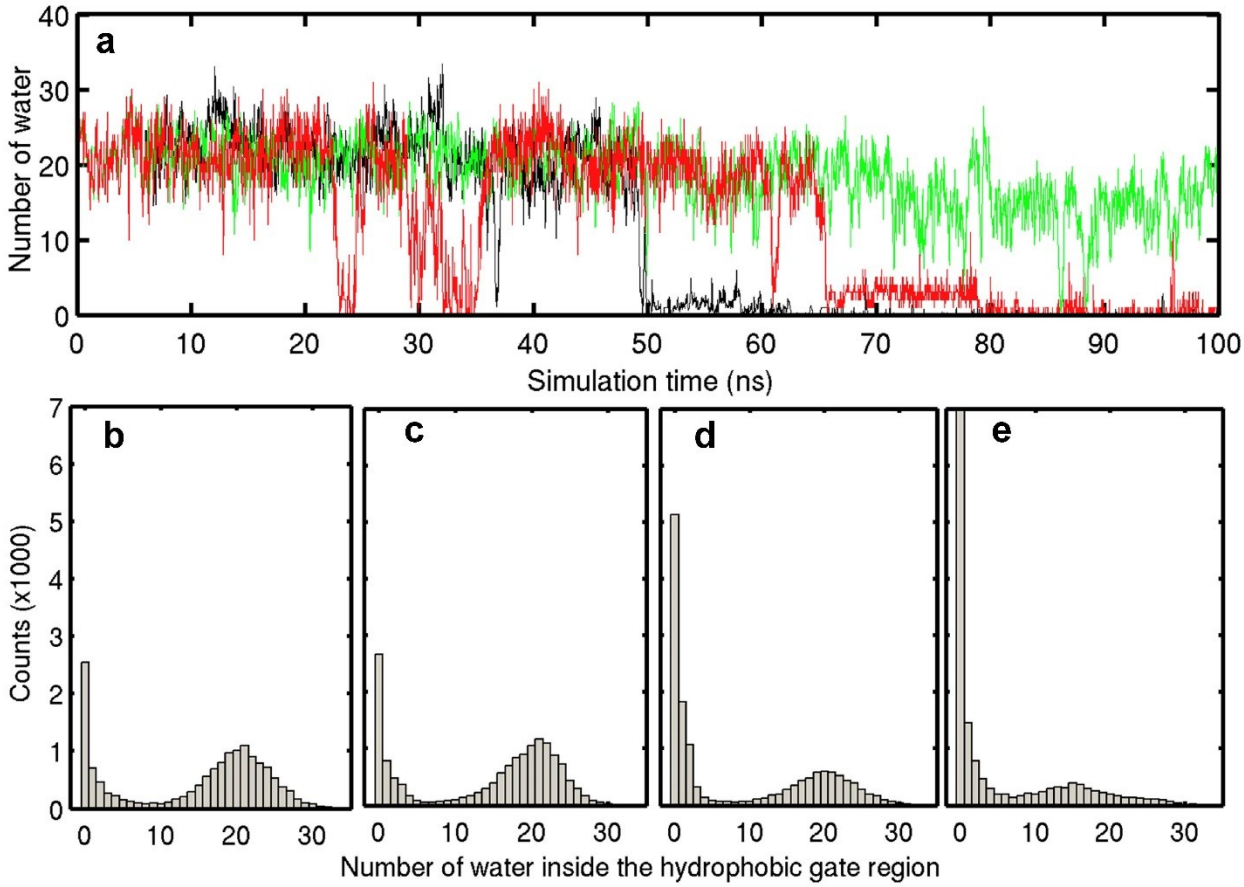

Figure 5.3.2. Channel hydration under different scenarios of propofol binding. (**a**) Time evolution of the number of water molecules in the hydrophobic gate region (N_{water}). Three replicate runs, 5PFL-1, 5PFL-2 and 5PFL-3, are colored in green, red and black, respectively. Histograms of N_{water} were generated based on three replicate runs for each system, (**b**) 0PFL; (**c**) 5PFL; (**d**) 3PFL; (**e**) 2PFL; and (**f**) 1PFL. Snapshots with a 20-picosecond interval were taken from each run. A total of 15000 structures were used for each histogram analysis.

To objectively evaluate and compare the channel hydration status among different systems, we made histograms for each system based on the data from all three replicate runs. Figure 5.3.2b–f shows that the distribution of the number of water molecules inside the channel gate is bimodal, with one peaking near 20 waters and the other peaking at zero water. We hypothesize that these two peaks correspond to the “open” and “closed” states of the channel, respectively. On the basis of this assumption, we used the value of 10 waters per channel—the groove between the two modes—as a threshold to categorize the state of the channel in each snapshot as “open” (≥10 waters per channel) or “closed” (otherwise). The channel open probabilities for the symmetric systems 0PFL and 5PFL are 68 ± 6% and 68 ± 6%, respectively. In contrast, the open probabilities for the asymmetric systems 3PFL, 2PFL, and 1PFL are only 42 ± 7%, 28 ± 6%, and 32 ± 6%, respectively. The errors represent 99.9% confidence intervals of the estimates. Using the same level of confidence interval for the differences between the estimated probabilities [279], we found that the channel open probability is significantly higher in the symmetric systems than in the asymmetric systems with a p-value < 0.001. The results clearly differentiate two groups of systems that are divided based on the propofol binding symmetry. Asymmetric propofol binding facilitated the transition from a fully hydrated channel to a dehydrated channel.

GLIC is expected to be mostly open and hydrated at pH 4.6 [222]. The channel in 0PFL or 5PFL was indeed hydrated for most of the simulation time. The dehydration occurred and resembled the observations from several previous simulations on GLIC [175,176,280,281]. Since GLIC is a proton-gated channel, imperfect imitation of pH conditions within the simulations could be one of the reasons to cause dehydration. In reality, we do

not have a complete set of titratable residues that has been experimentally proven to be responsible for pH activation of GLIC. Accurately predicting pKa's in membrane proteins remains challenging. Other imperfections in the simulation environment may also have compromised the time scale of channel hydration. However, for all of the simulated systems reported here, everything was identical except the number of propofol molecules. Any consequences induced by system imperfections are systematic and common to all the systems. Thus, it is reasonable to conclude that the observed propensity of changes in channel hydration status in Figure 5.3.2 results primarily from variation in propofol occupancy.

A significantly higher probability of dehydration promoted by asymmetric propofol binding is consistent with the inhibitory effect of propofol on GLIC [106,224]. It is known that propofol also inhibits cationic currents of nAChRs [6,282] and $5HT_3$ receptors [283]. The results observed here on GLIC are likely relevant to the inhibitory effect of propofol on these receptors as well.

The finding that asymmetric propofol occupancy facilitated the channel transition more effectively than 5PFL does not contradict the concentration dependence of anesthetic inhibition of GLIC [224]. The crystal structure presents the maximum binding sites. In order to make propofol observable in the crystal structure, propofol was added to GLIC in a saturating amount for crystallization. In functional measurements, however, propofol inhibited GLIC in concentrations (IC_{50}: 0.5–10 μM) several orders of magnitude lower than that used for crystallization [106,224]. In addition, the Hill coefficient of propofol inhibition was 0.42 [224], an indication of negative cooperative process, in which one propofol bound to GLIC reduces the ability of another propofol to inhibit channel. All of

these suggest that propofol completely inhibits GLIC at a concentration well below the saturated concentration and before it occupies all five sites. Once the channel falls into a closed state, an additional amount of anesthetics cannot resume the GLIC current (our own unpublished data). The crystal structure of the open channel GLIC with five propofol molecules bound symmetrically may only reflect a preferred conformation of GLIC at the crystallization conditions. The discrepancy between the functional state and the channel conformation captured in the crystal structures has also been observed recently on ELIC [105].

5.3.4. Asymmetric Propofol Binding Facilitated the Pore-Lining TM2 toward a Closed-Channel Conformation

It has long been proposed that TM2 helix tilting underlies the channel gating of pLGICs [111]. The lateral (δ) and radial (θ) tilting angles of the pore lining TM2 helices give quantitative measurements of pore conformational changes [176,183]. Compared to the closed-channel ELIC (δ ≈ −7.9°; θ ≈ −3.5°), the open-channel GLIC (δ ≈ 0.7°; θ ≈ 6.5°) has no more than 10° difference on both angles [26,28,120,281]. A combined crystallographic and functional study revealed the locally closed conformations of GLIC, demonstrating that a few degree changes in the lateral and radial tilting angles of TM2 are sufficient to stop GLIC current [211].

Figure 5.3.3 shows the lateral and radial tilting angles of TM2 for each of the five systems simulated to 100 ns. The angles are colored in green, purple, and black to represent three channel states: fully hydrated, transitional, and fully dehydrated at the hydrophobic gate region, respectively. For comparison, the lateral and radial tilting angles

of TM2 in the crystal structures of the open-channel GLIC [28,281] and the locally closed-channel GLIC [211] are also marked in Figure 5.3.3. For the fully hydrated state, the lateral and radial tilting angles of TM2 are highly populated near 0.7° and 6.5°, respectively, more or less the same as those in the open channel GLIC. Quantitative information about populations of tilting angles for each system is shown by histograms in Figure 5.3.4. A deviation by a few degrees in either the lateral or radial tilting angle could result in channel dehydration. The TM2 tilting angles associated with the dehydrated state are largely shifted toward the angles in the locally closed GLIC [211].

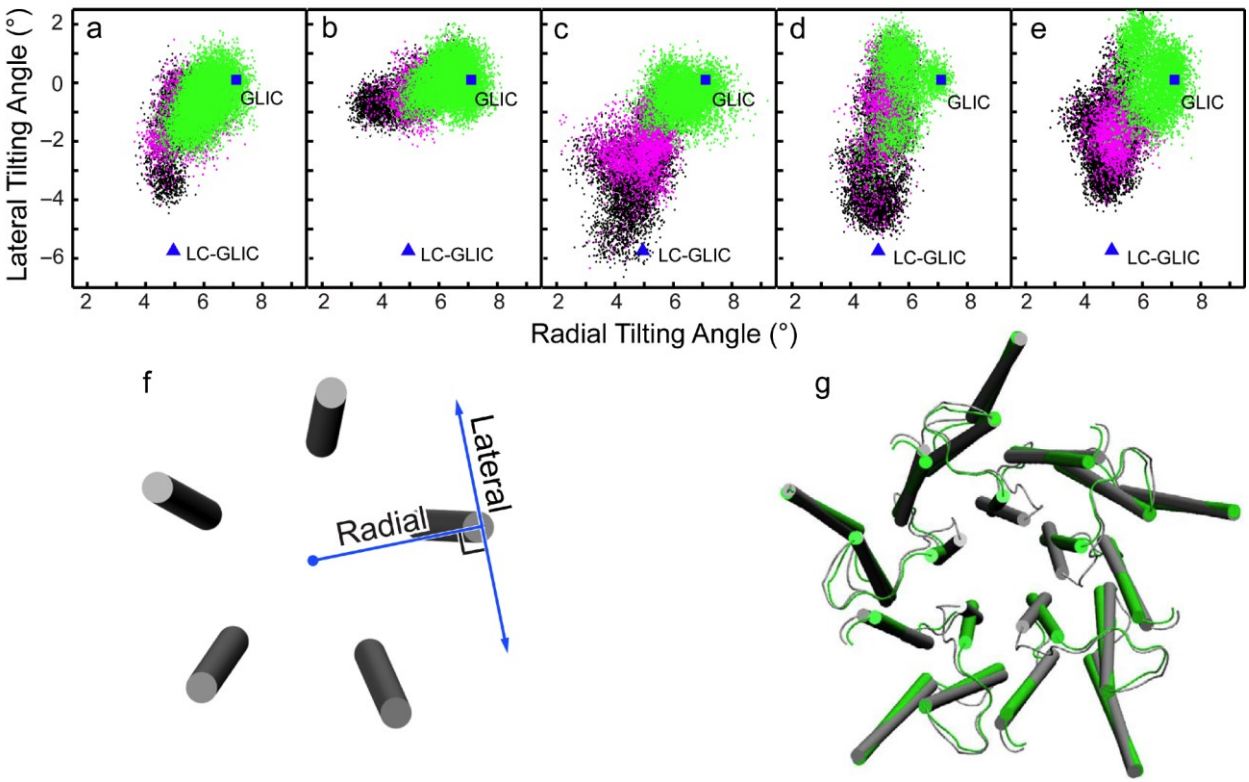

Figure 5.3.3. Distributions of lateral and radial tilting angles of TM2 for (a) 0PFL, (b) 5PFL, (c) 3PFL, (d) 2PFL, and (e) 1PFL. (**f**) Depiction of radial and lateral directions for calculating the tilting angles. (**g**) The aligned crystal structures of the open-channel GLIC (PDB ID: 3EAM; green) and the locally closed GLIC (PDB ID: 3TLS; gray). The colors in (a) – (e) denote the channel hydration states associated with the TM2 tilting angles as defined by N_{water}: green for a fully hydrated channel (N_{water} >10); Purple for a partially dehydrated channel (0< N_{water} ≤10) and black for a fully dehydrated channel (N_{water} =0). Each system summarizes a total of 15,000 structures, sampled evenly over 100 ns for each of the three replicates. For comparison, a blue square and a blue triangle mark the TM2 tilting angles for the crystal structures of the open-channel GLIC and the locally closed GLIC, respectively. Counts of each hydration state for each system are provided in **Figure 5.3.4**.

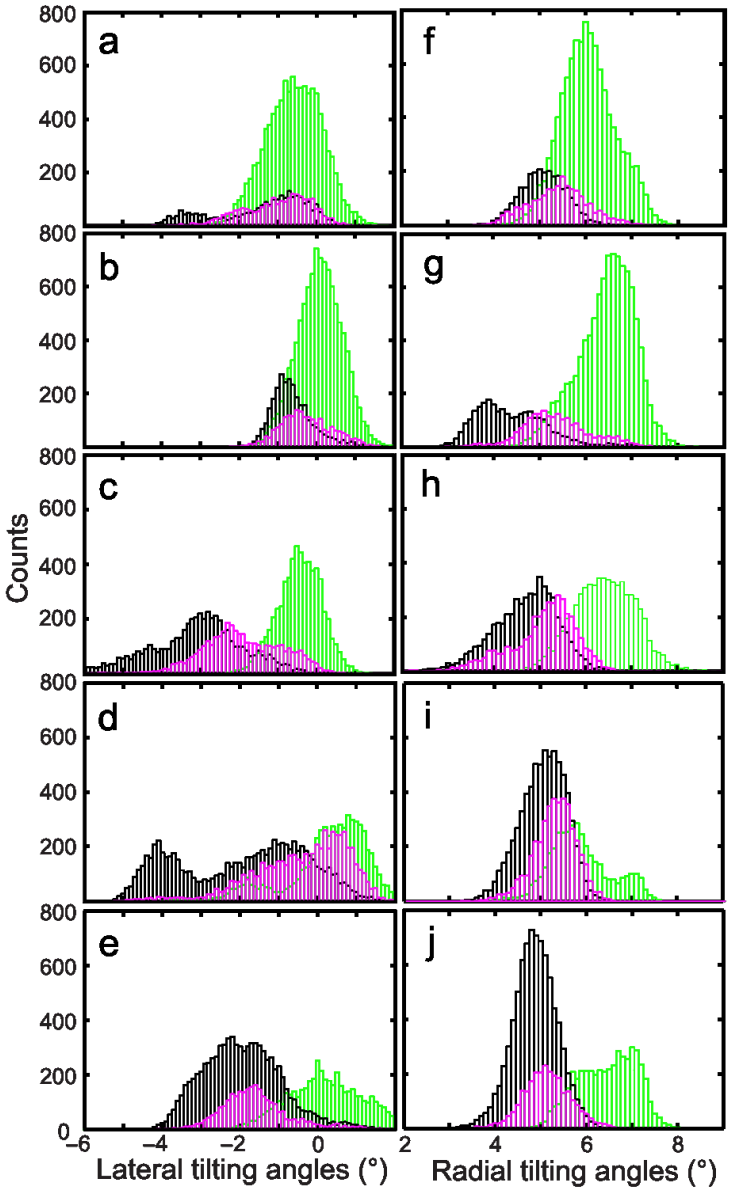

Figure 5.3.4. Histograms of the TM2 lateral tilting angles in (a) 0PFL; (b) 5PFL; (c) 3PFL; (d) 2PFL; and (e) 1PFL. Histograms of the TM2 radial tilting angles in (f) 0PFL; (g) 5PFL; (h) 3PFL; (i) 2PFL and (j) 1PFL. Colors mark the channel hydration statuses accompanying the TM2 tilting angles that were defined by N_{water}: green for a fully hydrated channel (N_{water} ≥10); purple for partially dehydrated (0<N_{water} <10) and black for fully dehydrated (N_{water} = 0). A bin size of 0.1° was used in the analysis. The same data used for **Figure 5.3.3** are used for the histograms presented here.

To evaluate conformational changes in other regions of GLIC, we also calculated lateral and radial tilting angles for TM1, TM3, and TM4 in all of the simulations. Consistent with the crystal structures of the open and locally closed GLIC channels (Figure 5.3.3g), these three helices, especially TM3 and TM4, showed much smaller conformational differences between the two channel states (**Figure 5.3.5**), whereas TM2 conformation correlates most sensitively to the channel state. Although the conformation differences for different channel states are also visible in other TM helices, they are less distinct than that observed in TM2.

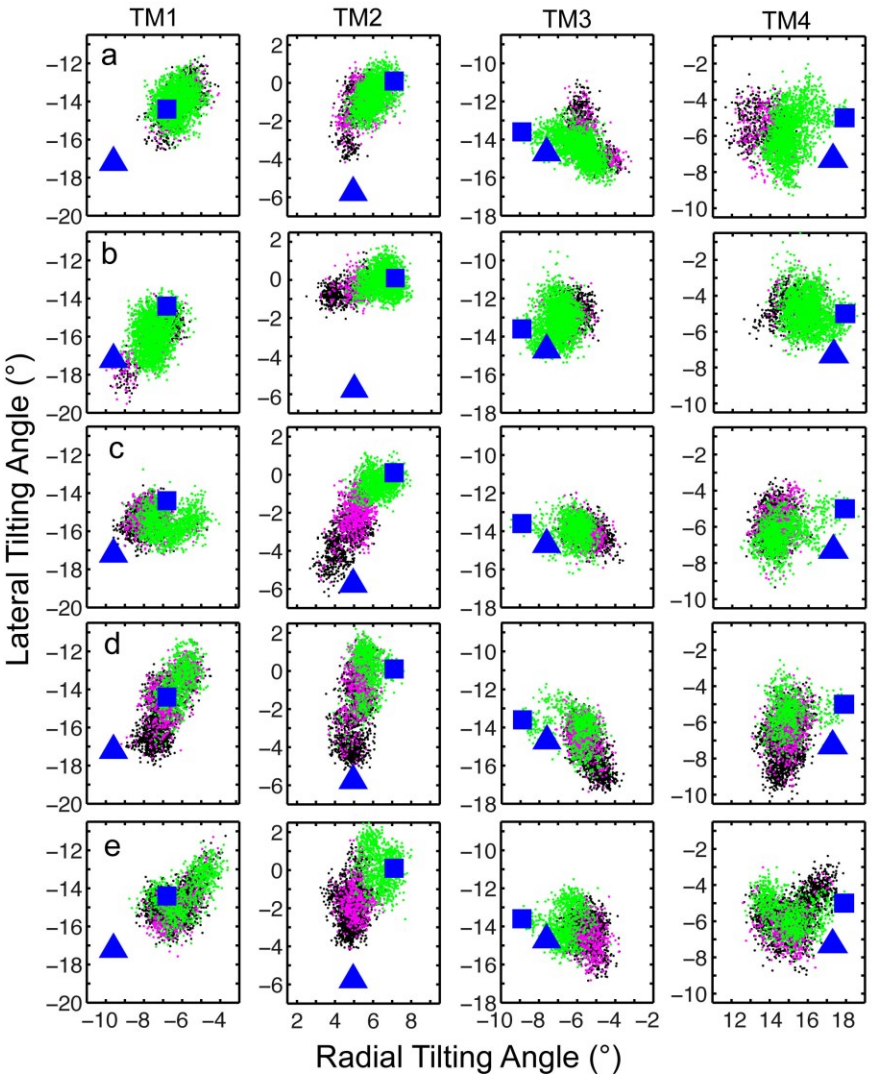

Figure 5.3.5. Distributions of lateral and radial tilting angles of TM1 (residues 196 to 217), TM2 (residues 221 to 246), TM3 (residues 253 to 282), and TM4 (residues 285 to 314) for (a) 0PFL, (b) 5PFL, (c) 3PFL, (d) 2PFL, and (e) 1PFL. Depiction of radial and lateral directions for calculating the tilting angles is shown in Figure 5.3.3. The colors denote the channel hydration statuses as defined by N_{water}: green for a fully hydrated channel (N_{water} >10); Purple for a partially dehydrated channel (0< N_{water} ≤10) and black for a fully dehydrated channel (N_{water} =0). Each system summarizes a total of 3,000 structures, sampled evenly over 100 ns for each of the three replicates. For comparison, a blue square and a blue triangle mark the tilting angles for the crystal structures of the openchannel GLIC (PDB ID: 3EAM) and the locally closed GLIC (PDB IDs: 3TLS and 3TLW), respectively. As indicated in the crystal structures, the TM2 tilting angles are most sensitive to the channel opening state than other TM helices.

The symmetry of propofol binding influenced the TM2 tilting angles (Figure 5.3.3 and Figure 5.3.4). Compared to the symmetric 0PFL and 5PFL, the asymmetric 3PFL and 2PFL as well as 1PFL had higher populations of TM2 whose lateral- and radial-tilting angles shifted more toward the locally closed-channel conformation [211]. In addition, 1PFL, 2PFL and 3PFL had broader distributions of the TM2 tilting angles than 0PFL and 5PFL, particularly in the lateral angles. The broadness of the distributions reflects the conformational heterogeneity, which can be quantified by the joint Shannon entropy [275]. The calculation of the joint Shannon entropies of the TM2 tilting angles using Equation (5.2) yielded the values of 7.00 ± 0.01, 6.81 ± 0.01, 6.82 ± 0.01, 6.04 ± 0.01, and 6.31 ± 0.01 for 1PFL, 2PFL, 3PFL, 5PFL, and 0PFL, respectively. One-way ANOVA with respect to propofol occupancy shows significant difference of the Shannon entropies among the five systems ($p < 0.001$). Post hoc Tukey HSD comparison tests indicate that 1PFL, 2PFL, and 3PFL are significantly different from 0PFL and 5PFL ($p < 0.001$). Clearly, asymmetric propofol binding increased the conformational heterogeneity of TM2.

Although the quaternary twist motion is thought to dominate channel conformation transitions in pLGICs [131,138,281,284], asymmetric motion has been observed to lead to channel opening [285] and closing [131,138]. Experimental data also support the role of asymmetric motion in channel functions [286,287]. An asymmetric and independent contribution of the TM2 residues to gating of nAChR was observed in a single-channel study [286]. Thus, it is not surprising to see spontaneous asymmetric motion in our simulations. After carefully examining individual trajectories, we found that TM2 helices in different subunits experienced different degrees of tilting at a given time point. Moreover, inward radial tilting (or contraction) and/or lateral tilting of the TM2 helix in one

or two subunits was sufficient to alter the channel hydration state. The same phenomena were also observed in other studies on GLIC [176,280,281]. We also performed ANM analysis on the crystal structure of GLIC. Among the 10 lowest frequency modes, which are coupled with the large-scale global domain motions, mode 3 is the only mode showing symmetric twisting motion (Figure 5.3.6). Asymmetric motions in other modes, especially asymmetric inward/outward motion among subunits, are expected to contribute to functional changes in channel conformations [131]. Thus, asymmetric anesthetic binding does not create new modes of motion, but rather shifts the population of asymmetric motion.

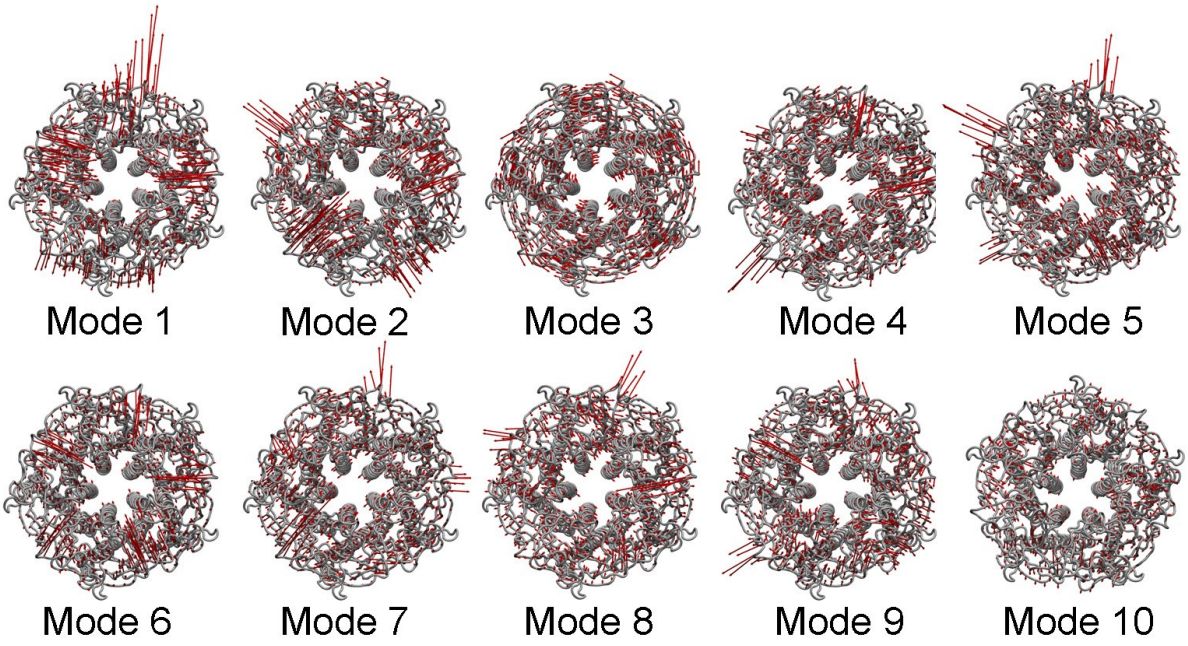

Figure 5.3.6. First ten modes identified by ANM analysis of GLIC. Note that only mode 3 shows symmetric motion.

5.3.5. Propofol Motion and Imposing Forces Affect the Channel Hydration Status

Propofol bound asymmetrically to GLIC facilitates a population shift of TM2 toward the closed-channel conformation and increases conformational entropy. To further understand why asymmetric propofol binding facilitates the conformational transition, we examined the forces imposed by propofol on each subunit.

Propofol binding imposed a force on GLIC. We calculated the force between propofol and residues within 5 Å of propofol and examined the time trajectory of the vector sum of all forces imposed on each subunit (Figure 5.3.7). The trajectories of the force for all simulations can be found in the online supporting material of the published manuscript [62]. Several characteristics about the force are noteworthy. The force trajectory generated by each propofol over simulation times assumes the shape of an ellipsoid. On the basis of principal component analyses, the primary component of the force is tangential to the pore and substantially larger than the second component that is mostly radial to the pore. Both the tangential and radial forces are well balanced in 5PFL (Figure 5.3.7), but obviously uneven in the systems of asymmetrical propofol binding. In addition to the force trajectories on all residues within 5 Å of propofol, we also examined the forces on individual residues in the binding cavity, T255 of TM3 and Y197 of TM1. Each residue experienced a force imposed by propofol at any given time. The force fluctuated along a narrow range of directions over the course of simulations. The time averaged net force resulted from dividing the accumulated force by the number of snapshots that were sampled evenly from each simulation trajectory. In most cases, the averaged net force became smaller when simulation time became longer. For example, the averaged net force on T255 of 3PFL was 1.7, 1.3, and 1.0 kcal/(mol·Å) at the 10-, 50-, and 100-ns

simulation, respectively. Even though the time averaged net force is not large, the propofol force at any given time is substantial to prevent the binding cavity from shrinking. Intuitively, an unevenly distributed force creates an unstable condition that could facilitate transitions, either to a direction leading channel closure (such as the case of anesthetic binding in GLIC) or to the direction of channel opening (such as the case of agonist binding in pLGICs). Indeed, when one of the propofol molecules in 5PFL-3 migrated out of the cavity after ~45 ns simulation, the channel was dehydrated soon thereafter.

The force analysis suggests that propofol imposes a larger force along the tangential direction than the radial direction to the pore. Impact of the force to conformational transition can be substantiated once the force becomes unbalanced among five subunits. Although it seems uncommon to link asymmetrically distributed force with conformational and ultimately functional changes, there is engrained experimental support for the biological significance of symmetry breaking [267]. For instance, an asymmetric protrusive force resulting from symmetry breaking in the actin assembly drives directional cell mobility [288,289]. The fact that asymmetric agonist binding activates Cys-loop receptors [59-61] also speaks for the involvement of a symmetry breaking in the process.

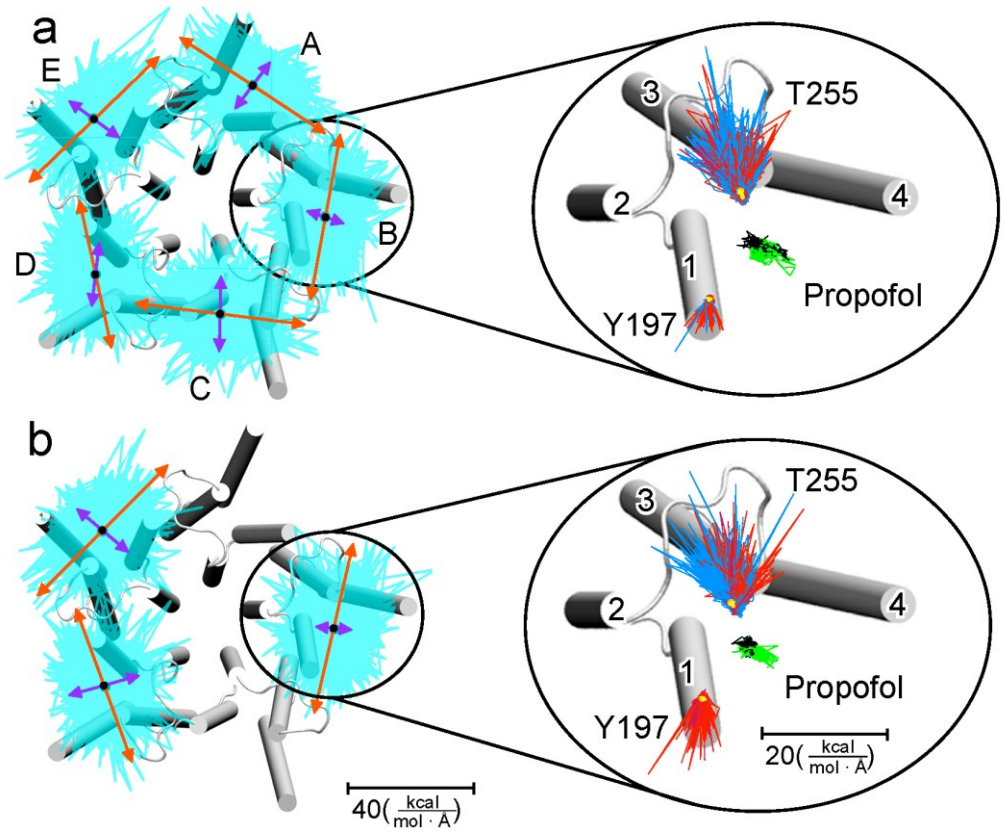

Figure 5.3.7. Representative projections of the propofol-force trajectories, (a) 5PFL-1 and (b) 3PFL-1. The force trajectory (cyan) over a 100-ns simulation for each subunit is centered on propofol, which is marked by a black dot. The shape of the overall force trajectory is ellipsoid with the longest axis tangential to the pore. The first (red arrows) and second (purple arrows) principal components of each force trajectory are scaled by their respective eigenvalues and projected onto the same plane as the force trajectory. Zoom-in views of the propofol force on individual residues Y197 and T255 of subunit B in (a) 5PFL and (b) 3PFL were generated based on the force calculation separately for each residue. The force trajectory is colored in blue and red for the first and last 50-ns simulation, respectively. The coordinate trajectory of the propofol's center of mass is shown in green and black for the first and last 50-ns simulation, respectively. The time averaged net force on Y197 and T255 for first 50-ns and entire 100 ns simulations are shown in orange and yellow arrows, respectively. Reference scales for the amplitude of the force in the overall and zoom-in views are shown.

5.3.6. Conclusions

The most important conclusion from this study is that transient symmetry breaking by asymmetric ligand binding in pLGICs facilitates changes in channel conformation. The simulations for systems that are otherwise identical except for the number of propofol occupancy provide compelling evidence to support the conclusion. Binding without perturbing symmetry in 5PFL preserved the open-channel conformation as observed in 0PFL. The result is consistent with the consensus that the symmetry feature retains global structural stability [254,259,260,263]. In contrast, asymmetric propofol binding perturbed the symmetry and facilitated conformational changes. The distinct difference resulting from asymmetric ligand binding does not come as a total revelation. As Blundell and his colleague stated based on their examinations of several enzymes, mild perturbation from perfect symmetry may be essential in some systems for dynamic functions [259]. It is also known that asymmetric agonist binding without occupying all five equivalent sites can produce the maximal opening of Cys-loop receptor channels [59-61]. It is likely that, no matter channel activation or inhibition, asymmetric ligand binding works more effectively to induce transitions from one state to another.

Our multiseeded, parallel simulations exceeded 1.5 μs in total. Although extending each set to the microsecond time scale [178,281] is desirable, such extensions for multiple μs simulations to cover all possible anesthetic-binding scenarios demand much more computational power that has not been available to us. Fortunately, the current simulation time scale is able to cover the transitions between different channel hydration states. Our statistical approaches with multiple independent runs have sufficient power to unequivocally differentiate the functional propensities of GLIC under different scenarios

of propofol binding. To generalize the functional role of asymmetric ligand binding in pLGICs requires further experimental investigations, which may be challenging but are not impossible. The most encouraging examples are the elegant experimental demonstrations that asymmetric agonist binding activates homo-pLGICs [59-61] and that anesthetic or alcohol binding to a single subunit in the homomeric α1 GlyR is sufficient to alter channel function [266].

APPENDIX A.

STRUCTURE CALCULATION OF THE GLYCINE RECEPTOR

A.1. MONOMER CALCULATION

One hundred (100) random structures were generated and annealed using Cyana-3.0 [84,290]. Structures were annealed using 2,000,000 steps and an annealing schedule modified slightly from the default annealing schedule in Cyana-3.0. Modifications to the annealing schedule include using a quadratic (vs. a quartic) cooling profile in the second annealing stage. With the large number of steps, decreasing the temperature more slowly in the second annealing stage improves the annealing. By default, the van der Waals (VDW) penalty is initially divided by four and restored to its default value at the end of the second annealing stage. In the modified algorithm the VDW penalty was initially divided by 4, then multiplied by 2 halfway through the second annealing stage, and restored to its default value at the end of the second annealing stage. This change was made to prevent structures from entering into minima with bad VDW contacts. Of the 100 structures calculated, the 32 structures with lowest target functions were refined. Refinement was performed using Cyana-3.0 and the annealing schedule outlined in Table A-1. Radii and weights were not adjusted at any point in the refinement schedule and parameters not reported below are identical to those in Cyana's default annealing algorithm. Two rounds of refinement were performed. The first round of refinement used an input temperature of 0.3 target function units per degree of freedom and 2,000,000 steps. The second used an initial temperature of 0.03 target function units per degree of freedom and 1,000,000 steps. From the 32 refined structures the 15 with lowest target function were obtained and reported.

Table A-1. Cyana Refinement Annealing Schedule

	Steps[1]	Starting T[2]	Ending T	Tau[3]	VDW[4]
Minimization	100	N/A	N/A	N/A	N/A
Pre-Equilibration	0.02N	T	T	1.0	10
Equilibration 1	0.02N	0.9T	0.9T	1.0	10
Equilibration 2	0.02N	0.855T	0.855T	1.0	10
First Cooling	0.36N	0.855T	0.154T	10.0	10
Second Cooling	0.44N	0.154T	0.0086T	10.0	5
Final Cooling	0.16N	0.0086T	0	1.0	20
Final MD	4000	0	0	1.0	20
Minimization	1000	N/A	N/A	N/A	N/A

[1]N is total number of steps. Pre-Equilibration and Final MD are not included when adding up to N. [2]T is the input temperature. Temperatures visited in between the starting and ending temperatures result from a linear interpolation between starting and ending temperatures. [3]Tau is the correlation time controlling coupling to the temperature bath. [4]VDW column shows the number of steps after which VDW forces are evaluated.

A.2. PENTAMER CALCULATION

The calculation of the pentamer structure was developed based on the symmetric arrangement of monomer subunits in a pentameric configuration. The intra-subunit NMR restraints were copied five times. We defined five groups of symmetric contacts within Cyana from which Cyana automatically generated 3996 angle identity restraints and 100,000 symmetric distance restraints. From the EM images we obtain a restraint on the radial distance of each monomer subunit from the pore. Tilting angles for TM2 with respect to the channel pore were obtained from RDC measurements in low-q bicelles [121]. The average angle between TM2 and the channel pore (13±1°) is within the range of angle values for proteins in the same superfamily of Cys-loop receptors: the α1 nAChR (12°) [291], the α4 nAChR (12±1° and 16±1° for α4 and α4β2 respectively) [169], and the $GABA_A$ receptor (15±2°)[166]. The angles all fall in the range of 11° to 17°. We considered the possibility that the presence of TM1 and TM4 may produce changes to the TM2 tilting angle and used a ±5° error term for this angle in the pentamer structure calculation (see section **A.2.3** Rotational Error). To generate Cyana distance restraints based on the EM and RDC restraints, a model of the pentamer was constructed using MATLAB® (2010a, The MathWorks, Inc., Natick, Massachusetts). Details for the construction of the model and generation of Cyana restraints are described below.

A.2.1 Atoms in the Model

Residues present in the model coming from TM2 correspond to the residues in TM2 over which the RDC data was reported (residues 253 to 265) [121]. Residues in TM1 (226 to 241), TM3 (290 to 302) and TM4 (402 to 414) were added to the model. The RMSD for backbone atoms listed was less than 0.5 Å. Coordinates for backbone atoms of the listed residues were extracted from the structure bearing the minimum RMSD to all other structures in the bundle and imported into MatLab. The imported coordinates and corresponding atoms define the monomer subunit used in construction of the pentamer model.

A.2.2 Pentamer Construction

The pentamer model was constructed by creating vertices for a pentagon inscribed on a unit circle lying in the membrane plane and centered at (0, 0, 0). The pentagon coordinates were multiplied by the radius obtained from the EM data. The radius was the distance from the center of the EM image to the peak in electron density after circular averaging of the EM images. Hydrogen and nitrogen coordinates for residues in TM2 were oriented according to the RDC constraints. The monomer was centered according to its center of density, moved to one of the vertices, and TM2 was oriented to face the pore. The center of density was calculated for the bundle of 15 monomer structures using the VolMap tool in VMD. The pentamer was created by moving subunits to each remaining vertex and applying a 72° rotation for each consecutive movement around the pentagon.

A.2.3 Rotational Error

The error reported in the RDC experiments was 1° for rotations about the 1st and 2nd principle axes and 10° around the 3rd principle axis. The 1st and 2nd principle axes correspond to tilting within the membrane while the 3rd principle axis corresponds to a rotation about the monomer's principle axis. In this model a 5° rotational variance was allowed about each of the monomer axes. The 5° rotational variance was accounted for by applying rotations ranging from -5° to 5° about each axis with a step size of 1°.

Coordinates resulting from these rotations were stored for each atom. The result is a cluster of 1331 (11x11x11) atom positions.

A.2.4 Atoms Restrained

For each TM domain restraints were created for atoms closest to the monomer center as well as farthest along the channel axis in both directions from the center of each TM domain were chosen to restrain. Atoms were also chosen at the midpoints along the channel axis, resulting in 5 atoms per TM domain for which restraints were imposed.

A.2.5 Upper and Lower Bound Limits

Self restraints were defined as restraints between identical atoms in different subunits. For example in TM1, restraints were calculated for the following combinations:

A1B1 B1C1 C1D1 D1E1
A1C1 B1D1 C1E1
A1D1 B1E1
A1E1

Where A1B1 = TM1 of chain A paired with TM1 of chain B, B1C1 = TM1 of chain B paired with TM1 of chain C, and so forth. These pairings were repeated for TM2, TM3, and TM4.

To determine the distance restraint to use in the Cyana calculation, pairwise distances were calculated between each atom position in each cluster. Where the cluster referred to is described under Rotational Error. The upper bound limit was the maximum distance calculated plus a 1 Å error term accounting for EM resolution. The lower bound limit was the minimum distance calculated minus 1 Å. For example, the distance restraint for atom (i) in the pair A1B1 is calculated as follows: The distance between atom (i) in TM1 of chain A and atom (i) in TM1 of chain B is calculated for each of the 1331 positions of atom (i) in the generated cluster. This results in a total of 1331 distances. The one to one correspondence of the number of atom positions stored in each cluster and the number of distances results from a symmetry assumption implicit in the model. Five-fold symmetry around the channel axis requires that any rotation applied to one subunit must necessarily be applied to all subunits. Therefore we only compute distances between points having the same applied rotations for each subunit. The upper bound limit was

calculated by taking the maximum value of the 1331 distances plus 1 Å, while the lower bound limit was calculated by taking the minimum value of the 1331 distances minus 1 Å.

Restraints were also calculated between TM1 and TM3 in a similar fashion.

That is the restraints were as follows:

A1B3 B1C3 C1D3 D1E3		A3B1 B3C1 C3D1 D3E1
A1C3 B1D3 C1E3	&	A3C1 B3D1 C3E1
A1D3 B1E3		A3D1 B3E1
A1E3		A3E1

In this case, atoms in TM3 were necessarily different from atoms in TM1. However, the relative position of the atoms along the channel axis was fixed. In other words, the atom closest to the center in TM3 was paired with the atom closest to the center in TM1.

A.2.6 Calculation

Similar to the monomer calculation 100 random structures were generated and annealed using Cyana-3.0. Structures were annealed in 500,000 steps using the modified Cyana annealing schedule as described for the monomer calculation. An input temperature of 8.5 target function units per degree of freedom, rather than the default of 8.0 target function units per degree of freedom, was also used for the pentamer calculation. Of the 100 structures calculated, thirty-two were refined using the refinement schedule described in Table A-1. Two rounds of refinement were also performed for the pentamer calculation. The first round of refinement used 500,000 steps and a temperature of 0.3 target function units per degree of freedom and the second round of refinement used 250,000 steps and a temperature 0.03 target function units per degree of freedom.

BIBLIOGRAPHY

(1) Unwin, N. *J Mol Biol* **2005**, *346*, 967.

(2) Franks, N. P.; Lieb, W. R. *Toxicol Lett* **1998**, *101*, 1.

(3) Couturier, S.; Bertrand, D.; Matter, J. M.; Hernandez, M. C.; Bertrand, S.; Millar, N.; Valera, S.; Barkas, T.; Ballivet, M. *Neuron* **1990**, *5*, 847.

(4) Sargent, P. B. *Annual review of neuroscience* **1993**, *16*, 403.

(5) Mori, T.; Zhao, X.; Zuo, Y.; Aistrup, G. L.; Nishikawa, K.; Marszalec, W.; Yeh, J. Z.; Narahashi, T. *Mol Pharmacol* **2001**, *59*, 732.

(6) Flood, P.; Ramirez-Latorre, J.; Role, L. *Anesthesiology* **1997**, *86*, 859.

(7) Khiroug, S. S.; Harkness, P. C.; Lamb, P. W.; Sudweeks, S. N.; Khiroug, L.; Millar, N. S.; Yakel, J. L. *J Physiol* **2002**, *540*, 425.

(8) Evers, A. S.; Steinbach, J. H. *Anesthesiology* **1997**, *86*, 760.

(9) Fabian-Fine, R.; Skehel, P.; Errington, M. L.; Davies, H. A.; Sher, E.; Stewart, M. G.; Fine, A. *J Neurosci* **2001**, *21*, 7993.

(10) Meyer, P. M.; Strecker, K.; Kendziorra, K.; Becker, G.; Hesse, S.; Woelpl, D.; Hensel, A.; Patt, M.; Sorger, D.; Wegner, F.; Lobsien, D.; Barthel, H.; Brust, P.; Gertz, H. J.; Sabri, O.; Schwarz, J. *Arch Gen Psychiatry* **2009**, *66*, 866.

(11) Lamb, P. W.; Melton, M. A.; Yakel, J. L. *J Mol Neurosci* **2005**, *27*, 13.

(12) Le Foll, B.; Chefer, S. I.; Kimes, A. S.; Shumway, D.; Stein, E. A.; Mukhin, A. G.; Goldberg, S. R. *Biol Psychiatry* **2009**, *65*, 714.

(13) Picciotto, M. R.; Zoli, M.; Rimondini, R.; Lena, C.; Marubio, L. M.; Pich, E. M.; Fuxe, K.; Changeux, J. P. *Nature* **1998**, *391*, 173.

(14) Wang, H.; Yu, M.; Ochani, M.; Amella, C. A.; Tanovic, M.; Susarla, S.; Li, J. H.; Wang, H.; Yang, H.; Ulloa, L.; Al-Abed, Y.; Czura, C. J.; Tracey, K. J. *Nature* **2003**, *421*, 384.

(15) Heeschen, C.; Weis, M.; Aicher, A.; Dimmeler, S.; Cooke, J. P. *The Journal of clinical investigation* **2002**, *110*, 527.

(16) Picciotto, M. R.; Zoli, M.; Lena, C.; Bessis, A.; Lallemand, Y.; Le Novere, N.; Vincent, P.; Pich, E. M.; Brulet, P.; Changeux, J. P. *Nature* **1995**, *374*, 65.

(17) Marubio, L. M.; del Mar Arroyo-Jimenez, M.; Cordero-Erausquin, M.; Lena, C.; Le Novere, N.; de Kerchove d'Exaerde, A.; Huchet, M.; Damaj, M. I.; Changeux, J. P. *Nature* **1999**, *398*, 805.

(18) Xu, W.; Orr-Urtreger, A.; Nigro, F.; Gelber, S.; Sutcliffe, C. B.; Armstrong, D.; Patrick, J. W.; Role, L. W.; Beaudet, A. L.; De Biasi, M. *J Neurosci* **1999**, *19*, 9298.

(19) Rudolph, U.; Crestani, F.; Benke, D.; Brunig, I.; Benson, J. A.; Fritschy, J. M.; Martin, J. R.; Bluethmann, H.; Mohler, H. *Nature* **1999**, *401*, 796.

(20) Yamauchi, M.; Sekiyama, H.; Shimada, S. G.; Collins, J. G. *Anesthesiology* **2002**, *97*, 412.

(21) Low, K.; Crestani, F.; Keist, R.; Benke, D.; Brunig, I.; Benson, J. A.; Fritschy, J. M.; Rulicke, T.; Bluethmann, H.; Mohler, H.; Rudolph, U. *Science* **2000**, *290*, 131.

(22) Vandenberg, R. J.; Handford, C. A.; Schofield, P. R. *Neuron* **1992**, *9*, 491.

(23) Smith, G. B.; Olsen, R. W. *J Biol Chem* **1994**, *269*, 20380.

(24) Brejc, K.; van Dijk, W. J.; Klaassen, R. V.; Schuurmans, M.; van Der Oost, J.; Smit, A. B.; Sixma, T. K. *Nature* **2001**, *411*, 269.

(25) Miller, P. S.; Smart, T. G. *Trends in pharmacological sciences* **2010**, *31*, 161.

(26) Hilf, R. J.; Dutzler, R. *Nature* **2008**, *452*, 375.

(27) Bocquet, N.; Nury, H.; Baaden, M.; Le Poupon, C.; Changeux, J. P.; Delarue, M.; Corringer, P. J. *Nature* **2009**, *457*, 111.

(28) Hilf, R. J.; Dutzler, R. *Nature* **2009**, *457*, 115.

(29) Hibbs, R. E.; Gouaux, E. *Nature* **2011**, *474*, 54.

(30) Celie, P. H.; van Rossum-Fikkert, S. E.; van Dijk, W. J.; Brejc, K.; Smit, A. B.; Sixma, T. K. *Neuron* **2004**, *41*, 907.

(31) Hansen, S. B.; Sulzenbacher, G.; Huxford, T.; Marchot, P.; Taylor, P.; Bourne, Y. *EMBO J.* **2005**, *24*, 3635.

(32) Dellisanti, C. D.; Yao, Y.; Stroud, J. C.; Wang, Z. Z.; Chen, L. *Nat Neurosci* **2007**, *10*, 953.

(33) Li, S. X.; Huang, S.; Bren, N.; Noridomi, K.; Dellisanti, C. D.; Sine, S. M.; Chen, L. *Nat Neurosci* **2011**, *14*, 1253.

(34) Yevenes, G. E.; Zeilhofer, H. U. *Br J Pharmacol* **2011**, *164*, 224.

(35) Taly, A.; Corringer, P. J.; Guedin, D.; Lestage, P.; Changeux, J. P. *Nature reviews. Drug discovery* **2009**, *8*, 733.

(36) Bondarenko, V.; Mowrey, D.; Tillman, T.; Cui, T.; Liu, L. T.; Xu, Y.; Tang, P. *Biochimica et biophysica acta* **2012**.

(37) Bondarenko, V.; Mowrey, D. D.; Tillman, T. S.; Seyoum, E.; Xu, Y.; Tang, P. *Biochimica et biophysica acta* **2014**, *(in press)*.

(38) Mowrey, D. D.; Cui, T.; Jia, Y.; Ma, D.; Makhov, A. M.; Zhang, P.; Tang, P.; Xu, Y. *Structure* **2013**, *21*, 1897.

(39) Bondarenko, V.; Mowrey, D.; Liu, L. T.; Xu, Y.; Tang, P. *Biochimica et biophysica acta* **2013**, *1828*, 398.

(40) Mowrey, D. D.; Liu, Q.; Bondarenko, V.; Chen, Q.; Seyoum, E.; Xu, Y.; Wu, J.; Tang, P. *J Biol Chem* **2013**, *288*, 35793.

(41) Chiara, D. C.; Dangott, L. J.; Eckenhoff, R. G.; Cohen, J. B. *Biochemistry* **2003**, *42*, 13457.

(42) Liu, L. T.; Willenbring, D.; Xu, Y.; Tang, P. *J Phys Chem* **2009**, *113*, 12581.

(43) Liu, L. T.; Haddadian, E. J.; Willenbring, D.; Xu, Y.; Tang, P. *J Phys Chem* **2010**, *114*, 626.

(44) Mowrey, D.; Haddadian, E. J.; Liu, L. T.; Willenbring, D.; Xu, Y.; Tang, P. *J Phys Chem* **2010**, *114*, 7649.

(45) Coates, K. M.; Flood, P. *Br J Pharmacol* **2001**, *134*, 871.

(46) Yamakura, T.; Chavez-Noriega, L. E.; Harris, R. A. *Anesthesiology* **2000**, *92*, 1144.

(47) Pan, J.; Chen, Q.; Willenbring, D.; Mowrey, D.; Kong, X. P.; Cohen, A.; Divito, C. B.; Xu, Y.; Tang, P. *Structure* **2012**, *20*, 1463.

(48) Lu, H.-M.; Liang, J. *PLoS Comput Biol* **2009**, *5*, e1000526.

(49) Chennubhotla, C.; Bahar, I. *Mol Syst Biol* **2006**, *2*, 36.

(50) Yen, J. Y. *Management Science* **1971**, *17*, 712.

(51) Bafna, P. A.; Purohit, P. G.; Auerbach, A. *PloS one* **2008**, *3*, e2515.

(52) Grosman, C.; Zhou, M.; Auerbach, A. *Nature* **2000**, *403*, 773.

(53) Mowrey, D.; Chen, Q.; Liang, Y.; Liang, J.; Xu, Y.; Tang, P. *PloS one* **2013**, *8*, e64326.

(54) Lynagh, T.; Lynch, J. W. *International journal for parasitology* **2010**, *40*, 1477.

(55) Mihic, S. J.; Ye, Q.; Wick, M. J.; Koltchine, V. V.; Krasowski, M. D.; Finn, S. E.; Mascia, M. P.; Valenzuela, C. F.; Hanson, K. K.; Greenblatt, E. P.; Harris, R. A.; Harrison, N. L. *Nature* **1997**, *389*, 385.

(56) Howard, R. J.; Murail, S.; Ondricek, K. E.; Corringer, P. J.; Lindahl, E.; Trudell, J. R.; Harris, R. A. *Proc Natl Acad Sci U S A* **2011**, *108*, 12149.
(57) England, P. M.; Zhang, Y.; Dougherty, D. A.; Lester, H. A. *Cell* **1999**, *96*, 89.
(58) Velisetty, P.; Chalamalasetti, S. V.; Chakrapani, S. *J Biol Chem* **2012**, *287*, 36864.
(59) Rayes, D.; De Rosa, M. J.; Sine, S. M.; Bouzat, C. *J Neurosci* **2009**, *29*, 6022.
(60) Beato, M.; Groot-Kormelink, P. J.; Colquhoun, D.; Sivilotti, L. G. *J Neurosci* **2004**, *24*, 895.
(61) Amin, J.; Weiss, D. S. *Proc Biol Sci* **1996**, *263*, 273.
(62) Mowrey, D.; Cheng, M. H.; Liu, L. T.; Willenbring, D.; Lu, X.; Wymore, T.; Xu, Y.; Tang, P. *J Am Chem Soc* **2013**, *135*, 2172.
(63) Rubboli, F.; Court, J. A.; Sala, C.; Morris, C.; Chini, B.; Perry, E.; Clementi, F. *The European journal of neuroscience* **1994**, *6*, 1596.
(64) Wevers, A.; Jeske, A.; Lobron, C.; Birtsch, C.; Heinemann, S.; Maelicke, A.; Schroder, R.; Schroder, H. *Brain research. Molecular brain research* **1994**, *25*, 122.
(65) Levin, E. D.; Rezvani, A. H. *Current drug targets. CNS and neurological disorders* **2002**, *1*, 423.
(66) Bondarenko, V.; Tillman, T.; Xu, Y.; Tang, P. *Biochimica et biophysica acta* **2010**, *1798*, 1608.
(67) Hamouda, A. K.; Jin, X.; Sanghvi, M.; Srivastava, S.; Pandhare, A.; Duddempudi, P. K.; Steinbach, J. H.; Blanton, M. P. *Biochimica et biophysica acta* **2009**, *1788*, 1987.
(68) daCosta, C. J.; Michel Sturgeon, R.; Hamouda, A. K.; Blanton, M. P.; Baenziger, J. E. *Biochem Biophys Res Commun* **2011**, *407*, 456.
(69) Jensen, A. A.; Frolund, B.; Liljefors, T.; Krogsgaard-Larsen, P. *Journal of medicinal chemistry* **2005**, *48*, 4705.
(70) Jozwiak, K.; Ravichandran, S.; Collins, J. R.; Wainer, I. W. *Journal of medicinal chemistry* **2004**, *47*, 4008.
(71) Wilson, G. G.; Karlin, A. *Neuron* **1998**, *20*, 1269.
(72) Arias, H. R.; Rosenberg, A.; Targowska-Duda, K. M.; Feuerbach, D.; Jozwiak, K.; Moaddel, R.; Wainer, I. W. *The international journal of biochemistry & cell biology* **2010**, *42*, 1007.
(73) Pandya, A.; Yakel, J. L. *Biochem Pharmacol* **2011**, *82*, 952.
(74) Weltzin, M. M.; Schulte, M. K. *J Pharmacol Exp Ther* **2010**, *334*, 917.

(75) Nirthanan, S.; Garcia, G., 3rd; Chiara, D. C.; Husain, S. S.; Cohen, J. B. *J Biol Chem* **2008**, *283*, 22051.
(76) Marley, J.; Lu, M.; Bracken, C. *J Biomol NMR* **2001**, *20*, 71.
(77) Baxter, N. J.; Williamson, M. P. *J Biomol NMR* **1997**, *9*, 359.
(78) Wishart, D. S.; Bigam, C. G.; Yao, J.; Abildgaard, F.; Dyson, H. J.; Oldfield, E.; Markley, J. L.; Sykes, B. D. *J Biomol NMR* **1995**, *6*, 135.
(79) Folta-Stogniew, E.; Williams, K. R. *J Biomol Tech* **1999**, *10*, 51.
(80) Strop, P.; Brunger, A. T. *Protein Sci* **2005**, *14*, 2207.
(81) Dascal, N. *Current protocols in neuroscience / editorial board, Jacqueline N. Crawley ... [et al.]* **2001**, *Chapter 6*, Unit 6 12.
(82) Delaglio, F.; Grzesiek, S.; Vuister, G. W.; Zhu, G.; Pfeifer, J.; Bax, A. *J Biomol NMR* **1995**, *6*, 277.
(83) Goddard, T. D., and Kneller, D. G. **2001**.
(84) Guntert, P.; Mumenthaler, C.; Wuthrich, K. *J Mol Biol* **1997**, *273*, 283.
(85) Cornilescu, G.; Delaglio, F.; Bax, A. *J Biomol NMR* **1999**, *13*, 289.
(86) Humphrey, W.; Dalke, A.; Schulten, K. *J. Mol. Graph.* **1996**, *14*, 33.
(87) Koradi, R.; Billeter, M.; Wuthrich, K. *J Mol Graph* **1996**, *14*, 51.
(88) Quek, G. X. J.; Lin, D.; Halliday, J. I.; Absalom, N.; Ambrus, J. I.; Thompson, A. J.; Lochner, M.; Lummis, S. C. R.; McLeod, M. D.; Chebib, M. *ACS chemical neuroscience* **2010**, *1*, 796.
(89) Nelson, M. E.; Kuryatov, A.; Choi, C. H.; Zhou, Y.; Lindstrom, J. *Mol Pharmacol* **2003**, *63*, 332.
(90) Zwart, R.; Vijverberg, H. P. *Mol Pharmacol* **1998**, *54*, 1124.
(91) Phillips, J. C.; Braun, R.; Wang, W.; Gumbart, J.; Tajkhorshid, E.; Villa, E.; Chipot, C.; Skeel, R. D.; Kale, L.; Schulten, K. *J Comput Chem* **2005**, *26*, 1781.
(92) Smart, O. S.; Neduvelil, J. G.; Wang, X.; Wallace, B. A.; Sansom, M. S. *Journal of molecular graphics* **1996**, *14*, 354.
(93) Bondarenko, V.; Yushmanov, V. E.; Xu, Y.; Tang, P. *Biophys J* **2008**, *94*, 1681.
(94) Jansen, M.; Bali, M.; Akabas, M. H. *J Gen Physiol* **2008**, *131*, 137.
(95) Anand, R.; Conroy, W. G.; Schoepfer, R.; Whiting, P.; Lindstrom, J. *J Biol Chem* **1991**, *266*, 11192.

(96) Cooper, E.; Couturier, S.; Ballivet, M. *Nature* **1991**, *350*, 235.
(97) Akabas, M. H.; Kaufmann, C.; Archdeacon, P.; Karlin, A. *Neuron* **1994**, *13*, 919.
(98) Tapia, L.; Kuryatov, A.; Lindstrom, J. *Mol Pharmacol* **2007**, *71*, 769.
(99) Saladino, A. C.; Xu, Y.; Tang, P. *Biophys J* **2005**, *88*, 1009.
(100) Blanton, M. P.; Cohen, J. B. *Biochemistry* **1992**, *31*, 3738.
(101) Hamouda, A. K.; Sanghvi, M.; Chiara, D. C.; Cohen, J. B.; Blanton, M. P. *Biochemistry* **2007**, *46*, 13837.
(102) Krause, R. M.; Buisson, B.; Bertrand, S.; Corringer, P. J.; Galzi, J. L.; Changeux, J. P.; Bertrand, D. *Mol Pharmacol* **1998**, *53*, 283.
(103) Collins, T.; Millar, N. S. *Mol Pharmacol* **2010**, *78*, 198.
(104) Flood, P.; Krasowski, M. D. *Anesthesiology* **2000**, *92*, 1418.
(105) Gonzalez-Gutierrez, G.; Lukk, T.; Agarwal, V.; Papke, D.; Nair, S. K.; Grosman, C. *Proc Natl Acad Sci U S A* **2012**, *109*, 6331.
(106) Nury, H.; Van Renterghem, C.; Weng, Y.; Tran, A.; Baaden, M.; Dufresne, V.; Changeux, J. P.; Sonner, J. M.; Delarue, M.; Corringer, P. J. *Nature* **2011**, *469*, 428.
(107) Duret, G.; Van Renterghem, C.; Weng, Y.; Prevost, M.; Moraga-Cid, G.; Huon, C.; Sonner, J. M.; Corringer, P. J. *Proc Natl Acad Sci U S A* **2011**, *108*, 12143.
(108) Tong, K. I.; Yamamoto, M.; Tanaka, T. *J Biomol NMR* **2008**, *42*, 59.
(109) Skopp, R. N.; Lane, L. C. *Appl Theor Electrophor* **1988**, *1*, 61.
(110) Ma, D.; Liu, Z.; Li, L.; Tang, P.; Xu, Y. *Biochemistry* **2005**, *44*, 8790.
(111) Tang, P.; Mandal, P. K.; Xu, Y. *Biophys J* **2002**, *83*, 252.
(112) Battiste, J. L.; Wagner, G. *Biochemistry* **2000**, *39*, 5355.
(113) Tang, P.; Hu, J.; Liachenko, S.; Xu, Y. *Biophys J* **1999**, *77*, 739.
(114) Hinton, J. F.; Newkirk, D. K.; Fletcher, T. G.; Shungu, D. C. *Journal of magnetic resonance. Series B* **1994**, *105*, 11.
(115) Ludtke, S. J.; Baldwin, P. R.; Chiu, W. *J Struct Biol* **1999**, *128*, 82.
(116) Haeger, S.; Kuzmin, D.; Detro-Dassen, S.; Lang, N.; Kilb, M.; Tsetlin, V.; Betz, H.; Laube, B.; Schmalzing, G. *Nat Struct Mol Biol* **2010**, *17*, 90.
(117) Twyman, R. E.; Macdonald, R. L. *J Physiol* **1991**, *435*, 303.

(118) Larkin, M. A.; Blackshields, G.; Brown, N. P.; Chenna, R.; McGettigan, P. A.; McWilliam, H.; Valentin, F.; Wallace, I. M.; Wilm, A.; Lopez, R.; Thompson, J. D.; Gibson, T. J.; Higgins, D. G. *Bioinformatics* **2007**, *23*, 2947.

(119) Diven, C. F.; Wang, F.; Abukhdeir, A. M.; Salah, W.; Layden, B. T.; Geraldes, C. F.; Mota de Freitas, D. *Inorg Chem* **2003**, *42*, 2774.

(120) Pan, J.; Chen, Q.; Willenbring, D.; Yoshida, K.; Tillman, T.; Kashlan, O. B.; Cohen, A.; Kong, X. P.; Xu, Y.; Tang, P. *Nature communications* **2012**, *3*, 714.

(121) Canlas, C. G.; Ma, D.; Tang, P.; Xu, Y. *J Am Chem Soc* **2008**, *130*, 13294.

(122) Langelaan, D. N.; Wieczorek, M.; Blouin, C.; Rainey, J. K. *Journal of chemical information and modeling* **2010**, *50*, 2213.

(123) Fatima-Shad, K.; Barry, P. H. *Proc Biol Sci* **1993**, *253*, 69.

(124) Yushmanov, V. E.; Mandal, P. K.; Liu, Z.; Tang, P.; Xu, Y. *Biochemistry* **2003**, *42*, 3989.

(125) Ballesteros, J. A.; Deupi, X.; Olivella, M.; Haaksma, E. E. J.; Pardo, L. *Biophys J* **2000**, *79*, 2754.

(126) Pless, S. A.; Dibas, M. I.; Lester, H. A.; Lynch, J. W. *J Biol Chem* **2007**, *282*, 36057.

(127) Bera, A. K.; Chatav, M.; Akabas, M. H. *J Biol Chem* **2002**, *277*, 43002.

(128) Ye, Q.; Koltchine, V. V.; Mihic, S. J.; Mascia, M. P.; Wick, M. J.; Finn, S. E.; Harrison, N. L.; Harris, R. A. *J Biol Chem* **1998**, *273*, 3314.

(129) Cheng, X.; Lu, B.; Grant, B.; Law, R. J.; McCammon, J. A. *J Mol Biol* **2006**, *355*, 310.

(130) Law, R. J.; Henchman, R. H.; McCammon, J. A. *Proc Natl Acad Sci U S A* **2005**, *102*, 6813.

(131) Szarecka, A.; Xu, Y.; Tang, P. *Proteins* **2007**, *68*, 948.

(132) Gao, F.; Bren, N.; Burghardt, T. P.; Hansen, S.; Henchman, R. H.; Taylor, P.; McCammon, J. A.; Sine, S. M. *J Biol Chem* **2005**, *280*, 8443.

(133) Bertaccini, E.; Trudell, J. R. *Int Rev Neurobiol* **2001**, *48*, 141.

(134) Tang, P.; Xu, Y. *Proc Natl Acad Sci U S A* **2002**, *99*, 16035.

(135) Vedula, L. S.; Brannigan, G.; Economou, N. J.; Xi, J.; Hall, M. A.; Liu, R.; Rossi, M. J.; Dailey, W. P.; Grasty, K. C.; Klein, M. L.; Eckenhoff, R. G.; Loll, P. J. *J Biol Chem* **2009**, *284*, 24176.

(136) Yonkunas, M. J.; Xu, Y.; Tang, P. *Biophys J* **2005**, *89*, 2350.

(137) Szarecka, A.; Xu, Y.; Tang, P. *Biophys J* **2007**, *93*, 1895.

(138) Haddadian, E. J.; Cheng, M. H.; Coalson, R. D.; Xu, Y.; Tang, P. *J Phys Chem* **2008**, *112*, 13981.

(139) Gasteiger, E.; Gattiker, A.; Hoogland, C.; Ivanyi, I.; Appel, R. D.; Bairoch, A. *Nucleic Acids Res* **2003**, *31*, 3784.

(140) Laskowski, R. A.; Macarthur, M. W.; Moss, D. S.; Thornton, J. M. *Journal of Applied Crystallography* **1993**, *26*, 283.

(141) Tirion, M. M. *Phys Rev Lett* **1996**, *77*, 1905.

(142) Suhre, K.; Sanejouand, Y. H. *Nucleic Acids Res* **2004**, *32*, W610.

(143) Wang, F.; Imoto, K. *Proc Biol Sci* **1992**, *250*, 11.

(144) Cheng, M. H.; Liu, L. T.; Saladino, A. C.; Xu, Y.; Tang, P. *J Phys Chem* **2007**, *111*, 14186.

(145) MacKerell, A. D., Bashford, D., Bellott, M., Dunbrack, R.L., Evanseck, J. D., Field, M. J., Fischer, S., Gao, J., Guo, H., Ha, S., Joseph-McCarthy, D., Kuchnir, L., Kuczera, K., Lau, F.T.K., Mattos, C., Michnick, S., Ngo, T., Nguyen, D. T., Prodhom, B., Reiher, W.E., Roux, B., Schlenkrich, M., Smith, J. C., Stote, R., Straub, J., Watanabe, M., Wiorkiewicz-Kuczera, J., Yin, D., Karplus, M. *J. Phys. Chem. B* **1998**, *102*, 3586.

(146) Liu, Z.; Xu, Y.; Saladino, A. C.; Wymore, T.; Tang, P. *J Phys Chem A* **2004**, *108*, 781.

(147) Morris, G. M.; Goodsell, D. S.; Halliday, R. S.; Huey, R.; Hart, W. E.; Belew, R. K.; Olson, A. J. *J Comput Chem* **1998**, *19*, 1639.

(148) Zacharias, M.; Straatsma, T. P.; McCammon, J. A. *J Chem Phys* **1994**, *100*, 9025.

(149) Chipot, C.; Pearlman, D. A. *Molecular Simulation* **2002**, *28*, 1

(150) Henchman, R. H.; Wang, H. L.; Sine, S. M.; Taylor, P.; McCammon, J. A. *Biophys J* **2003**, *85*, 3007.

(151) Liu, R.; Loll, P. J.; Eckenhoff, R. G. *FASEB J* **2005**, *19*, 567.

(152) Campagna, J. A.; Miller, K. W.; Forman, S. A. *N Engl J Med* **2003**, *348*, 2110.

(153) Forman, S. A.; Miller, K. W. *Can J Anaesth* **2011**, *58*, 191.

(154) Yamashita, M.; Mori, T.; Nagata, K.; Yeh, J. Z.; Narahashi, T. *Anesthesiology* **2005**, *102*, 76.

(155) Hosie, A. M.; Wilkins, M. E.; da Silva, H. M.; Smart, T. G. *Nature* **2006**, *444*, 486.

(156) Yamakura, T.; Borghese, C.; Harris, R. A. *J Biol Chem* **2000**, *275*, 40879.

(157) Chen, Z. W.; Manion, B.; Townsend, R. R.; Covey, D. F.; Reichert, D. E.; Steinbach, J. H.; Sieghart, W.; Fuchs, K.; Evers, A. S. *Mol Pharmacol* **2012**.

(158) Chiara, D. C.; Dostalova, Z.; Jayakar, S. S.; Zhou, X.; Miller, K. W.; Cohen, J. B. *Biochemistry* **2012**, *51*, 836.
(159) Chiara, D. C.; Hong, F. H.; Arevalo, E.; Husain, S. S.; Miller, K. W.; Forman, S. A.; Cohen, J. B. *Mol Pharmacol* **2009**, *75*, 1084.
(160) Eckenhoff, R. G. *Proc Natl Acad Sci U S A* **1996**, *93*, 2807.
(161) Li, G. D.; Chiara, D. C.; Sawyer, G. W.; Husain, S. S.; Olsen, R. W.; Cohen, J. B. *J Neurosci* **2006**, *26*, 11599.
(162) Eckenhoff, R. G.; Xi, J.; Shimaoka, M.; Bhattacharji, A.; Covarrubias, M.; Dailey, W. P. *ACS chemical neuroscience* **2010**, *1*, 139.
(163) Hall, M. A.; Xi, J.; Lor, C.; Dai, S.; Pearce, R.; Dailey, W. P.; Eckenhoff, R. G. *J Med Chem* **2010**, *53*, 5667.
(164) Stewart, D. S.; Savechenkov, P. Y.; Dostalova, Z.; Chiara, D. C.; Ge, R.; Raines, D. E.; Cohen, J. B.; Forman, S. A.; Bruzik, K. S.; Miller, K. W. *J Med Chem* **2011**, *54*, 8124.
(165) Hilf, R. J.; Bertozzi, C.; Zimmermann, I.; Reiter, A.; Trauner, D.; Dutzler, R. *Nat Struct Mol Biol* **2010**, *17*, 1330.
(166) Kandasamy, S. K.; Lee, D. K.; Nanga, R. P.; Xu, J.; Santos, J. S.; Larson, R. G.; Ramamoorthy, A. *Biochimica et biophysica acta* **2009**, *1788*, 686.
(167) Canlas, C. G.; Cui, T.; Li, L.; Xu, Y.; Tang, P. *J Phys Chem* **2008**, *112*, 14312.
(168) Cui, T.; Bondarenko, V.; Ma, D.; Canlas, C.; Brandon, N. R.; Johansson, J. S.; Xu, Y.; Tang, P. *Biophys J* **2008**, *94*, 4464.
(169) Cui, T.; Canlas, C. G.; Xu, Y.; Tang, P. *Biochimica et biophysica acta* **2010**, *1798*, 161.
(170) Xu, Y.; Seto, T.; Tang, P.; Firestone, L. *Biophys J* **2000**, *78*, 746.
(171) Tang, P.; Eckenhoff, R. G.; Xu, Y. *Biophys J* **2000**, *78*, 1804.
(172) Mayer, M.; Meyer, B. *Angew Chem Int Edit* **1999**, *38*, 1784.
(173) Takahashi, H.; Nakanishi, T.; Kami, K.; Arata, Y.; Shimada, I. *Nat Struct Biol* **2000**, *7*, 220.
(174) Ramos, A.; Kelly, G.; Hollingworth, D.; Pastore, A.; Frenkiel, T. *J Am Chem Soc* **2000**, *122*, 11311.
(175) Brannigan, G.; LeBard, D. N.; Henin, J.; Eckenhoff, R. G.; Klein, M. L. *Proc Natl Acad Sci U S A* **2010**, *107*, 14122.
(176) Willenbring, D.; Liu, L. T.; Mowrey, D.; Xu, Y.; Tang, P. *Biophys J* **2011**, *101*, 1905.
(177) Chen, Q. A.; Cheng, M. H.; Xu, Y.; Tang, P. *Biophys J* **2010**, *99*, 1801.

(178) Murail, S.; Wallner, B.; Trudell, J. R.; Bertaccini, E.; Lindahl, E. *Biophys J* **2011**, *100*, 1642.

(179) Hamouda, A. K.; Chiara, D. C.; Sauls, D.; Cohen, J. B.; Blanton, M. P. *Biochemistry* **2006**, *45*, 976.

(180) Hosie, A. M.; Clarke, L.; da Silva, H.; Smart, T. G. *Neuropharmacology* **2009**, *56*, 149.

(181) Gotti, C.; Riganti, L.; Vailati, S.; Clementi, F. *Curr Pharm Des* **2006**, *12*, 407.

(182) Zhang, L.; Oz, M.; Stewart, R. R.; Peoples, R. W.; Weight, F. F. *Br J Pharmacol* **1997**, *120*, 353.

(183) Cheng, X.; Ivanov, I.; Wang, H.; Sine, S. M.; McCammon, J. A. *Biophys J* **2007**, *93*, 2622.

(184) Jha, A.; Cadugan, D. J.; Purohit, P.; Auerbach, A. *J Gen Physiol* **2007**, *130*, 547.

(185) Lee, W. Y.; Free, C. R.; Sine, S. M. *J Neurosci* **2009**, *29*, 3189.

(186) Bahar, I.; Atilgan, A. R.; Erman, B. *Fold Des* **1997**, *2*, 173.

(187) Yang, L. W.; Liu, X.; Jursa, C. J.; Holliman, M.; Rader, A. J.; Karimi, H. A.; Bahar, I. *Bioinformatics* **2005**, *21*, 2978.

(188) Bouzat, C.; Gumilar, F.; Spitzmaul, G.; Wang, H. L.; Rayes, D.; Hansen, S. B.; Taylor, P.; Sine, S. M. *Nature* **2004**, *430*, 896.

(189) Chakrapani, S.; Bailey, T. D.; Auerbach, A. *J Gen Physiol* **2004**, *123*, 341.

(190) Schofield, C. M.; Jenkins, A.; Harrison, N. L. *J Biol Chem* **2003**, *278*, 34079.

(191) Absalom, N. L.; Lewis, T. M.; Kaplan, W.; Pierce, K. D.; Schofield, P. R. *J Biol Chem* **2003**, *278*, 50151.

(192) Shen, X. M.; Ohno, K.; Tsujino, A.; Brengman, J. M.; Gingold, M.; Sine, S. M.; Engel, A. G. *The Journal of clinical investigation* **2003**, *111*, 497.

(193) Tang, P.; Yan, B.; Xu, Y. *Biophys J* **1997**, *72*, 1676.

(194) Xu, Y.; Tang, P. *Biochimica et biophysica acta* **1997**, *1323*, 154.

(195) Downie, D. L.; Vicente-Agullo, F.; Campos-Caro, A.; Bushell, T. J.; Lieb, W. R.; Franks, N. P. *J Biol Chem* **2002**, *277*, 10367.

(196) Sudweeks, S. N.; Yakel, J. L. *J Physiol* **2000**, *527 Pt 3*, 515.

(197) Liu, Q.; Huang, Y.; Xue, F.; Simard, A.; DeChon, J.; Li, G.; Zhang, J.; Lucero, L.; Wang, M.; Sierks, M.; Hu, G.; Chang, Y.; Lukas, R. J.; Wu, J. *J Neurosci* **2009**, *29*, 918.

(198) Palma, E.; Maggi, L.; Barabino, B.; Eusebi, F.; Ballivet, M. *J Biol Chem* **1999**, *274*, 18335.

(199) Violet, J. M.; Downie, D. L.; Nakisa, R. C.; Lieb, W. R.; Franks, N. P. *Anesthesiology* **1997**, *86*, 866.

(200) Zhao, L.; Kuo, Y. P.; George, A. A.; Peng, J. H.; Purandare, M. S.; Schroeder, K. M.; Lukas, R. J.; Wu, J. *J Pharmacol Exp Ther* **2003**, *305*, 1132.

(201) Durrant, J. D.; Oliveira, C. A. d.; McCammon, J. A. *J Mol Graphics Modell* **2011**, *29*, 773.

(202) Nickalls, R. W.; Mapleson, W. W. *Br J Anaesth* **2003**, *91*, 170.

(203) Wu, J.; Kuo, Y. P.; George, A. A.; Xu, L.; Hu, J.; Lukas, R. J. *J Biol Chem* **2004**, *279*, 37842.

(204) Flood, P.; Coates, K. M. *Anesth Analg* **2002**, *95*, 83.

(205) Schumann, F. H.; Riepl, H.; Maurer, T.; Gronwald, W.; Neidig, K. P.; Kalbitzer, H. R. *J Biomol NMR* **2007**, *39*, 275.

(206) Spurny, R.; Billen, B.; Howard, R. J.; Brams, M.; Debaveye, S.; Price, K. L.; Weston, D. A.; Strelkov, S. V.; Tytgat, J.; Bertrand, S.; Bertrand, D.; Lummis, S. C.; Ulens, C. *J Biol Chem* **2013**, *288*, 8355.

(207) Jenkins, A.; Greenblatt, E. P.; Faulkner, H. J.; Bertaccini, E.; Light, A.; Lin, A.; Andreasen, A.; Viner, A.; Trudell, J. R.; Harrison, N. L. *J Neurosci* **2001**, *21*, RC136.

(208) Mittermaier, A. K.; Kay, L. E. *Trends in biochemical sciences* **2009**, *34*, 601.

(209) Kleckner, I. R.; Foster, M. P. *Biochimica et biophysica acta* **2011**, *1814*, 942.

(210) Palmer, A. G., 3rd; Kroenke, C. D.; Loria, J. P. *Methods in enzymology* **2001**, *339*, 204.

(211) Prevost, M. S.; Sauguet, L.; Nury, H.; Van Renterghem, C.; Huon, C.; Poitevin, F.; Baaden, M.; Delarue, M.; Corringer, P. J. *Nat Struct Mol Biol* **2012**, *19*, 642.

(212) Yamodo, I. H.; Chiara, D. C.; Cohen, J. B.; Miller, K. W. *Biochemistry* **2010**, *49*, 156.

(213) Lyu, P. C.; Sherman, J. C.; Chen, A.; Kallenbach, N. R. *Proc Natl Acad Sci U S A* **1991**, *88*, 5317.

(214) Richardson, J. S.; Richardson, D. C. *Science* **1988**, *240*, 1648.

(215) Varga, Z.; Kovacs, A. *Int J Quantum Chem* **2005**, *105*, 302.

(216) Horenstein, J.; Wagner, D. A.; Czajkowski, C.; Akabas, M. H. *Nat Neurosci* **2001**, *4*, 477.

(217) Bourne, Y.; Radic, Z.; Araoz, R.; Talley, T. T.; Benoit, E.; Servent, D.; Taylor, P.; Molgo, J.; Marchot, P. *Proc Natl Acad Sci U S A* **2010**, *107*, 6076.

(218) Ambrus, J. I.; Halliday, J. I.; Kanizaj, N.; Absalom, N.; Harpsoe, K.; Balle, T.; Chebib, M.; McLeod, M. D. *Chem Commun (Camb)* **2012**, *48*, 6699.

(219) Thompson, A. J.; Lester, H. A.; Lummis, S. C. *Q Rev Biophys* **2010**, *43*, 449.
(220) Auerbach, A. *J Physiol* **2010**, *588*, 573.
(221) Lee, W. Y.; Sine, S. M. *Nature* **2005**, *438*, 243.
(222) Bocquet, N. *Nature* **2007**, *445*, 116.
(223) Tassonyi, E.; Charpantier, E.; Muller, D.; Dumont, L.; Bertrand, D. *Brain Res Bull* **2002**, *57*, 133.
(224) Weng, Y.; Yang, L.; Corringer, P. J.; Sonner, J. M. *Anesth Analg* **2010**, *110*, 59.
(225) Chennubhotla, C.; Bahar, I. *PLoS Comput Biol* **2007**, *3*, 1716.
(226) Del Sol, A.; Arauzo-Bravo, M. J.; Amoros, D.; Nussinov, R. *Genome Biol* **2007**, *8*, R92.
(227) del Sol, A.; Fujihashi, H.; Amoros, D.; Nussinov, R. *Mol Syst Biol* **2006**, *2*, 2006 0019.
(228) Park, K.; Kim, D. *BMC bioinformatics* **2011**, *12 Suppl 1*, S23.
(229) Haliloglu, T.; Ben-Tal, N. *PLoS Comput Biol* **2008**, *4*, e1000164.
(230) Sidje, R. B.; Stewart, W. J. *Computational Statistics & Data Analysis* **1999**, *29*, 345.
(231) Krissinel, E.; Henrick, K. *J Mol Biol* **2007**, *372*, 774.
(232) Kabsch, W. *Acta Crystallogr. D Biol. Crystallogr.* **2010**, *66*, 133.
(233) Emsley, P.; Lohkamp, B.; Scott, W. G.; Cowtan, K. *Acta Crystallogr. D Biol. Crystallogr.* **2010**, *66*, 486.
(234) Adams, P. D.; Afonine, P. V.; Bunkoczi, G.; Chen, V. B.; Davis, I. W.; Echols, N.; Headd, J. J.; Hung, L. W.; Kapral, G. J.; Grosse-Kunstleve, R. W.; McCoy, A. J.; Moriarty, N. W.; Oeffner, R.; Read, R. J.; Richardson, D. C.; Richardson, J. S.; Terwilliger, T. C.; Zwart, P. H. *Acta Crystallogr. D Biol. Crystallogr.* **2010**, *66*, 213.
(235) Chen, V. B.; Arendall, W. B.; Headd, J. J.; Keedy, D. A.; Immormino, R. M.; Kapral, G. J.; Murray, L. W.; Richardson, J. S.; Richardson, D. C. *Acta Crystallogr. D Biol. Crystallogr.* **2010**, *66*, 12.
(236) Winn, M. D.; Ballard, C. C.; Cowtan, K. D.; Dodson, E. J.; Emsley, P.; Evans, P. R.; Keegan, R. M.; Krissinel, E. B.; Leslie, A. G.; McCoy, A.; McNicholas, S. J.; Murshudov, G. N.; Pannu, N. S.; Potterton, E. A.; Powell, H. R.; Read, R. J.; Vagin, A.; Wilson, K. S. *Acta Crystallogr. D Biol. Crystallogr.* **2011**, *67*, 235.
(237) Schrodinger, L. 2010.
(238) Purohit, P.; Auerbach, A. *J Gen Physiol* **2007**, *130*, 569.
(239) Purohit, P.; Auerbach, A. *J Gen Physiol* **2007**, *130*, 559.

(240) Andersen, N.; Corradi, J.; Bartos, M.; Sine, S. M.; Bouzat, C. *J Neurosci* **2011**, *31*, 3662.
(241) Mukhtasimova, N.; Sine, S. M. *Biophys J* **2013**, *104*, 355.
(242) Mowrey, D.; Cheng, M. H.; Liu, L. T.; Willenbring, D.; Lu, X.; Wymore, T.; Xu, Y.; Tang, P. *J Am Chem Soc* **2013**.
(243) Kash, T. L.; Jenkins, A.; Kelley, J. C.; Trudell, J. R.; Harrison, N. L. *Nature* **2003**, *421*, 272.
(244) Xiu, X.; Hanek, A. P.; Wang, J.; Lester, H. A.; Dougherty, D. A. *J Biol Chem* **2005**, *280*, 41655.
(245) Cadugan, D. J.; Auerbach, A. *Biophys J* **2010**, *99*, 798.
(246) Purohit, P.; Auerbach, A. *J Gen Physiol* **2010**, *135*, 321.
(247) Bourne, Y.; Talley, T. T.; Hansen, S. B.; Taylor, P.; Marchot, P. *EMBO J* **2005**, *24*, 1512.
(248) Sine, S. M.; Shen, X. M.; Wang, H. L.; Ohno, K.; Lee, W. Y.; Tsujino, A.; Brengmann, J.; Bren, N.; Vajsar, J.; Engel, A. G. *J Gen Physiol* **2002**, *120*, 483.
(249) Frueh, D. P.; Arthanari, H.; Koglin, A.; Vosburg, D. A.; Bennett, A. E.; Walsh, C. T.; Wagner, G. *Nature* **2008**, *454*, 903.
(250) Rao, B. D. *Methods in enzymology* **1989**, *176*, 279.
(251) Ishima, R.; Torchia, D. A. *Nat Struct Biol* **2000**, *7*, 740.
(252) Corringer, P. J.; Bertrand, S.; Galzi, J. L.; Devillers-Thiery, A.; Changeux, J. P.; Bertrand, D. *Neuron* **1999**, *22*, 831.
(253) Cymes, G. D.; Grosman, C. *Nature* **2011**, *474*, 526.
(254) Changeux, J. P.; Edelstein, S. J. *Science* **2005**, *308*, 1424.
(255) Lasalde, J. A.; Tamamizu, S.; Butler, D. H.; Vibat, C. R.; Hung, B.; McNamee, M. G. *Biochemistry* **1996**, *35*, 14139.
(256) Li, L.; Lee, Y. H.; Pappone, P.; Palma, A.; McNamee, M. G. *Biophys J* **1992**, *62*, 61.
(257) Lee, Y. H.; Li, L.; Lasalde, J.; Rojas, L.; McNamee, M.; Ortiz-Miranda, S. I.; Pappone, P. *Biophys J* **1994**, *66*, 646.
(258) daCosta, C. J.; Baenziger, J. E. *J Biol Chem* **2009**, *284*, 17819.
(259) Blundell, T. L.; Srinivasan, N. *Proc Natl Acad Sci U S A* **1996**, *93*, 14243.
(260) Goodsell, D. S.; Olson, A. J. *Annual review of biophysics and biomolecular structure* **2000**, *29*, 105.
(261) Lee, J.; Blaber, M. *Proc Natl Acad Sci U S A* **2011**, *108*, 126.

(262) Dayhoff, J. E.; Shoemaker, B. A.; Bryant, S. H.; Panchenko, A. R. *J Mol Biol* **2010**, *395*, 860.
(263) Anishkin, A.; Milac, A. L.; Guy, H. R. *Proteins* **2010**, *78*, 932.
(264) Verdon, G.; Boudker, O. *Nat Struct Mol Biol* **2012**, *19*, 355.
(265) Hemmings, H. C., Jr.; Akabas, M. H.; Goldstein, P. A.; Trudell, J. R.; Orser, B. A.; Harrison, N. L. *Trends in pharmacological sciences* **2005**, *26*, 503.
(266) Roberts, M. T.; Phelan, R.; Erlichman, B. S.; Pillai, R. N.; Ma, L.; Lopreato, G. F.; Mihic, S. J. *J Biol Chem* **2006**, *281*, 3305.
(267) Li, R.; Bowerman, B. *Cold Spring Harb Perspect Biol* **2010**, *2*, a003475.
(268) Cheng, M. H.; Coalson, R. D.; Tang, P. *J Am Chem Soc* **2010**, *132(46)*, 16442.
(269) Mackerell, A. D., Jr.; Feig, M.; Brooks, C. L., 3rd *J Comput Chem* **2004**, *25*, 1400.
(270) Vanommeslaeghe, K.; Hatcher, E.; Acharya, C.; Kundu, S.; Zhong, S.; Shim, J.; Darian, E.; Guvench, O.; Lopes, P.; Vorobyov, I.; Mackerell, A. D., Jr. *J Comput Chem* **2010**, *31*, 671.
(271) Hoover, W. *Phys. Rev. A.* **1985**, *31*, 1695.
(272) Nosé, S. *J. Chem. Phys.* **1984**, *81*, 511.
(273) Darden, T.; York, D.; Pedersen, L. *J Chem Phys* **1993**, *98*, 10089.
(274) Beckstein, O.; Sansom, M. S. *Phys Biol* **2004**, *1*, 42.
(275) McMillan, B. *Ann. Math. Statist.* **1953**, *24*, 196.
(276) Efron, B. *Ann Stat* **1979**, *7*, 1.
(277) Atilgan, A. R.; Durell, S. R.; Jernigan, R. L.; Demirel, M. C.; Keskin, O.; Bahar, I. *Biophys J* **2001**, *80*, 505.
(278) Bakan, A.; Meireles, L. M.; Bahar, I. *Bioinformatics* **2011**, *27*, 1575.
(279) Agresti, A.; Caffo, B. *Am. Stat.* **2000**, *54*, 280.
(280) Zhu, F.; Hummer, G. *Proc Natl Acad Sci U S A* **2010**, *107*, 19814.
(281) Nury, H.; Poitevin, F.; Van Renterghem, C.; Changeux, J. P.; Corringer, P. J.; Delarue, M.; Baaden, M. *Proc Natl Acad Sci U S A* **2010**, *107*, 6275.
(282) Furuya, R.; Oka, K.; Watanabe, I.; Kamiya, Y.; Itoh, H.; Andoh, T. *Anesth Analg* **1999**, *88*, 174.
(283) Barann, M.; Linden, I.; Witten, S.; Urban, B. W. *Anesth Analg* **2008**, *106*, 846.

(284) Taly, A.; Delarue, M.; Grutter, T.; Nilges, M.; Le Novere, N.; Corringer, P. J.; Changeux, J. P. *Biophys J* **2005**, *88*, 3954.
(285) Yi, M.; Tjong, H.; Zhou, H. X. *Proc Natl Acad Sci U S A* **2008**, *105*, 8280.
(286) Grosman, C.; Auerbach, A. *J Gen Physiol* **2000**, *115*, 637.
(287) Grandl, J.; Danelon, C.; Hovius, R.; Vogel, H. *Eur Biophys J* **2006**, *35*, 685.
(288) van der Gucht, J.; Sykes, C. *Cold Spring Harb Perspect Biol* **2009**, *1*, a001909.
(289) Wang, F. *Cold Spring Harb Perspect Biol* **2009**, *1*, a002980.
(290) Herrmann, T.; Guntert, P.; Wuthrich, K. *J Mol Biol* **2002**, *319*, 209.
(291) Montal, M.; Opella, S. J. *Biochimica et biophysica acta* **2002**, *1565*, 287.